2012

CRYOGENIC MACHINING AND BURNISHING OF AZ31B MAGNESIUM ALLOY FOR ENHANCED SURFACE INTEGRITY AND FUNCTIONAL PERFORMANCE

Zhengwen Pu
University of Kentucky, puzwen@gmail.com

Click here to let us know how access to this document benefits you.

Recommended Citation

CRYOGENIC MACHINING AND BURNISHING OF *AZ31B* MAGNESIUM ALLOY FOR ENHANCED SURFACE INTEGRITY AND FUNCTIONAL PERFORMANCE

_____

DISSERTATION

_____

A dissertation submitted in partial fulfillment of the
requirements for the degree of Doctor of Philosophy in the
College of Engineering
at the University of Kentucky

By
Zhengwen Pu

Lexington, Kentucky

Director: Dr. I.S. Jawahir, Professor of Mechanical Engineering

Lexington, Kentucky

2012

ABSTRACT OF DISSERTATION

CRYOGENIC MACHINING AND BURNISHING OF *AZ31B* MAGNESIUM ALLOY FOR ENHANCED SURFACE INTEGRITY AND FUNCTIONAL PERFORMANCE

Surface integrity of manufactured components has a critical impact on their functional performance. Magnesium alloys are lightweight materials used in the transportation industry and are also emerging as a potential material for biodegradable medical implants. However, the unsatisfactory corrosion performance of *Mg* alloys limits their application to a great extent. Surface integrity factors, such as grain size, crystallographic orientation and residual stress, have been proved to remarkably influence the functional performance of magnesium alloys, including corrosion resistance, wear resistance and fatigue life.

In this dissertation, the influence of machining conditions, including dry and cryogenic cooling (liquid nitrogen was sprayed to the machined surface during machining), cutting edge radius, cutting speed and feed rate, on the surface integrity of *AZ31B Mg* alloy was investigated. Cryogenic machining led to the formation of a "featureless layer" on the machined surface where significant grain refinement from 12 μm to 31 nm occurred due to dynamic recrystallization (DRX), as well as increased intensity of basal plane on the surface and more compressive residual stresses. Dry and cryogenic burnishing experiments of the same material were conducted using a fixed roller setup. The thickness of the processed-influenced layer, where remarkable microstructural changes occurred, was dramatically increased from the maximum value of 20 μm during machining to 3.4 mm during burnishing. The burnishing process also produced a stronger basal texture on the surface than the machining process.

Preliminary corrosion tests were conducted to evaluate the corrosion performance of selected machined and burnished *AZ31B Mg* samples in 5% *NaCl* solution and simulated body fluid (*SBF*). Cryogenic cooling and large edge radius tools were found to significantly improve the corrosion performance of machined samples in both solutions. The largest improvement in the material's corrosion performance was achieved by burnishing.

A finite element study was conducted for machining of *AZ31B Mg* alloy and calibrated using the experimental data. A user subroutine was developed and incorporated to predict the grain size changes induced by machining. Good agreements between the predicted and measured grain size as well as thickness of featureless layers were achieved. Numerical studies were extended to include the influence of rake angle, feed rate and cutting speed on the featureless layer formation.

KEYWORDS: Surface Integrity, Cryogenic Machining/Burnishing, Corrosion Resistance, Finite Element Analysis, Magnesium Alloys

<u>   Zhengwen Pu   </u>

<u>   April, 24th, 2012   </u>

CRYOGENIC MACHINING AND BURNISHING OF *AZ31B* MAGNESIUM ALLOY FOR ENHANCED SURFACE INTEGRITY AND FUNCTIONAL PERFORMANCE

By

Zhengwen Pu

I.S. Jawahir

Director of Dissertation

J. M. McDonough

Director of Graduate Studies

April, 30th, 2012

ACKNOWLEDGMENTS

Last but not least, I would like to thank my family for their unconditional love and support without which I would not have accomplished my goals in life. Special thanks are due to my fiancée, who let me realize that family should always be the first priority in life.

TABLE OF CONTENTS

LIST OF TABLES

CHAPTER 1: INTRODUCTION

1.1   Introduction

Failures of metallic materials due to wear, corrosion and/or fatigue often start at the surface of manufactured products. The quality of the surface produced by manufacturing processes has critical influence on the functional performance of the products. The concept of "surface integrity (SI)" was used to refer to the surface quality by Field and Kahles in 1964 and defined as "the inherent or enhanced condition of a surface produced in machining or other surface generating operation" (Field and Kahles, 1964). They also developed a systematic method to study and evaluate the characteristic features of machined surfaces in three different levels as shown in Table 1.1 (Field et al., 1972). Among these SI factors, residual stress is one of the most frequently studied due to its proved relationship with fatigue life (Leverant et al., 1979; Sasahara, 2005). Microstructural changes, especially "white layer" formation, are also well investigated because they were proved to reduce fatigue life (Hashimoto et al., 2006). Recently, more and more studies on surface integrity have been reported by researchers from various countries due to its close relationship with functional performance of the manufactured products (Jawahir et al., 2011). However, most of the current researches were conducted on difficult-to-machine materials, such as *AISI 52100* steel, nickel-based superalloys and titanium alloys. The purpose of these studies was mainly to avoid the formation of undesirable surface integrity, including tensile residual stresses, white layer and other surface defects. The possibility of using manufacturing processes to improve functional

performance of manufactured products through inducing desirable surface integrity has not been well investigated.

Table 1.1: Different levels of surface integrity (SI) (Field et al., 1972)

Minimum SI data set	*Standard SI data set*	*Extended SI data set*

Surface finish
Macrostructure (10× or less)
    Macrocracks
    Macroetch indications
Microstructure
    Microcracks
    Plastic deformation
    Phase transformation
    Intergranular attack
    Pits, tears, laps,
        protrusions
    Built-up edge
    Melted and redeposited
        layers
    Selective etching
Microhardness
	Minimum SI data set
	
	Fatigue tests (screening)
	Stress corrosion tests
	
	Residual stress and distortion
		Standard SI data set
		
		Fatigue tests (extended to obtain design data)
		
		Additional mechanical tests
		    Tensile
		    Stress rupture
		    Creep
		    Other specific tests
		    (e.g., bearing
		    performance, sliding
		    friction evaluation,
		    sealing properties of
		    surfaces)

The functional performance of metallic materials, including corrosion and wear resistance (Wang et al., 2006; Zhang et al., 2006) as well as fatigue life (Villegas et al., 2005), was substantially enhanced by surface nanocrystallization (SNC) induced by severe plastic deformation (SPD) processes. Machining is a SPD process involving large strains (typically 2–10), high strain-rates (up to 10^6 s^{-1}) and large heat generation. Nanocrystalline grain structure was found in the white layer of *AISI 52100* steel (Ramesh et al., 2005) and IN100 nickel-based superalloy (Wusatowska-Sarnek et al., 2011). The potential of machining as a SNC process was also supported by recent literature (Chandrasekar et al., 2011) where it was shown that nanocrystalline grain structures

2

could be found on the machined surface of various materials. However, the use of machining to enhance functional performance of materials through induced nano/ultrafine grain structures on the surface has not been reported.

Magnesium alloys are promising lightweight materials for both automotive and aerospace applications. Recently, they are also emerging as a novel biodegradable material for temporary internal fixation implants (Witte, 2010). However, one major limitation of the wide application has been their unsatisfactory corrosion performance. The poor corrosion resistance of *Mg* alloys also limits their applications as lightweight materials for the transportation industry (Luo, 2002). Grain refinement was proved to be an effective way to improve the corrosion resistance of magnesium alloys as well as their fatigue life (Wang et al., 2007). Therefore, there is a possibility that machining/burnishing can be used to enhance the functional performance of magnesium alloys by formation of a grain refinement layer on the surface.

In addition to grain size, other SI factors, such as residual stresses, were also reported to have remarkable influence on the corrosion resistance of magnesium alloys. Large compressive residual stresses induced by deep rolling were claimed to reduce the corrosion rate of a biphasic *MgCa3.0* alloy by a factor of approximately 100 (Denkena and Lucas, 2007). Crystallographic orientations, which could be changed significantly by machining (To et al., 2003; Velásquez et al., 2010), were reported recently to have a dramatic influence on the corrosion resistance of *AZ31 Mg* alloy (Song et al., 2010b). Strong basal texture on the surface resulted in significantly enhanced corrosion resistance (Song et al., 2010).

1.2 Research Objectives

The literature suggests that traditional manufacturing processes involving SPD such as machining and burnishing may be used to improve the corrosion resistance of magnesium alloys through inducing desirable surface integrity factors, such as grain refinement, compressive residual stresses and stronger basal texture. However, a systematic study is greatly needed since various SI factors are involved and will change at the same time during processing. Another concern is that grain growth may occur due to high temperature generated during machining/burnishing and the grain refinement may not be maintained on the workpiece surface/subsurface. This research is an attempt to address these concerns and its major objectives are:

1) Investigating the influence of processing conditions, especially the use of cryogenic cooling during processing, on surface integrity changes such as microstructure, crystallographic orientations, residual stresses, etc., generated by machining and burnishing;

2) Evaluating the resulting corrosion performance of machined and burnished samples processed under different conditions in both 5% *NaCl* solution and simulated body fluid (*SBF*); and

3) Developing a numerical method using finite element modeling (FEM) techniques to predict grain size changes in the surface and sub-surface induced by machining under different processing conditions.

1.3   Dissertation Outline

In the following Chapter 2, a literature review is conducted which covers experimental and numerical studies on surface integrity in machining/burnishing and its influence on functional performance. In Chapter 3, experimental results on the surface integrity resulting from machining under different conditions including cooling method (dry and cryogenic), cutting edge radius, cutting speed and feed rate are presented. The surface integrity factors investigated are microstructure, crystallographic orientations, residual stresses, hardness and surface roughness. Chapter 4 presents the experimental results on the surface integrity resulting from burnishing experiments. The same surface integrity factors were investigated as in machining. The main burnishing conditions studied are dry and cryogenic cooling. The selected machined and burnished Mg samples were subjected to corrosion test in both 5% $NaCl$ solution and SBF and these results are presented in Chapter 5. Chapter 6 presents a numerical study on the grain size changes and grain refinement layer thickness induced by machining. Good agreement with experimental observations was achieved by using a customized user subroutine combined with commercial FEM software. Finally, a summary of conclusions resulting from this work, as well as recommendations for future work, are presented in Chapter 7.

CHAPTER 2: LITERATURE REVIEW

Surface integrity (SI) of machined components has been studied since the 1950's. Residual stress is one of the most commonly studied SI factors. There are growing commercial interests in microstructural changes due to recent research findings that thin layers of nanocrystalline grain structures were produced on the machined surface of various materials. In general, this can improve the functional performance of machined products. Finite element methods for predicting surface integrity are rapidly emerging due to the growing power of computers. A review of these experimental and numerical studies is presented in this chapter.

Another important topic reviewed in this chapter is the influence of various SI factors on the functional performance of manufactured components, such as corrosion/wear/fatigue resistance. The focus of this part is on the corrosion resistance of *Mg* alloys since the unsatisfactory corrosion performance impedes their emerging application as biodegradable fixation implants and the application as lightweight materials for transportation industry. The mechanism for grain refinement in machining and empirical relationships concerning dynamic recrystallization (DRX) in *Mg* alloys are also reviewed, which provides a basis for explaining the experimental results presented in the following chapters as well for the modeling work in Chapter 6.

2.1   Surface Integrity in Machining

Machining is one of the most common manufacturing processes and is used for both metallic and non-metallic components. One of its key functions is to achieve the

desired geometry accuracy and the machined surfaces are often exposed to various thermal-mechanical loadings, such as a machined piston surface in a combustion engine. In addition to required geometric accuracy and surface finish, more and more researches have demonstrated the importance of material properties beneath the machined surface on the functional performance of machined components, such as residual stress, microstructures, etc., which are the focus of the literature survey in the present study.

2.1.1 Experimental studies on residual stresses

One of the earliest efforts to investigate the influence of machining on SI was conducted by Henriksen (Henriksen, 1951). He studied the changes of residual stresses caused by the machining process and claimed that mechanical effects were more important than thermal effects in the development of residual stresses. These residual stress changes were caused by heterogeneous plastic deformations, thermal contractions and/or phase transformation. There are mainly two types of residual stresses. One is macro residual stresses which vary within the body of the component over a scale much larger than the grain size. The other type is micro level and may vary from grain to grain or within one single grain. For most cases, the residual stresses reported from machining literature are macro level residual stresses.

Sadat and Bailey (Sadat and Bailey, 1987) studied the influence of cutting speed, feed rate and depth of cut on the residual stresses of machined *AISI 4340* steel. They showed that peak residual stresses were tensile at low speeds (30 and 60 m/min) for all feed rates, and compressive at high speed (90 m/min) for all feed rates. Peak residual stresses and the depth of stressed region increased with an increase in feed rate and depth of cut, but decreased with an increase in cutting speed.

7

M'Saoubi et al. (M'Saoubi et al., 1999) showed that increased cutting speed led to larger tensile residual stress on the machined surface but decreased the thickness of the tensile layer in orthogonal machining of *AISI 316L* steels as shown in Figure 2.1. They showed that feed rates had little influence on the surface residual stresses but increasing values of feed rate had a tendency to increase the compressive stress values in the sub-surface, and the thickness of the tensile layer. They claimed that it was due to a mechanical effect causing the augmentation of the compressive zone in the region of the workpiece situated below the cutting edge, leading to greater elastic relaxation after machining.
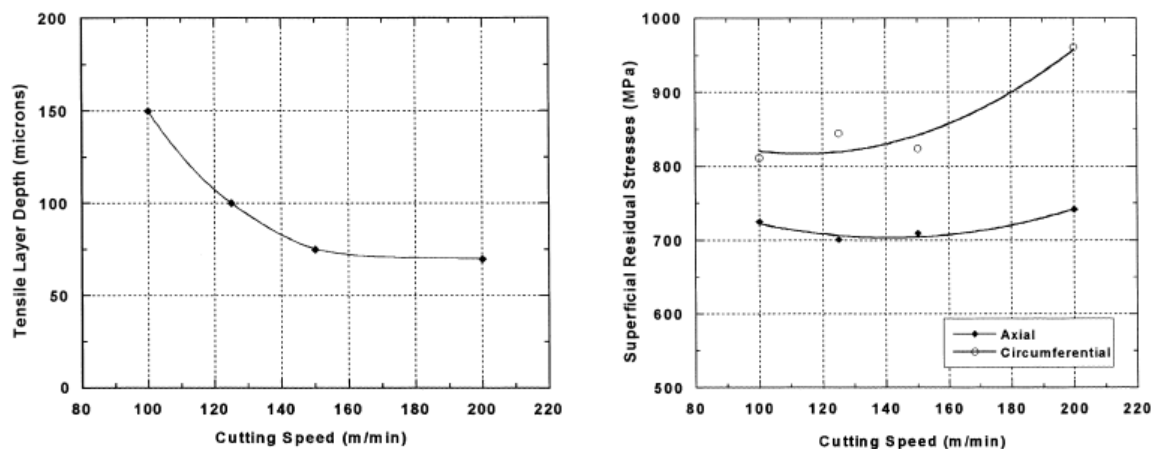
Figure 2.1: Surface residual stresses and tensile layer depth as functions of cutting speed (M'Saoubi et al., 1999).

Thiele et al. (Thiele et al., 2000) presented the results of an experimental investigation of the effects of cutting edge geometry and workpiece hardness on the residual stresses in finish hard-turning of *AISI 52100* steel. Large edge radius tools were found to produce more compressive residual stress in the axial and hoop directions than small edge radius tools. Small edge hone tools typically produced over-tempered surface

8

layers, which were in residual tension for low hardness (41 HRC) steel and in residual compression for high hardness (57 HRC) steel.

The importance of cutting edge radius of the tools on residual stresses was highlighted by Outeiro et al. (Outeiro et al., 2010) in orthogonal turning of *AISI 1045* steel. Large edge radius tools were found to increase the forces and temperatures, which led to increased tensile residual stresses on the machined surface.

2.1.2   Experimental studies on microstructural changes and surface nanocrystallization

Field and Kahles (Field and Kahles, 1971) were among the first to investigate the influence of machining on microstructures of the machined components. They found that significant changes had occurred after machining of various materials, including different steels and *Inconel 718*. A "white layer" was found on the hole surface after drilling of *AISI 4340* steel. This layer had a white appearance under optical microscope after using standard etchants and was claimed to be consisted of untempered martensite. The hardness of this layer was increased from 52 HRC to 61 HRC. An overtempered martensitic layer was also found below the "white layer" and its hardness was reduced to 43 HRC. Similar layers were reported frequently on other steels. Figure 2.2 shows an example of the white layer and the overtempered martensitic layer (often called "dark layer" due to its appearance under an optical microscope) on a machined *AISI 52100* steel (Chou and Evans, 1999).
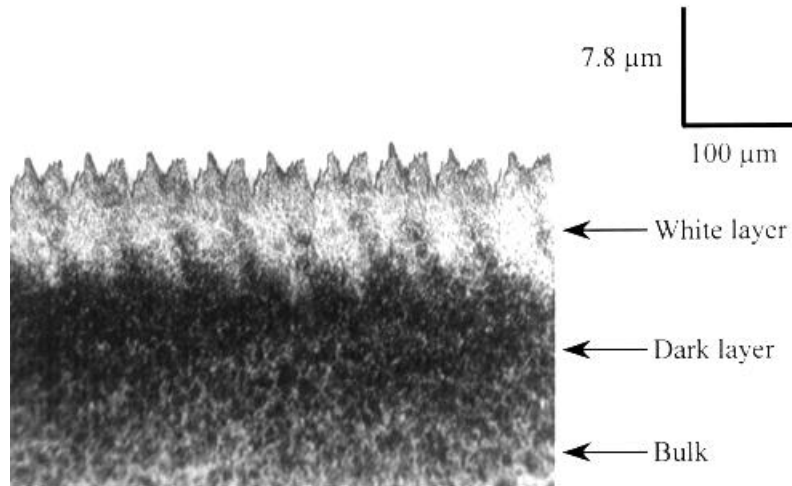
Figure 2.2: An example of white and dark layers formed at a hard turned surface of *AISI 52100* steel (Chou and Evans, 1999).

Numerous experimental and numerical studies have been conducted to investigate the influence of various machining conditions on the formation of "white layer" and their purpose was mainly to avoid the formation of this layer due to its detrimental effects on performance of the machined components. However, recent studies of the "white layer" by using advanced material characterization techniques, such as transmission electron microscopy (TEM), showed that nanocrystallized grain structures were formed in the "white layer" (Ramesh et al., 2005; Wusatowska-Sarnek et al., 2011) and brought up another possibility that "white layer" might sometimes be beneficial for some materials since surface nanocrystallization (SNC) was proved to be an effective way to improve functional performance of metallic materials (Lu and Lu, 1999).

Ramesh et al. (Ramesh et al., 2005) investigated the structure and properties of white layers formed during machining of hardened *AISI 52100* steel (62 HRC) at different cutting speeds using TEM and X-ray diffraction (XRD). They found that white layers produced at low-to-moderate cutting speeds were mainly due to grain refinement

induced by severe plastic deformation, whereas white layer formation at high cutting speeds was mainly due to thermally-driven phase transformation. The white layers at all speeds were found to be comprised of nanocrystallized grain structures which were coarser (~20 nm) at higher speed than those generated at lower speeds (~5 nm).

In an earlier work from Purdue University, Brown et al. (Brown et al., 2002) demonstrated that siginficant grain refinement occurred in the machined chips of various materials, such as copper, steels and nickel. Swarninathan et al. (Swarninathan et al., 2005) studied the variation of chip microstructures with cutting conditions in machining of oxygen-free high thermal conductivity (OFHC) copper, *Al 6061-T6* and *AISI 52100* steel. Figure 2.3 (a) shows the microstructure of partially detached OFHC copper chip (Swarninathan et al., 2005). While the grain structures were clearly visible in the bulk material, they disappeared in the machined chips and on the machined surface. It was shown in Figure 2.3 (b) that significant grain refinement from 20 μm to 216 ± 104 nm occurred in the machined chips (Swarninathan et al., 2005). Nanocrystallined grains of 75 nm were found in the machined chips of *Al 6061-T6* (Swarninathan et al., 2005). In a later work from the same group, it was found that the remarkable grain refinement also occurred in the machined surface of copper and grains of 175 ± 30 nm were found as shown in Figure 2.3 (c) (Chandrasekar et al., 2009). The hardness of the machined surface was increased from 57 to 155 kg·mm^{-2} and was similar to that reported in the machined chips (152 kg·mm^{-2}). They proved experimentally that strains in the machined chips and on the machined surface were similar to each other in value and led to the similarity in microstructures and hardness.

Wusatowska-Sarnek et al. conducted microstructural characterization of the white etching layer (WEL) formed during milling of an nickel-based superalloy *IN100* using TEM (Wusatowska-Sarnek et al., 2011). It was shown that a nanocrystallized layer with the thickness from 0.5 to 1 μm formed on the machined surface. The grain size in the nanocrystalline layer was between 15 and 70 nm. The measured hardness of the layer was increased from about 4.5 GPa to 7.5 GPa.
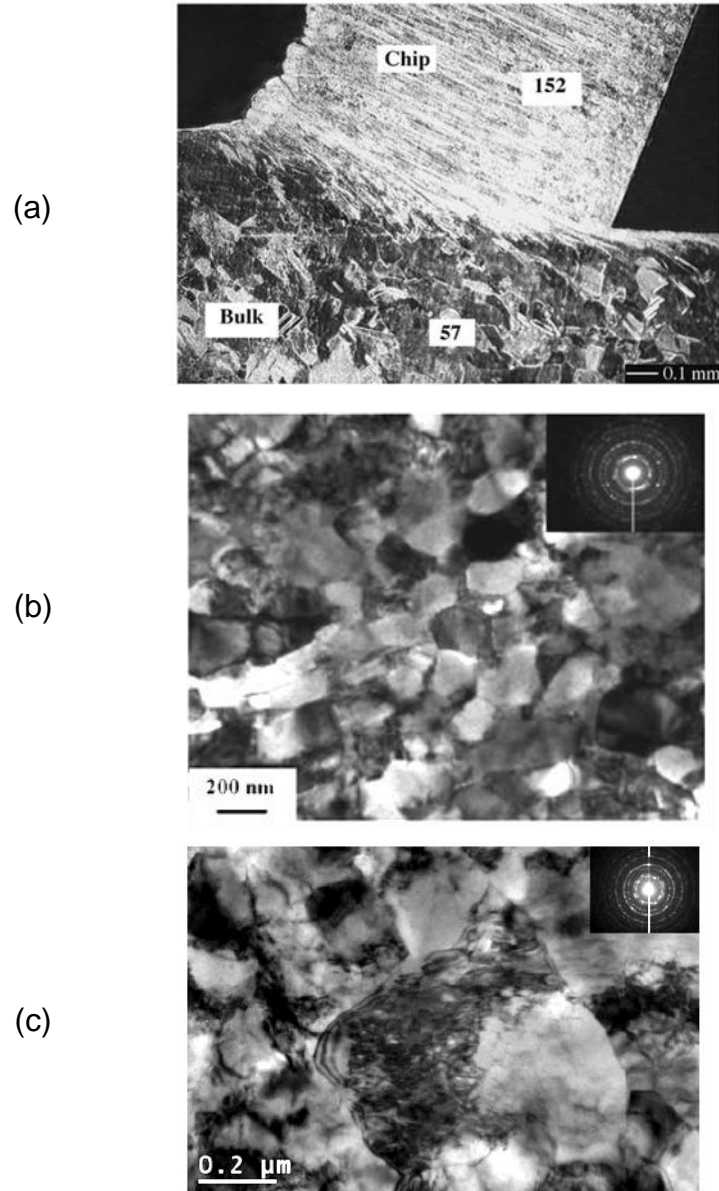
Figure 2.3: (a) Microstructure of partially detached OFHC copper chip (superimposed are average Vickers hardness values (kg/mm^2); (b) TEM image of microstructure of OFHC copper chips showing equiaxed grains of 216 ± 104 nm (Swaminathan et al., 2005); (c) TEM image of machined copper surface showing grains of 175 ± 30 nm (Chandrasekar et al., 2009).

2.1.3 Experimental studies on the influence of cryogenic machining on surface integrity

The beneficial effects of cryogenic machining on tool life, where liquid nitrogen was sprayed from the rake and/or flank side of the cutting tools, were reported on different materials such as steels (Ghosh et al., 2003) and titanium alloys (Hong et al., 2001; Dhananchezian and Kumar, 2011). However, very few researchers have reported the influence of cryogenic cooling on surface integrity induced by machining. Surface roughness on the machined surface was found to be reduced by cryogenic cooling compared with dry and flood cooling on *AISI 52100* steel (Ghosh et al., 2003) and *AISI 4037* steel (Dhar and Kamruzzaman, 2007). Less tensile residual stresses was generated on the machined surface of *AISI 52100* under cryogenic cooling compared with dry machining when an Al_2O_3 ceramic tool was used as shown in Figure 2.4 (Ghosh et al., 2003). The application of cryogenic cooling also reduced the thickness of white layers on *AISI 52100* steel to about 50% compared with dry machining with both polycrystalline cubic boron nitride (PCBN) tools and Al_2O_3 ceramic tools (Ghosh et al., 2003). Pusavec et al. investigated the influence of cryogenic machining on the surface integrity of *Inconel 718* and found that more compressive residual stresses and better surface finish were achieved compared with dry and minimum quantity lubrication (MQL) (Pusavec et al., 2011).
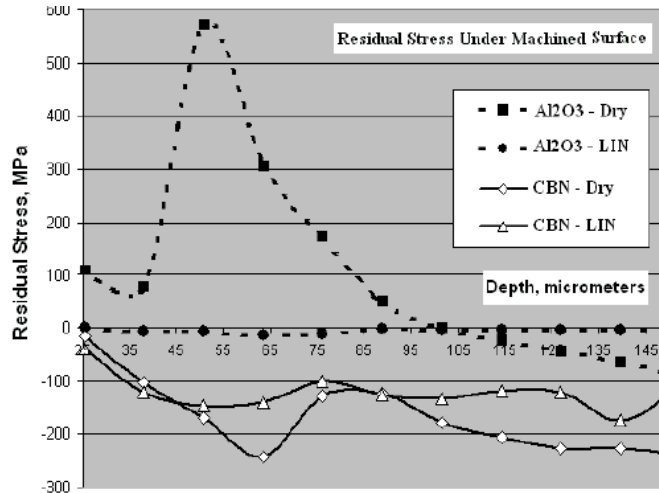
Figure 2.4: Residual stress as a function of depth under machined surface, radial sample direction (across turning lines) (Ghosh et al., 2003).

2.1.4 Finite element modeling of surface integrity in machining

Different factors of surface integrity in machining, such as microstructure and residual stresses, can be affected by various cutting conditions simultaneously. In addition to experimental studies, predictive models are greatly needed to further understand the mechanisms that drive the surface integrity changes and to find the optimum machining conditions that would lead to desirable surface integrity. Residual stress is one of the most commonly studied surface integrity factor in predictive models. Due to the improved performance and power of computers, finite element modeling (FEM) is becoming one of the widely used approaches to predict residual stresses induced by machining. Major advantages of FEM include the application of complex material behavior models which allow flow stress to change with strain, strain-rate and temperature. Also, "user subroutines" can be easily implemented to capture complex material changes during the machining process, such as phase transformations, dynamic recrystallization, etc., that influence the surface integrity. Obtaining appropriate

15

experimental data as input to calibrate the model is still an essential part of this implementation.

Ee et al. developed a thermal elastic-viscoplastic finite element model to evaluate the residual stresses remaining in a machined component (Ee et al., 2005). They used the model to study the influence of sequential cuts and cutting conditions on the residual stresses induced by orthogonal machining. Outerio et al. (Outeiro et al., 2006c) conducted both experimental and numerical studies using the commercial software Deform 2D to investigate the influence of various cutting conditions on residual stresses in machining of *AISI 316L* steel. Figure 2.5 shows that a good agreement between experiment and predicted data can be achieved by using this model. It was found from the numerical studies that the residual stresses tend to increase with cutting speed, uncut chip thickness and tool cutting edge radius. Also, sequential cuts were reported to increase the superficial residual stresses.
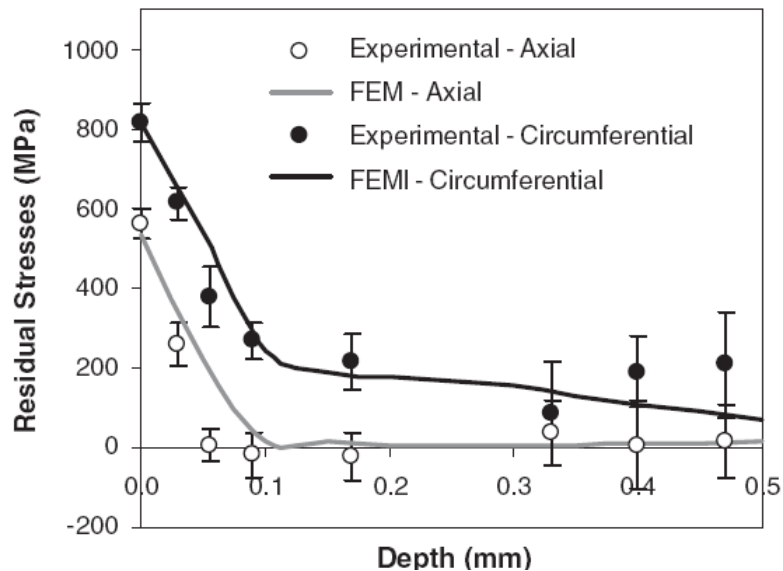
Figure 2.5: Comparison between experimentally and numerically obtained residual stresses (Outeiro et al., 2006c)

16

A hardness-based flow stress model was developed by Umbrello and implemented in Deform 2D through a customized user routine to simulate hard turning of *AISI 52100* steel (Umbrello et al., 2004). A hydrostatic stress-based fracture criterion was used to simulate chip separation. This model was proved successful not only in predicting residual stresses (Umbrello et al., 2010b) but also the white and dark layer formation. Figure 2.6 shows that a good agreement between the observed white and dark layers (Poulachon et al., 2001) and the predicted layers was achieved by using their hardness-based flow stress model (Umbrello et al., 2010a).
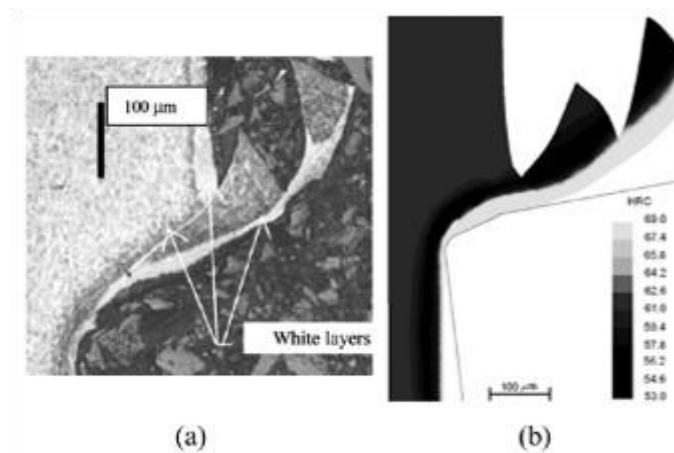
Figure 2.6: White and dark layers formation in machining of *AISI 52100* steel: (a) observed (Poulachon et al., 2001); (b) predicted (Umbrello et al., 2010a).

Microstructural changes during machining such as grain refinement induced by dynamic recrystallization (DRX) have significant influence on the surface integrity of the machined workpiece. However, very few studies have reported modeling of the microstructural changes due to the complexity of the problem. Caruso et al. expanded the model developed by Umbrello (Umbrello et al., 2004) and implemented another user subroutine where empirical equations concerning the grain size changes induced by DRX was used (Caruso et al., 2011). The model parameters were evaluated from experimental

data and then used to predict other cases. Good agreement between the measured and predicted grain size on the machined surface and in the sub-surface after hard turning of *AISI 52100* was achieved.

2.2   Experimental Studies on Surface Integrity in Burnishing

Burnishing is a manufacturing process used in industry to reduce surface roughness, increase hardness and/or introduce beneficial compressive residual stresses.

Rajesham and Tak investigated the influence of roller burnishing on aluminum alloy (Rajesham and Tak, 1989). They found that the surface finish was improved and the hardness was increased up to 0.4 mm below the burnished surface. Hassan and Al-Bsharat studied the influence of different ball burnishing conditions, including forces, ball diameter, speed and feed, on the surface roughness and hardness of two non-ferrous metals (Hassan and Al-Bsharat, 1996). Large diameter balls were found to be more effective in improving surface roughness, while small diameter balls more effective in increasing surface hardness. Klocke and Liermann conducted ball burnishing using a ceramic ball on turned 100Cr6 steel (Klocke and Liermann, 1998). In addition to 30-50% reduction of surface roughness, they found that burnishing shifted the tensile residual stresses induced by machining to large compressive residual stresses. The microstructures before and after burnishing were also studied and the white layer still existed after burnishing; no cracks or spalling were found.

Prevéy developed a new burnishing process, low plasticity burnishing (LPB), to induce deep compressive residual stress layers with a low degree of cold work (less than 3.5%) (Prevéy, 1998). He showed that large compressive residual stresses could be induced on nickel-based superalloy *IN718* by LPB. The thermal stability of compressive

18

residual stresses induced by LPB was also significantly improved over shot peening at 600 °C (Prevéy, 2000).

Zhang and Lindemann conducted roller burnishing on *AZ80 Mg* alloy and reported that more compressive residual stresses were achieved than in shot peening. (Zhang and Lindemann, 2005a). In addition to residual stress changes, it was found that a severely deformed layer about 700 µm was created near the burnished surface and the hardness of this layer was increased from 90 HV to 150 HV (Figure 2.7). Significant grain refinement occurred in the top 200 µm and the microstructures were not discernable using optical microscopy and scanning electron microscopy. At the depth of 200–700 µm from surface, a high density deformation twinning was observed.
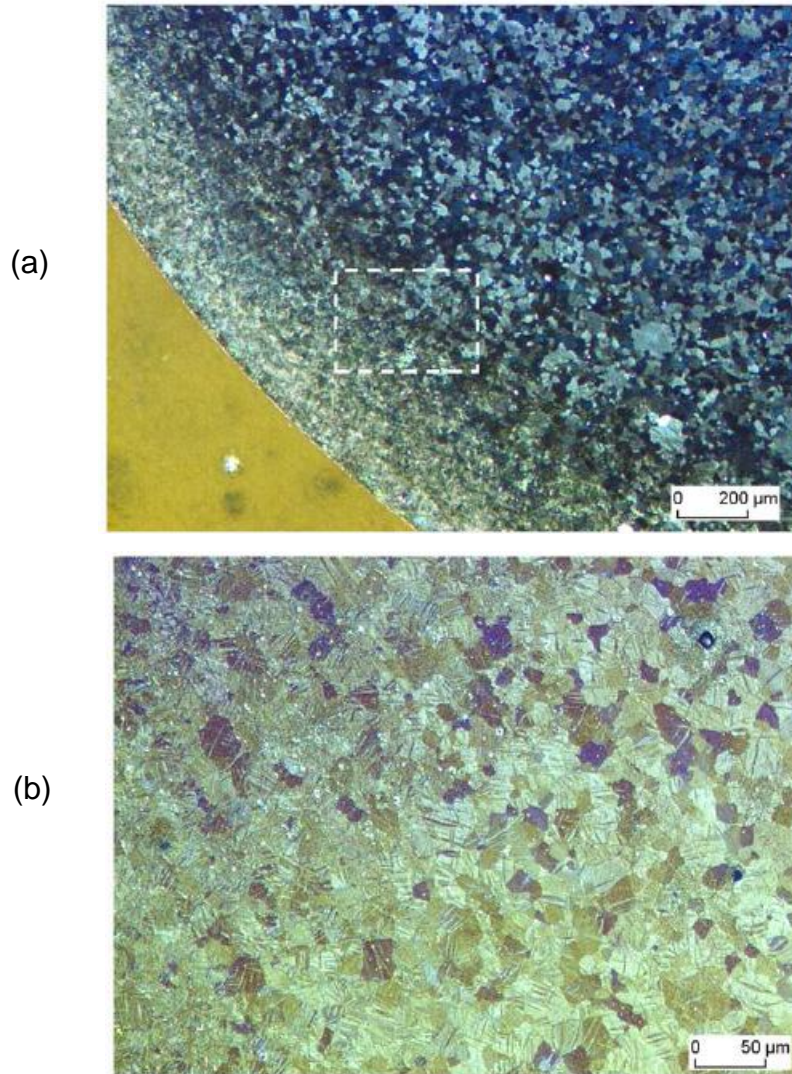
Figure 2.7: Light optical microscopy of roller burnished *AZ80 Mg* alloy with a roller force of 200 N: (a) overview; (b) detail of framed region (Zhang and Lindemann, 2005a).

2.3 Application of Magnesium Alloys in Biomedical Applications

In the U.S. alone, physician visits for orthopedic surgery reached 48,066,000 in 2006 (Cherry et al., 2008). Nine out of the twenty five most common orthopedic surgeries involve repair of bone fractures (Garrett et al., 2006). Internal bone fixation implants, such as bone plates and screws, are widely used to provide temporary fixation

for fractured bones. An example of fixation implants is shown in Figure 2.8 (a). Stainless steels and titanium alloys are two major biomaterials currently used for these implants. However, their excessive mechanical properties compared to bones may lead to stress shielding. The corrosion and fatigue of these materials will inevitably generate metallic ions and particles that may activate adverse tissue reactions. For example, after 6 years' service, a *316L* stainless steel spinal fixation device was removed from the patient and large number of discolored areas were found on the steel plate as shown in Figure 2.8 (a) (Mohanty et al., 2003). Scanning electron microscopy (SEM) picture in Figure 2.8 (b) shows that large corrosion pits were formed in the discolored areas, which contributed to the chronic inflammatory response around the component parts. It was also reported that all the screws were loose in the screw holes and were covered by slimy granulation tissue. To avoid the adverse reactions after bone healing, the fixation implants are required to be removed during a subsequent surgery, which adds additional morbidity (pain, refracture, etc.) to the patients and increases healthcare cost.
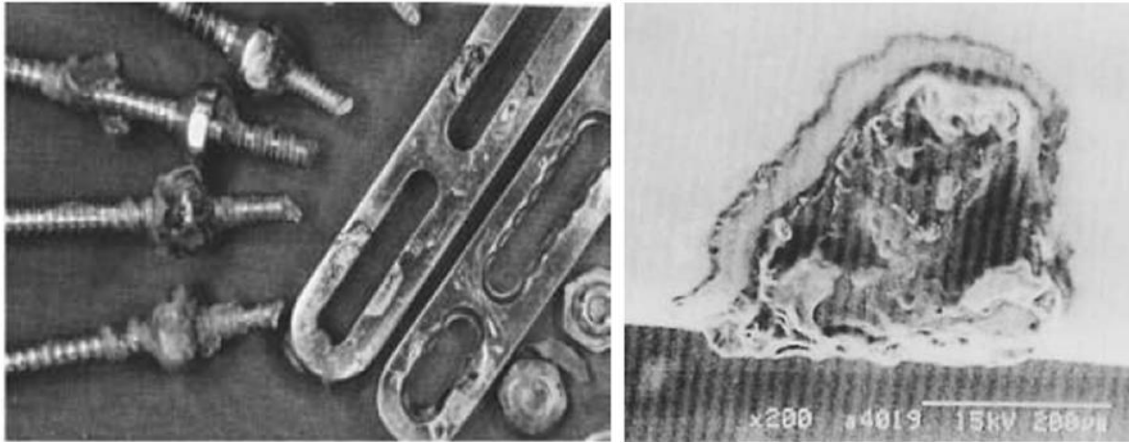
Figure 2.8: (a) Components of a *316L* stainless steel spinal fixation device after 6 years' service in human body and (b) SEM picture of the discolored surface of the metal plates in (a) showing area of corrosion (Mohanty et al., 2003).

While various approaches are being investigated to increase the bio-inertness of traditional implant materials, magnesium alloys are emerging as a novel biodegradable material in which the relatively fast corrosion phenomenon is used as a unique advantage for temporary fixation implants. The potential of magnesium alloys as a biodegradable implant material was explored by several researchers in the first half of the twentieth century (McBride, 1938; Troitskii and Tsitrin, 1944; Znamenskii, 1945). No systematic reaction and only little inflammation were observed in these human trials. A marked stimulatory effect for bone healing was reported (McBride, 1938). However, the premature failure of magnesium-based implants due to the poor corrosion resistance in physiological environments and gas bubbles generated due to the high corrosion rate impeded further investigation until recently. As shown in Figure 2.9, the *Mg*-based fixation implants need to hold their mechanical strength for at 12 weeks to allow sufficient healing time for the fractured bone, while premature failures of these implants

often occurred due to high corrosion rates in human body (some at only 3 weeks) (Pietak et al., 2006). Although numerous publications on the potential benefits of *Mg*-based biodegradable implants have emerged in the past decade (Witte, 2010), one of the major problem to be solved is to improve the corrosion resistance of *Mg* alloys.
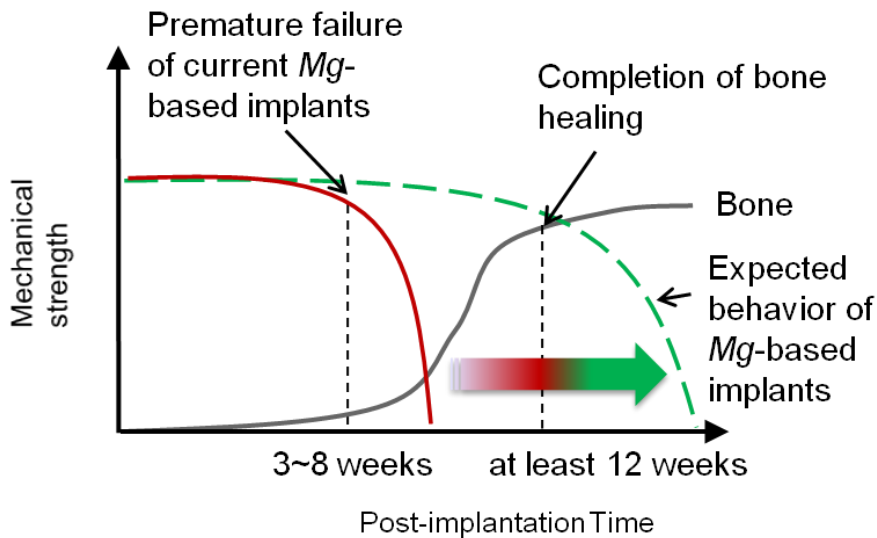
Figure 2.9: Premature failure of the current *Mg*-based implants and the expected behavior of improved *Mg*-based implants. Compiled from Pietak et al. (2006).

2.4 Effects of Surface Integrity on Functional Performance

Failure of metallic materials due to wear, corrosion and/or fatigue often starts at the surface of manufactured products. The functional performance of components can be significantly influenced by the surface integrity induced by the machining/burnishing processes. As shown in the previous section, unsatisfactory corrosion resistance is the major disadvantage of the current *Mg*-based biodegradable implants; it also limits the application of *Mg* alloys in automotive industry despite of the fact that desirable weight saving can be achieved by using *Mg* alloys (Luo, 2002). Therefore, the focus of the

literature review in this section is focused on the influence of various surface integrity factors on the corrosion performance of *Mg* alloys. Other functional performance factors, such as wear and fatigue life, as well as different materials, were also covered in this review.

2.4.1   Effect of grain size

Grain size of magnesium alloys has a remarkable influence on their corrosion resistance (Wang et al., 2007). Grain refinement from 25.7 μm to 4.5 μm induced by equal channel angular pressing (ECAP) led to better corrosion performance for *AZ31 Mg* alloy in simulated body fluid (*SBF*) (Alvarez-Lopez et al., 2010). It was also reported on pure magnesium that grain refinement from 125 μm to 2.6 μm by ECAP enhanced its corrosion resistance in 0.1 mol/L *NaCl* solution (Birbilis et al., 2010b). Figure 2.10 shows that a clear relationship between the corrosion current and the grain size exists in pure magnesium (Birbilis et al., 2010b) that samller grains lead to reduced corrosion current (improved corrosion resistance). The grain boundary of *AZ31B Mg* alloy was claimed as physical corrosion barriers and smaller grain size led to better corrosion resistance in 3.5 wt. % *NaCl* solution (Aung and Zhou, 2010). The critical influence of grain size on corrosion resistance was also reported on other materials, such as titanium (Balakrishnan et al., 2008b), stainless steel (Wang and Li, 2002), etc., and this relationship was claimed to be analogous to the classical Hall–Petch relationship which describes the dependence of hardness on grain size (Birbilis et al., 2010a).
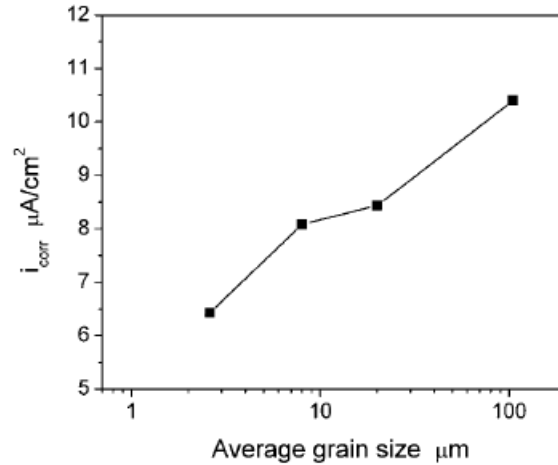
Figure 2.10: Corrosion current as function of grain size in 0.1 mole/L *NaCl*
(Birbilis et al., 2010b)

In addition to corrosion performance, the beneficial effects of grain refinement was reported on the fatigue life of *AZ31 Mg* alloy (Wang et al., 2007) as well as many other materials, such as titanium, *Al* alloys and copper (Mughrabi and Hoppel, 2010). Compared with the coarse-grained annealed copper, copper with a nanocrystalline surface layer obtained by using surface mechanical attrition treatment (SMAT) exhibited remarkably better wear resistance (Zhang et al., 2006)

2.4.2   Effect of crystallographic orientation

The changes of crystallographic orientations on the workpiece surfaces after machining were not often reported in the literature and most of them focused on machining of single crystals (To et al., 2003). The importance of crystallographic orientations on corrosion resistance was reported on both pure *Mg* (Liu et al., 2008) and *Mg* alloys (Song et al., 2010b). It was found both experimentally and theoretically that the (0001) basal plane of *AZ31 Mg* alloy is more corrosion resistant than the other planes due to its higher atomic coordination and thus lower surface energy (Song et al., 2010b).

Xin et al. prepared *AZ31 Mg* samples with different crystallographic orientations by cutting the sample at different degrees, 0°, 30°, 60° and 90°, to the rolled sheet as shown in Figure 2.11 (a) (Xin et al., 2011). Rolled sheet of *Mg* alloys was reported frequently to have a strong basal texture on the rolled surface (Chang et al., 2003). Therefore, the intensity of the basal texture on the *Mg* samples decreased with the larger angles as shown in Figure 2.11 (b). The hydrogen evolution method (Song et al., 2001) was used to evaluate the corrosion resistance of the *Mg* samples with different crystallographic orientations (smaller hydrogen volume, better corrosion resistance). As shown in Figure 2.11(c), a clear relationship between the corrosion resistance and the crystallographic orientation exists and this agreed with earlier data from the literature that the corrosion resistance of *Mg* alloys increases with increased intensity of basal texture. The effects of crystallographic orientations on corrosion resistance were also reported to outweigh those of grain size in pure titanium after ECAP (Hoseini et al., 2009).
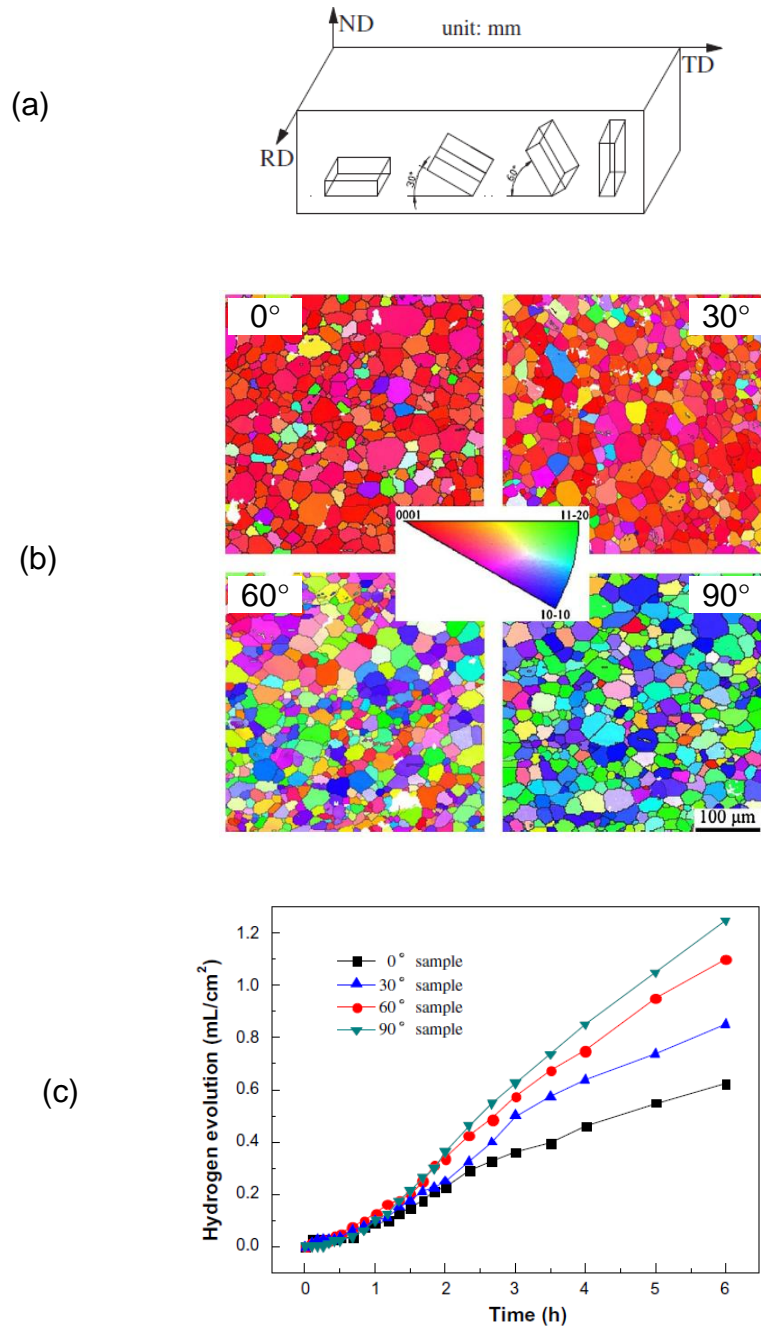
Figure 2.11: (a) Schematic illustration of sample preparation; (b) inverse pole figure maps of 0°, 30°, 60° and 90° Samples and (c) hydrogen evolution rates of the *AZ31 Mg* samples immersed in 3.5 wt.% *NaCl* (Xin et al., 2011).

2.4.3 Effect of residual stresses

The influence of residual stresses on fatigue life of manufactured components was frequently reported while the influence on corrosion resistance was less well known until recently. The pitting corrosion resistance of *AISI 316L* stainless steel was improved after inducing near-surface compressive residual stresses by sand blasting and wire brushing (Ben Rhouma et al., 2001). The high compressive residual stress generated in the subsurface via a deep rolling process was also claimed to reduce the corrosion rate of a biphasic magnesium-calcium alloy by a factor of approximately 100 (Denkena and Lucas, 2007). The corrosion performance of *7475-T7351* aluminum alloy was significantly improved by inducing large compressive residual stresses near the surface through low plasticity burnishing (LPB) (Scheel et al., 2010). It was also reported that large residual stresses would reduce the corrosion resistance of magnesium alloys, although the grain size of the alloys became smaller (Ralston and Birbilis, 2010). The influence of different machining and grinding procedures on stress corrosion cracking of *AISI 304* stainless steel was recently investigated, and high tensile stresses induced by grinding were also found to cause more severe pitting corrosion (Turnbull et al., 2011).

In addition to affecting corrosion resistance, residual stress has a critical influence on fatigue life. Leverant et al. studied the fatigue life of machined *Ti-6AI-4V* and showed that the surface residual stresses played a dominant role in the determination of fatigue microcrack growth rates and consequently the total fatigue life (Leverant et al., 1979). Matsumoto et al. conducted the rolling contact fatigue tests of *AISI 52100* steel after hard turning and grinding and also measured the residual stresses after processing (Matsumoto et al., 1999). They found that longer fatigue life was achieved by hard turning than

28

grinding which was attributed to the larger penetration depth of compressive residual stresses by turning. The significantly enhanced fatigue performance was also reported on various materials processed by LPB for critical applications, including *Ti-6Al-4V* (Hornbach et al., 2006) used in femoral hip stems and stainless steels *Alloy 450* and *17-4PH* used in steam turbines (Prevéy et al., 2010). These improvements were all attributed to the large compressive residual stresses induced by LPB.

2.5   Dynamic Recystallization and Grain Refinement

In addition to experimental studies, one objective of the present study is to develop a predictive model using FEM to investigate the influence of various cutting conditions on the surface integrity of the machined components. As shown in the previous sections, microstructural changes, especially grain size, have a remarkable influence on the corrosion resistance of *Mg* alloys. Therefore, the major objective of the FEM model is to predict the changes of surface grain size induced by machining. In order to develop the model, it is first necessary to understand the mechanism of grain refinement induced by machining.

Machining is a severe plastic deformation (SPD) process involving large strains and high strain-rates. Meyers et al. studied the deformation of various materials at high strain-rates ($>10^4$ s^{-1}) including copper, titanium and tantalum (Meyers et al., 1997). They found that grain refinement occurred in the shear band and the mechanism was rotational dynamic recrystallization (DRX). The mechanism of grain refinement in an *AZ91 Mg* alloy induced by a SPD process, SMAT, was studied by Sun et al. (Sun et al., 2007). As shown in Figure 2.12, twinning was claimed as the first step of grain refinement. Then dislocation movements on both basal plane and non-basal plane slip systems lead to

dislocation arrays which become the subgrain boundaries with high stored energy. The high strain energy stored in the sample significantly decreases the recrystallization temperature. At the same time, the severe plastic deformation at high strain-rate also rises the temperature. When the temperature is higher than the recrystallization temperature, DRX occurs, which leads to the formation of nanocrystallized grains. It is noted that the recrystallization temperature changes with the amount of plastic strain induced in the specimen. There are no phases changes in the *AZ31B Mg* alloy used for the current study and this simplifies the simulation of the machining process.
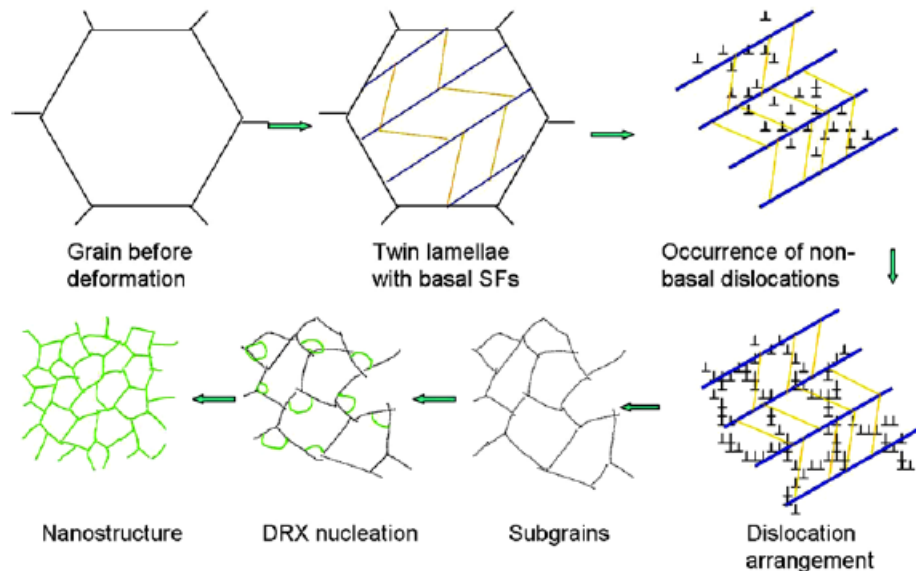
Figure 2.12: Schematic illustration of the grain refinement process of *AZ91D* alloy during SMAT (Sun et al., 2007).

The critical conditions for the onset of DRX in *AZ31 Mg* alloy in standard material property testing was investigated by several researchers (Wang et al., 2002; Huang et al., 2007a). For DRX to occur, a critical strain, ε_{cr}, needs to be reached. This critical value was found to be dependent on the strain-rate and temperature (Wang et al., 2002) , which can be calculated using the Zener-Hollomon parameter, Z, as:

$$\varepsilon_{cr} = 0.02039Z^{0.06} \qquad (2.1)$$

Z is defined as:

$$Z = \dot{\varepsilon} \times \exp(\frac{Q}{RT}) \qquad (2.2)$$

where $\dot{\varepsilon}$ is the strain-rate; Q is the activation energy; R is the gas constant and T is the temperature.

An empirical formula was used to predict the size of the recrystallized grains in *AZ31 Mg* alloy after FSP and was proved to be consistent with the experimental results (Chang, 2007). The formula is:

$$\frac{d_{rec}}{d_{init}} = 10^3 \times Z^{-1/3} \qquad (2.3)$$

where d_{rec} is the recrystallized grain size; d_{init} is the initial grain size and Z is the Zener-Hollomon parameter.

Reduced temperature during deformation leads to larger Z value as calculated by Equation (2.2), which will reduce the grain size after DRX according to Equation (2.3). To obtain ultrafine/nano level grain size, liquid nitrogen was used by several researchers to cool the processing zone. Chang et al. designed a fixture with two internal cooling channels during FSP of *AZ31 Mg* alloy and liquid nitrogen was used as the coolant (Chang et al., 2007). The authors claimed that the finest microstructure obtained by friction stir process (FSP), which was about 100-300 nm, was achieved. A *Cu* rod, which was cooled to -173 K by liquid nitrogen before processing, was subject to a surface mechanical grinding treatment (SMGT) and nanocrystalline grains smaller than 50 nm was achieved (Li et al., 2008).

2.6 Summary

The literature review presented in this chapter clearly shows that surface integrity can be remarkably changed by machining and burnishing. These changes will have a critical influence on the functional performance of machined and burnished components. Another important topic reviewed is the recent development of numerical methods in studying surface integrity changes, such as residual stresses, white layer formation, etc. Although numerous efforts have been made to understand the changes of surface integrity induced by machining/burnishing, most of them focused on avoiding the formation of undesirable surface integrity, such as tensile residual stresses, white layer and other surface defects. The possibility of using machining/burnishing to improve functional performance of manufactured products through inducing desirable surface integrity has not been adequately investigated. The experimental and numerical results presented in the following chapters will demonstrate the potential of using traditional manufacturing processes, machining and burnishing, to improve the corrosion resistance of *AZ31B Mg* alloy through inducing desirable surface integrity factors including nano/ultrafine grain structure, compressive residual stresses, strong basal texture, etc. Surface integrity resulting from different machining/burnishing conditions is presented as well as corrosion performance testing data on selected machined/burnished samples. A user subroutine is also developed and implemented in a commercial FEM software to predict the grain size changes induced by machining.

CHAPTER 3: EXPERIMENTAL STUDY ON SURFACE INTEGRITY IN MACHINING OF *AZ31B* MAGNESIUM ALLOY

3.1 Introduction

This chapter presents the results of an experimental investigation of the effect of machining conditions on the surface integrity of *AZ31B Mg* alloy. The surface integrity factors investigated include microstructures, crystallographic orientations and residual stresses, all of which have been proved to influence the corrosion performance of *Mg* alloys. In addition, surface roughness, hardness and chip microstructures/morphology were studied. The influence of cryogenic cooling on surface integrity is one of the most important topics investigated in this chapter. Cutting edge radius of the tools, cutting speed and feed rate were also found to have remarkable influences on the surface integrity of machined *AZ31B* alloy.

The results show that cryogenic machining with a large edge radius tool leads to significantly enhanced surface integrity in terms of: a) significant grain refinement to nanocrystalline level; b) large intensity of (0002) basal plane on the machined surface; c) 10 times larger compressive areas in the residual stress profiles; and d) improved surface finish. These changes should notably improve the functional performance of machined *AZ31B Mg* components. Corrosion test results of these machined samples will be presented in Chapter 5 and detailed discussion provided. The experimental results presented here serve as a basis for the development of predictive model for machining *AZ31B Mg* alloy which will be presented in Chapter 6.

3.2   Experiment Setup

The work material studied was the commercial *AZ31B-O Mg* alloy. The nominal composition by weight percentage (wt. %) is shown in Table 3.1. The work material was received in the form of a 3.22 mm thick sheet. Disc specimens having 130 mm diameter were cut from the sheet by vertical milling in the machine shop and subsequently subjected to machining.

Table 3.1: Nominal composition of *AZ31B-O* magnesium alloy (wt. %)

Al	Zn	Mn	Mg
2.5 - 3.5	0.7 - 1.3	0.2 – 1.0	balance

As shown in Figure 3.1 (a), a Mazak Quick Turn-10 Turning Center, equipped with an Air Products ICEFLY® liquid nitrogen delivery system, was used to conduct orthogonal turning of the *AZ31B Mg* discs. As shown in Figure 3.1 (b), liquid nitrogen was sprayed to the machined surface from the clearance side of the cutting tool at a flow rate of 0.6 kg/min during cryogenic machining (More details on the cryogenic cooling setup are provided in Section 3.4). The cutting tool material is uncoated carbide. The geometry of the grooved cutting tool is TNMG 432. The parameters of the grooves are: groove width, 1.84 mm; land length, 0.135 mm; groove radius, 1.068 mm; backwall height, 0.042 mm. A KISTLER 3-Component Tool Dynamometer was used to monitor the cutting and radial forces during machining. A FLIR Systems ThermaCam PM695 infrared camera was used to measure the whole field temperature of the *AZ31B Mg* discs during machining. The accuracy of the camera was ± 2 °C according to the manufacturer's manual. As shown in Figure 3.1 (b), the infrared camera was mounted on

the machine and did not move during cutting. The distance between the workpiece and the camera was 0.5 m.
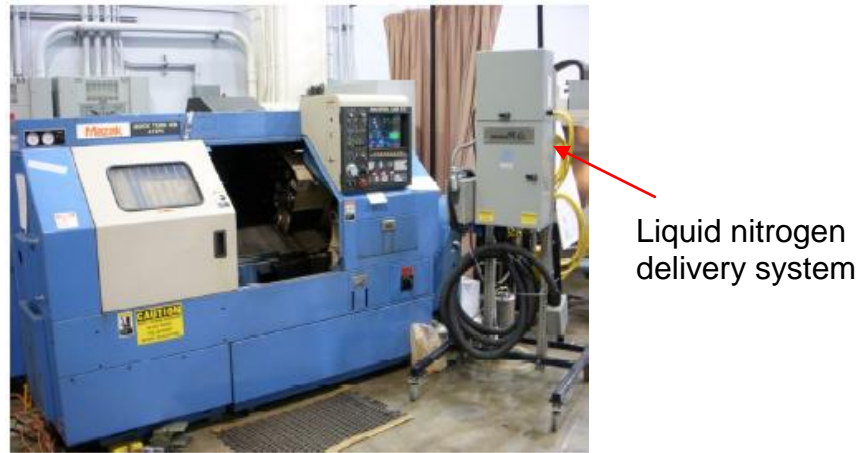
(a)
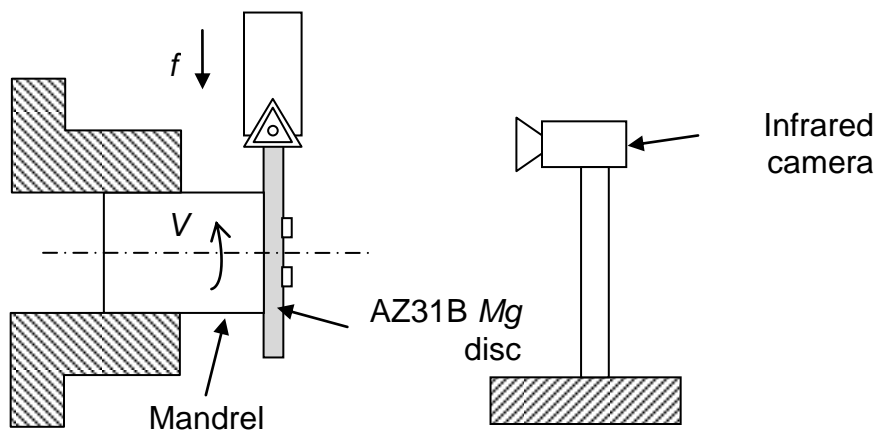
(b)

Figure 3.1: (a) Mazak Quick Turn-10 Turning Center equipped with a liquid nitrogen delivery system; (b) orthogonal turning of *AZ31B Mg* disc with application of liquid nitrogen and infrared camera location.

3.3   Characterization of Surface Integrity

Surface integrity includes many factors covering various aspects of the surface and sub-surface conditions resulting from manufacturing processes (Field et al., 1972).

The factors studied in this chapter were selected based on their importance relating to the corrosion performance of magnesium alloys. As reviewed in Chapter 2, the most important factors include microstructures, crystallographic orientations and residual stresses. In addition, other factors, such as surface roughness and hardness, were also investigated since they may also influence the corrosion performance. The studied surface integrity factors and their characterization methods are summarized below.

3.3.1 Microstructure

As shown in Figure 3.2, metallurgical samples were cut from the machined discs. After cold mounting, grinding and polishing, acetic picric solution was used as the etchant to reveal the grain structure. Optical microscopy and Scanning electron microscopy (SEM) were used to observe the microstructure of the *AZ31B Mg* discs as well as the machined chips.
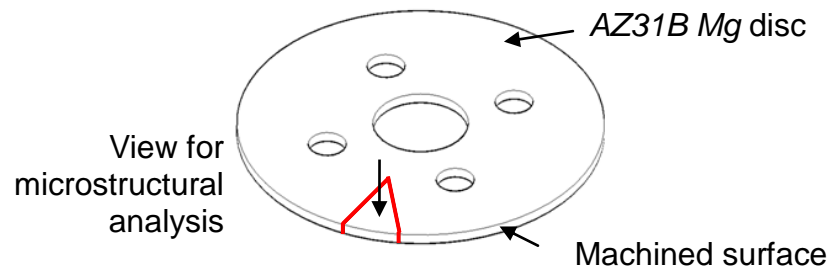
Figure 3.2: Sectioning of the metallurgical sample and view for microstructural analysis

3.3.2 Crystallographic orientations

The crystallographic orientations on the circumferential surfaces before and after machining were analyzed using a Bruker D8 Discover X-ray Diffractometer. The radiation used was *Cu-Kα* at 20 kV and 5 mA.

3.3.3 Residual stresses

The residual stress state in machined *AZ31B Mg* samples was analyzed by X-ray diffraction technique using the $\sin^2\psi$ method (Noyan and Cohen, 1987). The experiments were conducted at the X-ray Diffraction Center for Materials Research (CEMDRX), University of Coimbra, Portugal. The equipment used was iXRD from PROTO®. Figure 3.3 shows the experimental setup for residual stress measurements.

Figure 3.3: Experiment setup at the University of Coimbra (Portugal) for residual stress measurements on machined *AZ31B Mg* discs using iXRD from PROTO®

The complete disc was used without any sectioning to avoid possible changes of residual stresses during sample preparation. The parameters used in the X-ray analysis are shown in Table 3.2. To determine the in-depth residual stress profiles, successive layers of material were removed by electropolishing to avoid the modification of machining-induced stresses. The solution used for electropolishing of *AZ31B Mg* alloy is shown in Table 3.3. For each measurement, a tape was used to expose only a square window (2 mm × 5 mm) on the machined surface to make sure the same location was measured each time. It is noted that in the present study, the total penetration depth of the X-ray beam for *Mg* is 25 μm. Therefore, the first data point, which was measured on the surface, started at 25 μm from the machined surface. The peak breadth data was also

collected from the XRD measurement and used to compare the degree of work hardening under different machining conditions.

Table 3.2: X-ray diffraction parameters for residual stress measurement

Radiation	*Mn*-Kα
Voltage and current	20kV, 4 mA
Collimator diameter [mm]	5
Bragg angle 2θ [°]	151.06 (hkl) = (203)
X-ray elastic modulus [MPa^{-1}]	$\frac{1}{2}$S$_2$ = 29.32 × 10^{-6}, S$_1$ = -6.59× 10^{-6}
Number of ψ angles	30

Table 3.3: Solution used for electropolishing of *AZ31B Mg* alloy

Name	Quantity
Sodium thiocyanate	160 g
Butyl cellosovle	80 ml
Ethanol	800 ml
Distilled water	20 ml

3.3.4 Surface roughness

The surface roughness before and after machining was measured using Zygo New View 5300 measurement system which was based on white light interferometry.

3.3.5 Hardness

Sample segments with the same shape as shown in Figure 3.2 were cut from the machined discs, cold mounted, ground and polished. Microindentation tests were performed using a Vickers indenter on a CSM Micro-Combi Tester. The load used was 100 mN and the duration time was 10 s.

3.4 Effects of Edge Radius and Cooling Methods on Surface Integrity

The influence of cutting edge radius on surface integrity, especially residual stresses, is frequently reported in the literature. A larger edge radius was found to induce more compressive residual stresses in the surface layer. The application of liquid nitrogen during machining was reported to result in larger compressive residual stresses (Zurecki et al., 2003) and also reduce the white layer thickness of *AISI 52100* steel when compared to dry machining (Umbrello et al., 2012) using the same cutting parameters. More significant grain refinement was achieved on *AZ31B Mg* alloy after friction stir processing with the help of liquid nitrogen cooling (Huang et al., 2007b). Therefore, the focus of this section was to investigate the influence of cryogenic cooling and cutting edge radius on surface integrity of the machined *AZ31B Mg* alloy. The experiment matrix is shown in Table 3.4.

Table 3.4: Experiment matrix for machining under different edge radii and cooling methods

No.	Tool Edge Radius, r_n [μm]	Cooling Method	Cutting Speed, V [m/min]	Feed Rate, f [mm/rev]
1	30	Dry	100	0.1
2	70	Dry	100	0.1
3	30	Cryogenic	100	0.1
4	70	Cryogenic	100	0.1

The cutting tool edge radii were ground to two levels, 30 μm and 70 μm, by a grinding company. The actual values were measured by Zygo New View 5300 measurement system before machining to make sure the edge used was within the range. Typical oblique plots measured by Zygo for the tools with different edge radii are shown in Figure 3.4. They show the 3D representations of the cutting edge and provide a direct comparison of the differences in edge radius.
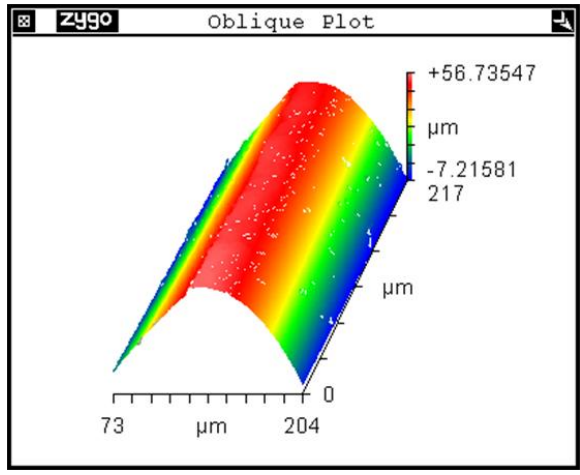
(a)
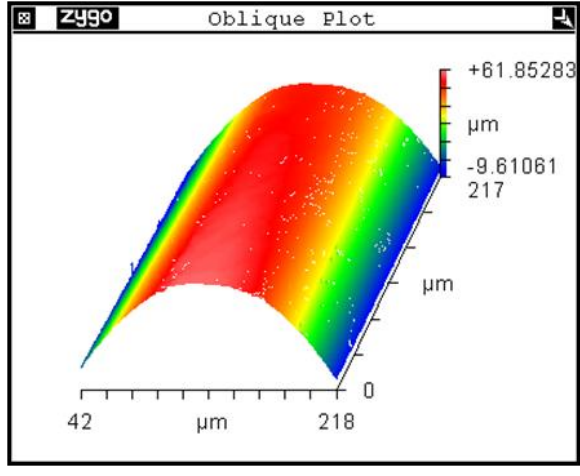
(b)

Figure 3.4: Typical oblique plots for edge radius measurement using ZYGO New View 5300: (a) 30 µm; (b) 70 µm.

For dry machining, no coolant or lubricant was used; for cryogenic machining, liquid nitrogen was sprayed via a nozzle from the clearance side of the tool to the machined surface as shown in Figure 3.5.

(a)

(b)
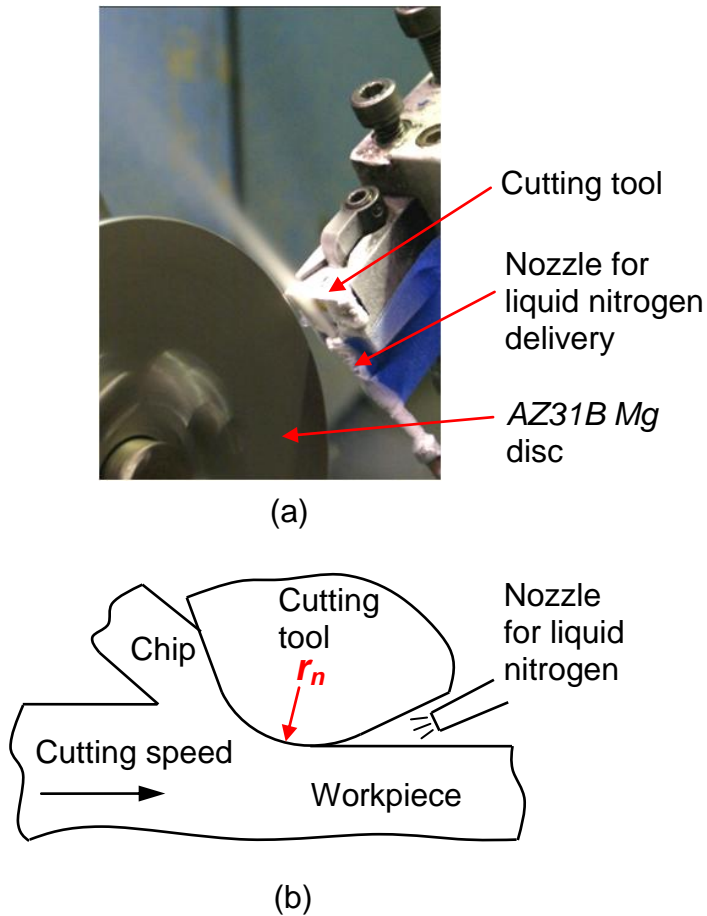
Figure 3.5: Experimental setup of cryogenic machining: (a) photo (tool approaching the workpiece) and (b) schematic diagram.

3.4.1 Cutting forces

The cutting and thrust force components measured by the dynamometer are shown in Figure 3.6. The application of liquid nitrogen did not have a large influence on either the cutting or thrust force. The maximum difference in cutting force between dry and cryogenic machining was only 3%, when tools with 70 μm cutting edge radius were used and cryogenic machining led to slightly smaller forces. This may be due to the fact that the liquid nitrogen was sprayed to the machined surface from the clearance side of

the cutting tool. It has little influence on the temperature of the primary and secondary deformation zones. Compared with data obtained under dry machining, the thrust force for cryogenic machining with 30 μm and 70 μm cutting edge radii was increased 12% and 7%, respectively. The increase is due to the effective cooling from the liquid nitrogen jet which enhances the mechanical properties of the material.

The influence of edge radius on thrust forces for both dry and cryogenic conditions was significant. There were 60% and 53% increases respectively in the thrust force under dry and cryogenic conditions when the cutting edge radius was increased from 30 μm to 70 μm.

The increase in the cutting forces was much smaller than that for the thrust force, the largest increase which was 10% (under dry conditions). Similar trends in the forces were observed by Albrecht (Albrecht, 1960). The larger force especially in the thrust direction were attributed to the increased ploughing effects caused by larger cutting edge radius. The increased ploughing effect should be desirable for the occurrence of strain-induced grain refinement in *Mg* alloy (Shi et al., 2007)   since greater severe plastic deformation will be induced on the machined surface and sub-surface.
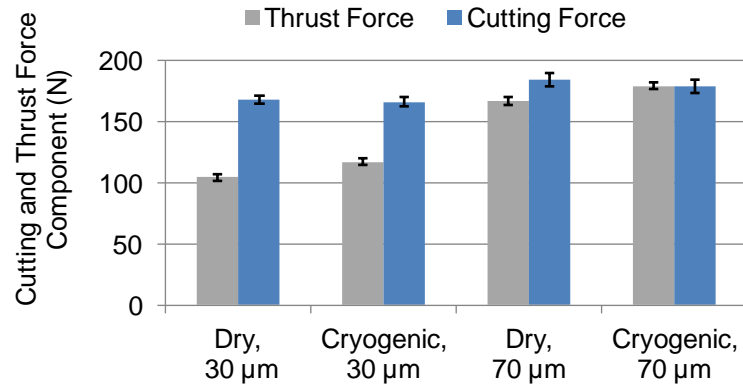
Figure 3.6: Force measurement results under different machining conditions ($V = 100$ m/min, $f = 0.1$ mm/rev).

3.4.2 Calibration of infrared camera and temperature analysis

The purpose of the temperature measurement using infrared camera was to measure the temperature of the machined surface. The emissivity of the material is a critical parameter and will influence the accuracy of the measurement temperatures. It was reported that linear relationships between the temperature measured by the infrared camera and the one measured by a thermal couple (the actual temperature) on *AZ31 Mg* alloy could be found when the emissivity was set to 0.18 (Liu et al., 2005; Liang and Yuan, 2008). In this study, the emissivity was set to 0.18. A hotplate was used to heat up the *AZ31B Mg* work material from room temperature up to 250 °C. A thermocouple and the infrared camera were used to measure the temperature of the *AZ31B Mg* disc at the same time. As shown in Figure 3.7, a linear relationship was found between the temperatures measured by infrared camera and thermocouple as:

$$T = 1.022T_{IR} - 23.36 \tag{3.1}$$

where T is the temperature measured by thermocouple (actual temperature) and T_{IR} is the temperature measured by infrared camera. Equation (3.1) was used to calculate the actual temperature of the machined surface using the data from infrared camera.
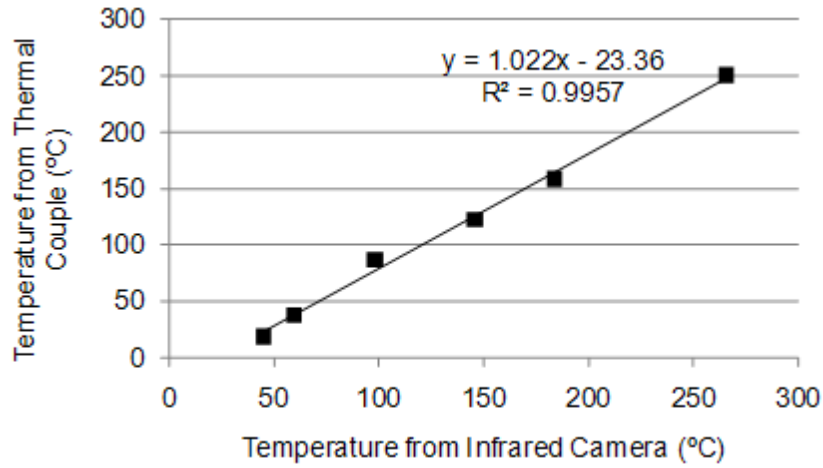
Figure 3.7: Relationship between temperatures measured by infrared camera and thermocouple.
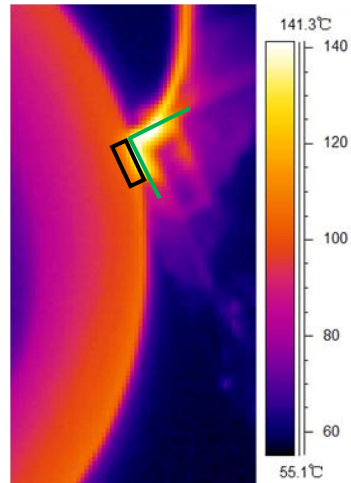
Figure 3.8: Example of temperature measurement using the infrared camera (dry machining, $r_n = 30$ μm, $V = 100$ m/min, $f = 0.1$ mm/rev).

Figure 3.8 shows a sample measurement of the temperature on the machined surface. The maximum temperature measured within the square box was given by the software and was subsequently used to calculate the actual temperature using Equation (3.1). Figure 3.9 shows the maximum temperature on the machined surface under different machining conditions. For dry machining with 30 μm cutting edge radius, the maximum temperature measured was 125 °C. This was in good agreement with the results measured by Kurihara et al. (Kurihara et al., 1981) who performed bar turning of the same material. The depth of cut used by the authors was 3 mm and the feed rate was 0.32 mm/rev, which were more aggressive than the cutting conditions used in this study. As expected, the maximum temperature was higher in their work than the one observed in this study (150 °C vs. 125 °C).

A significant reduction on the temperature of the machined surface was evident when liquid nitrogen was used. With the same cutting edge radius of 30 μm, the temperature dropped about 60% from 125 °C for dry machining to 52 °C under cryogenic condition. Although few researchers have investigated the influence of cryogenic cooling on the temperature of the machined surface, it was shown that the tool-chip interface temperature was reduced from 880 °C to 440 °C when liquid nitrogen was sprayed to the machined surface from the clearance side of the tool during turning of *Ti-6Al-4V* (Hong and Ding, 2001). This suggested that more reduction in temperature of the machined surface could be achieved and this agreed with the findings of this study.
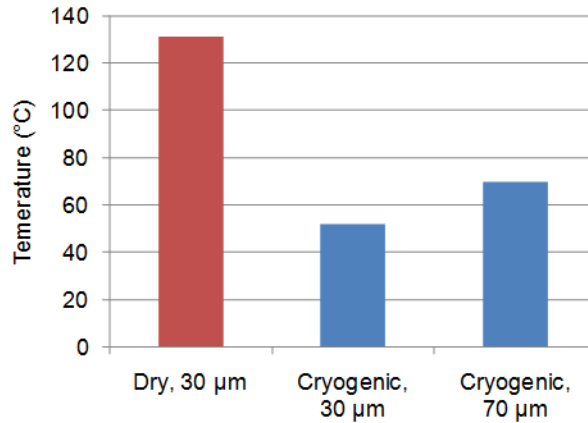
Figure 3.9: Maximum temperature on the machined surface under different machining conditions ($V = 100$ m/min, $f = 0.1$ mm/rev).

Under the same cryogenic condition, the temperature of the machined surface was increased from 52 °C to 71 °C when the cutting edge radius was changed from 30 μm to 70 μm. As shown in Figure 3.6, there was a 53% increase in thrust force, which resulted in more severe plastic deformation on the machined surface as well as larger friction, and this led to increased heat generation. The increase of workpiece temperature with larger cutting edge radius was also reported by Nasr et al. in orthogonal cutting of *AISI 316L* steel (Nasr et al., 2007).

3.4.3   Microstructural analysis

The microstructure near the surface before machining is shown in Figure 3.10. The grain boundaries were clearly visible near the surface, and there were some deformation twins in the region presumably resulting from the vertical milling process used to cut the disc specimens from the sheet.
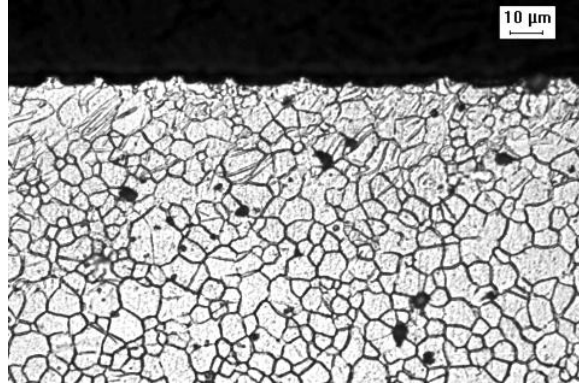
Figure 3.10: Microstructure near the surface before machining experiments.

Figure 3.11 shows the microstructures of the machined surface and chips created using different conditions. The microstructure of the machined surface using a 30 μm edge radius tool under dry conditions is similar to the initial microstructure shown in Figure 3.10, and the grain boundaries are still visible. However, using the same edge radius tool under cryogenic conditions, a "featureless" surface layer in which grain boundaries were no longer visible at this magnification (Figure 3.11 (b)) was formed; the layer was about 8 μm thick. The thickness of this layer increased to 15 μm with a 70 μm edge radius tool under cryogenic conditions (Figure 3.11 (d)) With the same edge radius of 70 μm, a featureless layer with a darker appearance about 20 μm formed under dry conditions. It was reported that the thickness of the tensile residual stress layers became greater with increased number of cutting passes (more rotations of the discs) (Outeiro et al., 2006b). The influence of sequential cuts on the machined surface should be more notable with large edge radius tools since the stagnation point will move upward and more material will flow to the machined surface (Yen et al., 2004). Therefore, machining using large edge radius tools will induce effects similar to burnishing and will change the microstructures of the machined surface to greater depths. The corresponding chip

microstructures in Figure 3.11 show that serrated chips were formed under all conditions. Grain boundaries are clearly visible in the interior of the chips and the grain structures do not change much, especially in Figure 3.11 (b). Similar featureless layers were found in the machined chips at the tool-chip interfaces. This similarity between the chip and the machined surface agrees well with a recent study where it was proved experimentally that the two regions (chip and the machined surface) experienced similar deformation during machining (Guo et al., 2011). The thickness of the featureless layer in the chips was reduced with larger edge radius tools, and could also be caused by the upward movement of the stagnation point (Yen et al., 2004). In addition to the microstructural changes at the tool-chip interface, notable differences occurred near the right edge of the saw-tooth which is caused by the fact that this portion of the material came from the machined surface of the previous cut.
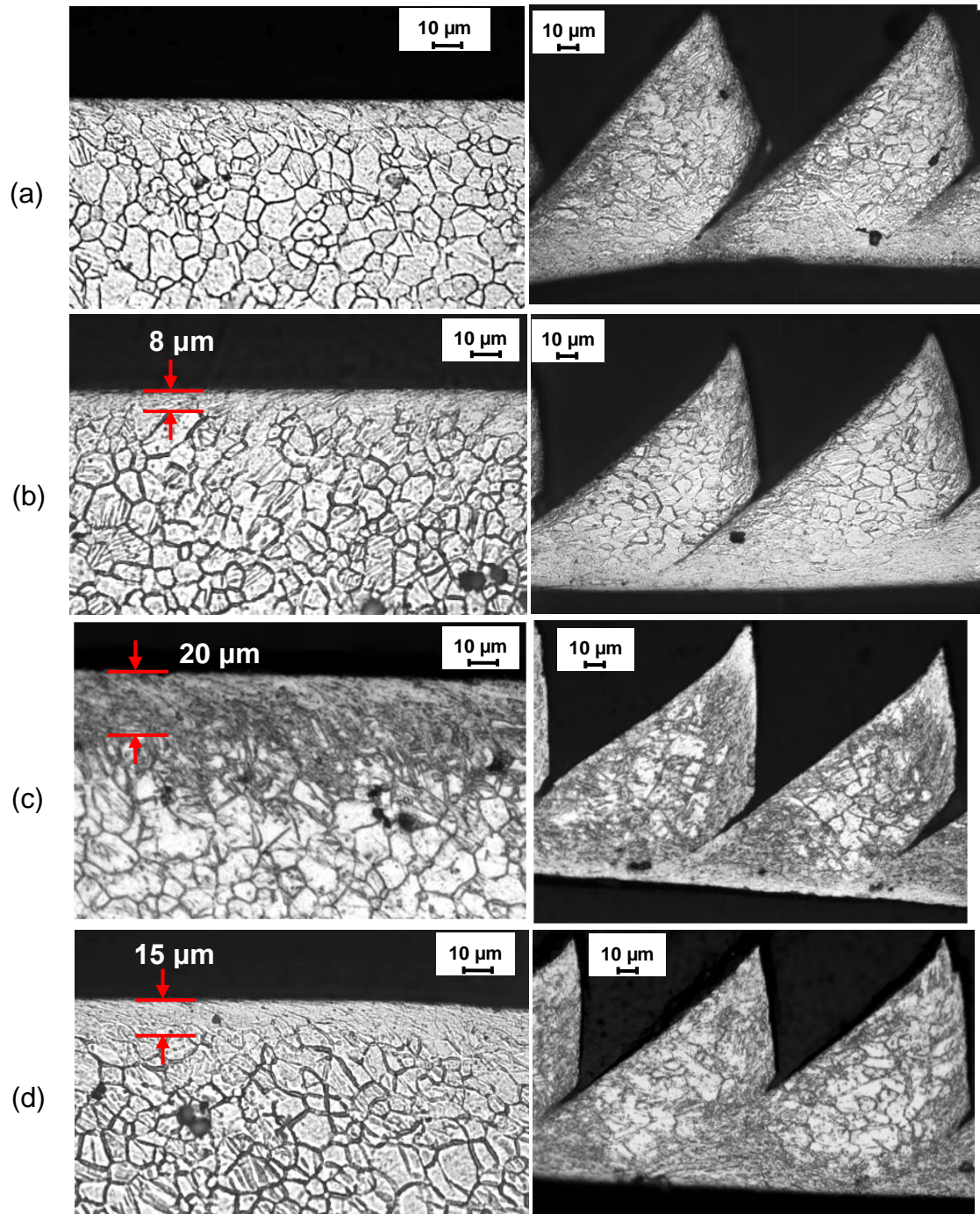
Figure 3.11: Microstructure of the machined surface and chips after machining under different conditons: (a) dry machining, $r_n = 30$ μm; (b) cryogenic machining, $r_n = 30$ μm; (c) dry machining, $r_n = 70$ μm; and (d) cryogenic machining, $r_n = 70$ μm. ($V = 100$ m/min, $f = 0.1$ mm/rev).

51

The appearance of the featureless layers formed under cryogenic machining (Figure 3.11 (b) and (d)) were similar to the "white layers" in the machined surfaces of *AISI 52100* steel (Ramesh et al., 2005) and nickel-based superalloy *IN-100* (Wusatowska-Sarnek et al., 2011) where significant grain refinement to nanocrystalline level was found due to dynamic recrystallization (DRX). To find the possible structures and properties of the featureless layer on machined surface of *AZ31B Mg* alloy, the samples machined with 70 µm edge radius tools under cryogenic condition (Figure 3.11 (d)) were further studied. The SEM pictures of the machined surface and chip were shown in Figure 3.12. Although the grain boundaries are clearly visible below the featureless layer (Figure 3.12 (a)), no features can be found within the layer at this magnification. In Figure 3.12 (b), the material on the left of the line was almost strain-free and that within the shear plane seems to have undergone severe plastic deformation. The grain structures on the right of the line were no longer discernable. Nano/ultrafined grain structures have been reported frequently on *Mg* alloys through strain-induced DRX in various processes, such as SMAT (Shi et al., 2007) and cryogenic burnishing (Pu et al., 2011). The disappearance of grain boundaries in Figure 3.12 (b) after the material had passed the shear plane are likely be caused by the formation of nano/ultrafined grains through DRX, whose structures could not be resolved under this magnification. This claim was also supported by the finding that nanocrystalline grain structures of about 20 nm in size formed in the adiabatic shear band formed when machining *30CrNi3MoV* steel (Duan and Wang, 2005). The mechanism for the dramatic decrease of grain size was rotational DRX which was previously found by Meyers and Pak (Meyers et al., 2001).

10 μm

(a)

25 μm
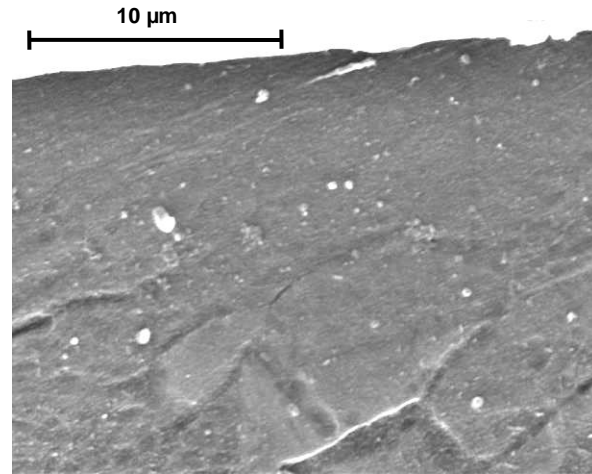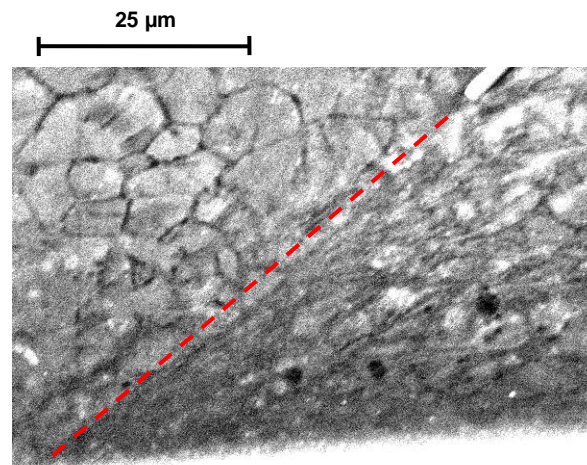
Shear plane

(b)

Figure 3.12: SEM pictures of (a) the machined surface and (b) chip using a 70 μm edge radius tool under cryogenic condition ($V = 100$ m/min, $f = 0.1$ mm/rev).

An empirical formula (Watanabe et al., 2001) was used to predict the size of the recrystallized grains in *AZ31 Mg* alloy after FSP with the application of liquid nitrogen, and this was proved to be consistent with the experimental results (Chang, 2007). The formula is:

$$\frac{d_{rec}}{d_{init}} = 10^3 \times Z^{-1/3} \tag{3.2}$$

where d_{rec} is the recrystallized grain size; d_{init} is the initial grain size; Z is the Zener-Hollomon parameter defined as:

$$Z = \dot{\varepsilon} \times \exp(\frac{Q}{RT}) \qquad (3.3)$$

where $\dot{\varepsilon}$ is the strain-rate; Q is the activation energy; R is the gas constant and T is the temperature. The temperature during FSP under cryogenic conditions was 200 ℃ and the calculated grain size after DRX was 250 nm (Chang, 2007). During cryogenic machining with a 70 µm edge radius tool, the temperature is only 71 ℃ and the strain-rate is much higher than FSP, which should result in significantly smaller grain size less than 250 nm that cannot be recognized by the optical microscope and SEM used in this study.

Phase imaging tapping-mode AFM was reported to successfully provide grain boundary details (Pang et al., 2002; Alexander, 2007) in the nano-scale materials. The accuracy of the grain size measurements was claimed to be comparable to TEM measurement with ±10% (Pang et al., 2002). In tapping-mode AFM, an oscillating cantilever scans the sample surface and tip-to-sample height is kept constant through a feedback loop. Instead of height difference, it measures the contrast in the phase angle between the driving and response frequencies, which is sensitive to material properties including composition, viscoelasticity and surface adhesion (Bharat and Jun, 2003). Figure 3.13 shows the AFM tapping mode phase image of the featureless layer at about 2 µm from the surface obtained after machining using a 70 µm edge radius tool cryogenic condition. Although no etching was used, some grain-like features with an average size of 31 nm are clearly shown in Figure 3.13. This result agrees with the findings that nanocrystallined grains were formed due to DRX in the "white layer" of *AISI 52100* steel

(Ramesh et al., 2005) and IN100 nickel-based superalloy (Wusatowska-Sarnek et al., 2011), as well as on the machined surfaces of copper (Guo et al., 2011).
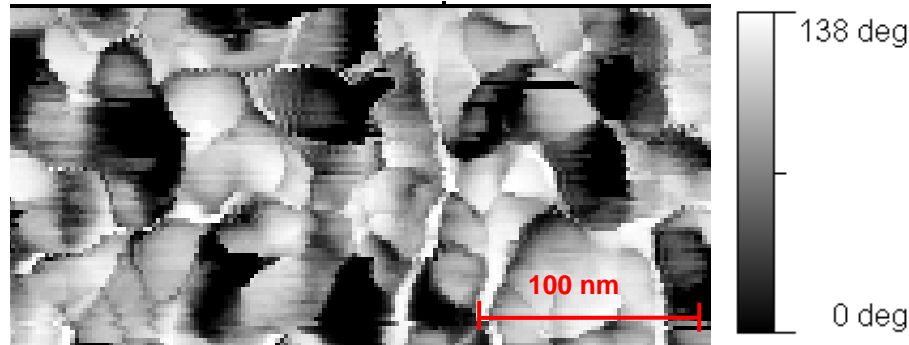
Figure 3.13: AFM tapping mode phase image of the featureless layer at about 2 μm from the surface obtained after machining using a 70 μm edge radius tool and cryogenic condition (V = 100 m/min, f = 0.1 mm/rev).

The featureless layer produced by dry machining using a 70 μm edge radius tool (Figure 3.11(c)) has a darker appearance than those under cryogenic conditions. Figure 3.14 shows the SEM pictures of the machined surface under this condition at different magnifications. Compared with the SEM picture of the machined surface after cryogenic machining using the same edge radius tools (Figure 3.12 (a)) under the same magnification, a clear transition from the initial microstructure to the featureless layer on the top was shown in Figure 3.14 (a), while the changes were abrupt under cryogenic conditions. Severe shear deformation started at about 20 μm below the machined surface. The grains were first elongated and then the grain boundaries disappeared near the surface. This process was very clear at a higher magnification as shown in Figure 3.14 (b) where grain elongation was evident from 10 to 20 μm below the machined. No grain boundaries were visible in the top 10 μm layer. It is expected that significant grain refinement occurs in this layer due to the large plastic strains imposed by machining with

a large edge radius tool. The minimum grain size achieved should be larger than that after cryogenic machining due to higher temperature according to Equation (3.2), which will be confirmed in future experiments. Using the same edge radius tool, the influence of dry machining on microstructure extended to greater depth than cryogenic machining. Similar differences in microstructures near the machined surface between dry and cryogenic conditions were reported recently on nickel-based superalloy *Inconel 718* (Kenda et al., 2011).

10 µm

(a)

10 µm

(b)
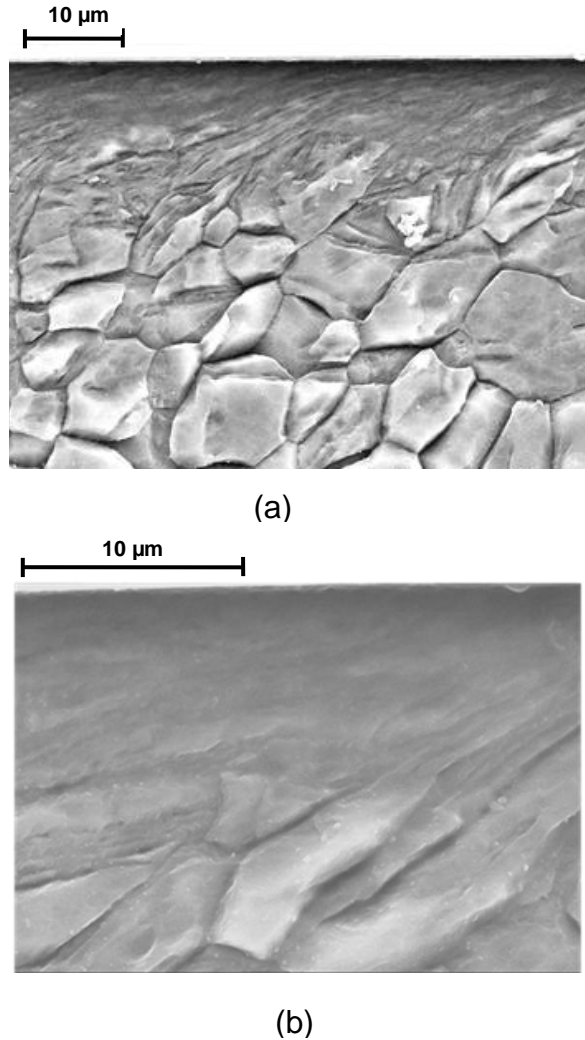
Figure 3.14: SEM pictures of the machined surface using a 70 µm edge radius tool under cryogenic condition: (a) ×2000 and (b) ×5000 magnification.

3.4.4 Crystallographic orientation

It was found recently that the corrosion resistance of *AZ31B Mg* alloy was enhanced with stronger intensity of (0002) crystallographic plane (Song et al., 2010b; Xin et al., 2011). Figure 3.15 shows the evolution of crystallographic orientations on the machined surface before and after cryogenic machining using a 70 µm edge radius tool

conditions. The relative height of the peak corresponding to the basal plane (0002) increased significantly after cryogenic machining. The relative intensity of the basal peak, which was calculated by dividing its absolute intensity by the absolute intensity of the most intense peak (1011), was used to quantitatively evaluate the texture changes using different machining conditions. As shown in Figure 3.15 (b), machining with larger edge radius tools led to stronger intensity of the basal peak under both dry and cryogenic conditions. The formation of strong basal texture was reported on *Mg* alloys after cryogenic burnishing (Pu et al., 2011). Machining with a large edge radius tool induces more ploughing effects on the workpiece surface and is closer to the burnishing process, which leads to the higher intensity of the basal planes appearing on the machined surface.

With the edge radius of 30 μm, dry machining led to larger increase in the basal peak intensity than did in cryogenic machining. With higher temperature, the local adhesion of the material and the flank side of the rounded cutting edge could be increased, which led to more severe shear deformation of the material near the workpiece. This was supported by a recent finding that less shear deformation occurred on the machined surface under cryogenic cooling conditions compared with dry machining (Kenda et al., 2011). However, this trend was reversed when the edge radius was increased to 70 μm where cryogenic machining led to the stronger basal texture. More deformation tends to occur at the basal plane when the temperature is near room temperature since the critical resolved shear stress (CRSS) for basal plane slip in *Mg* is the smallest at room temperature (Reedhill and Robertson, 1957). Machining using 70 μm edge radius tools induced more plastic deformation on the machined surface than machining using 30 μm edge radius tools, and dry machining using 70 μm edge radius

tools generated much higher surface temperature than 125 ℃ (dry machining with 30 µm

edge radius as shown in Figure 3.9). The higher temperature activated more non-basal

slip systems and led to weaker basal texture compared with cryogenic machining.
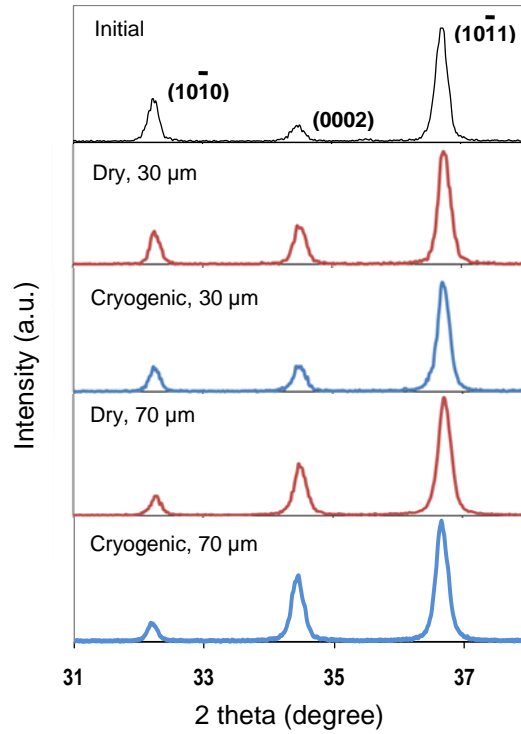
(a)
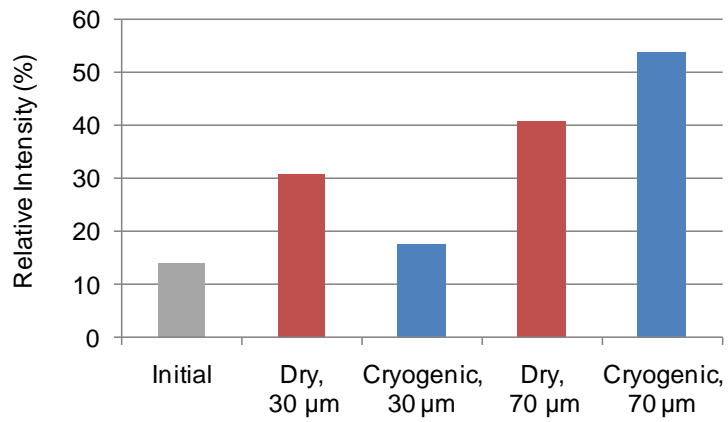
(b)

Figure 3.15: (a) Evolution of crystallographic orientations and (b) relative intensity of basal peak (0002) on the machined surface before and after machining under different conditions as shown in Table 3.4 ($V = 100$ m/min, $f = 0.1$ mm/rev).

3.4.5 Residual stresses

Figure 3.16 shows the measured residual stresses in the circumferential and axial directions after machining using cutting tools with two different edge radii under both dry and cryogenic conditions. As shown in Figure 3.16, the initial residual stresses in both directions were close to zero when the distance from the surface reached about 70 μm. With a 30 μm edge radius tool, compressive residual stresses were induced under both dry and cryogenic conditions up to 140 μm below the machined surface in the circumferential direction. The peak compressive stress for dry machining was about -40 MPa at a depth of 30 μm below the surface. These two parameters were almost the same when cryogenic cooling was used. Much larger differences were found in the axial direction between dry and cryogenic machining with the same edge radius of 30 μm. Tensile residual stress of 37 MPa was generated in the axial direction while cryogenic machining led to compressive residual stress of -39 MPa in that direction.

When the cutting edge radius was increased to 70 μm, the penetration depth of the compressive residual stresses were extended to about 200 μm in the circumferential direction under cryogenic conditions compared with 150 μm under dry conditions, a 54% increase. The residual stresses in the axial direction were also more compressive and extended to greater depths during cryogenic machining than those created during dry machining. For dry machining, the peak compressive stresses in both directions were reduced by about 16% when the cutting edge radius was increased from 30 μm to 70 μm which was due to the increased temperature resulting from more severe ploughing effects. For cryogenic machining, the peak compressive residual stress was reduced slightly in the circumferential direction and increased by 12% in the axial direction.
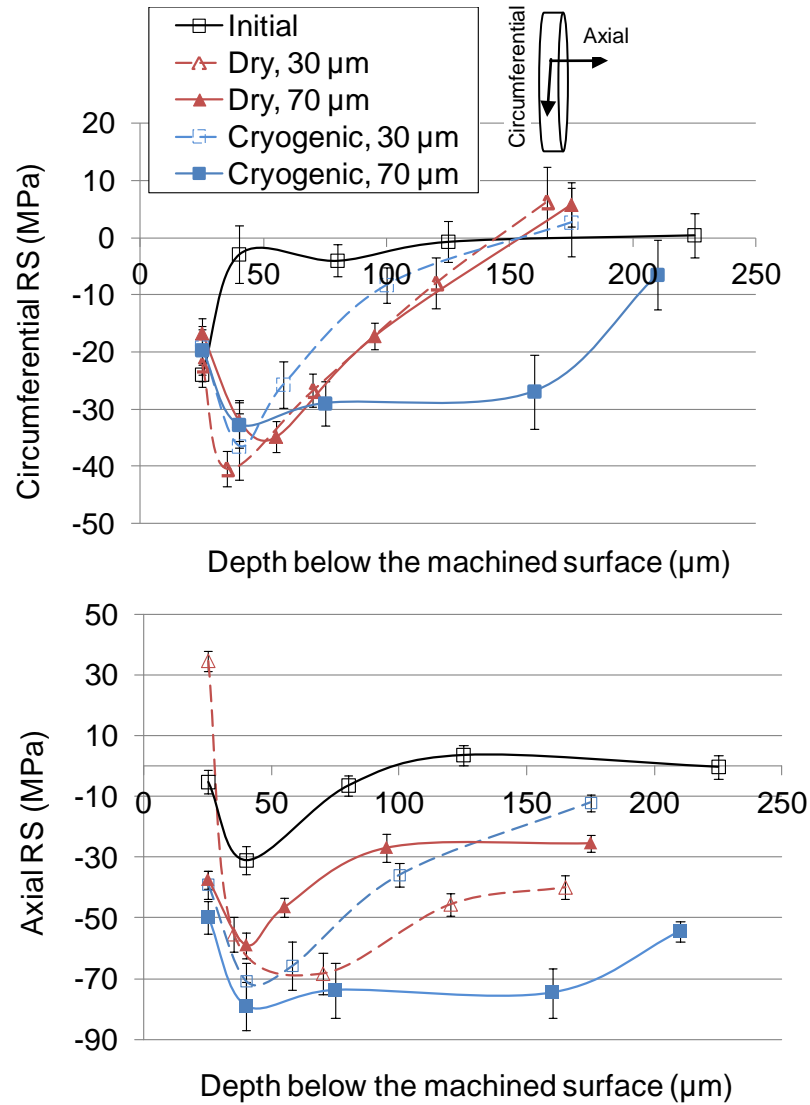
Figure 3.16: Residual stresses after machining using cutting tools with different edge radii and cooling conditions in (a) circumferential and (b) axial directions ($V = 100$ m/min, $f = 0.1$ mm/rev).

The compressive area which is the area defined by the compressive portion of the residual stress profile and the depth axis was claimed to have a notable influence on the fatigue life (Hashimoto et al., 2009). Figure 3.17 shows the compressive areas calculated by the integration of the residual stress profiles with respect to depth below the machined surface up to 200 μm before and after machining under different conditions. Compared

with the initial condition, cryogenic machining with 70 µm edge radius tools increased the compressive areas in both directions by a factor of about 10. With 30 µm edge radius tools, the application of liquid nitrogen led to a smaller compressive area compared with the one created dry machining. The trend was similar to the effect observed on crystallographic orientations and could also be caused by less severe plastic deformation on the machined surface under cryogenic conditions. An opposite trend was observed when the cutting edge radius was increased to 70 µm where cryogenic machining led to 72% and 97% increases in compressive areas, respectively in the circumferential and axial directions, compared with dry machining.

For dry machining, an increased cutting edge radius led to a reduction in compressive areas for both directions. On the contrary, large increases in compressive areas were obtained by cryogenic machining. The results suggest that more significant heat generation occurs when the large edge radius tools are used as shown in Figure 3.9 and this tends to induce more tensile residual stresses, if an inadequate cooling method was used. It also reveals a great opportunity to use cryogenic cooling combined with large edge radius tools to induce large and deep compressive residual stresses on the machined surface, which should enhance the functional performance of the components such as fatigue life and wear/corrosion resistance.
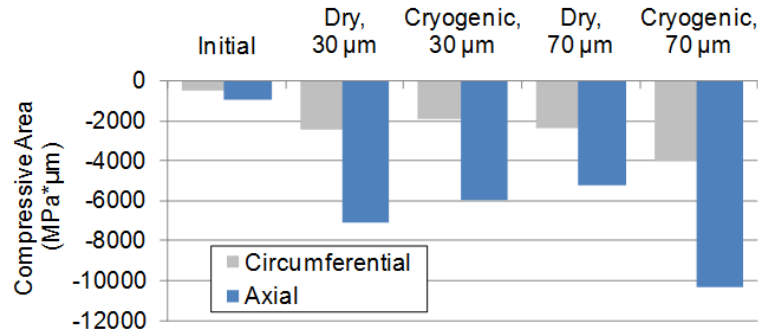
Figure 3.17: Compressive areas of the residual stress profiles before and after machining under different conditions ($V = 100$ m/min, $f = 0.1$ mm/rev).

3.4.6 Surface roughness

Most of the SPD processes used for grain refinement, such as SMAT (Tao et al., 2002) and surface nanocrystallization and hardening (SNH) (Villegas et al., 2005), are based on repetitive impacts of balls with the workpiece, and this frequently leads to an unsatisfactory surface finish that may impair the performance. Dramatic increase of surface roughness from 0.41 μm of the as-received material to 5.5 μm was reported after SNH of nickel-based *Hastelloy C-2000*. The surface roughness (R_a) before and after machining under different conditions is shown in Figure 3.18. All used machining and cooling conditions improve the surface finish, which is one of the advantages over other SPD processes since large surface roughness was found to decrease the corrosion resistance of *AZ31B Mg* alloy (Song and Xu, 2010). The application of liquid nitrogen cooling led to about 20% decrease in surface roughness for both 30 and 70 μm edge radius tools. Strong adhesive effects between the cutting tool and magnesium alloys were reported and the consequent formation of flank build-up was found to be more severe at higher temperature in dry machining of *AZ91 Mg* alloy (Tönshoff and Winkler, 1997).

Therefore, the better surface finish in cryogenic machining is attributed to the reduced temperature through effective cooling using the liquid nitrogen as shown in Figure 3.9. The beneficial effects of cryogenic machining on surface roughness was also reported on *AISI 4037* steel (Dhar and Kamruzzaman, 2007). For the same cooling conditions, machining using large edge radius tools led to increased surface roughness which may also be due to the larger temperature rise and greater adhesive effects between the workpiece and the cutting tool.
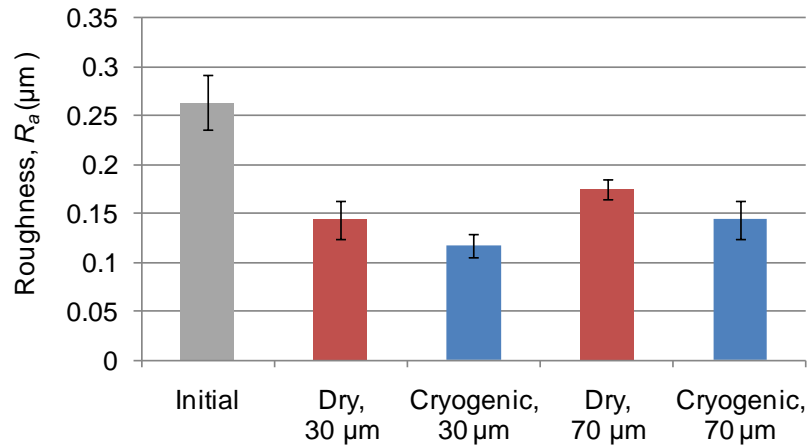
Figure 3.18: Surface roughness (R_a) before and after machining under different conditions ($V = 100$ m/min, $f = 0.1$ mm/rev).

3.4.7 Hardness

The hardness variation with depth below the machined surface under different conditions is shown in Figure 3.19. The hardness increased 87% from 52.3 ± 4.0 Hv in the bulk material to 96.6 ± 5.6 Hv at about 10 μm below the machined surface after cryogenic machining using the 70 μm edge radius tool. Using the same edge radius tool, the hardness increase was slightly smaller under dry conditions (85.8 ± 5.9 Hv). The hardness at this depth under dry and cryogenic machining using the 30 μm edge radius

tools is very similar to each other despite the differences in their microstructures as shown in Figure 3.11.
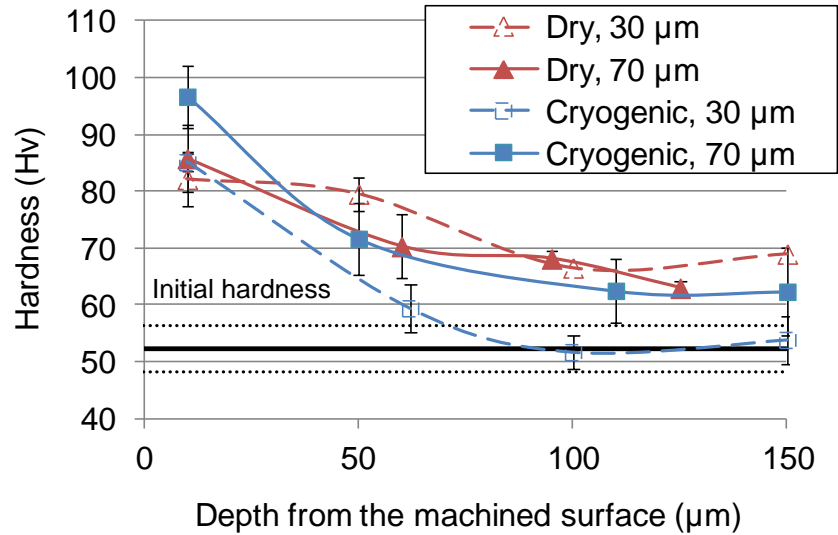
Figure 3.19: Hardness variation with depth below the machined surface under different conditions.

In addition to grain size, work hardening is another important factor that influences the hardness of a material. The amount of work hardening was successfully estimated by several researchers using the peak breadth measured from X-ray diffraction technique (Prevéy, 1987; Outeiro et al., 2006a). The peak breadth variation with depth below the machined surface under different conditions is shown in Figure 3.20. The peak breadth after cryogenic machining using the 70 μm edge radius tool increased by 62% compared with the initial peak breadth at the depth of 25 μm below the machined surface. Under dry condition, the increase was 40% using the same edge radius tool. Since significant grain refinement occurred within the first 10 μm after these two conditions, the broadening should be the combined effects of work hardening and reduced grain size.

The larger increase in peak breadth under cryogenic condition compared with dry condition could be resulting from more severe work hardening and/or smaller grain size.

Using the 30 µm edge radius tools, the same amount of work hardening was achieved in cryogenic and dry machining at the depth of 25 µm below the machined surface, which is not as expected. This could be due to the fact that more plastic deformation was induced on the workpiece by dry machining due to the stronger adhesion of the workpiece material to the cutting tool at higher temperature (Tönshoff and Winkler, 1997). This was supported by a recent finding that less shear deformation occurred on the machined surface under cryogenic cooling conditions compared with dry machining (Kenda et al., 2011). The changes in crystallographic orientations shown in Figure 3.15 also agree with this interpretation. Therefore, it could be concluded that the increased mechanical deformation outweighed the thermal effects during dry machining when using the 30 µm edge radius tool and this led to similar amount of work hardening with the cryogenic condition.
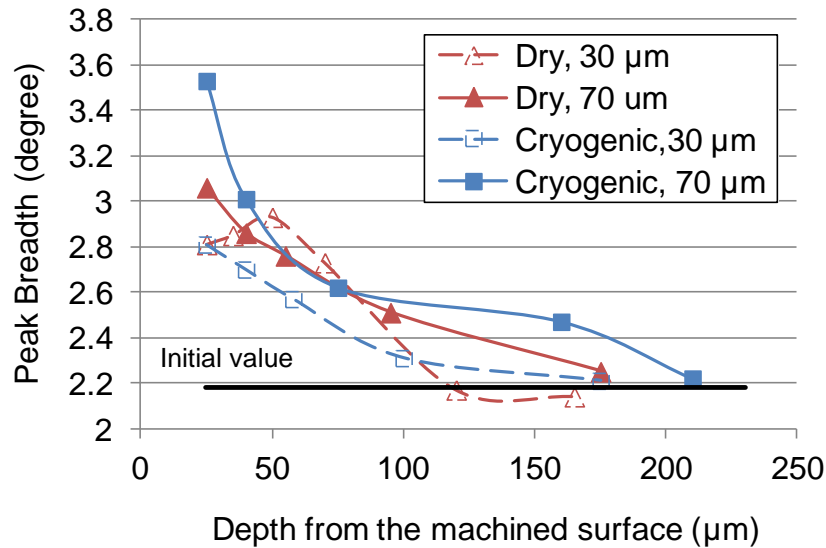
Figure 3.20: Peak breadth variation with depth below the machined surface under different conditions.

Instead of decreasing continually as when using other conditions, the peak breadth of the workpiece after dry machining with the 30 μm edge radius tool first increased to a maximum value at 50 μm depth from the surface, and then decreased. This could be due to the decreasing temperature from the surface to the bulk material. The high temperature at the surface outweighed the mechanical deformation effects. This change of peak breadth was also reflected by the hardness value (Figure 3.19) where the hardness after dry machining using the 30 μm edge radius tool remained almost the same from 10 μm to 50 μm below the machined surface while the values under other conditions dropped more abruptly. Under the same dry condition, this trend of peak breadth was not observed when the 70 μm edge radius tool was used, which could be caused by the fact that the mechanical deformation effects induced by the honed cutting edge outweighed the thermal effects.

68

Cryogenic machining with a 30 µm edge radius tool led to smallest changes in hardness compared with the initial value as shown in Figure 3.19. This agrees with the amount of work hardening as shown in Figure 3.20. Machining under cryogenic cooling conditions and the use of a relatively sharp tool tends to significantly decrease the temperature in the cutting zone, and thus significantly reduce the adhesion of the magnesium alloy with the uncoated carbide tool. Therefore, much less plastic deformation occurred on the workpiece and the smallest changes of hardness and work hardening were observed under this condition.

Under the same liquid nitrogen cooling condition, the hardness curves using the two different edge radii correlate well with the peak breadth curves, which suggest that the hardness and work hardening are intimately related. However, the influence of microstructural changes on hardness cannot be overlooked. Dramatic increase in hardness was reported on the same material after friction stir process (FSP) which was attributed to the significant grain refinement (Chang et al., 2008). The Hall-Petch relationship between the hardness and grain size was also found to be well followed in *AZ31 Mg* alloy (Chang et al., 2004). Therefore, the changes in hardness after machining are likely to be resulting from the combined effects of several surface integrity factors, such as microstructure and work hardening.

3.4.8 Chip morphology

Although not a surface integrity factor, chip control in machining is another essential issue in machining operations. Short broken chips are desired because unexpected long chips may damage the machined surface, leading to tool fracture, or even injure the operator. It was shown in Figure 3.11 that serrated chips were formed

69

under all four machining conditions reported herein. However, totally different chip morphology was observed as shown in Figure 3.21. Remarkable differences exist between dry and cryogenic machining using the 30 µm edge radius tools. The chips formed during dry machining were long and un-broken while small, spiral chips were formed when liquid nitrogen was applied. The latter chip morphology is more desirable and it suggests that cryogenic machining may allow better chip control in addition to creating surface integrity improvement. It was reported recently that the application of liquid nitrogen reduced the tool-chip contact length and increased the chip curl in cryogenic machining of *Ti-6Al-4V* (Bermingham et al., 2011). Although the liquid nitrogen was sprayed directly to the machined surface, it should also indirectly cool the cutting tool. This claim was supported by the layer of ice that covered the cutting tool before cutting began as shown in Figure 3.5 (a). The infrared images captured (Figure 3.22) clearly show the differences in chip morphology between dry and cryogenic machining using the 30 µm edge radius tools. The maximum temperatures at the tool-chip interface for dry and cryogenic machining are 131°C and 52 °C, respectively. The reduced temperature decreased the adhesion effects between the uncoated carbide tools and the magnesium alloy and reduced the tool-chip contact length, which increased chip curl and led to the formation of the spiral chips.

When the cutting edge radius of the tool increased to 70 µm, both dry and cryogenic machining led to the formation of ribbon-like chips. The increased cutting edge radius led to more negative effective rake angle, and also a notable increase in temperature. Both of these changes resulted in larger tool-chip contact length, and reduced chip curl. Also, more ploughing was induced and less material flowed into the

70

chips. It was evident from Figure 3.11 that the featureless layers in the chips became thinner with increased cutting edge radius and this may lead to the improved breakability of the chip. Therefore, the chips are not continuous as in dry machining when using the 30 µm edge radius tools. There are little differences in chip morphology between dry and cryogenic conditions when the cutting edge radius was 70 µm. This may be due to the fact that the thermal effects were outweighed by other factors, such as more negative effective rake angle due to the honed cutting edge.
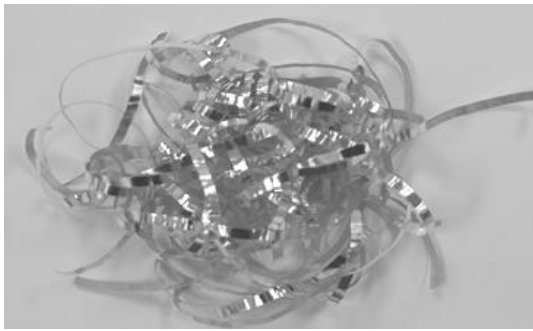
(a)   (b)

(c)   (d)

Figure 3.21: Chip morphology under different machining conditions: (a) dry, 30 µm; (b) cryogenic, 30 µm; (c) dry, 70 µm; and (d) cryogenic, 70 µm.
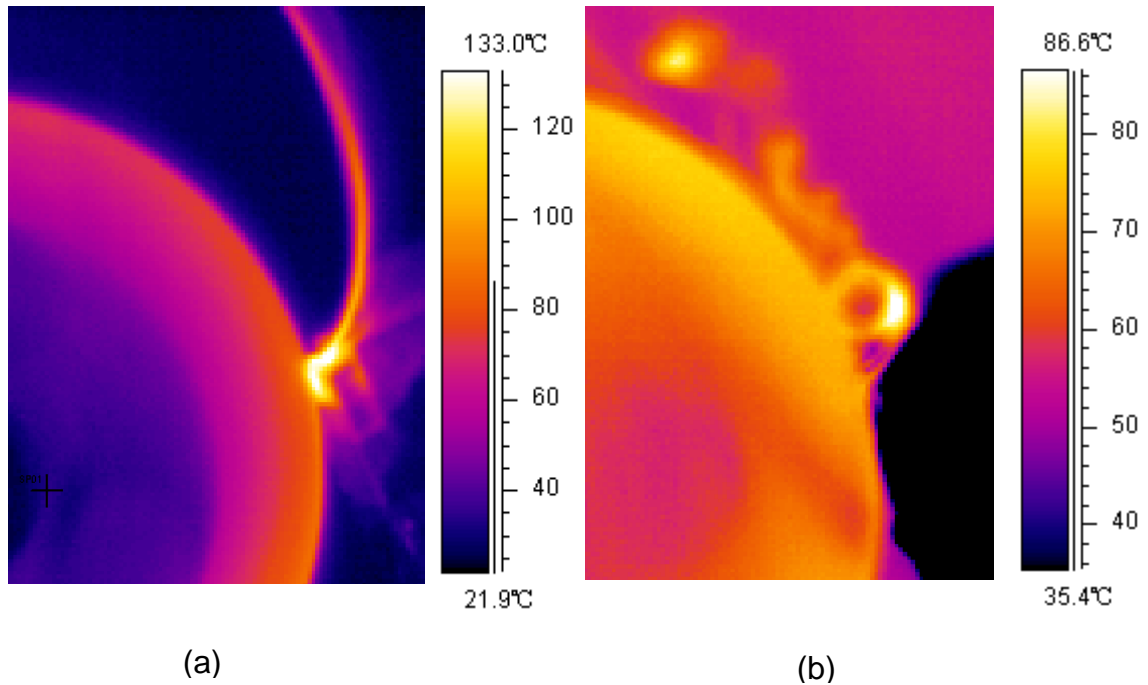
Figure 3.22: Infrared image of chip morphology under (a) dry and (b) cryogenic machining when using 30 μm edge radius tools ($V = 100$ m/min, $f = 0.1$ mm/rev).

3.5 Effects of Cutting Speed and Feed Rate on Surface Integrity

It has been shown in the previous section that a surface grain refinement layer where nanostructures exist can be fabricated by spraying liquid nitorgen to the machined surface. As reviewed in Chapter 2, grain refinement can remarkably improve the corrosion resistance of *AZ31B Mg* alloys and the grain refinement layer induced by cryogenic machining is desirable. However, the maximum thickness of this layer was only 15 μm and this was achieved when 70 μm edge radius tools were used. The major purpose of this part of experiments is to investigate whether thicker grain refinement layers can be achieved by adjusting cutting speed and feed rate. The cooling method was spraying liquid nitrogen to the machined surface from the flank side of the tool, and the

cutting edge radius of the tools used was 70 µm. The experimental matrix is shown in Table 3.5.

Table 3.5: Experiment matrix for machining under different cutting speeds and feed rates

No.	Feed Rate, f [mm/rev]	Cutting Speed, V [m/min]	Tool Edge Radius, r_n [µm]	Cooling Method
1	0.05	50	70	Cryogenic
2	0.05	100	70	Cryogenic
3	0.05	150	70	Cryogenic
4	0.15	50	70	Cryogenic
5	0.15	100	70	Cryogenic
6	0.15	150	70	Cryogenic
7	0.25	50	70	Cryogenic
8	0.25	100	70	Cryogenic
9	0.25	150	70	Cryogenic

3.5.1   Cutting forces

The cutting and thrust force components measured by the dynamometer under different cutting speeds and feed rates are shown in Figure 3.23. The cutting and thrust force components did not change much with the cutting speed at the feed rates of 0.05 mm/rev, which may be due to the fact that only a small amount of material was removed by cutting. It is noted that at this feed rate (50 µm/rev), which is smaller than the cutting edge radius of the tool (70 µm), the cutting force is smaller than the thrust forces; the ratio F_c / F_t is 0.8 for all the cutting speeds. This agrees with the finding from the literature (Liu et al., 2004), and it suggests that ploughing effects are dominant at this feed rate. When the feed rate was increased to 0.15 mm/rev, the forces in both directions decreased slightly with larger cutting speeds. Increasing cutting speed normally

influences the forces in two ways: a) increased heat generation leads to higher temperature and reduces the forces; and b) increased strain-rate leads to stronger work hardening and increases the forces. The decrease of forces at this feed rate can be due to the fact that thermal softening outweighed the work hardening effects; this was supported by the changes in chip morphology where a higher cutting speed led to continuous, unbroken chips while lower cutting speed generated short, discontinuous ribbon chips as shown in Figure 3.24 (b) and (c). When the feed rate of 0.25 mm/rev was used, the cutting and thrust forces increased with the increase in cutting speed. This may be caused by the fact that the work hardening effect outweighed the thermal softening effect. As shown in Figure 3.25, the chips for all the cutting speeds at this feed rate were needle-like and suggested that the materials had limited ductility. The F_c / F_t ratios for the feed rate of 0.25 mm/rev are all larger than 1.4 as shown in Figure 3.23 (c). This shows that the cutting effects are more dominant than the ploughing effects at the larger feed rate.
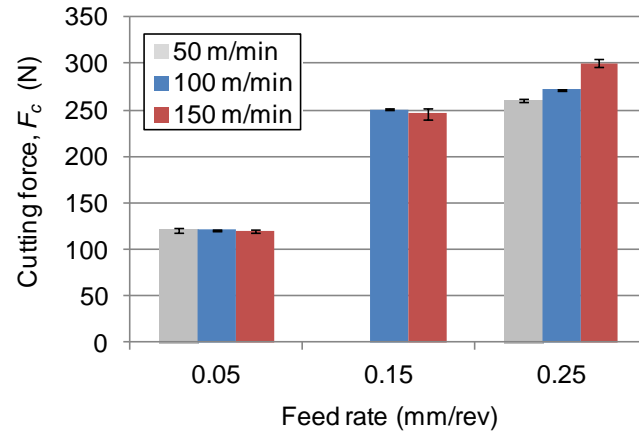
(a)
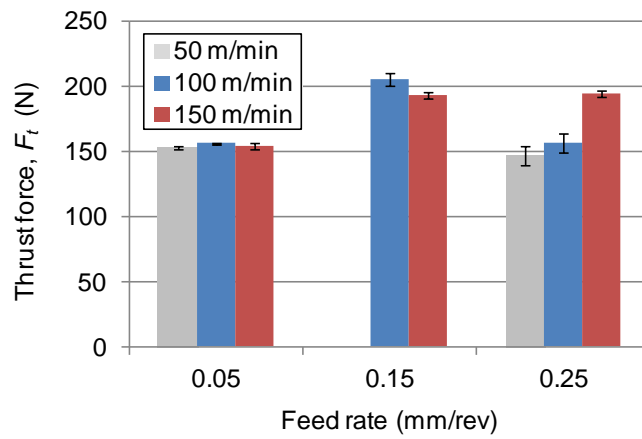
(b)
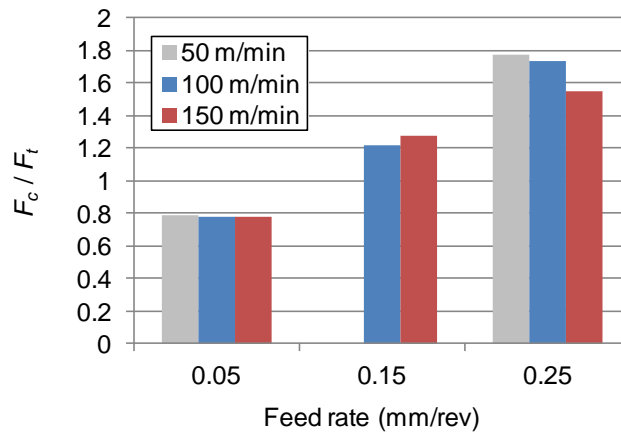
(c)

Figure 3.23: Measured forces under different cutting speeds and feed rates
(cryogenic cooling, $r_n = 70$ μm).

3.5.2 Microstructure and chip morphology

Figure 3.24 shows the microstructures of the machined surfaces and the corresponding chip morphology at the feed rate of 0.05 mm/rev and different cutting speeds. When the cutting speed was increased from 50 m/min to 100 m/min, the thickness of the featureless layer increased from 6 μm to 11 μm. The critical strain for DRX to start in *AZ31 Mg* alloy was found to be a function of the Zener-Hollomon parameter (defined in Equation (3.3)) as (Wang et al., 2002):

$$\varepsilon_{cr} = 0.02039Z^{0.06} \tag{3.4}$$

It was reported that the cutting temperature increased dramatically with increased cutting speed (Kurihara et al., 1981). Increasing the cutting speed from 50 m/min to 100 m/min should lead to a large increase in temperature and results in a smaller *Z* value according to Equation (3.3), which reduces the critical strain for DRX to start. Therefore, the thickness of the featureless layer was increased. However, further increase of the cutting speed decreases the thickness of the featureless layer as shown in Figure 3.24 and this may be due to the occurrence of grain growth after the nanocrystalline grains were formed. It was reported that grain growth could easily occur in the recrystallized grain structures of *Mg* alloys due to their low melting temperature (Chang et al., 2008). The temperature rise at the machined surface was also found to significantly limit the grain refinement achieved on the machined surface of copper and a very small cutting speed of 0.6 m/min was used to prevent grain growth (Calistes et al., 2009). The liquid nitrogen in this study was sprayed directly to the machined surface, and it was expected that the surface temperature was the lowest. Therefore, the nanocrystalline grain structures close to the machined surface were retained due to the liquid nitrogen cooling and the refined

grains below the machined surface grew, leading to a decrease in the featureless layer thickness. The chip shape produced for all cutting speeds at this feed rate was un-broken, continuous chips. The chips become more tangled as cutting speed increases, which suggest that the temperature was increased.
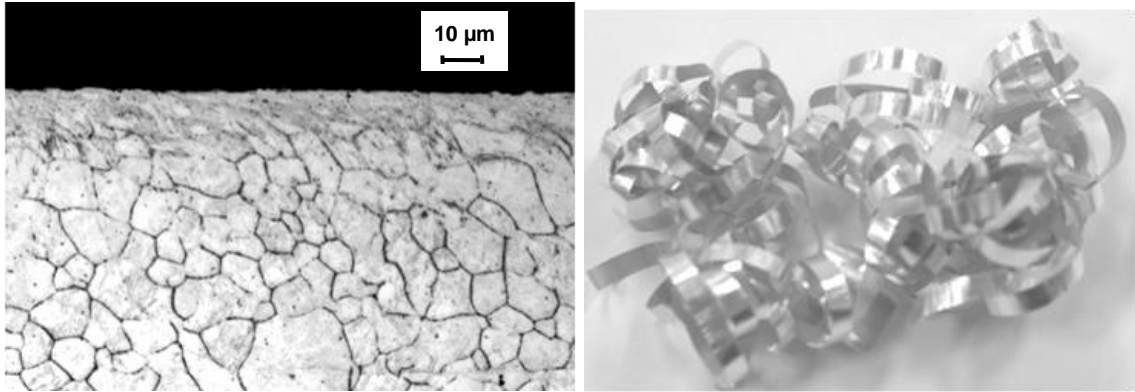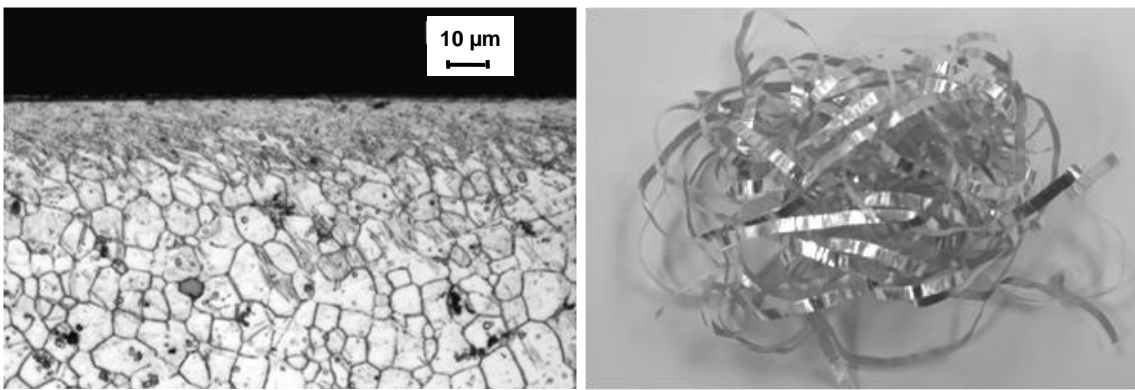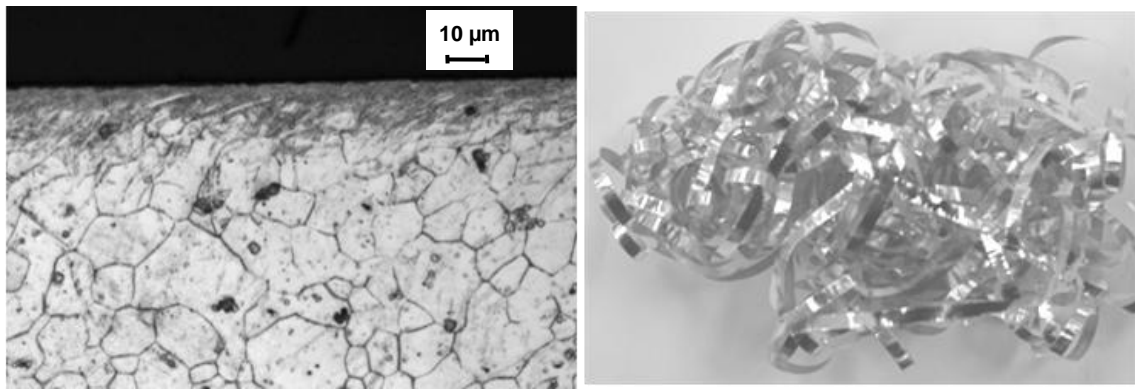
Figure 3.24: Microstructures of the machined surface and chip morphology after cryogenic machining under different cutting speeds: (a) 50 m/min; (b) 100 m/min; and (c) 150 m/min ($f = 0.05$ mm/rev, $r_n = 70$ μm).

Figure 3.25 shows the microstructures of the machined surfaces and the corresponding chip morphology at the feed rate of 0.15 mm/rev and different cutting speeds. Remarkable differences in the microstructures and the chip morphology were found when the cutting speed was changed. The chip shape changed from needle to short, discontinuous ribbon when the cutting speed was increased from 50 m/min to 100 m/min. The needle chips indicate that the ductility of the workpiece is relatively low. Given the same work material, this decrease in ductility suggests that the temperature at the cutting zone is relatively low. Further increase in the cutting speed to 150 m/min changes the chip morphology to long, continuous ribbons, which indicate better ductility. The changes in chip morphology agree with the literature that increasing the cutting speed results in significant increase in cutting temperature (Kurihara et al., 1981).

The featureless layer when cutting at 50 m/min has a dark appearance, while the layer under 100 m/min is similar to the white layer shown in Figure 3.11 (d). This similarity is caused by the lack of variation in cutting conditions. All the other conditions are the same except that the feed rate is increased from 0.1 mm/rev to 0.15 mm/rev. In addition to the surface layer, noteworthy differences in the microstructures below the top layers are also evident. While there is no twinning visible when cutting at 100 m/min, it is visible up to more than 50 μm away from the top surface under 50 m/min. Twinning is the dominant deformation mode in *Mg* alloys at room temperature (Sun et al., 2007). Therefore, the large amount of twinning formed under the cutting speed of 50 m/min was due to the low temperature at the machined surface which should be smaller than the maximum temperature for a more severe cutting condition (71 °C) as shown in Figure 3.9 (f = 0.1 mm/rev, V = 100 m/min, r_n = 70 μm).
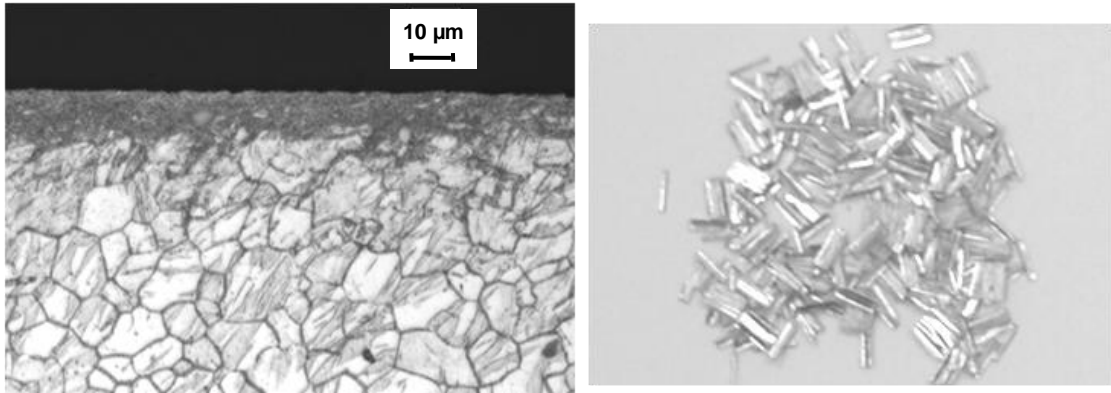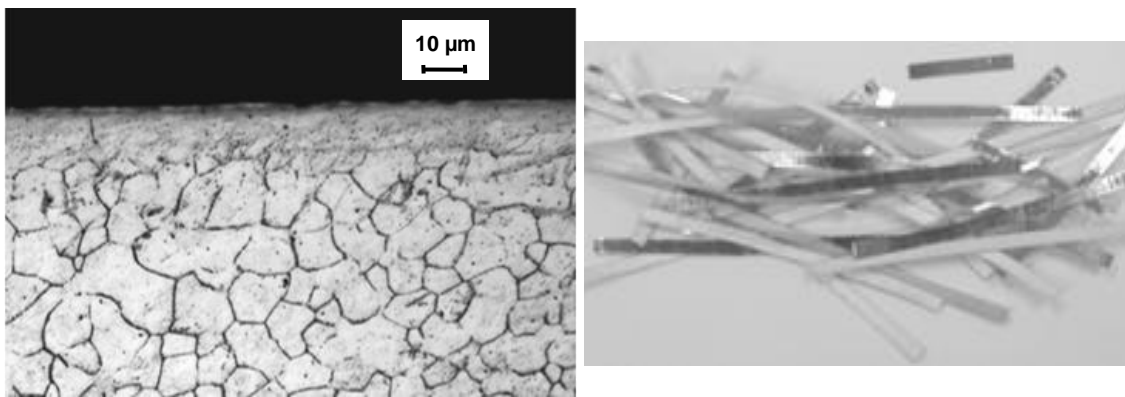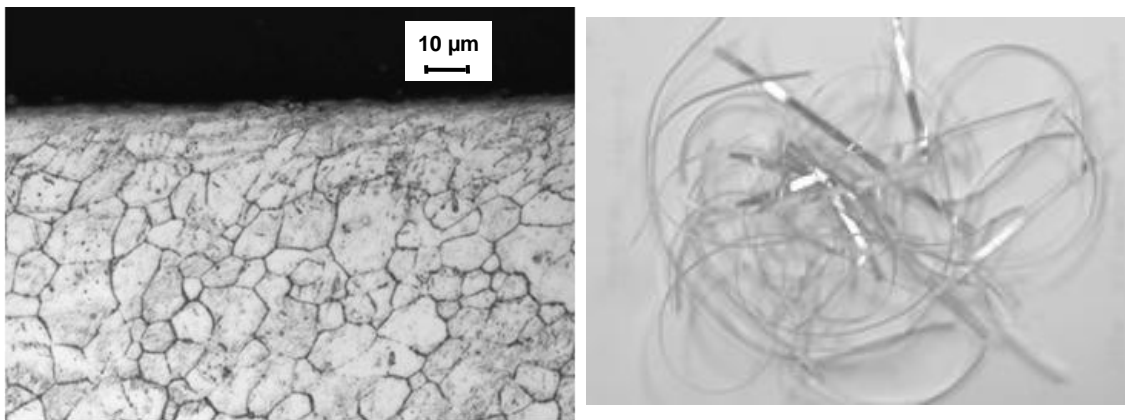
Figure 3.25: Microstructures of the machined surface and chip morphology after cryogenic machining under different cutting speeds: (a) 50 m/min; (b) 100 m/min; and (c) 150 m/min ($f = 0.15$ mm/rev, $r_n = 70$ μm).

To investigate the possible structure of the featureless layer formed under 50 m/min and 0.05 mm/rev (Figure 3.25 (a)), SEM was used to observe the surface microstructure. Figure 3.26 (a) shows an overview of the microstructure near the machined surface after cryogenic machining produced when using a 70 μm edge radius tool at 0.05 mm/rev feed rate and 50 m/min cutting speed. Twinning and grain boundaries are clearly visible about 10 μm away from the surface, while there are no apparent grain structures in the top surface layer. An expanded view of that layer is shown in Figure 3.26 (b), and no discernable structures can be found. Figure 3.26 (c) was taken at the location with greater depth than Figure 3.26 (b) and it shows that a transition occurs. Grain boundaries are clearly visible in the bottom half of the figure while they become vague in the top half. The grain refinement in *AZ91 Mg* alloys induced by a SPD process was found to take place in three steps (Sun et al., 2007). Twinning was claimed as the first step of grain refinement and divided the original coarse grains into finer twin platelets. Then, dislocation movements on both basal plane and non-basal plane slip systems led to dislocation arrays which became the subgrain boundaries with high stored energy. The high energy stored in the sample significantly decreased the recrystallization temperature. Simultaneously, the heavy plastic deformation at high strain-rate also raised the temperature of the sample. Once the local temperature was higher than the recrystallization temperature, DRX took place, which was the last step, and this led to the formation of nanocrystallized grains. It can be concluded from this process that the recrystallization temperature and critical strain must be achieved for DRX to start even though the required temperature will be significantly lower than the one without any plastic deformation. According to this theory, the microstructures shown in Figure 3.26

(b) should be high density dislocation arrays and are still in the second step of the grain refinement process. Due to the lower temperature at this small cutting speed ($<$ 71 °C), DRX was not initiated and therefore it does not have the "white" appearance as the featureless layers formed under higher cutting speed (100 m/min), where the third step of the grain refinement process was completed (Figure 3.25 (b)). This conclusion is further supported by the microstructure formed under the same cutting speed (50 m/min), but higher feed rate (0.25 mm/rev) as shown in Figure 3.27 (a) where the featureless layer has a "white" appearance. Increased feed rate from 0.15 mm/rev to 0.25 mm/rev led to a increase in cutting force as shown in Figure 3.23 and led to a higher temperature, which allowed DRX to occur.

The featureless layer formed at a cutting speed of 150 m/min has a similar appearance with the one under 100 m/min, which suggest that DRX occurrs and dislocation arrays evolve into nanocrystalline grain structures. However, the thickness of this layer was reduced slightly from 10 μm to 6 μm. This finding agrees with previous finding from the microstructures of the machined surface at the feed rate of 0.05 mm/rev, where a further increase in cutting speed reduced the thickness of the featureless layer, and the cause for these reductions is the grain growth due to the increased temperature.
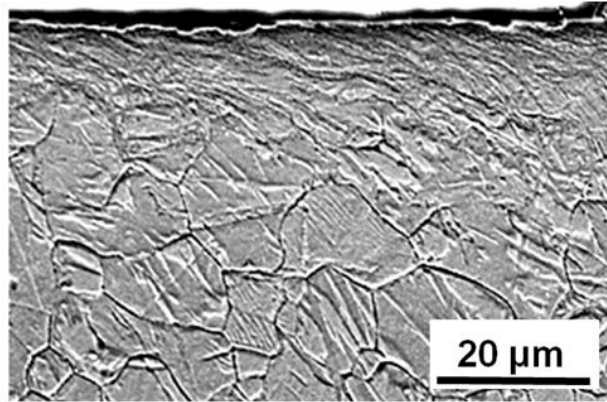
(a)
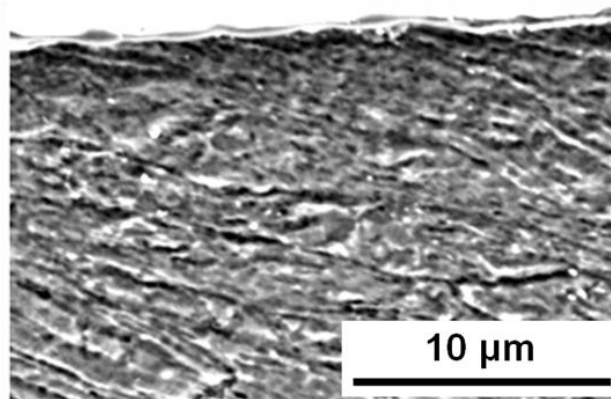
(b)
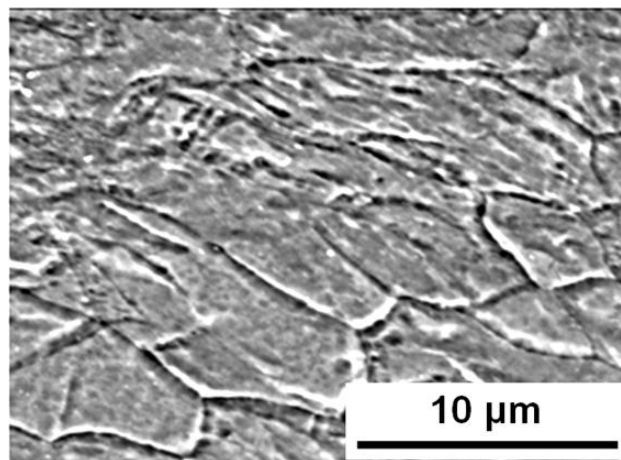
(c)

Figure 3.26: Microstrucutre of the machined surface after cryogenic machining: (a) overview; (b) top surface layer; and (c) below the top layer ($f = 0.15$ mm/rev, $V = 50$ m/min, $r_n = 70$ μm).

Figure 3.27 shows the microstructures of the machined surfaces and the corresponding chip morphology at the feed rate of 0.25 mm/rev and different cutting speeds. The chips formed under all different cutting speeds are needle-like chips which suggest limited ductility of the workpiece. As shown in Figure 3.23, the cutting forces increase as the feed rate increases, which suggest a heavier plastic deformation (larger strain and strain-rate) at the shear plane. The increased forces also implied that the increased strain hardening effects induced by higher cutting speed outweighed the thermal softening effects. It was proved that the ductility of magnesium alloys decreased remarkably with increased strain-rate (Langdon et al., 2003). Therefore, the formation of needle-like chips should be caused by the increased strain-rates.

A featureless layer similar to the one in Figure 3.11 (d) formed at the cutting speed of 50 m/min as shown in Figure 3.27 (a). Further increase in the cutting speed led to the disappearance of this layer. It can be observed from Figure 3.27 (b) and (c) that some grains near the machined surface are slightly larger than the ones in Figure 3.27 (a), which indicates that grain growth occurs at these two cutting speeds, and this agrees with the findings from the other two feed rates, as well.
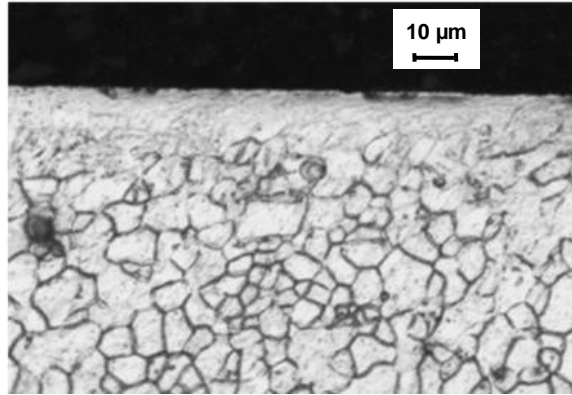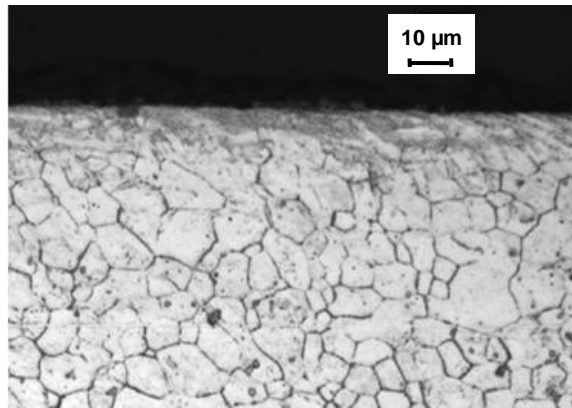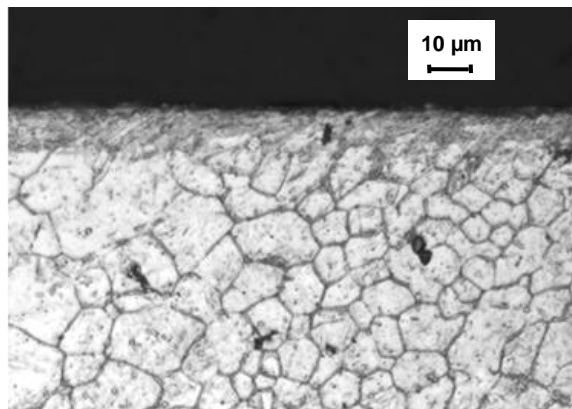
Figure 3.27: Microstructures of the machined surface and chip morphology after cryogenic machining under different cutting speeds: (a) 50 m/min; (b) 100 m/min; and (c) 150 m/min ($f = 0.25$ mm/rev, $r_n = 70$ μm).

3.5.3 Crystallographic orientation

In addition to grain size, crystallographic orientation was recently found to be a major factor that can significantly influence the corrosion resistance of magnesium alloys. Stronger intensity of (0002) crystallographic plane was found to improve the corrosion resistance of *AZ31B Mg* alloy (Song et al., 2010b; Pu et al., 2011; Xin et al., 2011). The relative intensity of the (0002) peak on the machined surface after cryogenic machining under different cutting speeds and feed rates is shown in Figure 3.28. The relative intensity of the (0002) peak on the initial material before the machining experiments was 14%. Cryogenic machining under all the selected cutting speeds and feed rates increased the intensity of the (0002) basal plane on the machined surfaces. The strongest relative intensity observed in this study was 76%, and this was achieved under the cutting speed of 100 m/min and the feed rate of 0.15 mm/rev. The increase of basal texture on the machined surface should be caused by the shear deformation induced by the rounded cutting tool, since the basal plane slip of *Mg* alloys is the dominant deformation mode, especially when the temperature is close to room temperature (Reedhill and Robertson, 1957). Therefore, theoretically, the relative intensity of the (0002) basal plane should be dependent on two major surface factors: the value of the plastic strain and temperature. A clear decreasing trend with increased cutting speed was found at the feed rate of 0.25 mm/rev. Based on the previous analysis, the increase of cutting speed at this feed rate led to increased temperature. Therefore, the decrease of the (0002) basal plane intensity could be caused by the increase of temperature, which leads to the activation of non-basal slip systems in *Mg* alloys.

At the feed rate of 0.15 mm/rev, the intensity of the basal plane was increased when the cutting speed was increased from 50 m/min to 100 min/min. The temperature at these two cutting speeds may be smaller than the critical value. The work hardening effects induced by a higher cutting speed on the machined surface outweighed the thermal softening effects, which led to increased shear deformation on the machined surface and therefore increased intensity of basal plane. However, with further increase in the cutting speed, the additional temperature rise may activate more non-basal slip systems, and therefore the intensity of the basal plane decreased. At the feed rate of 0.05 mm/rev, the relative intensity at the cutting speed of 150 m/min was 75%, and similar to the maximum value in the group. Decreasing the cutting speed reduced the relative intensity. However, it is not clear why the cutting speed of 100 m/min led to the smallest intensity at this feed rate. The influence of crystallographic orientations on the workpiece before machining on cutting forces, chip formation and surface finish was reviewed and summarized by Liu et al. (Liu et al., 2004). However, most of the current research in the literature was conducted on single crystals and few of them studied how crystallographic orientations were changed after machining polycrystalline materials. Since its critical importance on corrosion resistance of *Mg* alloys was found recently (Song et al., 2010b), it is expected that more studies will be conducted to investigate the influence of machining on the resulting crystallographic orientations on the workpiece. At this point, no solid conclusion could be made on how they change with cutting speed and feed rate.
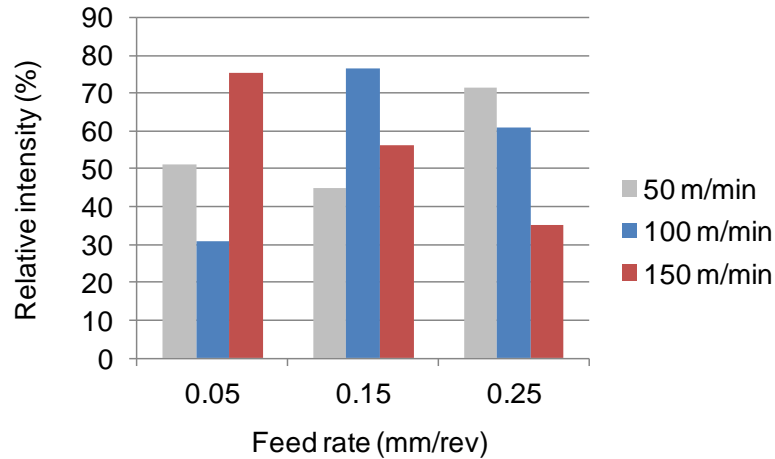
Figure 3.28: Relative intensity of basal peak (0002) on the surface after cryogenic machining under different cutting speed and feed rate ($r_n = 70$ μm).

3.5.4 Surface roughness

Figure 3.29 shows the surface roughness (R_a) after cryogenic machining under different cutting speeds and feed rates using 70 μm edge radius tools. The surface roughness before machining was 0.26 μm. Cryogenic machining under all the selected cutting speeds and feed rates led to improved surface finish. This is a unique advantage of using cryogenic machining to induce surface grain refinement compared with other SPD techniques, such as SMAT, which may notably deteriorate the surface finish. The smallest surface roughness achieved was 0.07 μm, where the cutting speed of 50 m/min and the feed rate of 0.15 mm/rev were used. At the feed rates of 0.05 mm/rev and 0.25 mm/rev, the surface roughness decreases, as the cutting speed increases, which agree, with the finding in machining of *Mg* alloys reported by other researchers (Denkena and Lucas, 2007; Guo and Salahshoor, 2010). However, increased cutting speed resulted in about 70% increase in surface roughness at the feed rate of 0.15 mm/rev. Strong adhesive effects between magnesium alloys and uncoated carbide tools were reported (Tönshoff

and Winkler, 1997). The adhesion should become more severe at higher temperature. Large increases in temperature were observed when the cutting speed was increased from 50 m/min to 150 m/min, which was supported by the changes in chip morphology shown in Figure 3.25. In addition to the thermal effects, the thrust force at the feed rate of 0.15 mm/rev was found to be larger than in other two feed rates as shown in Figure 3.23 (b). The combined effects of high temperature and thrust force reflect the causes for the increased surface roughness at the feed rate of 0.15 mm/rev.
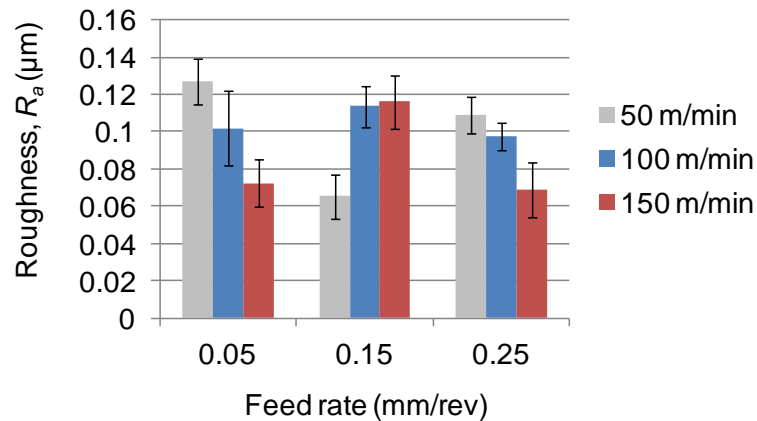
Figure 3.29: Surface roughness (R_a) after cryogenic machining under different cutting speed and feed rate ($r_n = 70$ μm).

3.6 Summary

An experimental investigation has been performed to study the effect of the different machining parameters, including cooling method (dry, cryogenic), cutting edge radius of the tool, cutting speed and feed rate, on the surface integrity of the machined *AZ31B Mg* alloy. The surface integrity factors investigated include surface roughness, microstructure, crystallographic orientations, residual stresses and hardness. Major observations from this experimental study can be summarized as follows:

- Significant reduction of surface temperature was achieved during cryogenic machining, where liquid nitrogen was sprayed onto the machined surface from the clearance side of the tool. Compared with dry machining, cryogenic machining reduced the surface temperature of *AZ31B Mg* alloy from 125 ºC to 52 ºC during machining using edge radius tools with 30 µm edge radius ($V = 100$ m/min, $f = 0.1$ mm/rev). The temperature was increased to 71 ºC when the cutting edge radius was increased to 70 µm under the same cryogenic cooling conditions.

- Better surface finish was achieved after cryogenic machining than dry machining. Using the cutting speed of 100 m/min and the feed rate of 0.1 mm/rev, the application of liquid nitrogen reduced the surface roughness (R_a) by about 20% for machining using both 30 µm and 70 µm edge radius tools. Machining with larger edge radius tools increased the surface roughness. Using the tools with 70 µm edge radius, the surface roughness after cryogenic machining was dependent on the cutting speed and feed rate. The best surface finish achieved was $R_a = 0.07$ µm, where the cutting speed of 50 m/min and the feed rate of 0.15 mm/rev were used.

- Cryogenic machining led to the formation of featureless surface layers which has an appearance similar to "white layer" on machined steels and nickel-based superalloys. AFM tapping mode phase image suggested that significant grain refinement from an initial value of 12 µm to about 31 nm occurred in this featureless layer due to DRX induced by severe plastic deformation. The thickness of this layer was dependent on cutting edge radius, cutting speed and feed rate. The maximum thickness achieved was 15 µm where the edge radius used was 70 µm, the cutting speed was 100 m/min and the feed rate was 0.1 mm/rev (Figure 3.11 (d)). Under the same conditions except

for cooling method, dry machining led to the formation of a 20 μm featureless surface layer as shown in Figure 3.11 (c). Using SEM, it was found that the top 10 μm of this layer was similar to the featureless layer formed under cryogenic machining, and severe shear deformation was evident in the bottom 10 μm of this layer.

A different type of featureless layer formed under cryogenic machining using 70 μm edge radius tools at 50 m/min and 0.15 mm/rev. The appearance of this layer was darker than the other featureless layers, and further investigation using SEM show that a large density of dislocations existed in this layer.

The results on microstructural changes also suggest that optical microscopy may not be adequate to accurately characterize the resulting microstructures from different machining conditions. Advanced characterization techniques, such as SEM, TEM or AFM, are needed.

- The hardness of the machined surface was increased after both dry and cryogenic machining compared with the initial value. The largest increase of 57%, was observed on the sample with the thickest grain refinement layer (cryogenic machining, $r_n = 70$ μm, $V = 100$ m/min, $f = 0.1$ mm/rev). However, the hardness was not only dependent on the microstructures, but also on the work hardening and residual stresses.

- The combination of cryogenic cooling and large cutting edge radius extended the depth of compressive residual stresses to about 200 μm below the surface and increased the compressive areas by a factor of 10 times compared with the sample before machining experiments. Without the application of liquid nitrogen, the residual stresses became more tensile when the cutting edge radius was increased.

- A remarkable increase in the relative intensity of the (0002) basal plane was achieved on the machined surface after cryogenic machining, which should significantly enhance the corrosion resistance of magnesium alloys. This initial intensity of the basal plane before machining was 14%, and this increased to 76% after cryogenic machining when using the 70 µm edge radius tool, a cutting speed of 100 m/min and a feed rate of 0.15 mm/rev.

  With 30 µm edge radius tools, the intensity of basal plane was stronger under dry condition due to more intense shear deformation caused by stronger adhesion of tool-workpiece material at higher temperature. This trend was reversed when the cutting edge radius was increased to 70 µm, which was caused by the activation of more no-basal slip systems at high surface temperature during dry machining.

  A dependence of the basal plane intensity on the cutting speed and feed rate was also observed. At the feed rate of 0.25 mm/rev, the intensity decreases with increased cutting speed, which could be explained by the activation of more no-basal slip systems. However, the relationships between the intensity and the cutting speed at 0.05 mm/rev and 0.15 mm/rev were nonlinear, and further investigation is needed to establish the possible causes.

CHAPTER 4: EXPERIMENTAL STUDY ON SURFACE INTEGRITY IN BURNISHING OF *AZ31B* MAGNESIUM ALLOY

4.1   Introduction

It has been shown in Chapter 3 that cryogenic machining with honed cutting tools can enhance the surface integrity of *AZ31B Mg* alloy in terms of grain refinement, compressive residual stresses, etc., which may significantly improve its corrosion resistance in many applications. Controlled ploughing effects in machining are desirable since this induces severe plastic deformation on the workpiece surface and sub-surface and facilitate dynamic recrystallization (DRX). However, the maximum depth of the grain refinement layer achieved by cryogenic machining described in Chapter 3 was only 15 μm. In order to improve the corrosion resistance of *AZ31B Mg* alloy to a greater extent, a thicker grain refinement layer is needed. One major objective of this chapter is to investigate the potential of using the burnishing process with a fixed roller to increase the grain refinement layer thickness in *AZ31B Mg* alloy.

In addition to grain refinement, other surface integrity factors that may influence the corrosion resistance were also investigated, including crystallographic orientations, residual stresses, hardness and surface roughness. Possible influence of cryogenic cooling on the surface integrity in burnishing was also studied. The characterization methods for surface integrity used in this chapter are the same as those applied in Chapter 3, except that for hardness where a different microhardness tester was used, and these details will be described in the corresponding section of this chapter.

4.2 Experiment Setup

The burnishing experiments were conducted on a Mazak Quick Turn-10 Turning Center equipped with an Air Products and Chemicals ICEFLY® liquid nitrogen delivery system. For dry burnishing, no cooling method was used; for cryogenic burnishing, liquid nitrogen was sprayed at the tool-workpiece region at 0.6 kg/min via the ICEFLY system. The experimental setup is shown in Figure 4.1. . The *AZ31B Mg* work material was received in the form of a 3.22 mm thick sheet. Disc specimens having 130 mm diameter were cut from the sheet by vertical milling in the machine shop and subsequently subjected to burnishing. The disc was fixed in the lathe chuck and rotated during processing. A machining clearance cut using an uncoated carbide insert was conducted to reduce the diameter from 130 mm to 128 mm at the feed rate of 0.1 mm/rev and the cutting speed of 100 m/min in order to standardize initial burnishing conditions. Then, a fixed roller (no rotation) made of high speed tool steel was pushed against the discs at a constant feed rate of 0.01 mm/rev. The radial force (F_r) and tangential force (F_t) during burnishing were measured using a KISTLER 3-Component Tool Dynamometer. The diameter of the used burnishing roller is 14.3 mm. The burnishing speed, i.e., the linear speed at the contact point between the fixed roller and the rotating disc, was set to 100 m/min. The burnishing process was stopped when the final diameter was reduced to 126 mm.
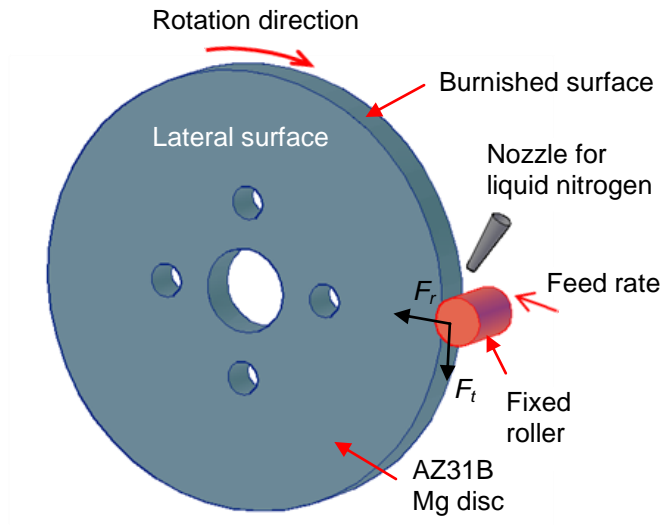
Figure 4.1: Schematic of the burnishing process using a fixed roller.

4.3 Results and Discussions

The force and temperature created during burnishing were measured and compared with those that developed during machining. A comprehensive study on the surface integrity of the burnished *AZ31B Mg* alloy was conducted. This includes the analysis of microstructure, residual stresses, crystallographic orientations, hardness, work hardening and surface roughness. The characterization methods used were the same as described in details in Chapter 3 for machined samples except that a different microhardness tester was used which will be described in details in the corresponding section.

4.3.1   Force and temperature

Figure 4.2 shows forces measured during dry and cryogenic burnishing, as well as the largest forces observed during cryogenic machining ($r_n = 70$ µm, $V = 150$ m/min, $f =$

0.15 mm/rev). The forces during burnishing were remarkably larger than during machining. The radial force components during dry and cryogenic burnishing were 1278 N and 1500 N, respectively. The largest radial force during machining was only 205 N; an increase of about 7 times was observed in burnishing. The differences in force values in the tangential direction are smaller, and with an increase of about 3 times that of the machining ones. The remarkable increase in forces should lead to more severe plastic deformation on the surface and sub-surface of the workpiece and therefore modify the microstructures to a larger depth. Similar to the trend observed in machining, the application of liquid nitrogen to the burnished surfaces led to 18% increase in the radial force, which is also caused by the reduced thermal softening effects. The tangential forces were also increased by 16% when liquid nitrogen was applied compared with dry burnishing.
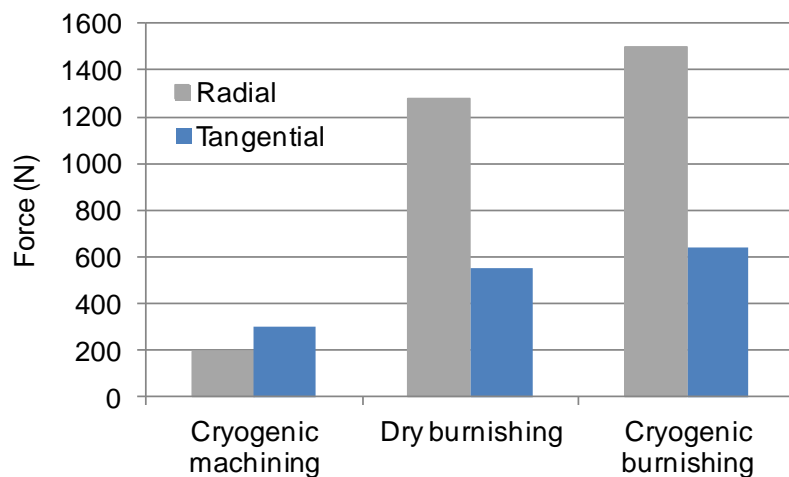
Figure 4.2: Comparison of measured forces during cryogenic machining ($r_n = 70$ μm, $V = 150$ m/min, $f = 0.15$ mm/rev) and burnishing under dry and cryogenic conditions.

Figure 4.3 (a) shows an overview of the temperature field captured by the infrared camera during cryogenic burnishing. The temperature analysis method used was the same

as in Chapter 3. The black body in the image is the burnishing tool consisting of the fixed roller and the fixture. Contrary to the image captured during machining, the material at the processing zone was blocked by the burnishing tool. The first point where the material appeared in the image is defined as the exit point A. Two profiles were taken from this point. Figure 4.3 (b) shows the data obtained from Profile 1 which is in the radial direction from point A. The temperature on the burnished surface was 80 °C and smaller than the one 10 mm away from the surface (90 °C). The decrease in temperature is caused by the effective cooling when liquid nitrogen was sprayed to the burnished surface. This claim was also supported by the data obtained in Profile 2 (tangential direction) as shown in Figure 4.3 (c). Instead of decreasing with increased distance from the contact point as observed during cryogenic machining, the temperature increased from 80 °C to 113 °C at about 100 mm away from the exit point. Then, the temperature reduced and stabilized at about 100 °C. It can be concluded that the temperature will be much higher, if no cooling method is used, as in dry burnishing, which should then result in a larger grain size.
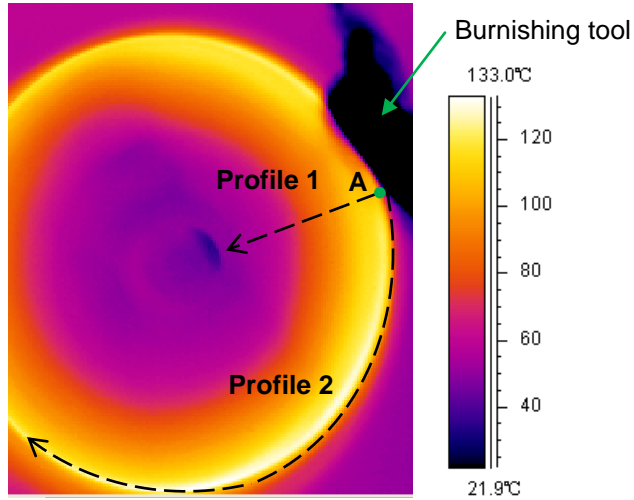
(a)
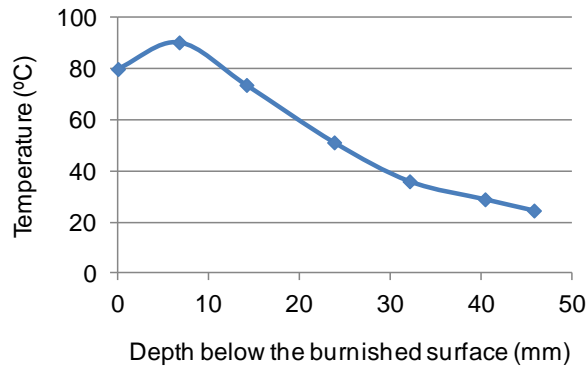
(b)
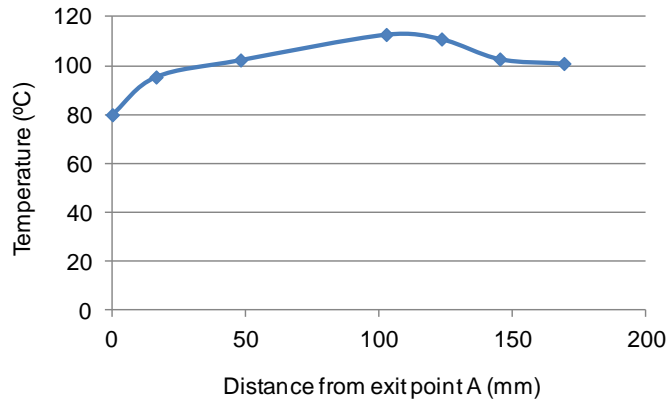
(c)

Figure 4.3: (a) Overview of temperature field during cryogenic burnishing captured by infrared camera; (b) variation of temperature with distance from the surface at the exit point A; and (c) variation of temperature with distance from the exit point A.

4.3.2 Microstructure

An overview of cross-sectional microstructures near the surface after burnishing under both dry and cryogenic conditions is shown in Figure 4.4. Clear process-influenced layers generated by the burnishing process can be identified under both conditions. The thickness of this layer produced by dry and cryogenic burnishing is 3.1 mm and 3.4 mm, respectively. Clearly, the objective of a thicker refined surface layer by using the burnishing process was obtained. After etching, the process-influenced layers can be identified with naked eyes without even using the microscope. An example is shown in Figure 4.4 (c), which indicates that the process-influenced layers have varying different degrees of chemical reactions with the etchant compared with the bulk material. The interfaces between the initial and the process-influenced microstructures are very clear for both conditions. The interface formed after cryogenic burnishing is shown at higher magnification in Figure 4.5. While no twinning can be seen in the initial material, there is a high density of deformation twins above the interface. Twinning is the dominant deformation mode at low temperature for *Mg* alloys. The location of the twins is at the bottom of the process-influenced layer and is more than 3 mm away from the burnished surface; it is expected that the plastic strain at this depth is relatively small and the temperature is low. Therefore, only the first step of the grain refinement process (Sun et al., 2007) was finished and more plastic strains are needed to induce further dislocation movement to facilitate the occurrence of DRX. The interface formed after dry burnishing is similar to the one after cryogenic burnishing. Similar twinning layers have also been reported by other researchers at the bottom of the process-influenced zones induced by

rolling burnishing of *AZ80 Mg* alloy (Zhang and Lindemann, 2005a) and by surface mechanical attrition treatment (SMAT) on *AZ91D Mg* alloy (Sun et al., 2007).

(a)

(b)

(c)
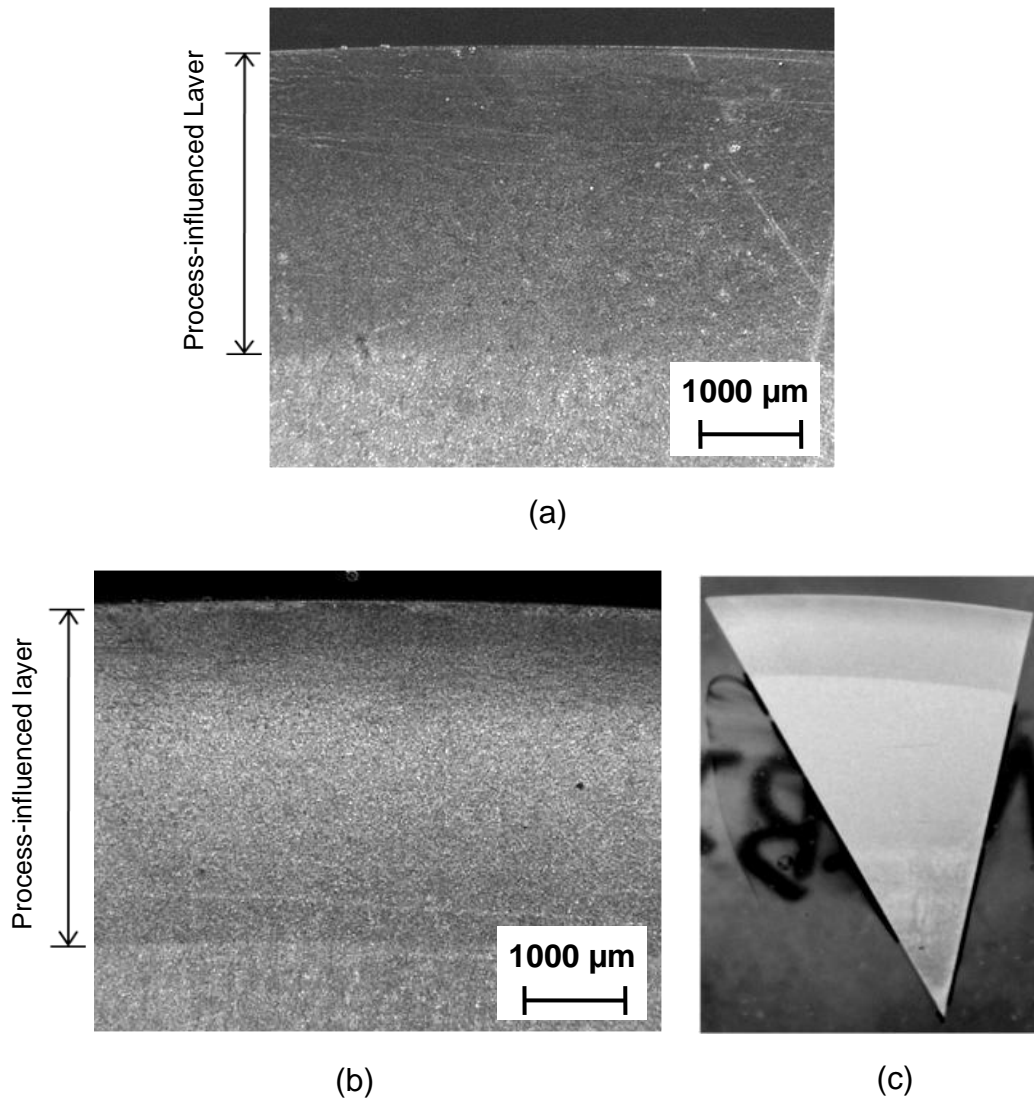
Figure 4.4: (a) Microstructure near the surface after dry burnishing; (b) microstructure near the surface; and (c) photo of the sample after cryogenic burnishing.
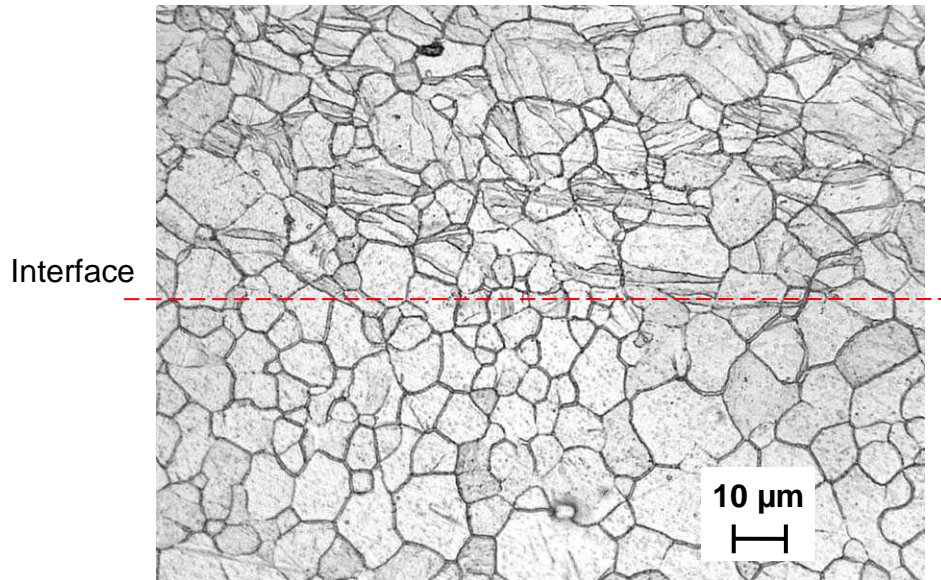
Figure 4.5: Interface between the initial and the process-influenced microstructures after cryogenic burnishing.

The microstructures near the surface before and after burnishing under dry and cryogenic conditions are shown in Figure 4.6. Some deformation twins are shown in the microstructure before burnishing which is likely induced by the vertical milling process which was used in removing the disc samples from the sheet. It is evident in Figure 4.6 (b) that the grain size is significantly reduced by dry burnishing. Under the same magnification, the grain boundaries near the surface after cryogenic burnishing are not discernable as shown in Figure 4.6 (c). Scanning electron microscopy was used to further investigate the microstructure near the topmost surface after cryogenic burnishing. As shown in Figure 4.7, a majority of the grains near the burnished surface are smaller than 1 μm. The average longitudinal axis grain size is 523 ± 131 nm. A comparison of the longitudinal axis grain size distribution before and after burnishing is shown in Figure 4.8. The average grain size before burnishing was 11.9 μm and the scatter of the grain

size was large. Although not as significant as in cryogenic burnishing, grain refinement also occurred under dry burnishing and the average grain size was reduced to 1.4 µm.

An empirical relationship between the recrystallized grain size and the Zener-Holloman parameter was shown in Equation (3.2). According to this relationship, the grain size after dynamic recrystallization (DRX) will decrease with a larger Z value. Since the burnishing speed and the feed rate for both dry and cryogenic burnishing were the same, the strain-rates would be almost the same. With the application of liquid nitrogen cooling during cryogenic burnishing, the temperature at the processing zone should be lower than in dry burnishing, which leads to a larger Z value. Therefore, the finding that more significant grain refinement is achieved under cryogenic conditions correlates with the empirical relationship Equation (3.2).
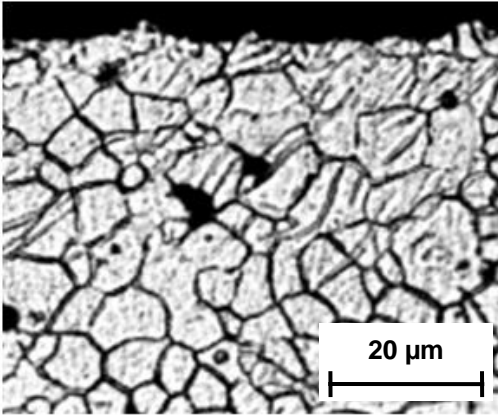
(a)
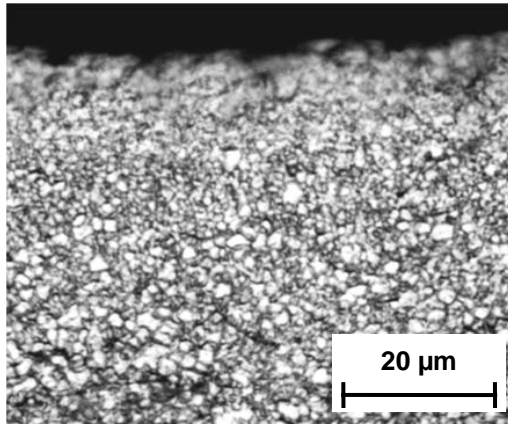
(b)
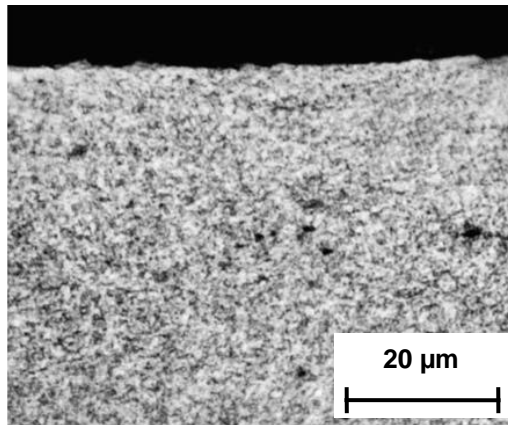
(c)

Figure 4.6: Microstructures near the surface (a) before burnishing, (b) after dry burnishing, and (c) after cryogenic burnishing.
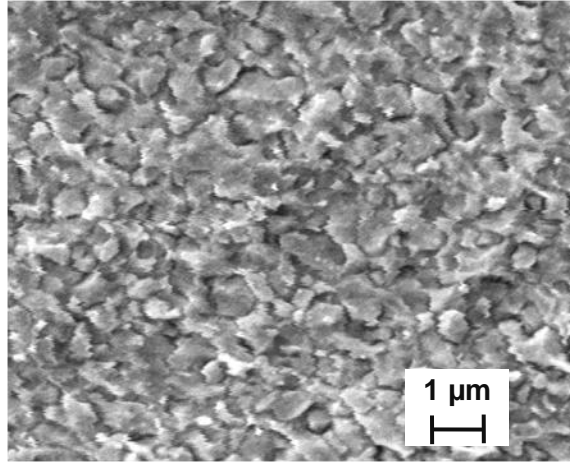
Figure 4.7: SEM picture of the microstructure near the topmost surface after cryogenic burnishing.
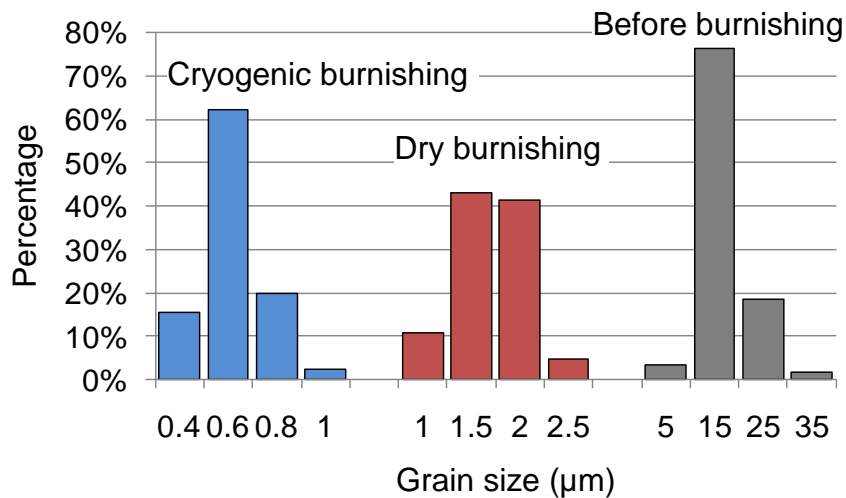
Figure 4.8: Distribution of average longitudinal axis grain size before and after burnishing under dry and cryogenic conditions.

To investigate the grain refinement process, typical microstructures within the process-influenced layer after dry and cryogenic burnishing at different depths from the surface are shown in Figure 4.9 and Figure 4.10, respectively. The grain size under cryogenic burnishing was remarkably smaller than the one after dry burnishing. The percentage of recystallized grains decreased with increasing distance from the surface

under both conditions. It was reported that the volume fraction of recrystallized grains in *AZ31 Mg* alloy decreased with smaller strain in a sigmoidal scheme (Fatemi-Varzaneh et al., 2007; Beer, 2010). Therefore, the decreased percentage of recrystallized grains is likely caused by the reduction in plastic strains with increased distance from the burnished surface. As show in Figure 4.9 (c) and Figure 4.10 (d), ultrafine grains were visible to the depth of 812 μm under dry burnishing and 1118 μm under cryogenic burnishing, respectively. The thickness of grain refinement layer under both conditions was more than 40 times larger than that achieved by machining, which is caused by the more severe plastic deformation induced by the large burnishing forces. It is also evident that the DRX starts first at the boundaries of the grains and sub-grains as shown in Figure 4.9 (d) and Figure 4.10 (d). This agrees with the DRX mechanism reported by many researchers that high energy stored in the grain boundaries can significantly decrease the recrystallization temperature (Meyers et al., 2001; Sun et al., 2007). Similar to the findings from Figure 4.5, large density of deformation twinning was found at the bottom of the process-influenced layer for both dry and cryogenic burnishing as shown in Figure 4.9 (e) and Figure 4.10 (e).
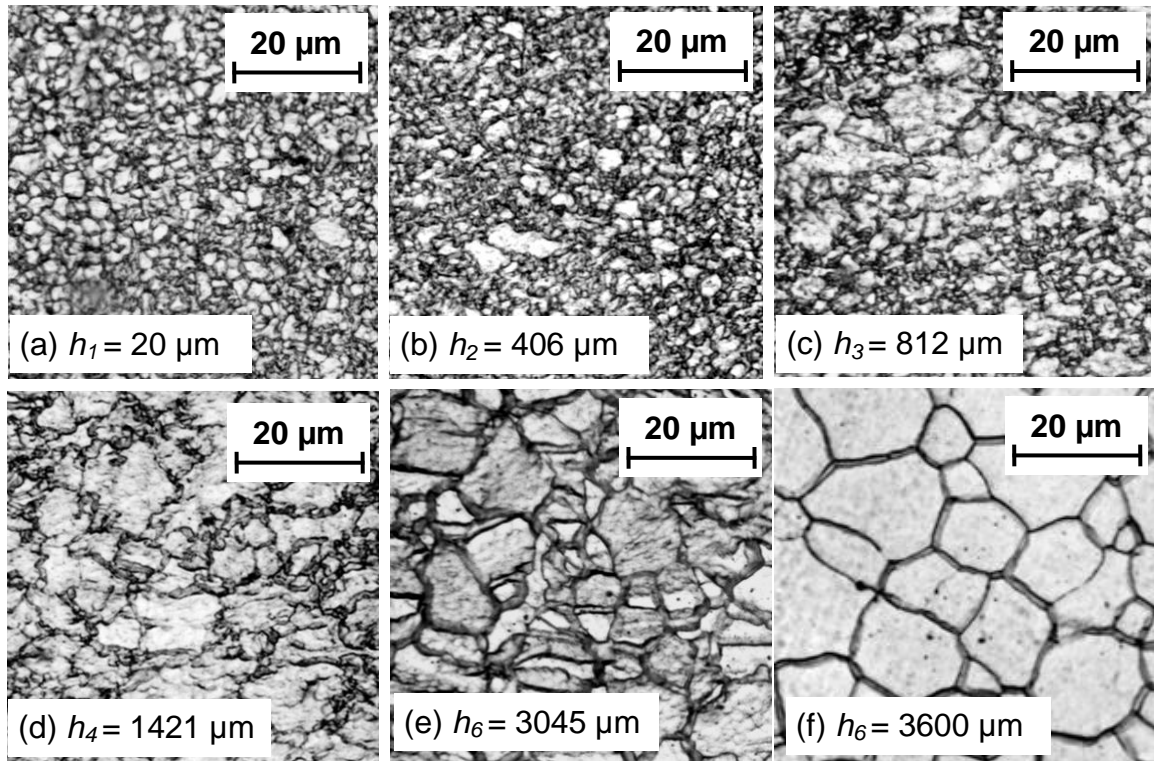
Figure 4.9: Typical microstructures at different depths from the surface after dry burnishing.
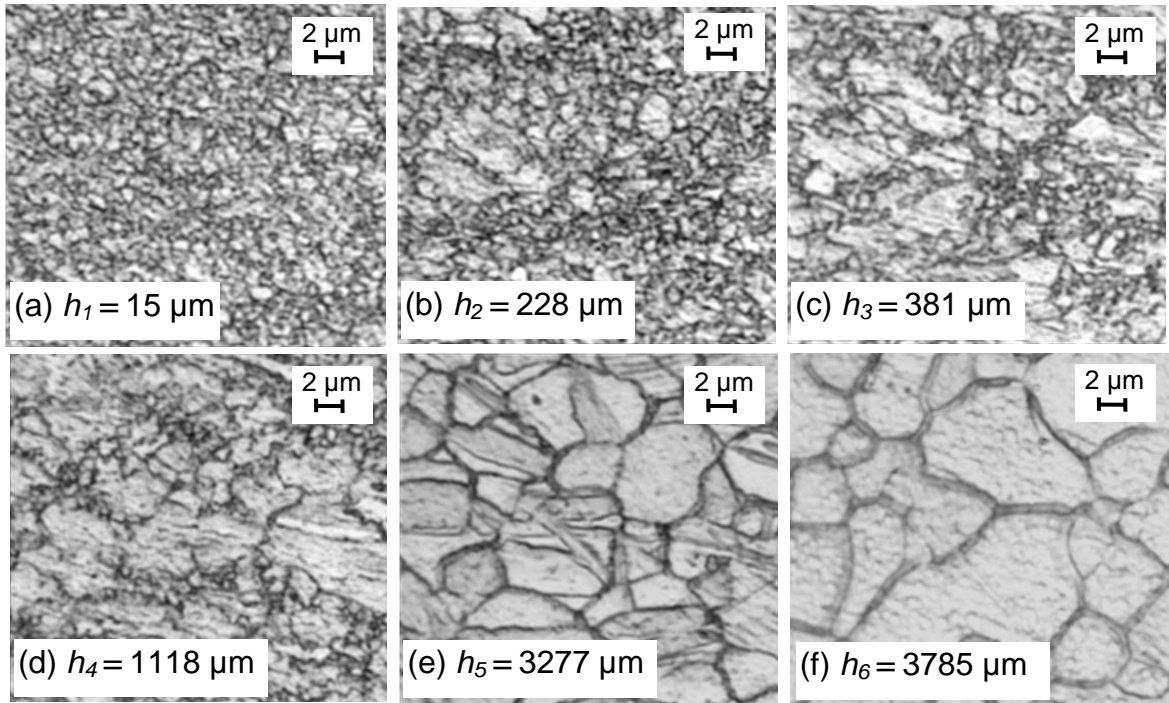
Figure 4.10: Typical microstructures at different depths from the surface after cryogenic burnishing.

4.2.3 Crystallographic orientation

Figure 4.11 shows the evolution of texture caused by burnishing. The relative heights of the peaks corresponding to the basal plane (0002) increased significantly after both dry and cryogenic burnishing, and became the strongest peak, which indicates that strong basal textures were created by the used process. The application of liquid nitrogen during burnishing does not have a significant influence on the crystallographic orientations. This suggests that the mechanical deformation induced by burnishing is the major cause for the texture changes. It was reported in Chapter 3 that increased ploughing effects induced by large edge radius tools resulted in remarkable increase in the intensity of the basal plane. The deformation of the workpiece induced by the ploughing effects in

machining and by burnishing is somewhat similar to that in rolling. It has been reported frequently that the rolled surfaces of *AZ31 Mg* often exhibit strong basal textures (Chang et al., 2003; Sakai et al., 2011). Therefore, it is expected that a burnished surface would become basal textured, which should then result in better corrosion resistance (Song et al., 2010b).
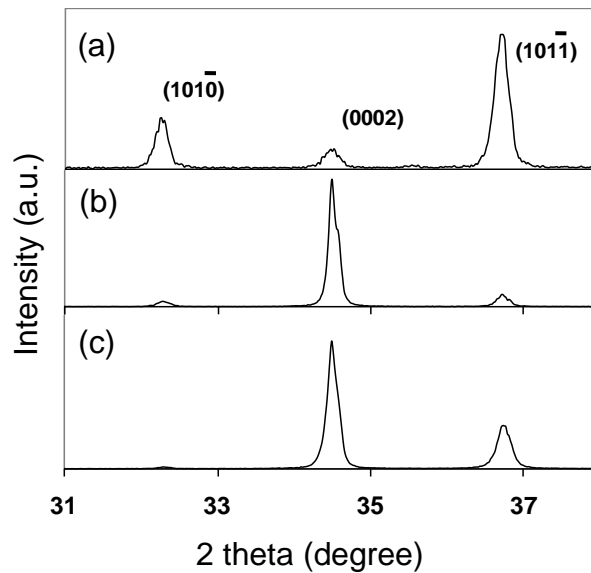
Figure 4.11: Evolution of crystallographic orientations: (a) before burnishing; (b) after dry and (c) cryogenic burnishing.

4.3.4 Residual stresses

Figure 4.12 shows residual stresses of the ground and burnished *AZ31B* surfaces at the depth of 25 μm from the surface (the smallest achievable depth due to limits in the penetration depth of X-ray in this material). The circumferential residual stresses were claimed to be more critical than axial ones for performance of a disc in service (Umbrello et al., 2010b). Although the axial residual stress in the burnished samples are more

compressive than in the ground sample, the circumferential residual stresses become less compressive or more tensile after burnishing compared with its state before burnishing, which is different from what has been reported in most literature, and this suggests that burnishing normally induces more compressive residual stresses (Zinn and Scholtes, 1999; Denkena and Lucas, 2007; Scheel et al., 2010; Salahshoor and Guo, 2011). The contradictory findings from this study and the literature data may be caused by the different roller settings. The roller was fixed in this study while it was allowed to rotate in most literature examples. The fixed tool setting not only led to large radial forces but also about 600 N tangential force (Figure 4.2). The latter is normally close to zero when using a conventional rotating roller. Another possibility is that the applied radial force exceeds a critical value and leads to tensile residual stresses. This was supported by finding where the peak residual stress in *AZ31 Mg* alloy induced by deep rolling first became more compressive with increased pressure and then more tensile when the pressure exceeded certain value (Zinn and Scholtes, 1999). The residual stresses after roller burnishing in *AZ80 Mg* alloy became less compressive when the burnishing force was increased from 200 N to 300 N (Zhang et al., 2005). Also, increased burnishing pressure led to more tensile residual stresses in the *MgCa0.8* alloy (Salahshoor and Guo, 2011). In the current study, cryogenic machining, where radial forces are the smallest (Figure 4.2), led to the formation of large compressive residual stresses on the same material, and cryogenic burnishing, where the radial force is the largest, resulted in the largest tensile residual stresses. Both the results from literature (Zinn and Scholtes, 1999; Zhang et al., 2005; Salahshoor and Guo, 2011) and the current study suggest that a critical burnishing pressure exists beyond which tensile residual stresses will be induced.
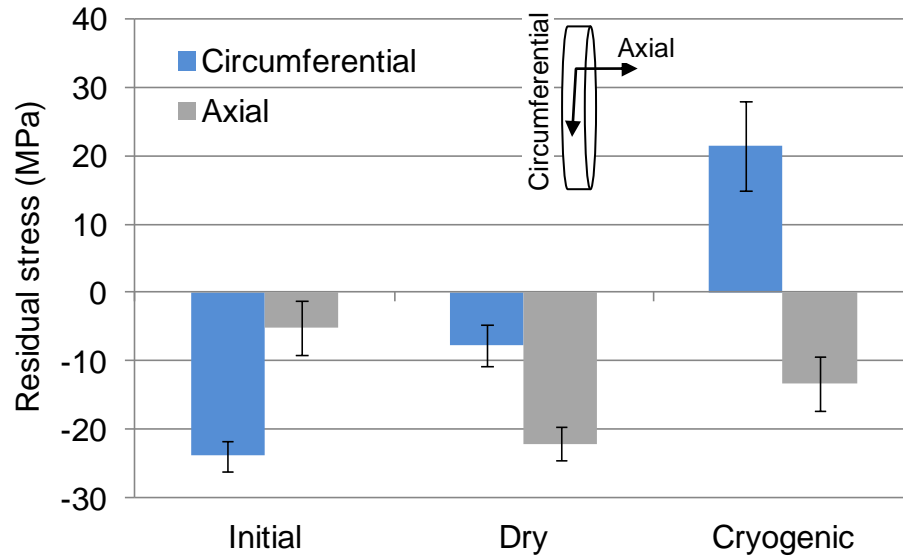
Figure 4.12: Residual stress at 25 μm from the surface of *AZ31B Mg* disc before burnishing and after burnishing under dry and cryogenic conditions.

Figure 4.13 shows the variation of residual stresses with depth below the surface before and after cryogenic burnishing in circumferential and axial directions. The residual stresses in both directions before burnishing were compressive and approached zero at a depth of 225 μm. Tensile residual stresses were generated in the circumferential direction after cryogenic burnishing. The largest tensile stress is 27 MPa, which is 18% of the tensile yield stress of this material. The circumferential residual stress was reduced to almost zero at the depth of 75 μm and then stabilized at about 20 MPa when the depth exceeded 330 μm. However, the peak compressive stress in the axial direction was changed from -31 MPa to -85 MPa after cryogenic burnishing, which is 85% of the compressive yield stress of *AZ31B Mg* alloy (110 MPa); the depth of the peak value was also shifted deeper from 40 μm to 515 μm. The depth of the compressive layer exceeded 1 mm. The large differences in the two directions is a result of the anisotropic plastic deformation induced by the burnishing process in a thin plate specimen. Severe material

flow in the axial direction occurred during the burnishing process, which can be concluded from visual observations of the burr formation after burnishing. The width of the disc increased from 3.22 mm to 5.5 mm on the topmost surface which was clear evidence of material side flow.
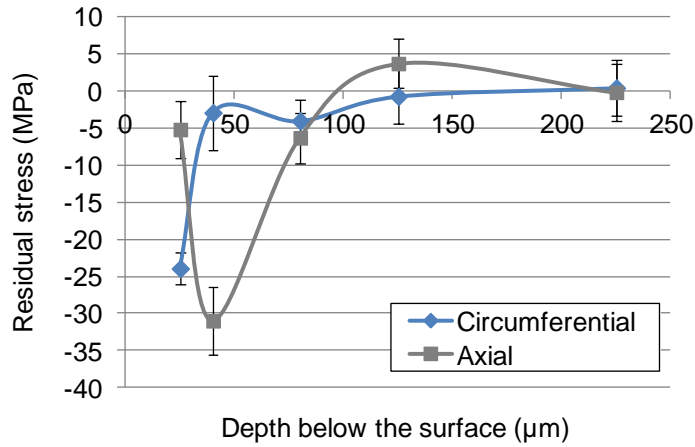
(a)
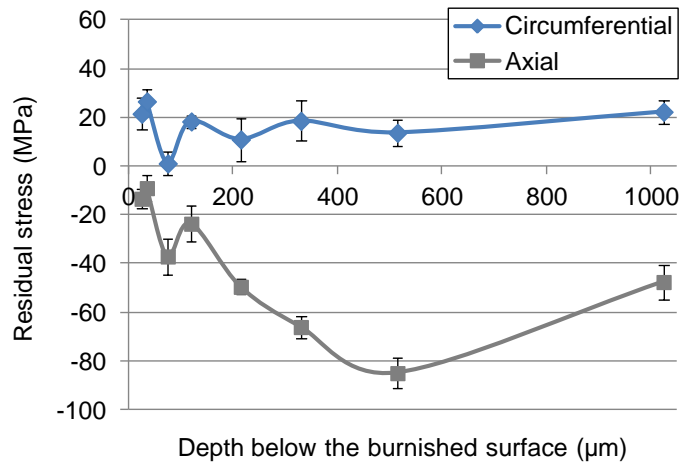
(b)

Figure 4.13: Variation of residual stresses with depth below the surface: (a) before and (b) after cryogenic burnishing in circumferential and axial directions.

111

4.3.5　Hardness and work hardening

Due to the large thickness of the process-influenced layer, a more time-efficient microhardness tester, a Future Tech FM-7 system, was used to measure the hardness in the burnished samples. A Vickers indenter was used at 50 g load and 15 s duration time. Significant increases in hardness values were observed near the burnished surface under both dry and cryogenic conditions. The maximum hardness measured was 110 HV after cryogenic burnishing and 97 HV after dry burnishing, which may reflect more significant grain refinement under cryogenic conditions. The hardness also drops more abruptly with distance below the surface in burnished specimen under dry condition than in the one under cryogenic condition. For example, at the depth of about 650 μm, the hardness obtained in the cryogenically burnished specimen is 92 HV while the hardness in dry burnished specimen is only 71 HV. This agrees with the finding that grain refinement layer induced by cryogenic burnishing is thicker than dry burnishing.
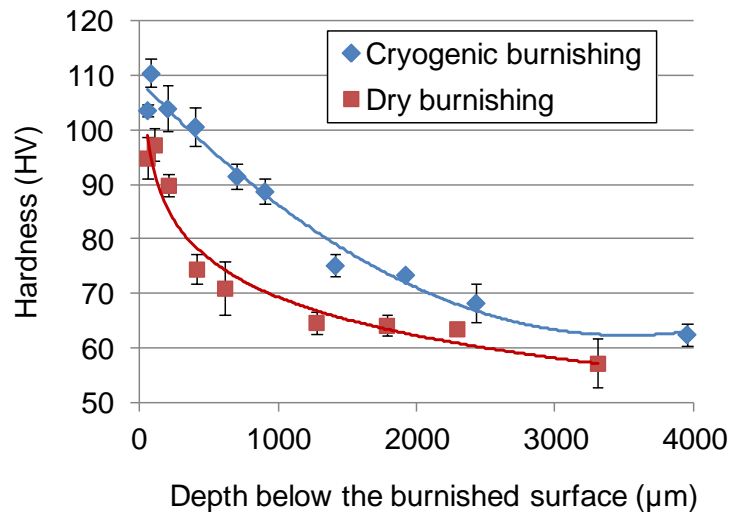
Figure 4.14: Variation of residual stresses with depth below the surface (a) before and (b) after cryogenic burnishing in circumferential and axial directions.

The amount of cold work was successfully estimated by the breadth of the X-ray diffraction peaks where larger breadth indicates more work hardening (Prevéy, 1987). Figure 4.15 (a) shows the XRD peak breadth at a depth of 25 μm from the surface after machining (r_n = 70 μm, V = 100 m/min, f = 0.1 mm/rev) and burnishing under dry and cryogenic conditions. The increased hardness obtained under cryogenic burnishing could also be caused by the stronger work hardening as shown in Figure 4.15 (a), in addition to the grain refinement. It is evident that in both machining and burnishing that the application of liquid nitrogen increases the work hardening on the workpiece surface. Although much larger forces were observed during burnishing than in machining, less work hardening was induced by burnishing which could be caused by the higher temperature. The maximum workpiece temperature measured during cryogenic machining was 71 °C (Figure 3.9), while the value was 113 °C during cryogenic burnishing (Figure 4.3). As shown in Figure 4.3 (c), there were large portions of the disc where the temperature was larger than 100 °C, and this might induce some degree of annealing effects.

Figure 4.15 (b) shows the variation of peak breadth with depth below the surface before and after cryogenic machining (r_n = 70 μm, V = 100 m/min, f = 0.1 mm/rev) and burnishing. Although remarkable work hardening was induced by cryogenic machining near the surface, it reduced to the initial value at a depth of 200 μm. A small increase in peak width was observed in the initial disc which is caused by the sample preparation procedure where vertical milling was used to cut the disc from the sheet. The work hardening induced by cryogenic burnishing decreased significantly with depth in the first 400 μm, but did not return to the initial status after more than 1 mm. The notable increase

in the thickness of the work hardening layer by cryogenic burnishing is due to the repetitive nature of the process where no material was removed as in machining and plastic deformation accumulates on the surface during each rotation.
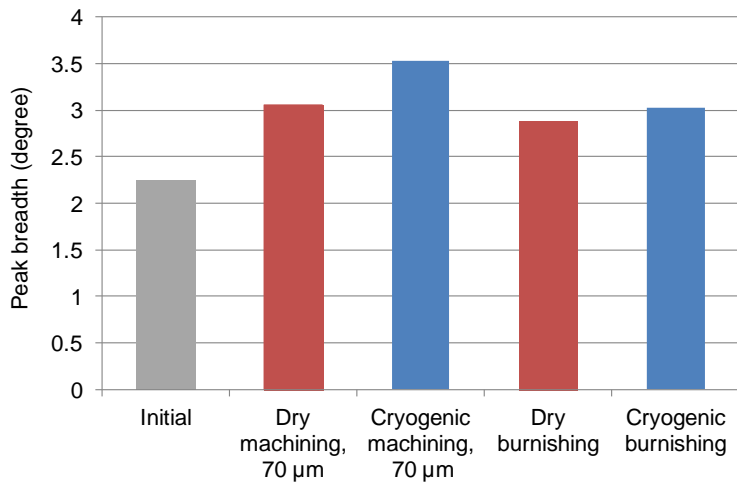
(a)
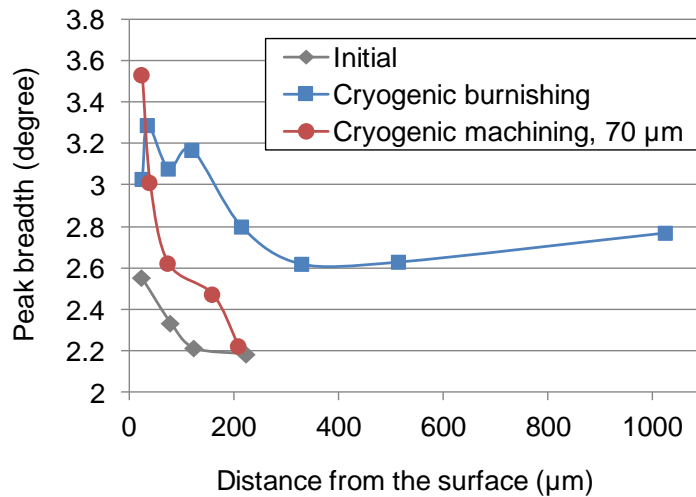
(b)

Figure 4.15: (a) Peak breadth at a depth of 25 μm from the surface before and after machining ($r_n = 70$ μm, $V = 100$ m/min, $f = 0.1$ mm/rev) and burnishing under dry and cryogenic conditions; and (b) variation of peak breadth with depth below the surface before and after cryogenic machining ($r_n = 70$ μm, $V = 100$ m/min, $f = 0.1$ mm/rev) and burnishing.

4.3.6 Surface roughness

Figure 4.16 shows the surface roughness (R_a) before and after burnishing under dry and cryogenic conditions. The surface roughness reduced from 0.26 µm to 0.22 µm after dry burnishing. The application of liquid nitrogen led to slightly better surface roughness (0.20 µm). This trend agrees with the finding from machining experiments as shown in Figure 3.18. However, while most burnishing processes reported in literature generate better surface finish than machining (Hassan and Al-Bsharat, 1996; Salahshoor and Guo, 2011), the burnishing processes used in this study lead to worse surface finish compared with machining. The surface roughness in the machining experiments ranges from 0.07 µm to 0.17 µm as shown in Figure 3.18 and Figure 3.29. This disagreement is likely caused by the fixed roller setting used in this study inducing strong ploughing effects as well as significant heat generation with material side flow. The higher temperature increased the adhesive effects between the magnesium workpiece and the steel roller, which could lead to the formation of unstable build-up edge on the roller, and therefore damaged the surface finish. This claim was supported by the finding in Chapter 3 that machining with larger edge radius tools increased the surface roughness since honed tools induced more ploughing effects and heat generation.

The formation of build-up edge may be reduced by adjusting the burnishing conditions, such as burnishing speed and feed rate as well roller material, which were not changed in the current study. By optimization of these burnishing conditions, better surface finish could likely be achieved.
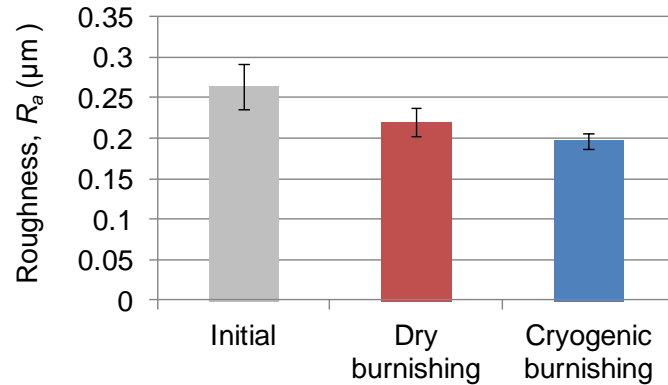
Figure 4.16: Surface roughness (R_a) before and after burnishing under dry and cryogenic conditions.

4.4 Summary

A custom made burnishing tool where the tool was fixed has been used to process the *AZ31B Mg* alloy. The influence of burnishing using both dry and cryogenic conditions on several aspects of surface integrity was investigated, including microstructures, crystallographic orientations, residual stresses, hardness and surface roughness. Major observations from this experimental study can be summarized as follows:

- The forces generated during burnishing were remarkably larger than those required during machining of the same type specimens. The radial forces during dry and cryogenic burnishing were 1278 N and 1500 N, respectively. The largest radial force during machining was only 205 N.

- The temperature of the workpiece first increased with the distance away from the liquid nitrogen nozzle from 80 °C to 113 °C, and then stabilized at 100 °C during cryogenic burnishing.

- The process-influenced layers where microstructures were significantly changed were much thicker after burnishing than machining. While the maximum thickness of the grain refined layers was only 20 μm after machining, and these layers after burnishing were notably extended to 3.1 mm in dry burnishing and 3.4 mm in cryogenic burnishing.

  Grain refinement induced by DRX occurred in the process-influenced layers after burnishing. The average grain size near the topmost surface was reduced from an initial value of 11.9 μm to 0.5 μm after cryogenic burnishing and 1.4 μm after dry burnishing. The percentage of recystallized grains decreased with distance below the burnished surface. Ultrafine grains were visible to the depth of 812 μm below the surface in dry burnishing and 1118 μm in cryogenic burnishing.

- The relative intensity of the (0002) basal plane, which was the weakest compared with other peaks before burnishing, was significantly increased and became the strongest after burnishing. This seems to have significantly enhanced the corrosion resistance of *AZ31B Mg* alloy. The application of liquid nitrogen during burnishing did not have any significant influence on the crystallographic orientations.

- The residual stresses at the depth of 25 μm from the surface became more tensile after burnishing in the circumferential direction, compared with the initial status, and are more compressive in the axial direction. The application of liquid nitrogen during burnishing led to the formation of more tensile residual stresses in both directions.

  Tensile residual stresses of about 20 MPa were induced by cryogenic burnishing in the circumferential direction up to 1 mm from the burnished surface. However, large compressive stress was generated in the axial direction. The peak

compressive stress was -85 MPa, which is 85% of the compressive yield stress of *AZ31B Mg* alloy (110 MPa); the depth of the peak value was 515 μm below the burnished surface. The depth of the compressive residual stress layer in the axial direction exceeded 1 mm.

The large difference in residual stress values in the two directions could be caused by the different deformation directions. Bur formation was evident after both dry and cryogenic burnishing which suggested severe flow of the material in the axial direction during the burnishing process. Further studies are needed to investigate the possible causes for the different distribution of residual stresses in the two directions.

- The hardness near the burnished surface after dry and cryogenic burnishing was increased by 70% and 93%, respectively compared with the initial material. The hardness after dry burnishing decreases more abruptly with the increase in depth below the burnished surface than that after cryogenic burnishing.

- The surface roughness after burnishing under both dry and cryogenic conditions was reduced from 0.26 μm to 0.22 μm and 0.20 μm, respectively, which agrees with the finding in machining (Chapter 3) that the application of liquid nitrogen improves the surface finish. However, the surface roughness after burnishing was larger than the surface roughness after machining and is contradictory with the literature where burnishing normally generates better surface finish. This is more likely caused by using the fixed tool where the adhesive effects between the workpiece and the tool became more severe, and cause the temperatures to increase.

CHAPTER 5: EXPERIMENTAL STUDY ON CORROSION PERFORMANCE OF MACHINED AND BURNISHED *AZ31B* MAGNESIUM ALLOY

5.1   Introduction

Poor corrosion resistance of *Mg* alloys limits their application to a great extent. It has been reported recently that the corrosion performance of *Mg* alloys strongly depends on microstructure (especially grain size), crystallographic orientations and residual stresses, all of which were found to be significantly modified by the machining/burnishing processes as shown in Chapters 4 and 5.

To evaluate the corrosion resistance of *AZ31B Mg* alloy processed under various machining and burnishing conditions, corrosion tests in both 5 weight percent (wt.) % *NaCl* solution and simulated body fluid (*SBF*) were conducted. Remarkable improvement in corrosion performance has been achieved by cryogenic machining and burnishing under some conditions. The nano/ultrafined grain refinement layers induced by machining/burnishing act as protective coatings and significantly improve the corrosion resistance. Crystallographic orientations were found to be another critical factor, especially for burnished samples. The influence of residual stresses was evident on samples machined using different cutting speeds as well as electrochemical measurements on burnished samples.

This study demonstrates the success of a novel approach to enhance the corrosion resistance of *Mg* alloys by cost-effective and industrially available processes, cryogenic machining and burnishing, by tailored surface integrity.

5.2   Corrosion Performance of Machined *AZ31B Mg* Alloy

To evaluate the corrosion performance of the machined *AZ31B Mg* alloy, samples were cut from the machined discs. The specimen shape was similar to the metallurgical samples shown in Figure 3.2. The area of the machined surface for each sample was about 60 mm^2. The conditions for the machined *AZ31B Mg* samples selected for corrosion tests are shown in Table 5.1. Conditions that led to notable differences in microstructures, crystallographic orientations and/or residual stresses were chosen for the corrosion study.

Table 5.1: Machining conditions for samples subjected to corrosion tests

No.	Tool Edge Radius, r_n [μm]	Cooling Method	Cutting Speed, V [m/min]	Feed Rate, f [mm/rev]
1	30	Dry	100	0.1
2	70	Dry	100	0.1
3	30	Cryogenic	100	0.1
4	70	Cryogenic	100	0.1
5	70	Cryogenic	50	0.05
6	70	Cryogenic	100	0.05
7	70	Cryogenic	150	0.05
8	70	Cryogenic	100	0.25

To evaluate the corrosion performance, the machined samples were immersed in two different solutions. One solution was 5% weight percent (wt.) *NaCl* solution and the corrosion test was conducted at room temperature. This test was conducted to evaluate the corrosion performance for the transportation industry, such as automotive and aerospace applications. The other solution used was simulated body fluid (*SBF*) and its composition is shown in Table 5.2 (Song and Song, 2007). The pH value of the *SBF* was

adjusted to 7.4. The solution was kept in an incubator to maintain the temperature at 37 ± 1 °C. This test was conducted to evaluate the corrosion performance of magnesium alloys in the human body environment.

Table 5.2: Composition of simulated body fluid (*SBF*)

Name	Concentration [g/L]
NaCl	8
KCl	0.4
CaCl$_2$	0.14
NaHCO$_3$	0.35
C$_6$H$_{12}$O$_6$	1
MgSO$_4$.7H$_2$O	0.2
KH$_2$PO$_4$.H$_2$O	0.1
Na$_2$HPO$_4$.7H$_2$O	0.06

The immersion time was 85 hours for the test in 5 wt. % *NaCl* solution and 10 days for the test in the *SBF*. After immersion, the samples were taken out of the solutions and the corrosion products were removed by chromic acid (200 g/L *CrO$_3$* and 10 g/L *AgNO$_3$*). After washing with distilled water and drying, photos were taken by a camera to show the overview of the corroded surface. A Zygo New View 7300 measurement system was used to measure the corrosion depth. A 2 mm ×2 mm 3D topographic picture of the severely corroded area was recorded for each condition; the depth of the deepest pits was obtained by the corresponding line profiles.

5.2.1 Corrosion performance in 5% wt. *NaCl* solution

Figure 5.1 shows the photos of machined *AZ31B Mg* samples under different cooling conditions and cutting edge radius after the corrosion test in 5 wt. % *NaCl* for 85 hours. Differences in corrosion performance were found between different machining

conditions. The white or light grey portions on the photos in Figure 5.1 represent the original surface, while the dark portions are the places where large amounts of *Mg* were lost due to corrosion. It is obvious that dry machining using a 30 µm edge radius tool led to the worst corrosion performance. With the same edge radius, the application of liquid nitrogen during machining significantly improves the corrosion performance. However, when the cutting edge radius was increased to 70 µm, the differences of the corroded surface were limited between the dry and cryogenic conditions. Under the same dry cutting conditions, increasing the cutting edge radius from 30 µm to 70 µm remarkably improves the corrosion resistance of the *AZ31B Mg* alloy.

The differences in corrosion performance correlates well with the thickness of the "featureless layer" reported in Chapter 3. The sample machined using a 30 µm tool under dry condition, which exhibited the worst corrosion, has no featureless layer. All other samples have different thickness of the featureless layer (8-15 µm). It could be concluded that the featureless layer which consisted of nanocrystallined grain structures served as a protective coating and improved the corrosion resistance of *AZ31B Mg* alloy. This result agrees with the recent finding that grain refinement improves the corrosion resistance of *Mg* alloys (Wang et al., 2007; Alvarez-Lopez et al., 2010; Birbilis et al., 2010b).
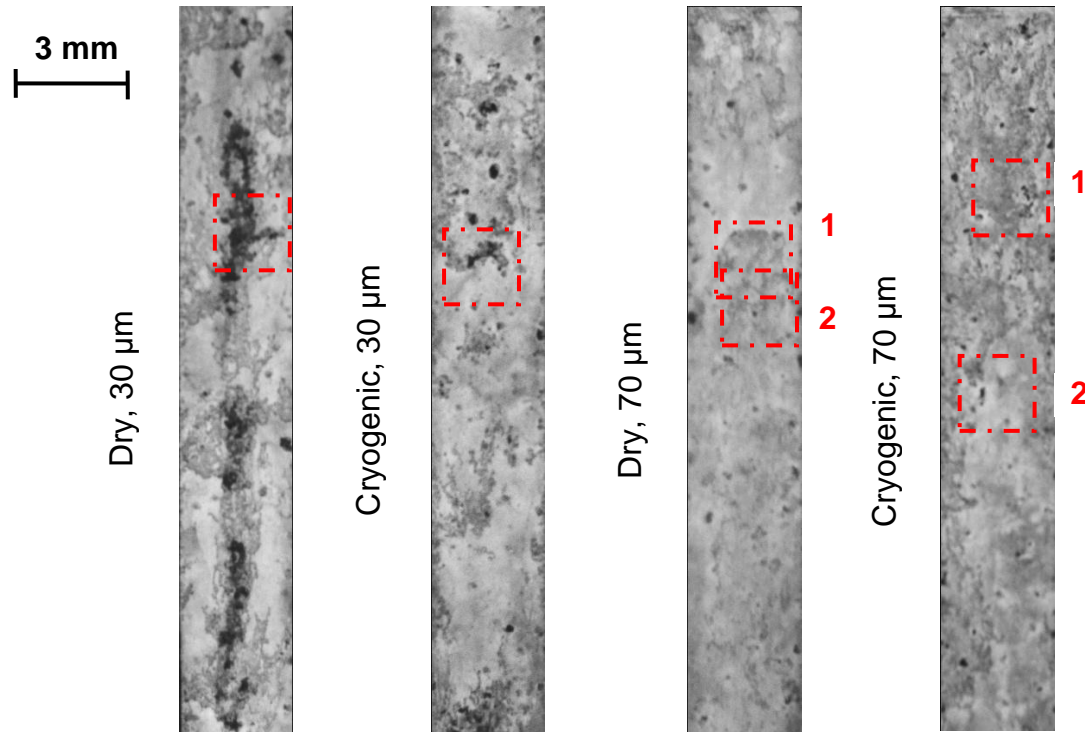
Figure 5.1: Photos of machined *AZ31B Mg* samples under different cooling conditions and cutting edge radii after corrosion test in 5 wt. % *NaCl* for 85 hours ($V = 100$ m/min, $f = 0.1$ mm/rev).

Figure 5.2 and Figure 5.3 show the Zygo 3D topographic pictures of the severely corroded area as marked by red square in Figure 5.1, and the corresponding line profiles. While the total corroded area is much smaller on the sample machined under cryogenic condition (Figure 5.1) using the 30 μm edge radius tools, the maximum depths of the corrosion pits are almost the same: 198 μm and 171 μm for cryogenic and dry conditions, respectively. As shown in Figure 5.3, the application of liquid nitrogen does not lead to notable differences in the total corroded area. However, cryogenic machining results in about 183% increase in the maximum depth of the corrosion pits (130 μm vs. 71 μm).
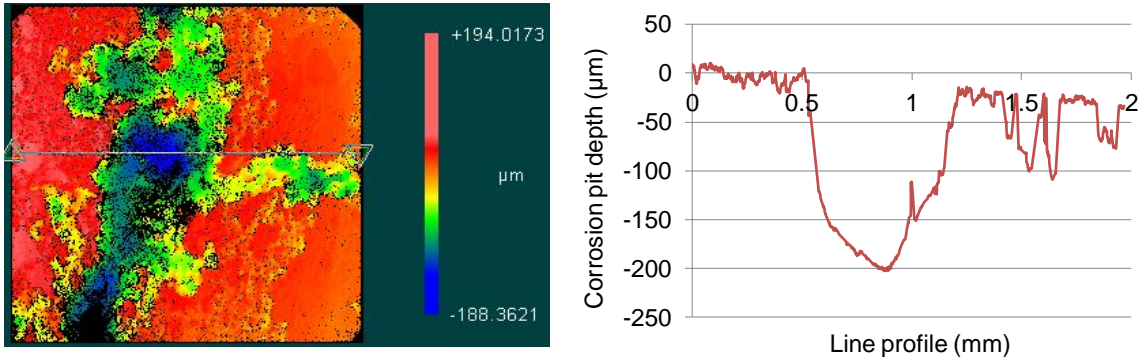
(a) dry, 30 μm
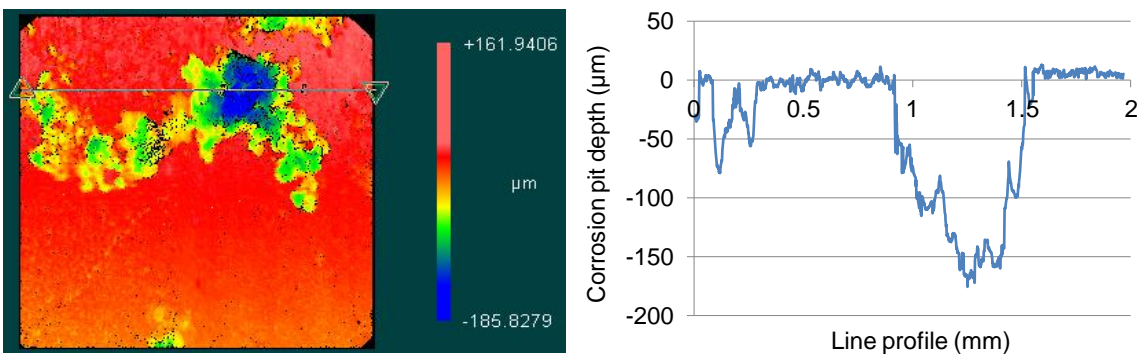
(b) cryogenic, 30 μm

Figure 5.2: Zygo 3D topographic pictures of the corroded area as marked by red square in Figure 5.1 and corresponding line profiles ($V = 100$ m/min, $f = 0.1$ mm/rev).

The results obtained when using both 30 μm and 70 μm edge radius tools show that the application of liquid nitrogen does not lead to notable reduction in the maximum corrosion pit depth, and it even increases significantly when the large edge radius tool was used. This could be explained by the microstructures of the machined samples in Figure 3.11; large amount of deformation twins, which were reported to increase the corrosion rate of *AZ31B Mg* alloy (Aung and Zhou, 2010), formed below the featureless layers when liquid nitrogen was used. Therefore, after the 5 wt. % *NaCl* solution

penetrates the featureless layer, the twinning areas in the samples after cryogenic machining are more easily corroded, and this leads to deeper corrosion pit.
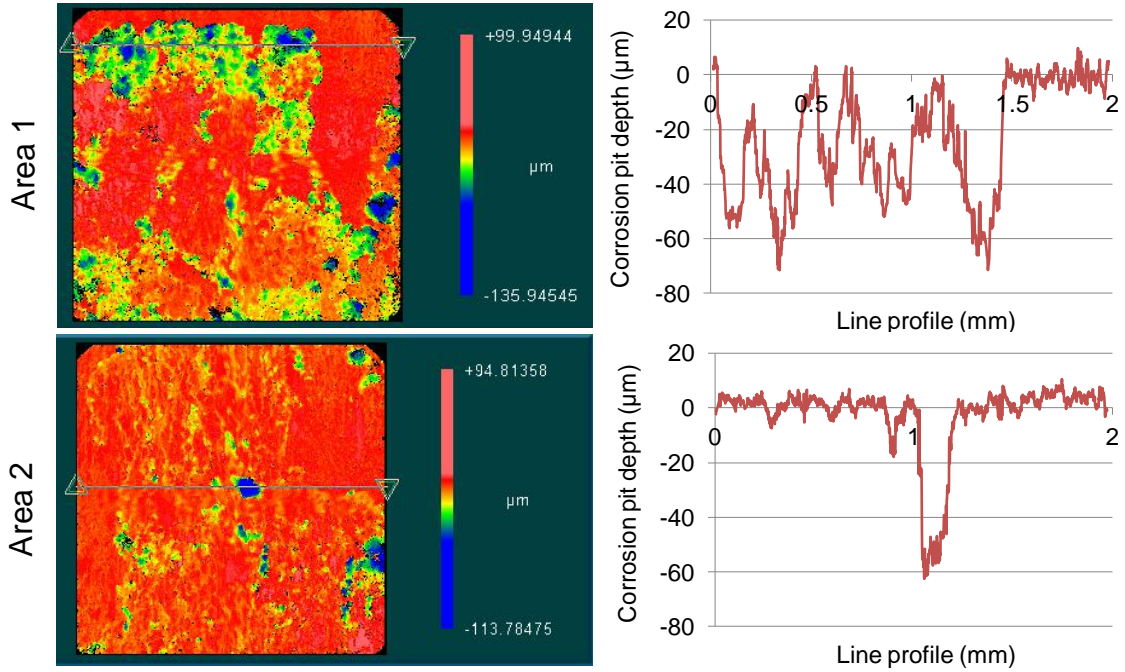
(a) dry, 70 μm
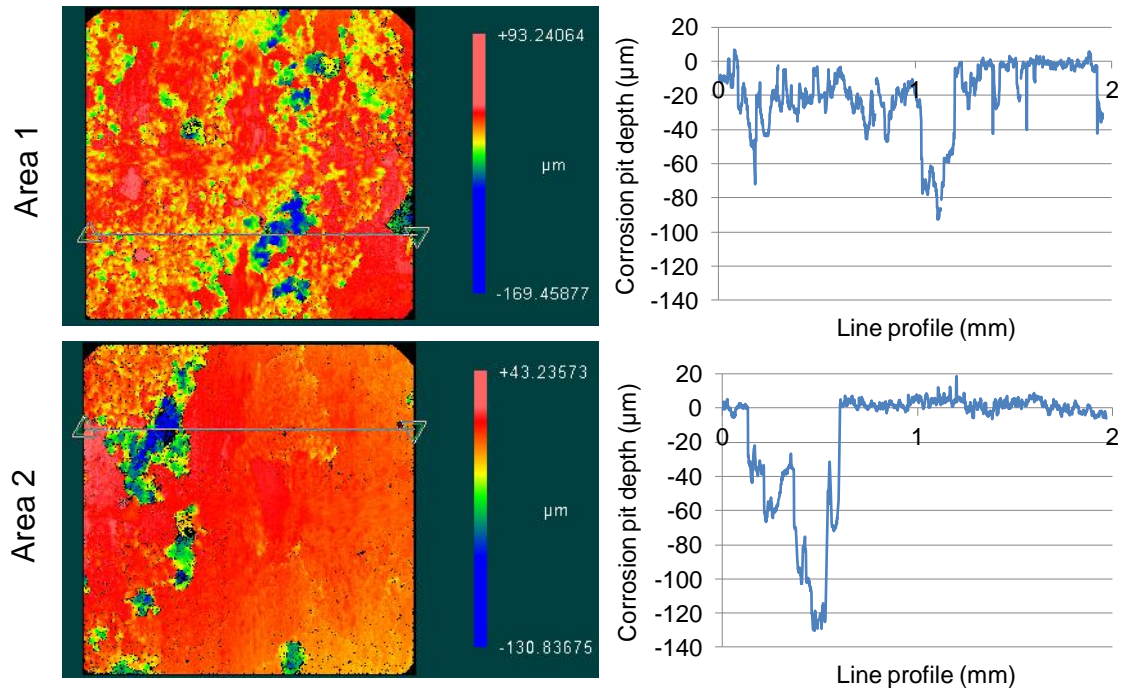
(b) cryogenic, 70 μm

Figure 5.3: Zygo 3D topographic pictures of the corroded area as marked by red square in Figure 5.1 and corresponding line profiles ($V = 100$ m/min, $f = 0.1$ mm/rev).

The influence of cutting speed on the corrosion resistance of *AZ31B Mg* alloy was found to be remarkable. Both Figures 5.4 and 5.5 show that the total corroded areas increased with the use of the increased cutting speed during machining. The maximum corrosion depth also increased from 40 μm at 50 m/min to 77 μm at 100 m/min and 164 μm at 150 m/min. The observable microstructrual differences among these conditions are not significant since featureless layers with thickness ranging from 3 to10 μm were formed on all three samples as shown in Figure 3.24. The different corrosion behaviors could be caused by the difference in residual stresses. It was reported that the cutting temperature in machining *Mg* alloys increased dramatically with increased cutting speed (Kurihara et al., 1981). The higher temperature caused by increased cutting speed induces more tensile residual stresses on the machined surface, which could increase the corrosion rate remarkably (Denkena and Lucas, 2007).
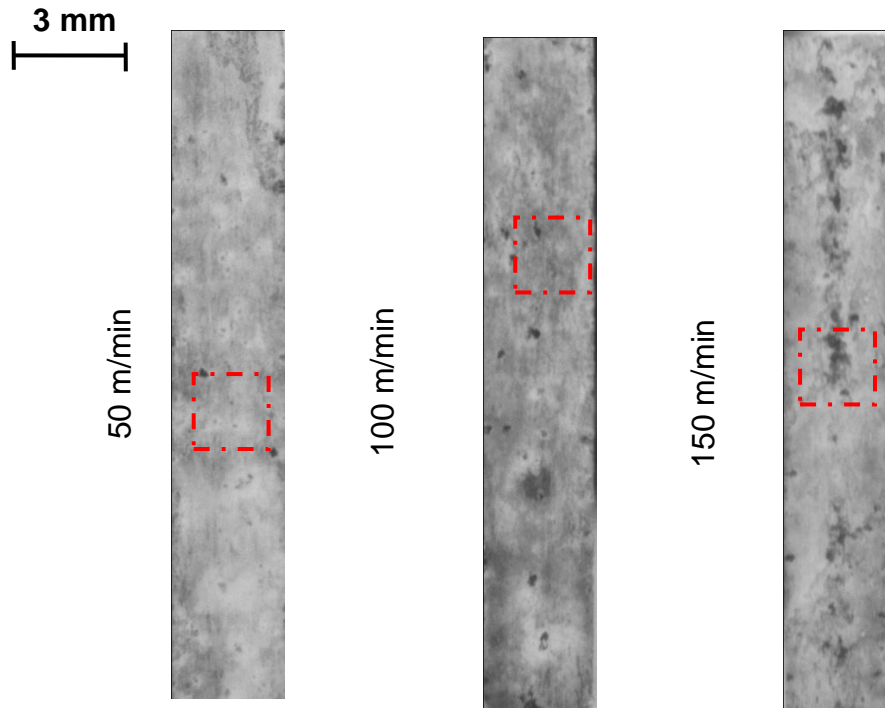
Figure 5.4: Photos of machined *AZ31B Mg* samples under different cutting speeds after corrosion test in 5 wt. % *NaCl* for 85 hours (cryogenic, $r_n = 70$ μm, $f = 0.05$ mm/rev).
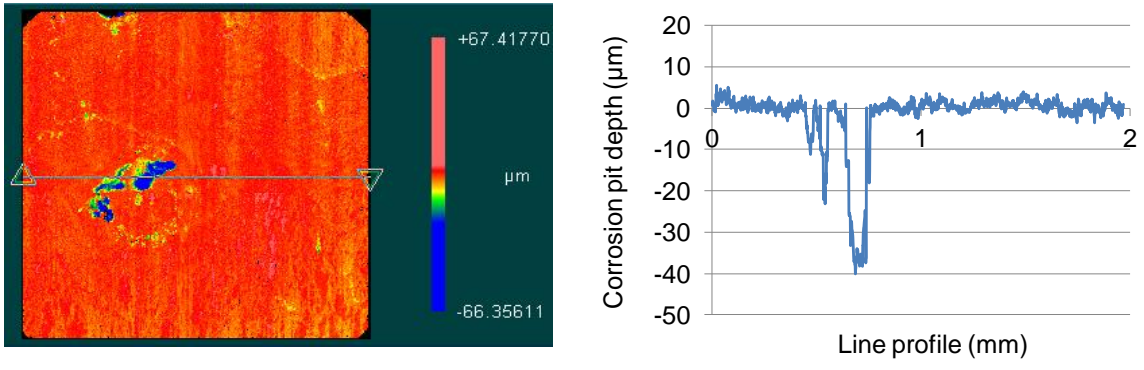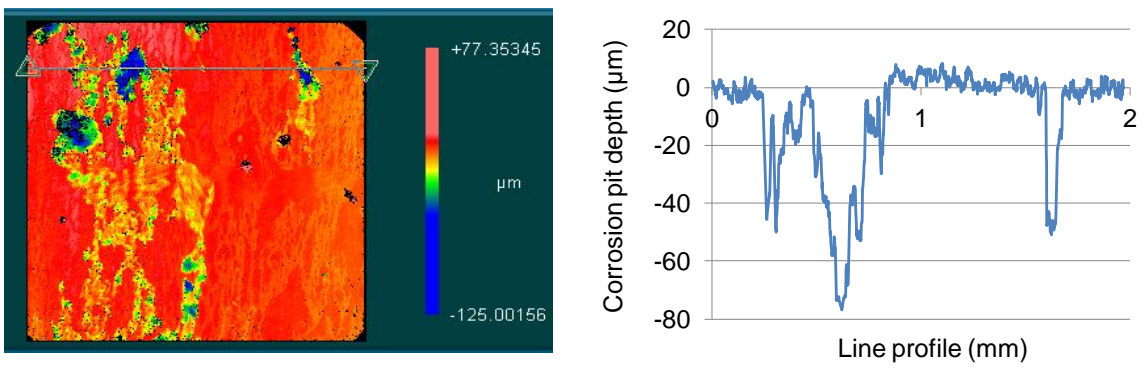
(a) 50 m/min

(b) 100 m/min
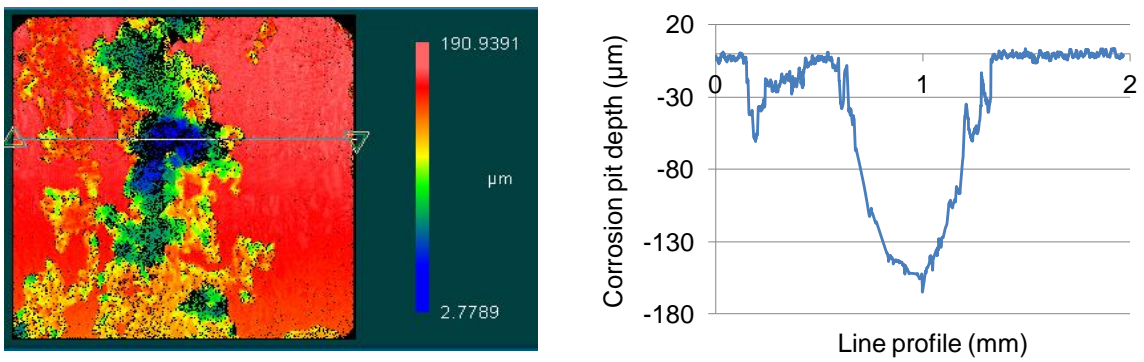
(c) 150 m/min

Figure 5.5: Zygo 3D topographic pictures of the corroded area as marked by red square in Figure 5.4 and corresponding line profiles (cryogenic, $r_n = 70$ µm, $f = 0.05$ mm/rev).

The influence of feed rate during machining on the corrosion resistance of *AZ31B Mg* alloy after machining is shown in Figures 5.6 and 5.7. The thickness of the featureless layer on the sample machined using the feed rate of 0.05 mm/rev was about 10 μm (Figure 3.24b) while no featureless layer was observed using a feed rate of 0.25 mm/rev. It is expected that much better corrosion resistance should be found on the sample machined under the small feed rate. However, it was shown that the maximum depth of the corrosion pits for the two feed rates were almost the same at about 80 μm; the corroded area of the sample machined at the feed rate of 0.05 mm/rev is a little smaller than the one using 0.25 mm/rev. It was shown in Figure 3.27 that the higher feed rate led to the strength of the basal texture being twice as large as the one machined using a smaller feed rate, which may contribute to its good corrosion resistance. Also, due to the high material removal rate at 0.25 mm/rev, more heat could be removed by the chips and thereby reduced the temperature at the cutting zone, which may induce more compressive residual stresses.
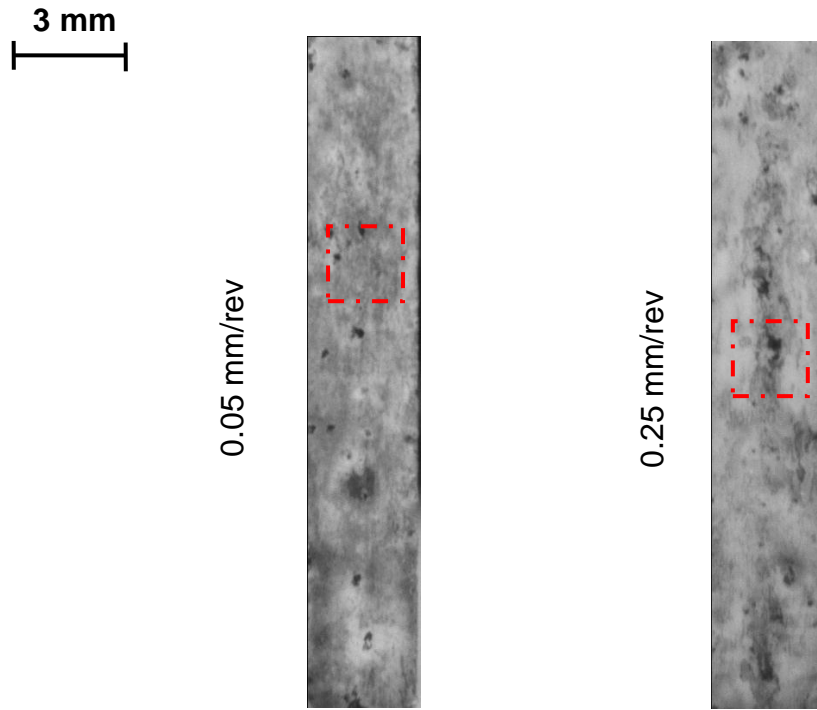
Figure 5.6: Photos of machined *AZ31B Mg* samples under different cutting speeds after corrosion test in 5 wt. % *NaCl* for 85 hours (cryogenic, $r_n = 70$ µm, $V = 100$ m/min).
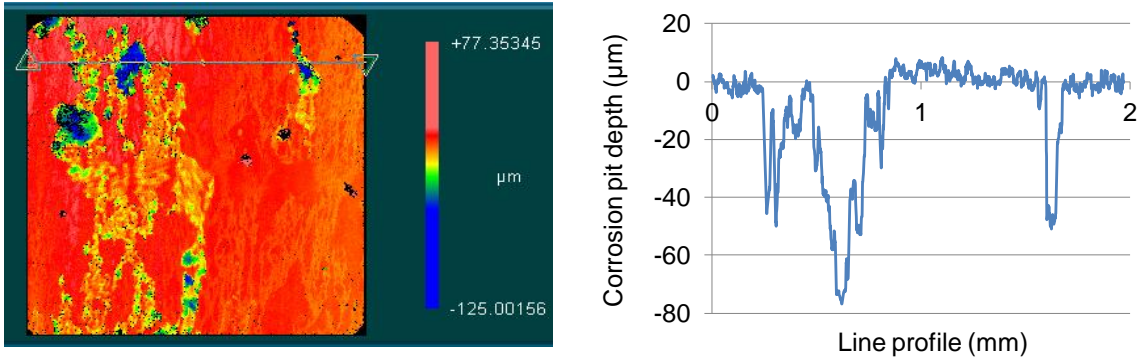
(a) 0.05 mm/rev
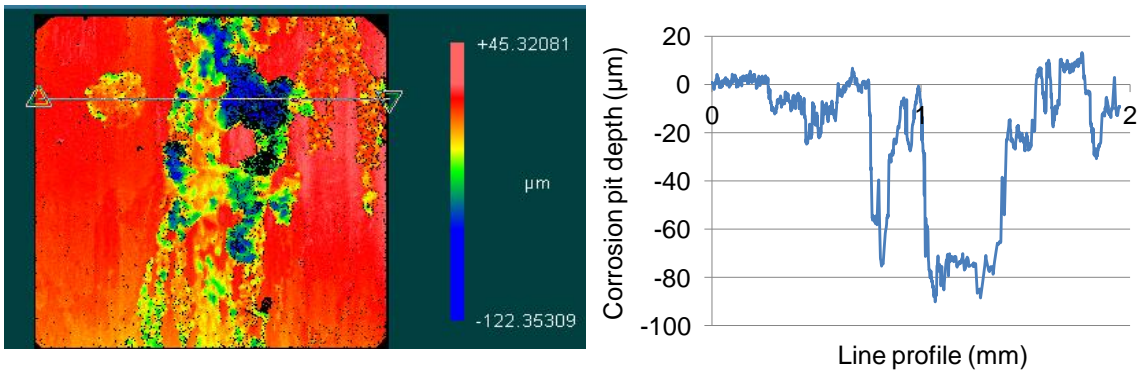
(b) 0.25 mm/rev

Figure 5.7: Zygo 3D topographic pictures of the corroded area as marked by red square in Figure 5.6 and corresponding line profiles (cryogenic, $r_n = 70$ µm, $V = 100$ m/min).

5.2.2 Corrosion performance in *SBF*

Figure 5.8 shows the photos of *AZ31B Mg* samples machined under different cooling conditions and cutting edge radii after corrosion test in *SBF* for 10 days. Similar to the corrosion performance in 5 wt. % *NaCl*, dry machining using the 30 µm cutting edge radius tool led to the poorest corrosion resistance. This finding further proves that the featureless layers formed on the other three samples as shown in Figure 3.11 acted as protective coatings and prevented the matrix from further corrosion.

133
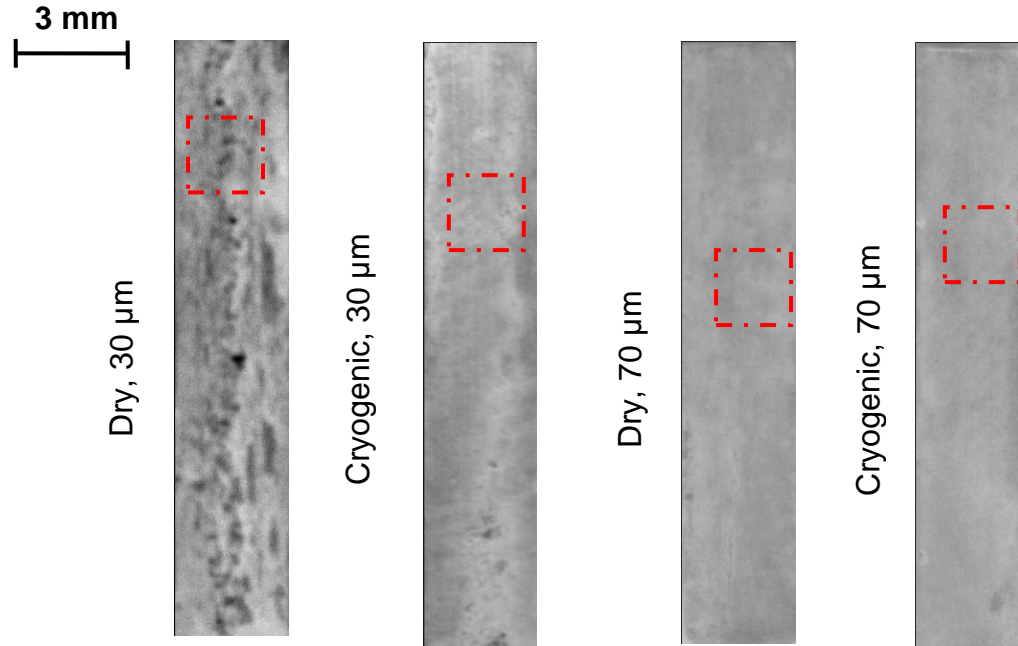
Figure 5.8: Photos of machined *AZ31B Mg* samples under different cooling conditions and cutting edge radii after corrosion test in *SBF* for 10 days ($V = 100$ m/min, $f = 0.1$ mm/rev).

Using 30 μm edge radius tools, the maximum depth of the corrosion pits on the machined samples under cryogenic cooling was reduced significantly from 167 μm to 73 μm, when compared with dry machined specimens as shown in Figure 5.9. This finding is different from the results obtained in 5 wt. % *NaCl* solution which suggest that the deformation twins might not reduce the corrosion resistance of *AZ31B Mg* alloy in *SBF*. Even greater reductions in the maximum depth of corrosion pits were found on samples machined using 70 μm edge radius tools. Almost no corrosion damage can be found on the sample machined using cryogenic condition with the large edge radius tool. This finding agrees with the expectation in Chapter 3, since the surface integrity induced by cryogenic machining with the 70 μm edge radius tool was the best in terms of nano grain structures, strongest basal texture, and large and deep compressive residual stresses.
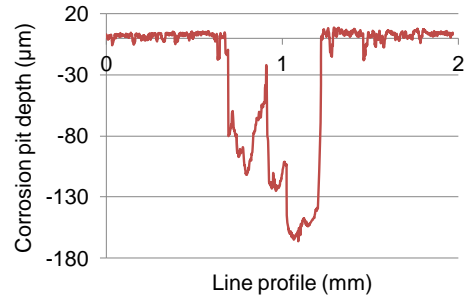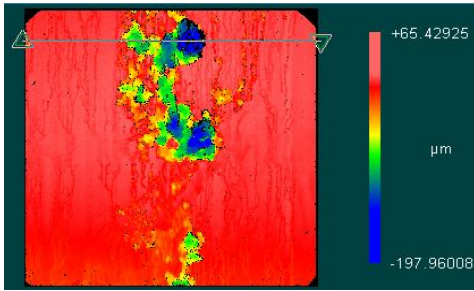
(a) dry, 30 μm
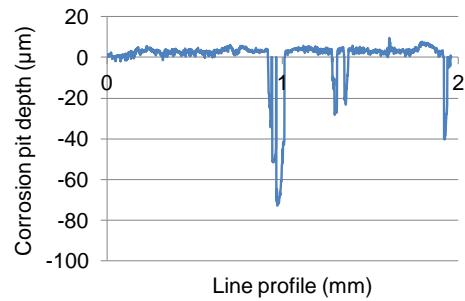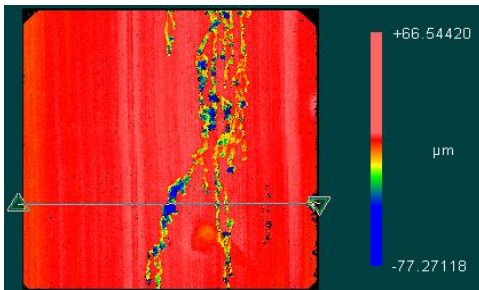
(b) cryogenic, 30 μm
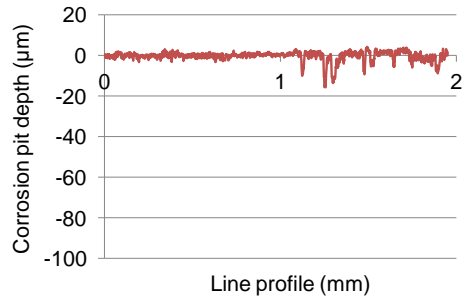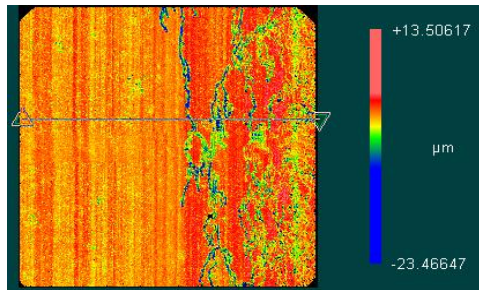
(c) dry, 70 μm
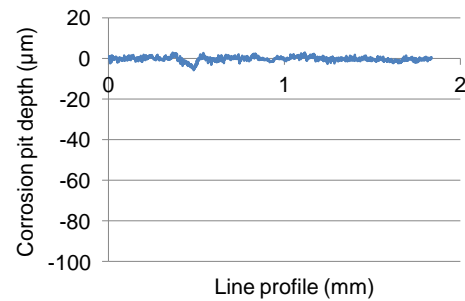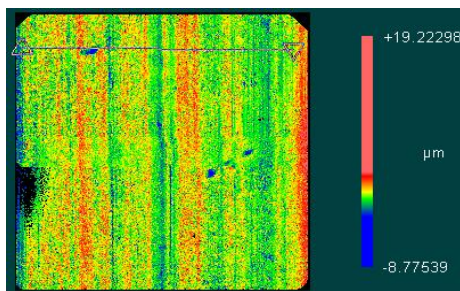
(d) cryogenic, 70 μm

Figure 5.9: Zygo 3D topographic pictures of the corroded area as marked by red square in Figure 5.8 and corresponding line profiles ($V = 100$ m/min, $f = 0.1$ mm/rev).

When cutting tools with 70 µm cutting edge radius was used under cryogenic cooling conditions, all machined *AZ31B Mg* samples exhibited little corrosion damage after 10 days' immersion in *SBF* no matter what the cutting speeds used as shown in Figure 5.10. The corrosion resistance under the smallest cutting speed (50 m/min) was the best with almost no visible corrosion pits even in the Zygo topographic pictures (Figure 5.11). The corrosion damage using cutting speeds of 100 m/min and 150 m/min is in the shape of thin lines whose maximum depth is only about 40 µm.
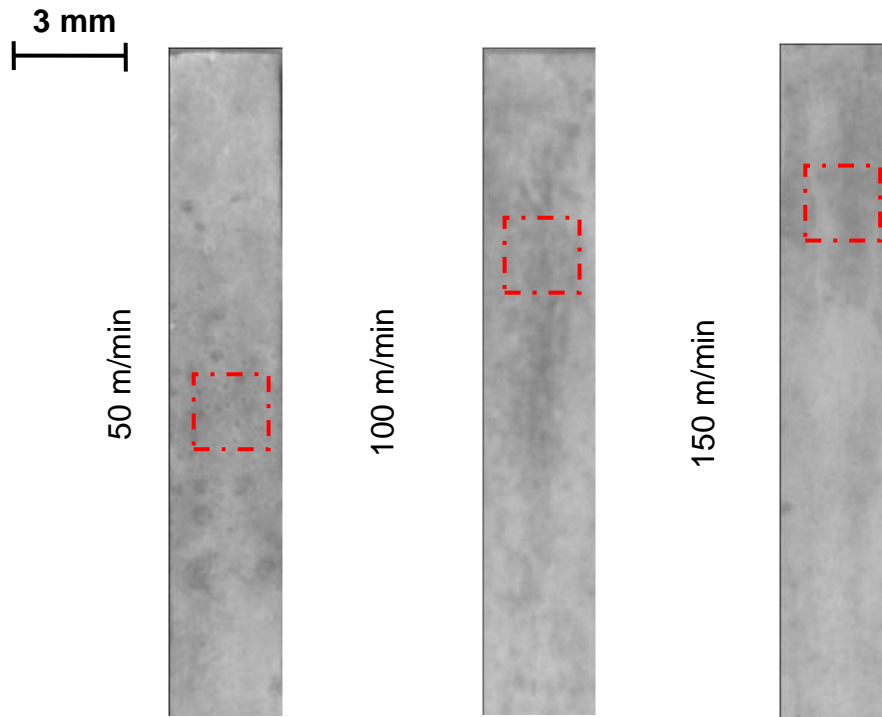
Figure 5.10: Photos of machined *AZ31B Mg* samples under different cutting speeds after corrosion test in *SBF* for 10 days (cryogenic, $r_n = 70$ µm, $f = 0.05$ mm/rev).
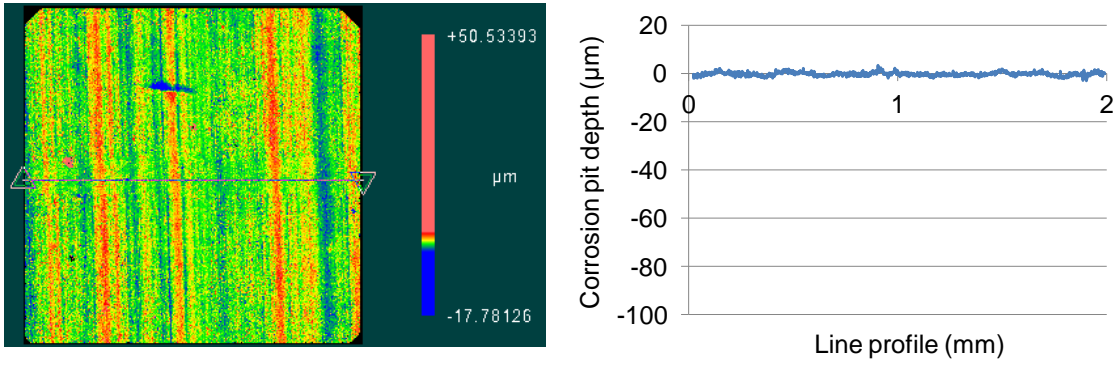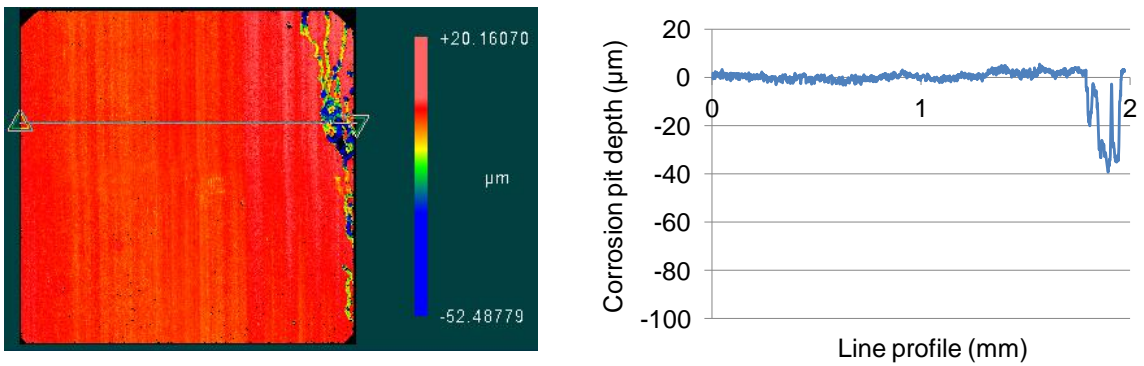
(a) 50 m/min

(b) 100 m/min
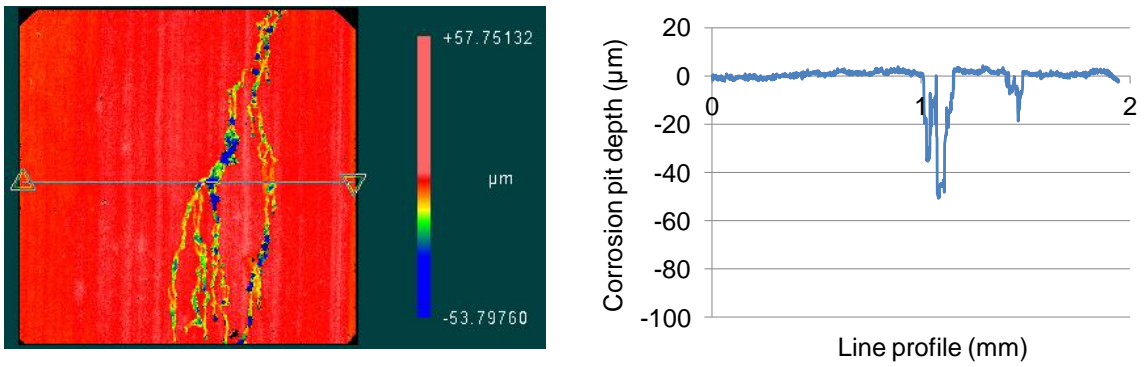
(c) 150 m/min

Figure 5.11: Zygo 3D topographic pictures of the corroded area as marked by red square in Figure 5.10 and corresponding line profiles (cryogenic, r_n = 70 µm, f = 0.05 mm/rev).

Different from the corrosion results in 5 wt. % *NaCl* solution, larger feed rate led to more corrosion damage on the machined *AZ31B Mg* alloy as shown in Figure 5.12. The maximum depth of the corrosion pits are almost the same at about 40 μm. However, the surface machined under a larger feed rate is much rougher with several corrosion lines deeper than 10 μm, while the one machined using a smaller feed is relatively smooth as shown in Figure 5.13. The cause for the different behaviors in the two solutions should be the differences in corrosion mechanism since 5 wt. % *NaCl* is a more aggressive solution than *SBF*.
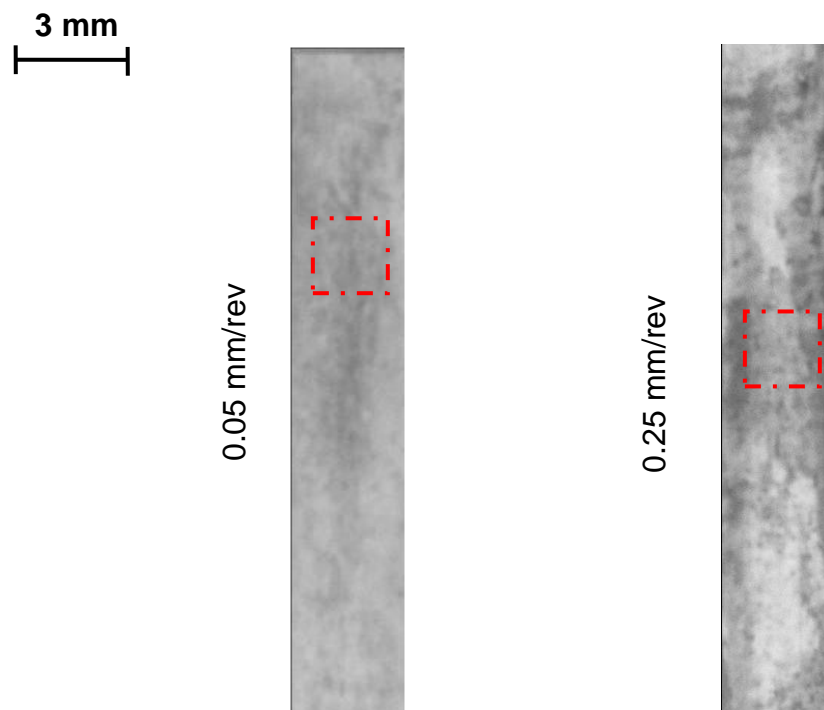
Figure 5.12: Photos of machined *AZ31B Mg* samples under different cutting speeds after corrosion test in *SBF* for 10 days (cryogenic, $r_n = 70$ μm, $V = 100$ m/min).
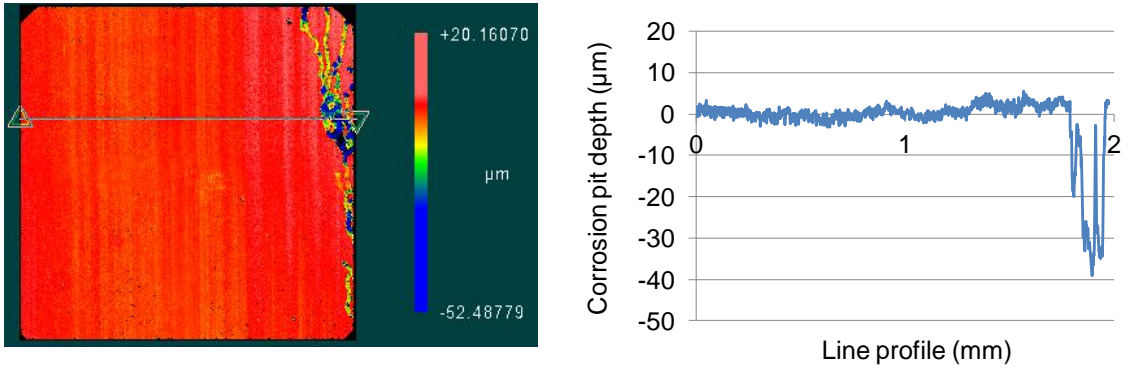
(a) 0.05 mm/rev
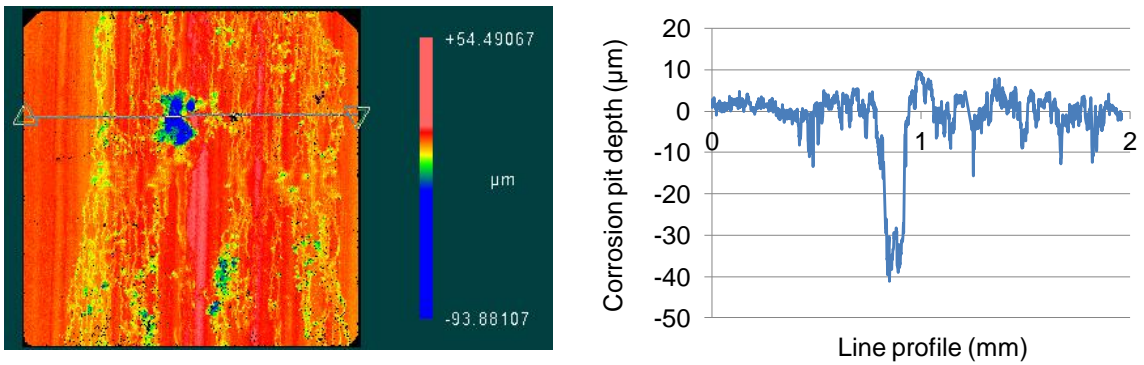
(b) 0.25 mm/rev

Figure 5.13: Zygo 3D topographic pictures of the corroded area as marked by red square in Figure 5.12 and corresponding line profiles (cryogenic, $r_n = 70$ µm, $V = 100$ m/min).

5.3   Corrosion Performance of Burnished *AZ31B Mg* Alloy

A comprehensive study using four different methods was conducted to evaluate the corrosion resistance of burnished *AZ31B Mg* alloy: (a) constant immersion test, (b) hydrogen evolution test (Song et al., 2001), (c) in-situ corrosion observation, and (d) electrochemical measurements. To investigate the influence of burnishing on the corrosion resistance, an un-burnished sample was also tested as a reference for comparison purposes. As the surface roughness (R_a) of the burnished surfaces was reduced from the initial 0.8 µm to about 0.2 µm under both dry and cryogenic conditions,

to eliminate the possible influence of surface roughness on corrosion resistance (Song and Xu, 2010), the un-burnished samples were ground successively using up to 4000 grit *SiC* paper prior to all the corrosion tests in order to have similar surface roughness. All the corrosion tests were conducted in 5 wt. % *NaCl* solution at room temperature.

In the constant immersion tests, the burnished and ground surfaces were immersed in the solution for 200 hours. After immersion, the corrosion products were removed by chromic acid (200 g/L CrO_3 and 10 g/L $AgNO_3$); after washing with distilled water and drying, photos were taken by a camera. Replicated samples for ground and cryogenic-burnished surfaces were also taken out after 30 hours' immersion. Without cleaning the corrosion products, the samples underwent the same procedure as used for the original microstructural analysis to investigate the cross-sectional microstructures after corrosion.

For hydrogen evolution test, the ground and burnished surfaces (the lateral surfaces, which are perpendicular to the burnished surface, were covered with epoxy resin) were exposed to the solution for 7 hours. Pipettes were used to collect the evolved hydrogen from the samples (Song et al., 2001). Three replicates were measured for each surface.

For in-situ corrosion observation, the lateral surfaces of the burnished samples prepared under dry and cryogenic conditions were exposed to the 5 wt.% *NaCl* solution and the corrosion features at several times were recorded by camera. After immersion for 70 hours, the samples were taken out of the solutions and cleaned with the chromic acid. Topographic morphologies of the corroded surfaces were taken by using a Zygo NewView 6000 measurement system which was based on white light interferometry.

For electrochemical test, a Solatron 1280 potentiostat system was used to obtain the polarization curves and AC impedance. The ground and burnished surfaces were exposed to the *NaCl* solution. Platinum gauze was used as a counter electrode and a *KCl*-saturated *Ag/AgCl* electrode was used as a reference in the cell. During AC impedance measurements, the frequency ranged from 17,777 Hz to 0.1 Hz with 7 points/decade, and the amplitude of the sinusoidal potential signal was 5mV with respect to the OCP. Potentiodynamic polarization curve measurements were performed at a potential scanning rate of 0.1 mV/s from −0.3 V vs. OCP to −1.0 V (*Ag/AgCl*).

5.3.1   Constant immersion test

As shown in Figure 5.14, dramatic differences in surface morphologies can be found between the ground and burnished surfaces after the 200 hours immersion test; the differences between burnished samples under dry and cryogenic conditions are much smaller for the same testing duration than the difference between ground and burnished surfaces. The ground surface after immersion is very rough; large and deep pits are visible all over the surface. On the dry and cryogenic burnishing surfaces, there are only some small pits in the surfaces and the corroded areas of the burnished samples are smaller than those in the ground ones. This suggests that much less *Mg* was corroded from the burnished surfaces than the ground surface.

To investigate the depth of corrosion pits, topographic maps of the severely corroded portion of each surface (marked as square boxes in Figure 5.14) were obtained using Zygo NewView 6000 measurement system as shown in Figure 5.15 (a) – (c). The depth profiles along the dotted lines shown in Figure 5.15 (a) – (c) are presented in Figure 5.15 (d). The profiles show that the corrosion pits on the ground samples are very

deep; the maximum measured depth is 512 µm while the pits on the burnished surfaces are less than 200 µm deep. Figure 5.15 also shows that the corrosion that occurred on the burnished samples is more uniform than that on the ground one.
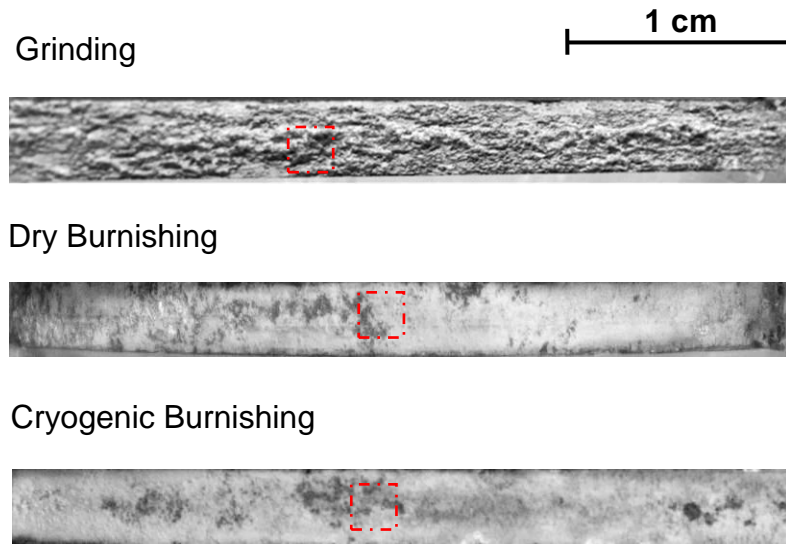
Figure 5.14: Surface morphology of *AZ31B Mg* samples processed by different treatments after immersion in 5 wt. % *NaCl* solution for 200 hours (details in the square boxes are shown in Figure 5.15).
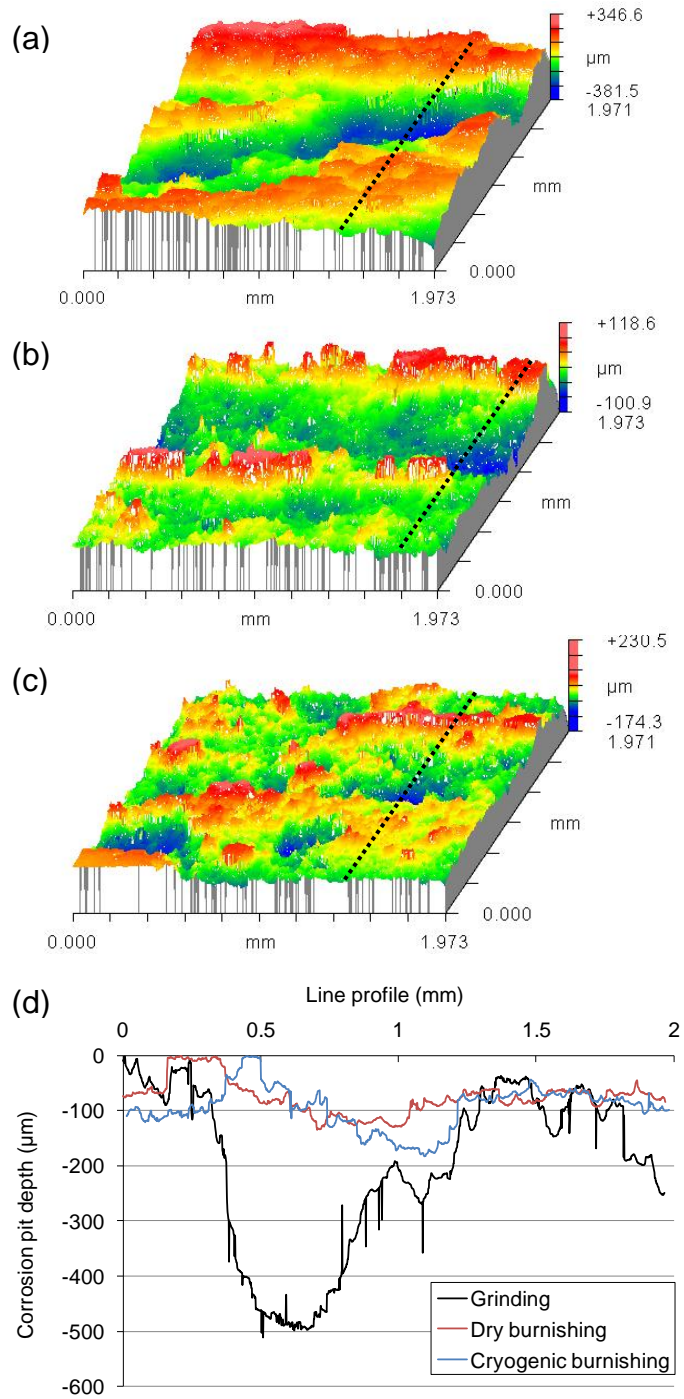
Figure 5.15: Topographic maps of square boxes in Figure 5.10 obtained by Zygo: (a) ground; (b) dry- and (c) cryogenic-burnished samples; and (d) corrosion pit depth profiles along the dotted lines.
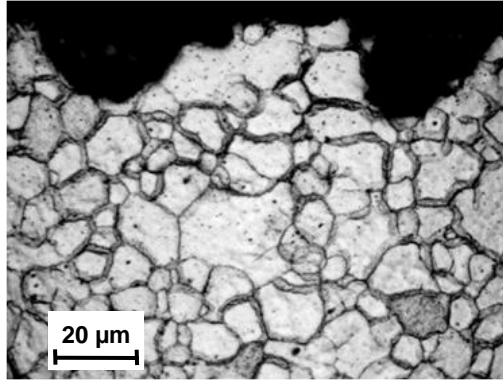
(a)
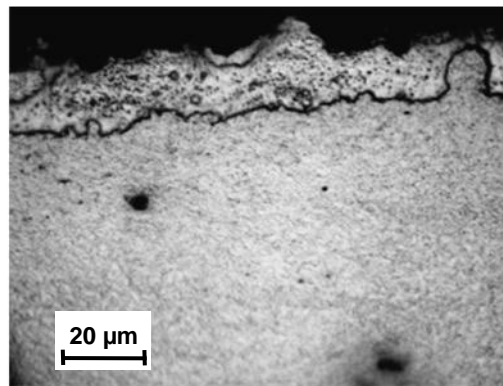
(b)

Figure 5.16: Typical cross-sectional microstructures of (a) ground, and (b) cryogenic-burnished samples after immersion in 5% wt. *NaCl* solution for 30 hours.

Typical cross-sectional microstructures of ground and cryogenic-burnished samples after 30 hours' immersion test are shown in Figure 5.16. There are significant differences in corrosion morphology between the samples prepared by grinding and cryogenic burnishing. Wide and deep corrosion pits are present on the ground sample. The grain boundaries are clearly visible, and do not show any barrier effect to corrosion development. The surface after cryogenic burnishing is much smoother and corrosion occurred more uniformly, with small and shallow pits. The grain boundaries are not visible at this scale, and the microstructure is similar to the one shown in Figure 4.6 (c),

which suggests that corrosion occurred within the grain refined layer after 30 hours' immersion. The uniformity in corrosion may be due to the similarity in grain size and the electrochemical homogenization (Orlov et al., 2011) induced by the burnishing process. Different from the ground sample, a layer of corrosion products adhered to the cryogenic-burnished surface as shown in Figure 5.16 (b). Apparently, the uniform corrosion products better protect the substrate from corrosion. This finding is directly supported by the literature that a higher density of grain boundaries promoted better mechanical adhesion through an oxide pegging mechanism (Tao and Li, 2006; Balakrishnan et al., 2008a).

5.3.2   Hydrogen evolution test

The hydrogen evolution measurement was used to continually monitor the corrosion process of the ground and burnished surfaces in the first 7 hours. As shown in Figure 5.17, there is a remarkable difference between the ground and burnished surfaces while little difference can be detected on burnished surfaces created under both dry and cryogenic conditions. The total volume of hydrogen generated in 7 hours from the ground surface is 55% more than that from either the dry or cryogenic burnished surfaces. As 1 mL of hydrogen evolution roughly corresponds to 1 mg of *Mg* dissolved (Song, 2009), the result indicates that in 7 hour immersion, 55% more *Mg* was corroded from the ground sample than from the burnished ones. The results agree with the constant immersion test data that the burnished samples under both dry and cryogenic conditions have similar corrosion resistance, and are both much more corrosion resistant than the ground sample.
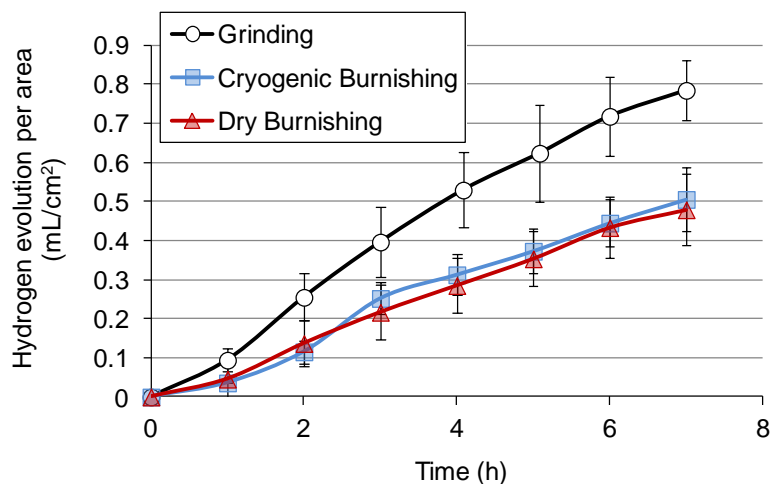
Figure 5.17: Hydrogen evolution of *AZ31B* samples processed by different treatments in 5 wt. % *NaCl* solution.

5.3.3 Electrochemical corrosion behavior

The polarization curves of samples after grinding, dry and cryogenic burnishing are presented in Figure 5.18 (a). The corrosion potentials for both burnishing condition are more negative than the ground sample. The cathodic polarization current densities of the burnished surfaces are lower than that of the ground surface, while the latter has smaller anodic polarization current densities than the formers. The decreased cathodic polarization current densities of the burnished surfaces could be associated with their finer grains and (0002) grain orientation. Grain refinement may lead to dissolution of impurities in the grain boundaries, less cathodic sites in the alloy for cathodic reaction and thus improved corrosion resistance (Song and Xu, 2010; Song and Xu, 2011). It has also been demonstrated (Song et al., 2010b) that the basal textured surface has lower polarization current densities. However, these cannot explain the increased anodic polarization current densities. The accelerated anodic process on burnished samples

146

(Figure 5.18 (a)) can only be ascribed to the enhanced micro circumferential tensile stress. In theory, micro-scale residual stresses can reduce the activation energy required for an atom to leave the metal lattice and get into the solution. Therefore, it should not be surprising that a stressed metal has a high anodic dissolution rate. This may explain the phenomenon that cryogenic-burnished samples whose residual stresses are more tensile (Figure 4.12) also have larger anodic current densities than the dry-burnished ones. An accelerated anodic process can lead to reduced corrosion resistance, while decreased cathodic current densities will give rise to a retarded corrosion process. In this study, it seems that the influence of the accelerated anodic process on corrosion has been overwhelmed by the effect of the cathodic current reduction by burnishing.

Figure 5.18 (b) shows the Nyquist plots of *AZ31B Mg* samples obtained after grinding and burnishing when tested in 5 wt. % *NaCl*. All spectra have a clear capacitive arc at the high frequency region. The diameter of this capacitive loop is associated with the charge-transfer resistance. It has been shown by several researchers that a larger diameter indicates better corrosion resistance for magnesium alloys (Makar and Kruger, 1990; Song et al., 2010a). The diameters for the burnished samples under dry and cryogenic conditions are larger than that of the ground sample. This agrees well with their corrosion damage shown in Figure 5.14 as well as the hydrogen evolution test results (Figure 5.17). Thus, it can be concluded that the burnished samples prepared by dry and cryogenic conditions are similar to each other, and are both significantly better than the ground sample in their corrosion resistance.
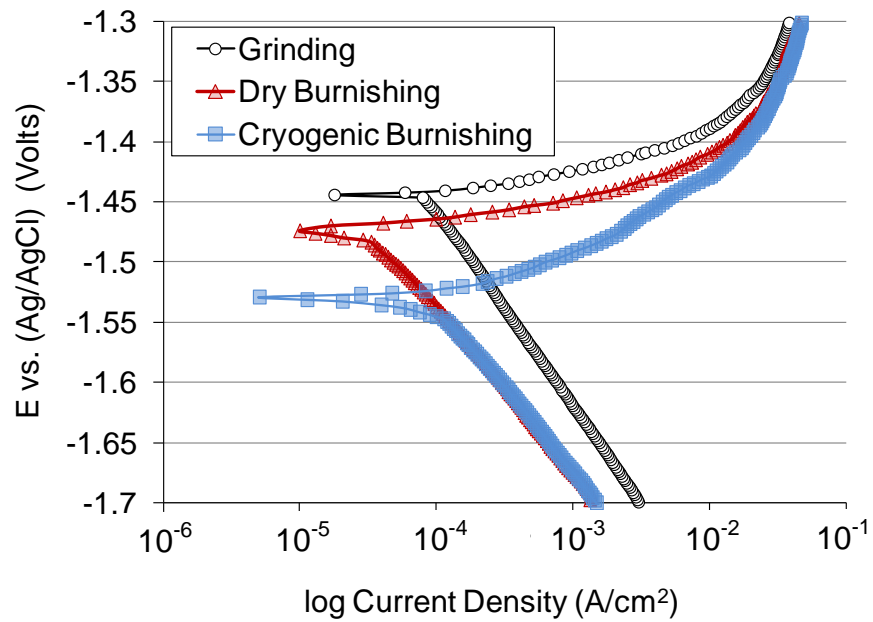
(a)
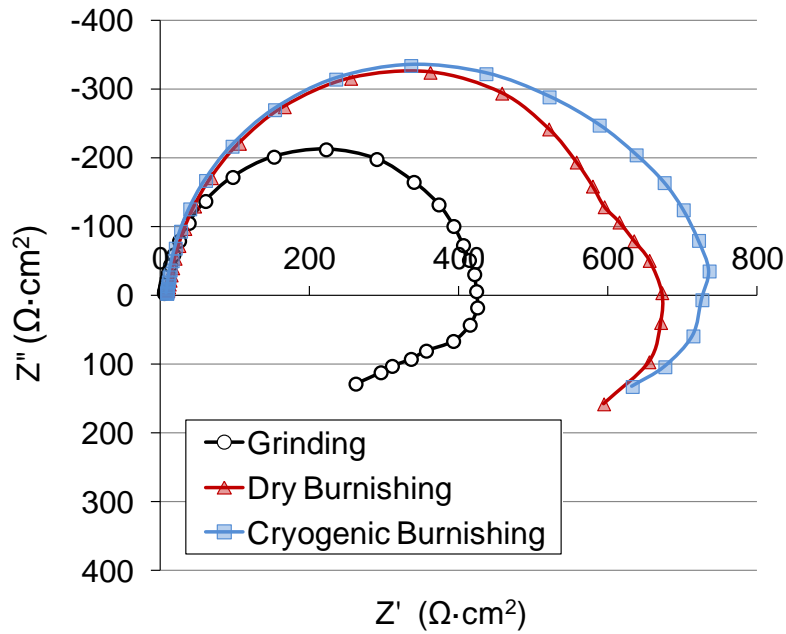
(b)

Figure 5.18: (a) Polarization curves and (b) Nyquist plots of *AZ31B Mg* samples after grinding, dry and cryogenic burnishing in 5 wt.% *NaCl* solution

5.3.4 Corrosion test of lateral surfaces

To further investigate the effect of grain size, grain orientation and residual stress on corrosion performance, the lateral surfaces (perpendicular to the burnished surfaces as shown in Figure 4.1) of the burnished samples were exposed to 5 wt. % *NaCl* solutions for 70 hours. Photos taken at the end of the immersion test (Figure 5.19 (a) and (c)) showed that the burnished surface layer (the process-affected region) had generally less corrosion damage than the bulk region. The topographic pictures from Zygo New View 6000 measurement system and the corresponding line depth profiles (Figure 5.19 (b) and (d)) actually show three different zones formed on the lateral surface during the immersion test. This data basically agrees with the previous results (Figures 5.14 - 5.18) that burnishing enhanced the corrosion resistance of *AZ31B Mg* alloy. More detailed examination of the lateral surface reveals that there are two different types of corrosion damage within the process-influenced layer. More material is dissolved in Zone 1 (up to about 1 mm below surface) of the cryogenic-burnished sample; Zone 2 (from 1 mm to 2 mm) is relatively more corrosion resistant than Zone 1. The thickness of Zone 1 on the dry-burnished sample is about half that obtained under cryogenic conditions and the corrosion resistant Zone 2 is thicker than Zone 1. As Zone 1 has the finest grains, grain refinement obviously cannot explain the faster corrosion rate as described here.
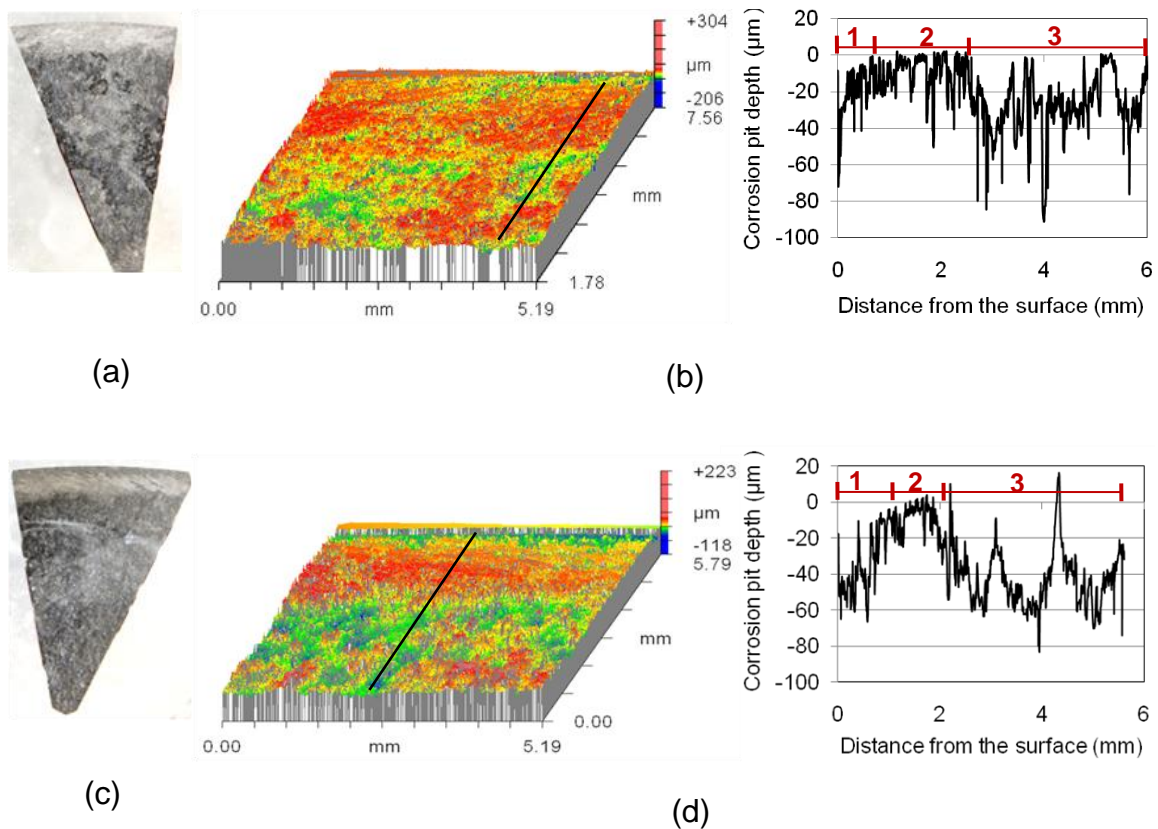
Figure 5.19: Typical corrosion features of (a) dry-, and (c) cryogenic-burnished samples after immersion in 5 wt. % *NaCl* solution for 70 hours; and the corresponding topographic map and depth profile of the black line of (b) dry-, and (d) cryogenic-burnished samples.

To find possible causes of the reduced corrosion resistance in Zone 1, the evolution of texture with the depth from the cryogenic-burnished surface was investigated using XRD. To obtain the crystallographic orientations of the material in the top 0.5 mm, a lead tape was used to cover the rest of the sample. To evaluate the texture at depths of 2 mm and 6 mm, a window of about 1 mm wide was cut in the lead tape and used to mask the rest of the sample. The evolution of texture with the depth below the cryogenic-burnished surface is shown in Figure 5.20 (the XRD method is the same as described in Chapter 3). No basal peak is found in the top 0.5 mm, which corresponds to Zone 1 in Figure 5.19 (d). The strength of the basal texture increases with the increase in

depth. The rolled surface of *Mg* alloys has been reported to have strong basal texture (Song et al., 2010b). The decrease of basal texture from the bulk to the surface is obviously caused by the burnishing process, and this agrees with the fact that the basal plane is parallel to the burnished surface (Figure 4.11). The lower corrosion resistance of Zone 1 where the grain size was small should be attributed to the lack of the basal texture. This conclusion is supported by literature which shows that the corrosion rate of *AZ31B Mg* dramatically increases with decreasing basal texture intensity (Xin et al., 2011). It is also consistent with the result that the corrosion resistance of ECAPed *Ti* with weaker basal texture being lower than the material with a strong basal texture, even if the grain size is smaller (Hoseini et al., 2009).
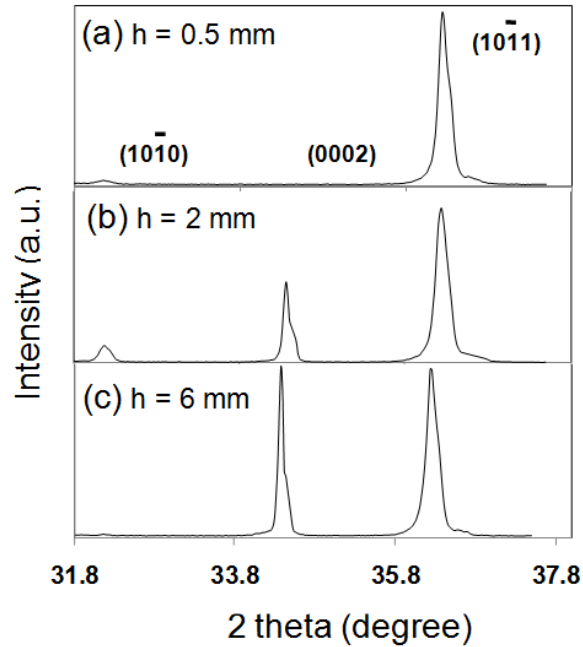
Figure 5.20: Evolution of texture on the lateral surface at different depth after cryogenic burnishing. and depth profile of the black line of (b) dry-, and (d) cryogenic-burnished samples.

5.4 Summary

An experimental investigation has been performed to study the influence of the used machining and burnishing conditions on the corrosion resistance of *AZ31B Mg* alloy specimens. The effects of different processing parameters on corrosion resistance were also investigated, especially cooling method (dry vs. cryogenic). Major observations from this experimental corrosion study can be summarized as follows:

- With the same cutting edge radius of 30 μm, the application of liquid nitrogen during machining significantly improved the corrosion resistance of *AZ31B Mg* alloy in both 5 wt. % *NaCl* solution and *SBF*.

- The featureless layers formed during machining where nano-grain structures exists, which act as protective coatings and significantly improved the corrosion resistance in the two solutions tested.

- Large amount of twinning underneath the featureless layer was found to increase the maximum depth of corrosion pits on the machined samples immersed in 5 wt. % *NaCl* solutions while showing no influence in *SBF*.

- Using the same edge radius of 70 μm and cryogenic cooling, it was found that cutting speed has more influence on corrosion resistance than does feed rate. A larger cutting speed decreased the corrosion resistance which may be due to the larger tensile residual stresses induced by higher cutting temperatures. The differences in corrosion resistance induced by cutting speed were more obvious when the specimens were tested in the 5 wt. % *NaCl* solution than in the *SBF*. On the other hand, the difference in corrosion resistance induced by feed rate was more notable in the *SBF* than in the 5 wt. % *NaCl*.

- Both dry and cryogenic burnishing significantly improved the corrosion resistance of *AZ31B Mg* alloy in 5 wt. % *NaCl* solution as compared to the ground material.

- Similar to the results obtained from machined samples, the thick grain refinement layers induced by burnishing act as protective layers and led to the enhanced corrosion resistance. There is little difference between the burnished samples prepared under dry and cryogenic conditions, which suggested that further grain refinement down to smaller than 1μm did not result in better corrosion resistance.

- Crystallographic orientations of exposed specimen surfaces have a dramatic influence on the corrosion resistance of burnished *AZ31B Mg* alloy. Materials with smaller

grain size but little basal texture are less corrosion resistant than the ones with similar grain size and strong basal texture.

- Residual stresses increased the anodic polarization current densities of burnished samples, but decreased the cathodic polarization current densities. Thus, their influence on overall corrosion resistance is relatively less evident and outweighed by the grain size and the texture effects. Further investigation is needed to study the influence of residual stresses on corrosion resistance.

CHAPTER 6: FINITE ELEMENT MODELING OF SURFACE INTEGRITY IN MACHINING *AZ31B* MAGNESIUM ALLOY

6.1   Introduction

In the previous chapter, surface integrity changes induced by machining and burnishing, especially microstructual changes were shown to notably influence the corrosion performance of *AZ31B Mg* alloy. In order to improve the functional performance of machined components, it is critical to have a better control of the surface integrity than the current industrial practices where surface roughness is the only criterion for most manufacturers. It was shown in Chapters 3 and 4 that the surface integrity can be changed by many processing conditions, including cooling methods, tool edge radius, etc. These factors are not independent and will interact with each other, which make it more complex to understand their relationships with the resulting surface integrity issues; large number of experimental studies are needed, which is time consuming and not cost-effective.

Finite element modeling (FEM) has been used widely in machining to reduce the need for extensive experiments and help researchers to better understand the metal cutting mechanism though the prediction of information near the cutting tool that cannot be easily measured, such as strain, strain-rate and temperature. In this chapter, a FE study for machining of *AZ31B Mg* alloy was developed and calibrated using the experimental data obtained in Chapter 3. A user subroutine was developed to predict the formation of featureless layers induced by machining based on the dynamic recystallization (DRX) mechanism in *AZ31B Mg* alloys. The user subroutine was calibrated using the

experimental data reported in Chapter 3. Good agreements between the predicted and measured grain size as well as thickness of featureless layers (due to the limited scale of observation using optical microscope) were achieved.

6.2   Finite Element Model Setup

The commercial FEM software DEFORM-2D^{TM}, a Lagrangian implicit code, was used to simulate the orthogonal cutting process of *AZ31B Mg* alloy. The workpiece was initially meshed with 8000 isoparametric quadrilateral elements. The element density around the cutting edge, along the machined surface and in the machined chip was set to be much larger than at the other location as shown in Figure 6.1. The smallest element dimension on the workpiece is about 10 μm. The workpiece was assumed to be rigid visco-plastic material and the elastic portion was neglected. The tool was meshed with 3000 elements and assumed to be rigid but conduct heat. A plane-stress coupled thermo-mechanical analysis was performed.

The mesh and boundary conditions for the FE model are shown in Figure 6.1. The major groove parameters listed in Chapter 3 were used to construct the grooved cutting tool. The bottom of the workpiece was fixed in the vertical direction and allowed to move horizontally at the velocity that equaled the cutting speed. No velocity boundary conditions were applied for the left and right ends. For thermal analysis, the temperatures at the bottom and left sides of the workpiece as well as the top and right sides of the cutting tool were set to equal to the room temperature, T_{room}, which was 20 °C. The top and right sides of the workpiece as well as the left and bottom sides of the cutting tool (marked by red lines in Figure 6.1) were allowed to exchange heat with the environment; the convection coefficient was 20 W/ (m^{2}K), which is the default value for free air

convection in DEFORM 2D (normally in the range of 5-25 W/(m²K)). An environmental window for heat exchange was defined as shown in Figure 6.1 and the width of the windows is 1 mm. The window is fixed in its position and does not move with the workpiece. The local convection coefficient in the window can be adjusted to simulate the cryogenic cooling effects and is one of the major parameter to be calibrated for modeling cryogenic machining.
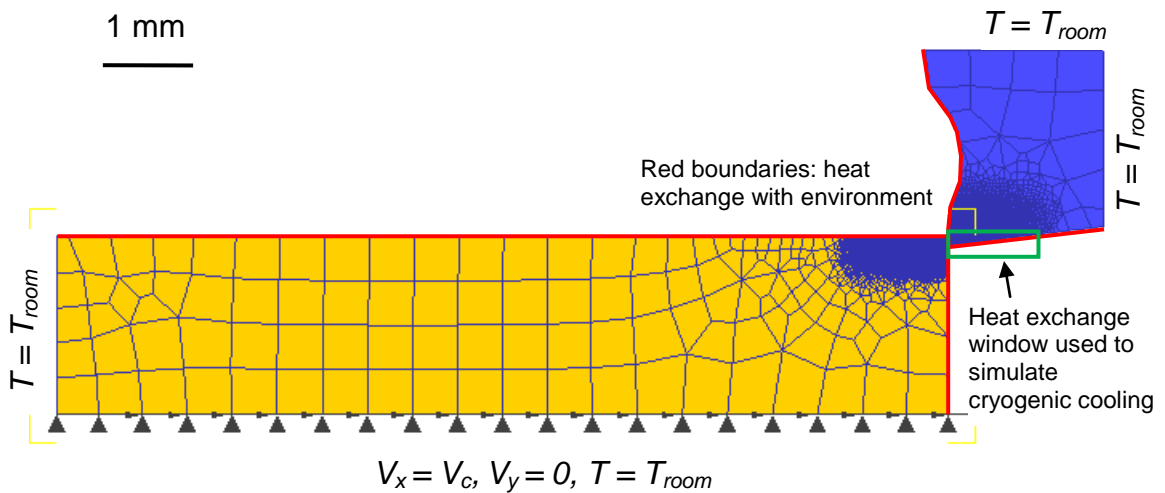
Figure 6.1: Mesh and boundary conditions for the FE model.

6.2.1 Material properties

The physical and thermal properties of *AZ31B Mg* alloy used in the FE model are listed in Table 6.1 (Hibbins, 1998). The default values for the uncoated carbide tool (15% cobalt content) in DEFORM was used and also listed in the table.

Table 6.1: Physical and thermal material properties of *AZ31B Mg* alloy (Hibbins, 1998) and the uncoated carbide tool

	AZ31B Mg alloy	Cutting tool
Melting temperature [K]	891	N/A
Young's Modulus [GPa]	45	N/A
Possion's ratio	0.35	0.23
Thermal Conductivity [W/(mK)]	77+0.096 T	82.24
Specific heat capacity [J/(kgK)]	1000+0.666T	5.79
Thermal expansion coefficient [K^{-1}]	2.48×10^{-5}	6.3×10^{-6}

6.2.2 Flow stress model

The Johnson–Cook constitutive equation was implemented in the FE code by a user subroutine used to model the material behavior of *AZ31B Mg* alloy during machining. The equation is:

$$\sigma = (A + B \cdot \varepsilon^n) \cdot [1 + C \cdot \ln(\frac{\dot{\varepsilon}}{\dot{\varepsilon}_0})] \cdot [1 - (\frac{T - T_{room}}{T_m - T_{room}})^m]$$

(6.1)

where σ is the equivalent flow stress; ε is the equivalent plastic strain; $\dot{\varepsilon}$ is the equivalent plastic strain-rate (s^{-1}); $\dot{\varepsilon}_0$ is the reference equivalent plastic strain-rate (s^{-1}); T is the temperature of the work material; T_m is the melting temperature of the work material and T_{room} is the room temperature (20 ℃). Coefficient A is the yield strength

(MPa); B is the hardening modulus (MPa); C is the strain-rate sensitivity coefficient; *n* is the hardening coefficient and m the thermal softening exponent.

Hasenpouth (Hasenpouth, 2010) performed a wide range of mechanical tests of *AZ31B Mg* sheet where the strain-rates varied from 0.003 s^{-1} to 1500 s^{-1} and the temperature from room temperature to 250 ºC. After data fitting, the constants for the Johnson-Cook constitutive model were found for both rolling and transverse directions and are shown in Table 6.2. The average of the two directional values was used as the start values for the Johnson-Cook constants in the FE model. The values of A and B were adjusted slightly in the calibration process and will be explained in details in the corresponding section below.

Table 6.2: Initial Johnson-Cook constants of *AZ31B Mg* alloy

(Hasenpouth, 2010)

	Rolling Direction	Transverse Direction	Average
A [MPa]	133.1	193.8	163.5
B [MPa]	345.8	296.8	321.3
n	0.293	0.380	0.337
C	0.016	0.016	0.016
m	1.849	1.808	1.829

6.2.3 Friction model

The influence of different tool-chip friction models on FEM results was investigated by Filice et al. (Filice et al., 2007) and it was found that as long as the friction coefficient was well calibrated, both cutting forces and chip morphology could be well predicted independent of which friction model was used. In this study, a simple constant shear friction model is applied:

$$\tau = \mu \cdot \tau_0 \tag{6.2}$$

where τ is the frictional stress between the tool and the chip and work material, τ_0 is the shear flow stress of the work material and μ is a friction coefficient. it was reported that the application of liquid nitrogen decreased the friction coefficient in a contact sliding friction test (Hong et al., 2002), especially when the contact force was low (200-300 N). However, the test was conducted at room temperature which is different than the actual machining environment. The influence of cryogenic cooling on friction coefficient was not well reported by other literature. In the present study, the same friction coefficient was used for both dry and cryogenic machining.

6.2.4 Fracture criterion

It was shown in Chapter 3 that the machined chips of *AZ31B Mg* alloy under all the tested conditions were serrated. Therefore, tt is necessary to simulate the chip serration process in the FE model in order to accurately predict the forces and temperatures. There are two types of approaches that are utilized to simulate serrated chip formation. The first one is by using damage or material failure models together with the standard Johnson-Cook material model (Obikawa and Usui, 1996; Shivpuri et al., 2002;

Umbrello, 2008). It is assumed that by using this method that the chip segmentation occurred by crack initiation at critical points which is then followed by propagation inside the primary shear zone. The presence of adiabatic shear bands support the theory of saw-tooth chip formation by crack initiation since it was reported that the adiabatic shear bands are commonly the precursors to fracture (Bai and Dodd, 1992). The other approach to simulate serrate chips is to use a modified material flow stress model incorporating "flow softening" effects. Flow softening is due to microscopic level changes and is represented by a decrease in stress with increasing strain beyond a critical strain value. Below that critical strain, the material exhibits strain hardening. The standard Johnson-Cook material model agrees well with the material flow stress curves obtained from Split-Hopkinson Pressure Bar Test. However, it is noted that the levels of strain, strain-rate and temperature achieved with this experimental method are lower than the actual values that occur during the machining. The achievable maximum strain by the Split-Hopkinson Pressure Bar is about 0.5 and strain-rate is about 10^3 s^{-1} (Calamaz et al., 2008) while the actual machining process involves large shear strain (typically 2–10) and higher strain-rates (up to 10^6 s^{-1}) rates. Outside the experimental range, the standard Johnson-Cook model is extrapolated and the flow stress will keep increasing with increased strain which was proved wrong by several researchers who reported that the flow stress decreased after the strain reached a critical value in *Ti* alloys (Miller et al., 1999). The flow softening of *Ti* alloys was found to be caused by DRX (Ding and Guo, 2004). The second approach of incorporating flow softening becomes more popular recently due to the increased understanding of the material behaviors, especially on *Ti* alloys where large amount of material testing data has been reported. The second

161

approach is also preferred by the author since DRX is proved to occur during machining of *AZ31B Mg* alloy in Chapter 3 and should be the caused for flow softening. However, due to the limitation of the existing material testing data on *Mg* alloys, it is not possible at this time to develop a good material constitutive model incorporating DRX effects. Therefore, the first approach is used in the current study. The Cockroft and Latham's fracture criterion (Cockcroft and Latham, 1968) were reported to successfully simulate the formation of serrated chips in machining *Ti* alloys (Shivpuri et al., 2002; Umbrello, 2008). This criterion is used in the current study and is expressed as:

$$\int_0^{\bar{\varepsilon}_f} \sigma_1 d\bar{\varepsilon} = D \tag{6.3}$$

where $\bar{\varepsilon}_f$ is the effective strain; σ_1 is the maximum principal stress; *D* is a value calculated for each element by DEFORM for each step by using Equation (6.3). When the calculated *D* value of any elements is larger than $D_{critical}$, which is a material constant, the flow stress of these elements is forced to be only 10% of the original value, which is the stress calculated using Equation (6.1). The changes of damage value, effective stress and effective strain during one chip segmentation cycle are shown in detail in Appendix A, which demonstrated the ability of the fracture criterion to simulate the chip segmentation process during machining. The DEFORM software automatically reduced the flow stress of those elements whose calculated *D* values are larger than $D_{critical}$ to 10% of the original flow stress. This forced reduction of flow stress crudely simulates the "flow softening" induced by DRX. It is expected that by calibration of the material constants using the experimental data reported in Chapter 3 a reasonable agreement between the FE model and the measured data on force, temperature and chip morphology

162

can still be achieved. In part this approximate technique is used because the procedures for simulating microstructural changes during machining are both new and complex. Despite its obvious importance, very few attempts to address this problem have been reported (Caruso et al., 2011). Microstructure level changes are very different for different materials and limited help can be obtained from the literature if the workpiece materials used are not the same.

6.2.5 Evaluation of friction coefficient μ and critical damage value $D_{critical}$ using measured force

The calibration process of the FE model for machining *AZ31B Mg* alloy is shown in Figure 6.2. The values of the friction coefficient μ and the critical damage value $D_{critical}$ were determined through an iterative calibration process using the experimental data on cutting forces and chip morphology from dry machining with a 30 μm edge radius tool. The heat transfer coefficient h_1 at the tool-chip interface was fixed at 1000 kW/ (m^2 K) at this stage of calibration; this value was used by several researchers and good agreement with experimental data was reported (Filice et al., 2007; Umbrello et al., 2007). The studied range for μ was from 0.1 to 0.7. The initial estimated value of $D_{critical}$ was found by integrating a published flow stress curve of *AZ31B Mg* alloy (Hasenpouth, 2010) from beginning of deformation to fracture. The final value of $D_{critical}$ and μ were found when a reasonable agreement between the experimental and numerical results was obtained.

It was reported that the value of $D_{critical}$ was majorly responsible for the chip morphology and the value of μ was responsible for cutting forces in machining (Umbrello, 2008). However, it was found in the calibration process that the value of $D_{critical}$ has a significant influence on both the chip morphology and the cutting forces.

163

Figure 6.3 shows the influence of critical damage value $D_{critical}$ and friction coefficient μ on forces predicted by the FE model. With the same μ value of 0.7, the cutting force was increased 30% when the $D_{critical}$ value changed from 35 to 55.
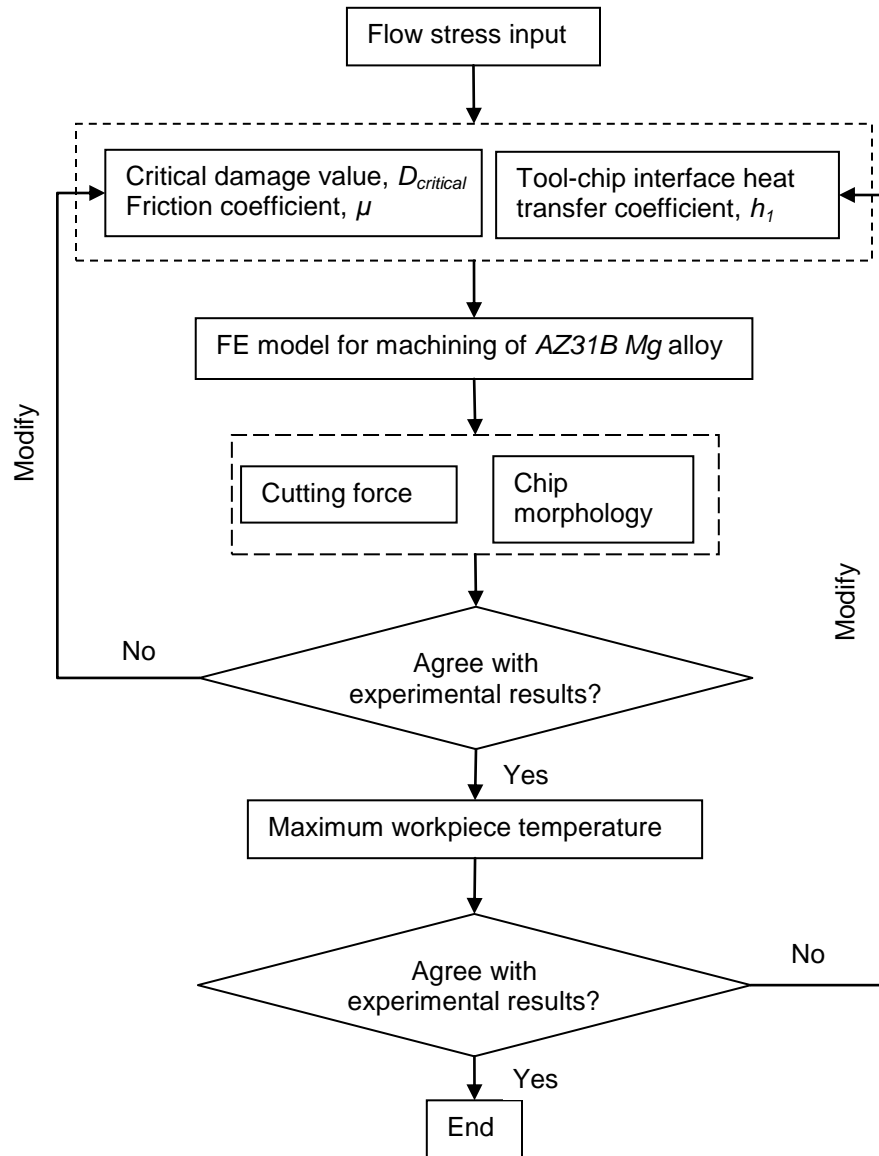
Figure 6.2: Flow chart for the calibration of the FE model for machining *AZ31B Mg* alloy.
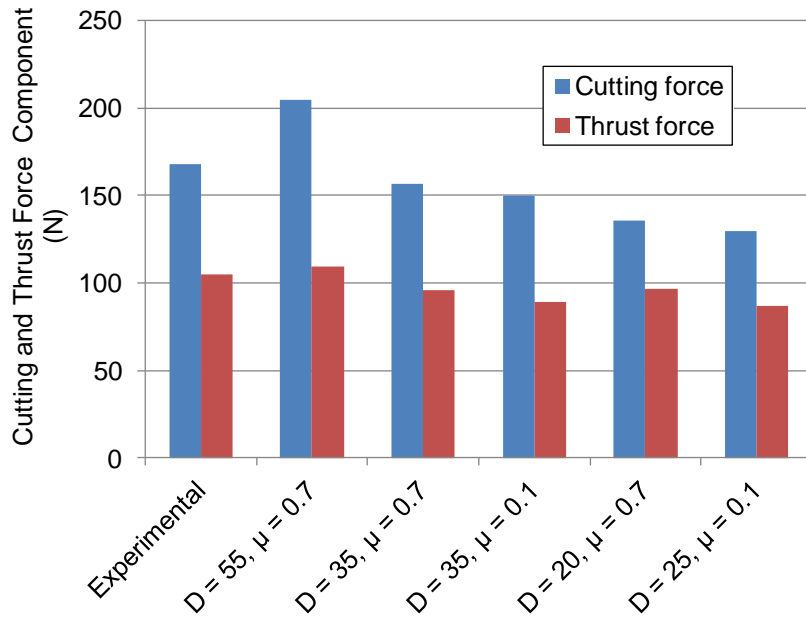
Figure 6.3: Influence of critical damage value $D_{critical}$ and friction coefficient μ on forces predicted by the FE model.

It was found that the best agreement in cutting force was achieved (7% difference between the experiment and predicted values) when the values of $D_{critical}$ and μ were 35 and 0.7, respectively. The predicted thrust forces were 8% smaller than the experimental results. When the calibrated FE model was used to predict the forces in dry machining with 70 μm edge radius tool, the differences between them and experimental data in cutting force and thrust forces were 8% and 9% respectively. With both cutting edge radii, the predicted thrust forces were smaller than the experimental results, which agree with most literature that FE models tended to underestimate the thrust forces (Filice et al., 2007; Umbrello et al., 2007).

One objective of the present FE model is to predict the formation of featureless layer induced by DRX during machining and it was shown in Chapter 3 that the thrust force remarkably influenced the thickness of the featureless layers. Therefore, it is of

great importance for the FE model to predict the thrust forces accurately and the predicted cutting force is less important for the present study. Although increasing the value of $D_{critical}$ results in larger forces in both cutting and thrust directions, it tends to change the chip morphology remarkably. To increase the predicted thrust force, the values of Johnson-Cook constants were adjusted slightly. As shown in Figure 6.4, much better agreement in thrust forces were achieved when the value of A was increased from 163 MPa to 200 MPa and the value of B was increased from 321 MPa to 400 MPa. After this adjustment, the differences between the predicted thrust forces and the experimental ones were 3.1% when 30 µm edge radius tools were used and less than 1% when 70 µm edge radius tools were used. At the same time, the predictions of the cutting forces were still in reasonable range (less than 12%). The underestimate of the A and B values for the FE models could be caused by the differences between the materials testing conditions where the constants were obtained and the actual conditions involved in a machining process. It could also be caused by the overlooking of the microstructure level changes during the machining process.
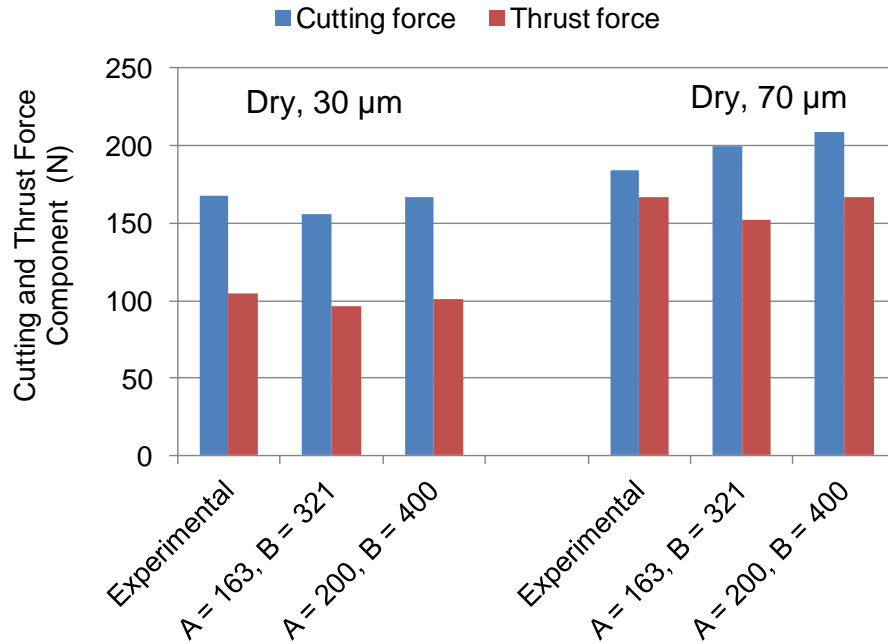
Figure 6.4: Influence of Johnson-Cook constants *A* and *B* on forces predicted by the FE model.

6.2.6 Evaluation of friction coefficient μ and critical damage value $D_{critical}$ using observed chip morphology

To compare the predicted and measured chip morphology, three parameters were used to evaluate the chip shape as shown in Figure 6.5, the lengths of peak, valley and pitch. The influence of critical damage value $D_{critical}$ and friction coefficient μ on chip morphology is shown in Figure 6.6. In addition to forces, good agreement of chip morphology was achieved when the values of $D_{critical}$ and μ were 35 and 0.7, respectively. A comparison between experimental data and predicted values is shown in Figure 6.7. The differences range from 10% to 20%. Since there is no clear correlation between the featureless layers on the workpiece and the chip morphology, the importance of chip

167

morphology calibration was less than forces and temperature and this level of differences

was deemed adequate.
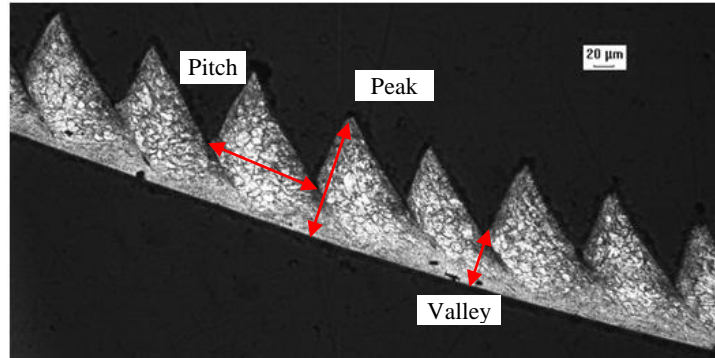
Figure 6.5: Chip morphology after dry machining with a 30 µm edge radius
($V = 100$ m/min, $f = 0.1$ mm/rev).
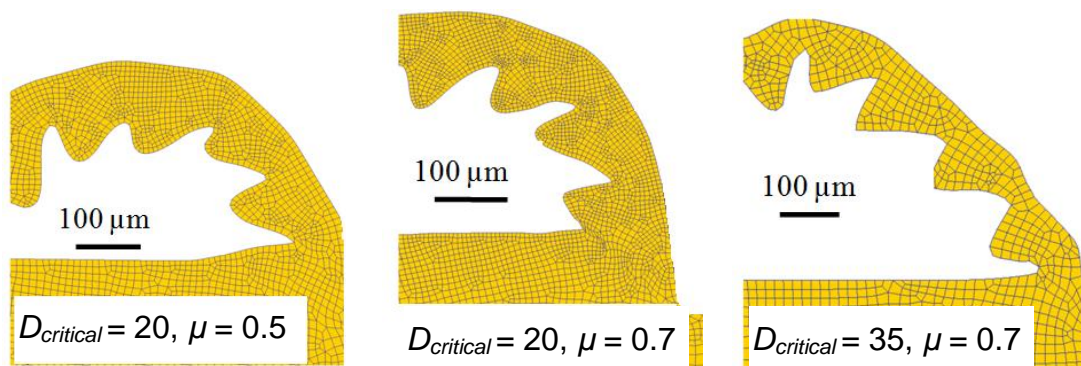
Figure 6.6: Numerically obtained chip morphology at different combination of critical
damage value $D_{critical}$ and friction coefficient μ.
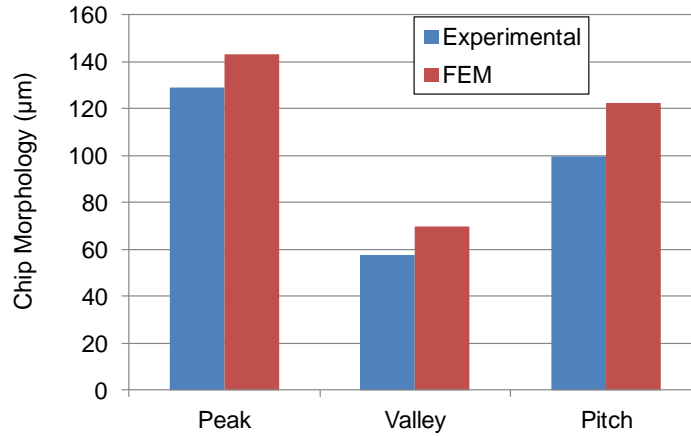
Figure 6.7: Comparison of chip morphology (defined in Figure 6.5) between experimental data and predicted values (dry machining, $r_n = 30$ µm, $V = 100$ m/min, $f = 0.1$ mm/rev).

6.2.7 Evaluation of heat transfer coefficients h_1 and h_2 using measured temperature

The remarkably differences in microstructures between dry and cryogenic machining shown in Figure 3.11 proved that temperature is one of the most important factors. A two step calibration of the FE model was conducted to find the values of heat transfer coefficients. First, the heat transfer coefficient at the tool-chip interface h_1 was determined through an iterative process using the temperature measurement data from dry machining using the 30 µm tool (Figure 3.9). Then the value of h_1 was fixed and the convection coefficient h_2 of the local environment window defined in Figure 6.1 was determined through another iterative process using the temperature measurement data from cryogenic machining using the 30 µm tool (Figure 3.9).

It was found that when the initial choice of h_1 value of 1000 kW/ $(m^2$ K) was used the maximum temperature on the workpeice was about 180 °C, which was higher than the measured value of 125 °C. A good agreement between the predicted and measured

169

temperature was achieved when the h_1 value was increased to 5000 kW/ (m^2 K). Figure 6.9 (a) shows the predicted temperature distribution on the workpiece for dry machining with a 30 μm edge radius tool when the h_1 value of 5000 kW/ (m^2 K) was used. The temperature starting from the start point of the newly formed surface along the workpiece was measured in the FE model and shown in Figure 6.10. The temperature gradually drops with increased distance from the start point and the maximum temperature is 135 °C, about 8% higher than the measured value.

To simulate the cryogenic cooling effects, the local heat exchange window was used as shown in Figure 6.1. The width of the widows is 1 mm which is assumed to the contact length between the machined surface and the liquid nitrogen jet. This use of the window only change the convection coefficient of the machined surface which is covered by the window from the initial value of 20 kW/ (m^2 K) to the value of h_2. The window does not change any other boundary conditions in the FE model. Figure 6.8 (b) and (c) show the predicted temperature distributions during cryogenic machining when different convection coefficients were used within the window. Figure 6.9 shows the temperature profiles along the newly formed machined surface. A good agreement with measured temperature was achieved when the convection coefficient h_2 was set to 5000 kW/(m^{2}K). The predicted maximum temperature on the machined surface was 51 °C, about 2% lower than the measured value.
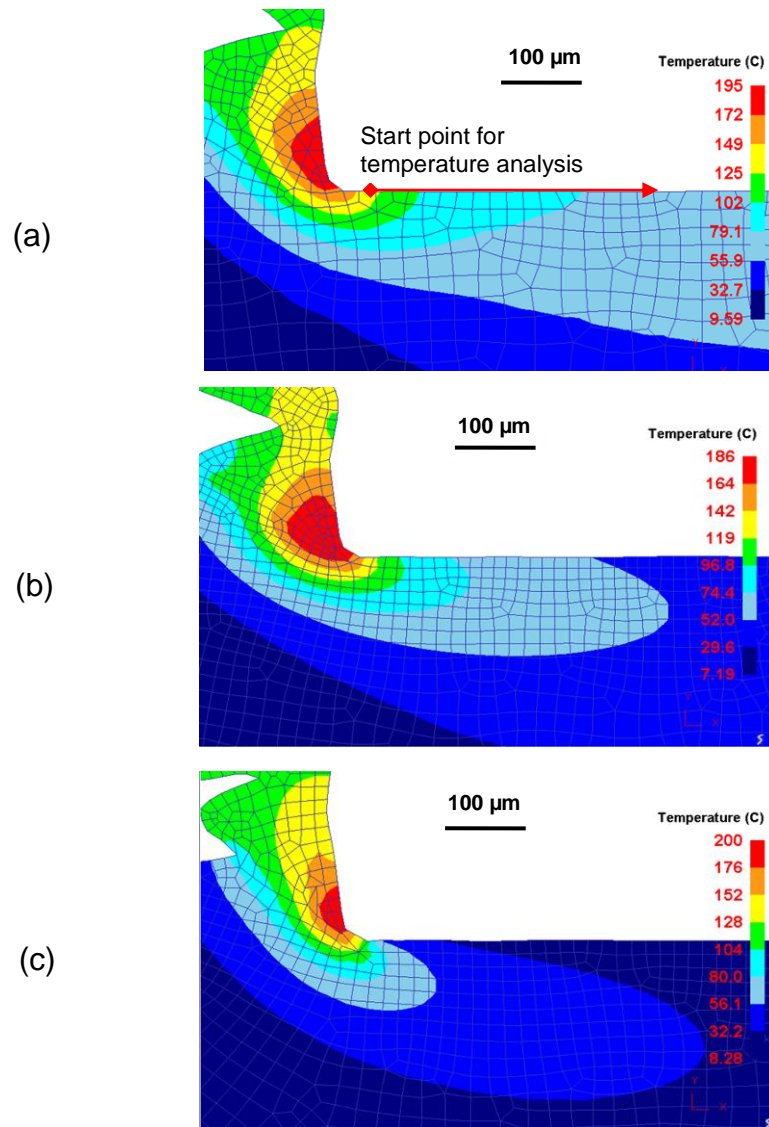
Figure 6.8: Predicted temperature distribution for (a) dry machining, and cryogenic machining when different convention coefficient h_2 was used: (b) 500, (c) 5000 kW/ (m^2K) ($r_n = 30$ µm, $V = 100$ m/min, $f = 0.1$ mm/rev).
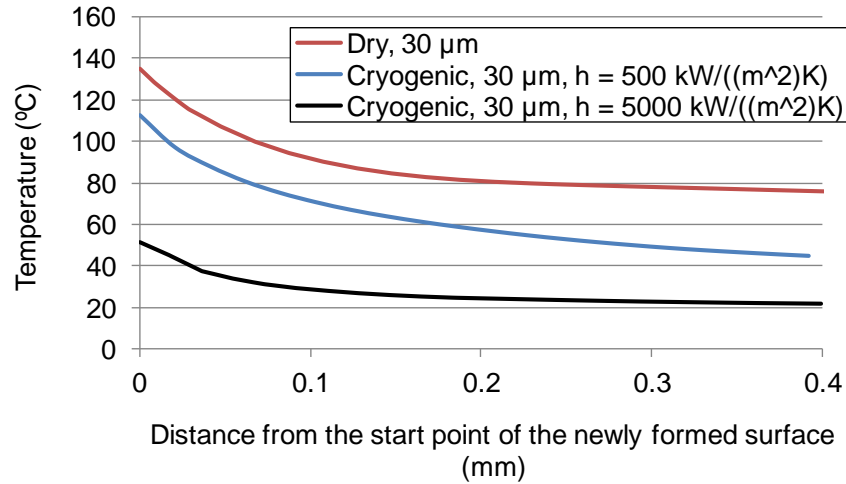
Figure 6.9: Predicted temperature from the start point of the newly formed surface (marked by red line in Figure 6.8) for dry machining, and cryogenic machining when different convention coefficient h_2 was used: 500 and 5000 kW/ (m^{2}K) (r_n = 30 μm, V = 100 m/min, f = 0.1 mm/rev).

6.2.8 Validation of the FE model

After the calibration process was completed, the important constants in the FE models were determined as shown in Table 6.3. The only difference in terms of constants between dry and cryogenic machining is the convection coefficient in the local heat exchange window, h2. All the other constants have the same value for dry and cryogenic machining. To evaluate the performance of the calibrated FE model, machining simulations under different edge radii and cooling conditions were conducted and compared with the experimental data obtained in Chapter 3. Two factors that have critical influence on the formation of the featureless layers were considered for the validation, thrust force and temperature.

Table 6.3: Summary of important constants used in the FE model

Johnson-Cook constants	A = 200 MPa, B = 400 MPa, n = 0.337, C = 0.016, m = 1.829
Critical damage value, $D_{critical}$	35
Friction coefficient, μ	0.7
Heat transfer coefficient at the tool-chip interface, h_1 (For both dry and cryogenic conditions)	5000 kW/ (m^2 K)
Convection coefficient in the local heat exchange window, h_2 (For cryogenic condition only)	5000 kW/ (m^2 K)

Figure 6.10 shows the comparison of measured and predicted forces under dry and cryogenic conditions (V = 100 m/min, f = 0.1 mm/rev). The measured data on dry machining with the 30 µm edge radius tools was used for calibration and all the other three conditions were used for validation purpose. Good agreements between the measured and predicted thrust forces were achieved. The maximum difference is 4%. The cutting forces were not as important as thrust force in the present study since the latter one directly relates with the thickness of featureless layers. The predicted cutting forces were overestimated in most cases. The maximum error is 19% when the 70 µm edge radius tools were used under cryogenic conditions.
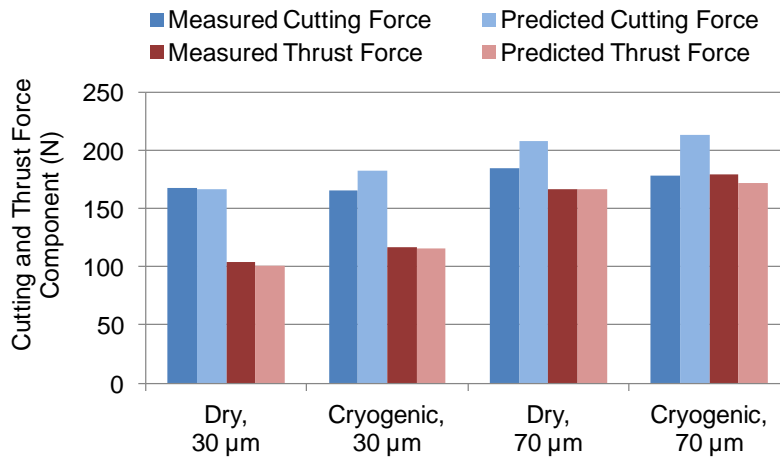
Figure 6.10: Comparison of measured and predicted forces under dry and cryogenic conditions ($V = 100$ m/min, $f = 0.1$ mm/rev).

Figure 6.11 shows the comparison of measured and predicted maximum workpiece temperature under dry and cryogenic conditions (V = 100 m/min, f = 0.1 mm/rev). The measured data on cryogenic machining with the 70 μm edge radius tools was used for validation purpose. The difference between the predicted and measured temperature is 7% which shows that the FE model is capable of temperature prediction.
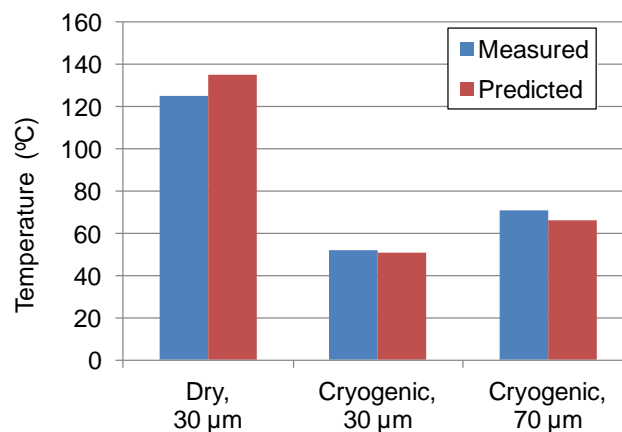
Figure 6.11: Comparison of measured and predicted maximum workpiece temperature under dry and cryogenic conditions ($V = 100$ m/min, $f = 0.1$ mm/rev).

6.3 User Subroutine for Predicting Grain Size and Hardness

In order to predict the grain size and featureless layer thickness after machining, it is important to understand the mechanism for the grain refinement. It has been shown in Chapter 3 that the significant grain refinement was induced by dynamic recrystallization (DRX). The critical conditions for the onset of DRX in *AZ31 Mg* alloy in standard material property testing was investigated by several researchers (Wang et al., 2002; Huang et al., 2007a). For DRX to occur, a critical strain, ε_{cr}, needs to be reached. This critical value was found to be dependent on the strain-rate and temperature (Wang et al., 2002) , which can be calculated using the Zener-Hollomon parameter (defined in Equation (3.3)), Z, as:

$$\varepsilon_{cr} = 0.02039Z^{0.06} \tag{6.4}$$

In the DEFORM subroutine, when the calculated strain on the workpiece exceeds the critical strain, the initial grain size, d_{init}, will be replaced with the grain size after DRX, d, which can be calculated by Equation (3.2). This calculation is carried out continuously for every element in the workpiece for each step.

The Hall-Petch relationship between the hardness and grain size was also found to be well followed in *AZ31 Mg* alloy (Chang et al., 2004). Therefore, the hardness can be estimated based on the grain size using the Hall-Petch relationship. It is noted that this method does not take into account fully the effect of strain hardening which was proved to exist on the workpiece in Chapter 3. It is expected that the predicted hardness will be smaller than the measured value. The Hall-Petch relationship for the *AZ31B Mg* alloy used in this study was found by using the measured hardness on the initial material (12 μm, 52.3 HV) and on the featureless layer induced by cryogenic machining using the 70

175

μm edge radius tools (31 nm, 96.6 HV). The relationship between the hardness H and grain size d using this was found to be:

$$H = 52.391 + 9.039d^{-0.5} \qquad (6.5)$$

The constants in Equation (3.2) and Equation (6.4) were found by the authors in the same material but different manufacturing processes. Therefore, it is expected these constants to be calibrated using the results from the present study before the subroutine can accurately predict the featureless layers induced by machining. The flowchart for the calibration of the subroutine is shown in Figure 6.12. The exponents in Equation (3.2) and Equation (6.4) were found to be the most important constants and were determined by calibration.

Figure 6.13 shows the variation of predicted strain and critical strain with distance below the machined surface before calibration for cryogenic machining with the 70 μm edge radius tools. The data was taken from 0.1 mm away from the start point of the newly formed machined surface as shown in Figure 6.14 (a). It shows that the predicted recrystallized layer is more than 50 μm thick, which is much larger than the measured value (15 μm). It can be found from Figure 6.13 that the critical strain at the depth of 15 μm needs to be equal to 1.9 in order to have a recrystallized layer with the thickness of 15 μm (ε_{cr} = 1.9). Since the Zener-Hollomen parameter at the depth of 15 μm can also be calculated using the calibrated FE model, the exponent in Equation (6.4) can be found. The exponent, a, was found to be increased from 0.06 to 0.075. The predicted grain size on the surface was found to be about 50 nm, which is slightly larger than the measured 31 nm. After calibration, the exponent in Figure 6.12, b, was found to be -0.205.

176

Machining Conditions

- Tool edge radius
- Cutting speed
- Cooling method
- Rake angle
- Feed rate

↓

Validated FE Model

↓

Strain (ε)
Strain-rate ($\dot{\varepsilon}$)
Temperature (T)

→ **Zenner-Holloman**
$$Z = \dot{\varepsilon} \exp(\frac{Q}{RT})$$

→ **Critical strain**
$$\varepsilon_{cr} = 0.02039Z^a$$

DRX does not occur
$$d = d_{init}$$
$$H = H_{init}$$

← N — $\varepsilon > \varepsilon_{cr}$?

↓ Y

DRX occurs
$$d = 10^3 \cdot Z^{-b} d_{init}$$
$$H = 52.391 + 9.0388 d^{-0.5}$$

Modify *b*

Grain size is different

N — Predicted featureless layer agrees with experimental data? — N

Layer thickness is different

Modify *a*

↓

End

Figure 6.12: Flow chart for the calibration of the user subroutine to predict the featureless layer on the machined surface.
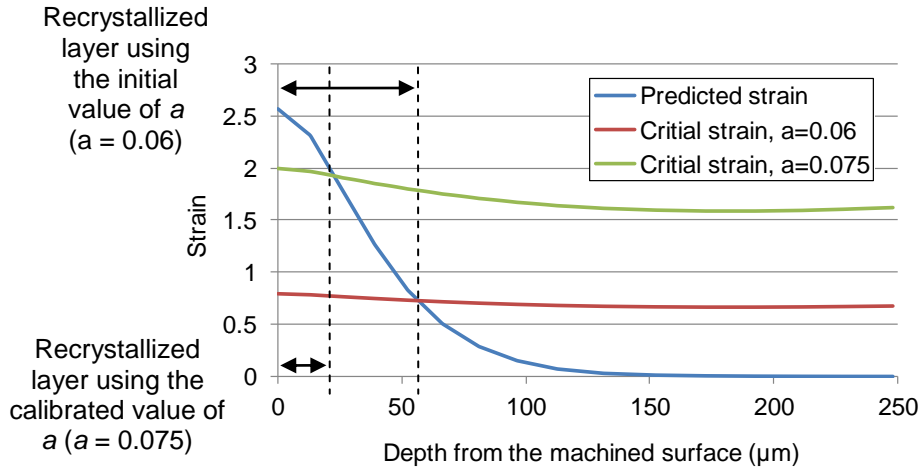
Figure 6.13: Variation of predicted strain and critical strain with distance from the machined surface before and after calibration of exponent *a* in Equation (6.4) (cryogenic, $r_n = 70$ μm, $V = 100$ m/min, $f = 0.1$ mm/rev).

The predicted grain size distributions after calibration under different machining conditions are shown in Figure 6.14. Only the experiment data from cryogenic machining with the 70 μm edge radius tool was used for the calibration and all the other three groups were used for validation. It shows that good agreement was achieved between the predicted grain size and the measured data (Figure 3.11). For both dry and cryogenic conditions, machining with the larger edge radius tool led to the formation of thicker grain refinement layers. The data on variation of grain size with depth below the machined surface was extracted at the location 0.1 mm away from the start point of newly formed surface (the point where the workpiece leaves the cutting edge) as shown in Figure 6.14 (a). Figure 6.15 (a) shows the variation of grain size with depth below the machined surface under different machining conditions. Grain refinement on the surface and sub-surface was successfully predicted by the user subroutine. The predicted grain size within the first 12 μm on the machined surface after cryogenic machining using the 70 μm edge radius tool is about 40 nm, which is very close to the measured grain size of
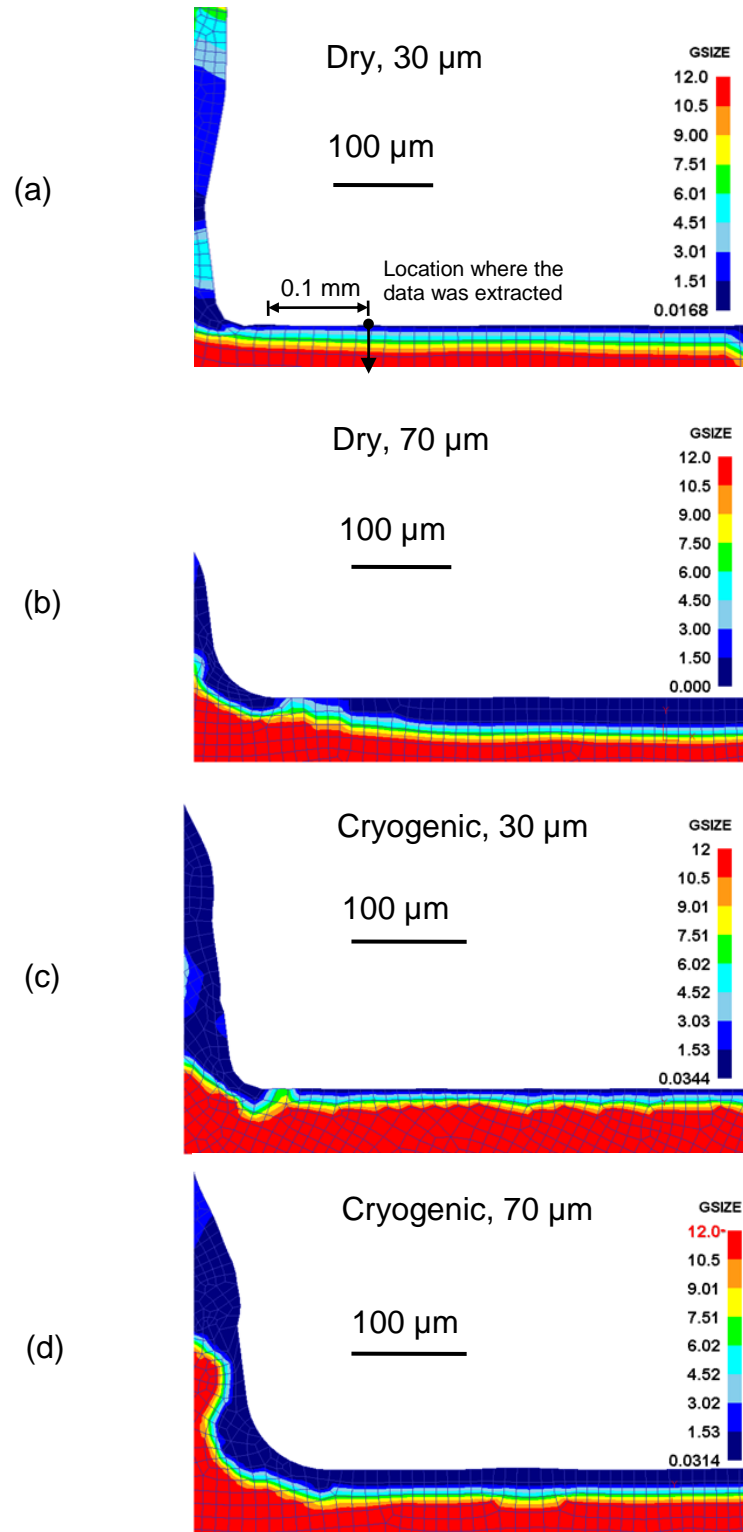
Figure 6.14: Predicted grain size distribution after machining using different cooling methods and tools with various edge radii (V = 100 m/min, f = 0.1 mm/rev).
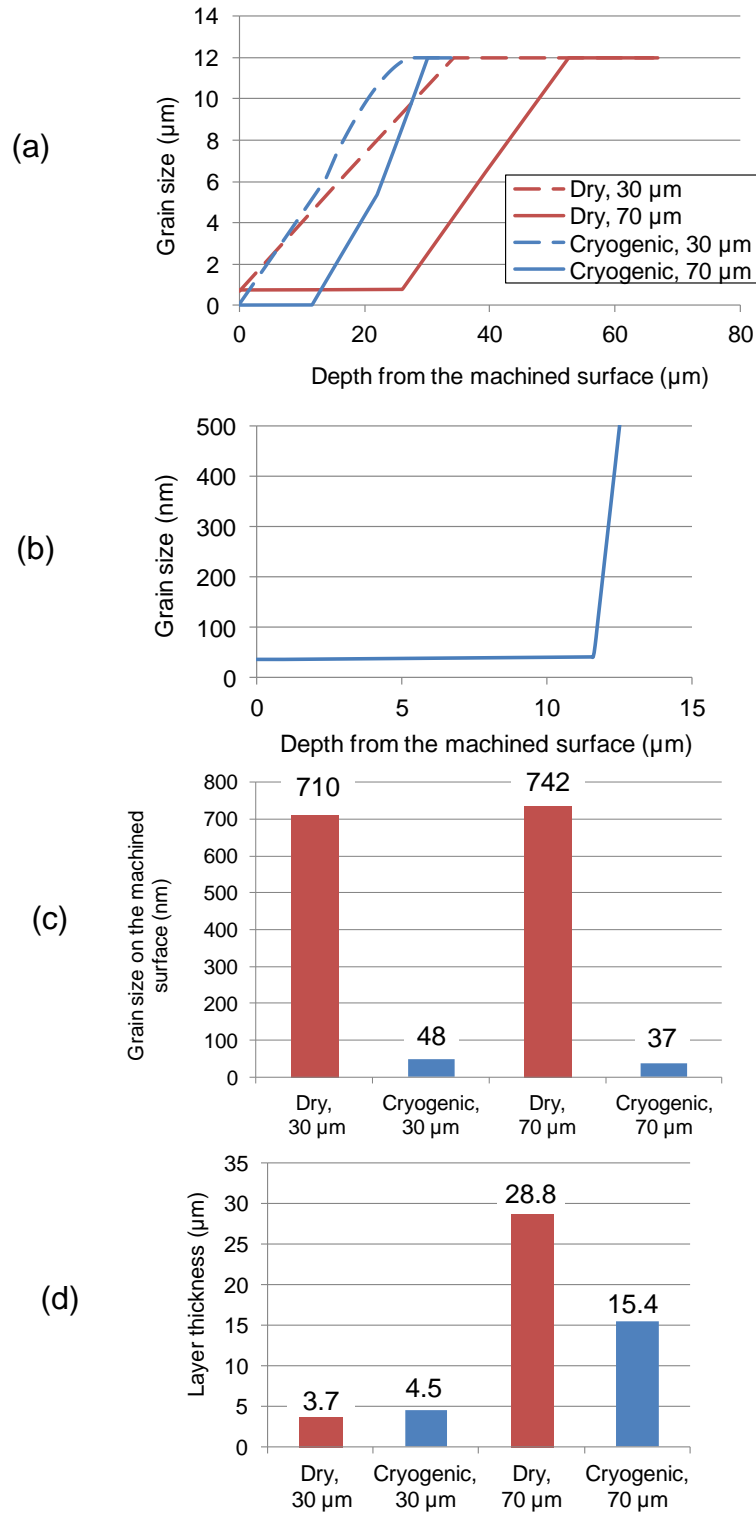
Figure 6.15: (a) Predicted variation of grain size with depth below the machined surface; (b) enlarged view on the machined surface after cryogenic machining with the 70 µm edge radius tool; (c) predicted grain size on the machined surface and (d) thickness of the featureless layers under different machining conditions ($V = 100$ m/min, $f = 0.1$ mm/rev).

f31 nm. The sudden increase of grain size after 12 µm is very similar to the observed microstructure in Figure 3.11 where a clear interface between the featureless layer and the bulk material is shown. The grain size distribution in the machined chips is not the focus of the present study. An example of the predicted grain size distribution in the machined chips is provided in Appendix B. The approach used in the current study to predict grain size is new and very few studies on grain size prediction have been reported (Caruso et al., 2011).

Figure 6.15 (c) shows the grain size on the machined surface. The influence of cryogenic cooling on grain size is predicted to be dramatic, which is as expected when one recalls the experimental data. For both edge radii, cryogenic cooling results in significantly smaller grain size. It is assumed that the grain size in the featureless layer is smaller than 2 µm which approaches the limit of the optical microscope used in the study. Therefore, the thickness of the predicted featureless layers can be measured from Figure 6.15 (a). Edge radius does not play an important role in determining the grain size on the machined surface but has remarkably influence on the thickness of the featureless layers as shown in Figure 6.15 (d). This agrees with the finding from the experimental data shown in Figure 3.11. The predicted thickness of the featureless layer on machined surface after cryogenic machining using the 70 µm edge radius tool is 15.4 µm which agrees well with the measured value. The predicted value for dry machining using the 70 µm edge radius tool is 28.8 µm and is a little larger than the measured value shown in Figure 3.11 (20 µm). This may be due to the fact that the user subroutine does not take consideration of grain growth after DRX. Figure 6.16 (a) shows the variation of predicted temperature with depth from the machined surface under different machining conditions.

It shows the temperatures within the first 80 μm from the machined surface under cryogenic conditions are significantly lower than those under dry conditions. The surface
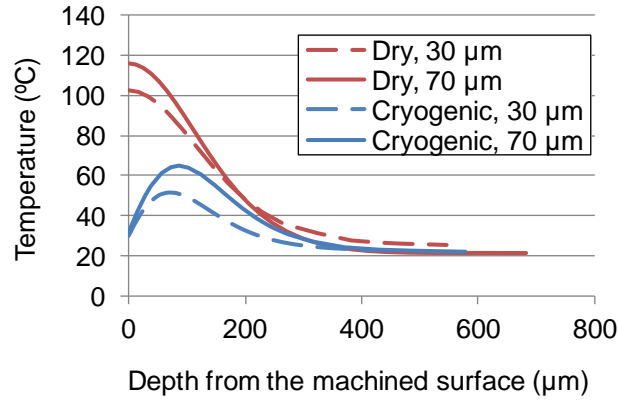
(a)
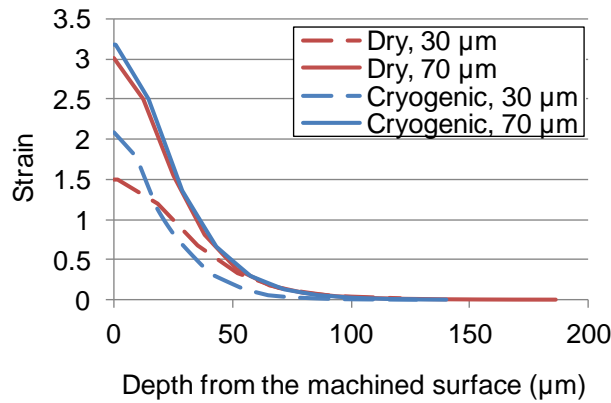
(b)

Figure 6.16: Variation of (a) predicted strain and (b) temperature with depth from the machined surface under different machining conditions ($V = 100$ m/min, $f = 0.1$ mm/rev).

temperature under cryogenic cooling was less than 30% of that under dry conditions when the 30 μm edge radius tools were used. This trend observed from the predicted data agrees well with the temperature measurement shown in Figure 3.9. Therefore, it is highly possible that a certain amount of grain growth occurs after DRX during dry machining and in turn this leads to the reduction of thickness of the featureless layer. This claim was also supported by Calistes et al. (Calistes et al., 2009) who reported that

ultrafined/nano grain structure were only found on the top of the machined surface of copper when the cutting speed was very low (< 3 m/min) during dry machining.

Although no featureless layer was observed on the machined surface after dry machining using the 30 µm edge radius tool in Figure 3.11, it is possible that a very thin grain refinement layer formed and it cannot be recognized by the optical microscope used in this study. The user routine predicted that the featureless layer under these conditions is 3.7 µm. The predicted thickness of the featureless layer on the workpiece after cryogenic machining using the 30 µm edge radius tool is 4.5 µm, which is smaller than the measured value of 8 µm. These differences could be caused by the size of the used element since the average element dimension is about 10 µm and is larger than the thickness of the featureless layer under this condition. The increase of the thickness under cryogenic conditions compared with dry conditions could be caused by the increased strain as shown in Figure 6.16 (b). The strain on the machined surface was increased 40% when cryogenic cooling was applied. Much smaller difference in the strain was observed when the 70 µm edge radius tool was used.

Figure 6.17 shows the predicted hardness after machining using different cooling methods and tools with various edge radii. The predicted hardness at 10 µm from the machined surface is about 60 Hv for dry machining using both 30 µm and 70 µm edge radius tools, which is much smaller than the measured value of about 80 Hv. This large difference between the predicted and measured hardness could be caused by the lack of consideration for the dislocations in the interior of grains and residual stress in the user subroutine since it was proved in Chapter 3 that strain hardening contributes remarkably to the hardness of the machined workpiece. Figure 6.18 shows the comparison of

predicted and measured hardness after cryogenic machining using 70µm edge radius tools. The predicted hardness at 10 µm is 96 Hv, which agrees well with the measured hardness. However, the predicted hardness drops significantly when the depth from the machined surface is larger than 15 µm and returns to initial value at the depth of 30 µm while the measured hardness changes more gradually and is still larger than the initial value at the depth of 150 µm. This finding further proves that the strain hardening is the dominant factor in determining the hardness especially when the microstructure remains similar (outside of featureless layer).
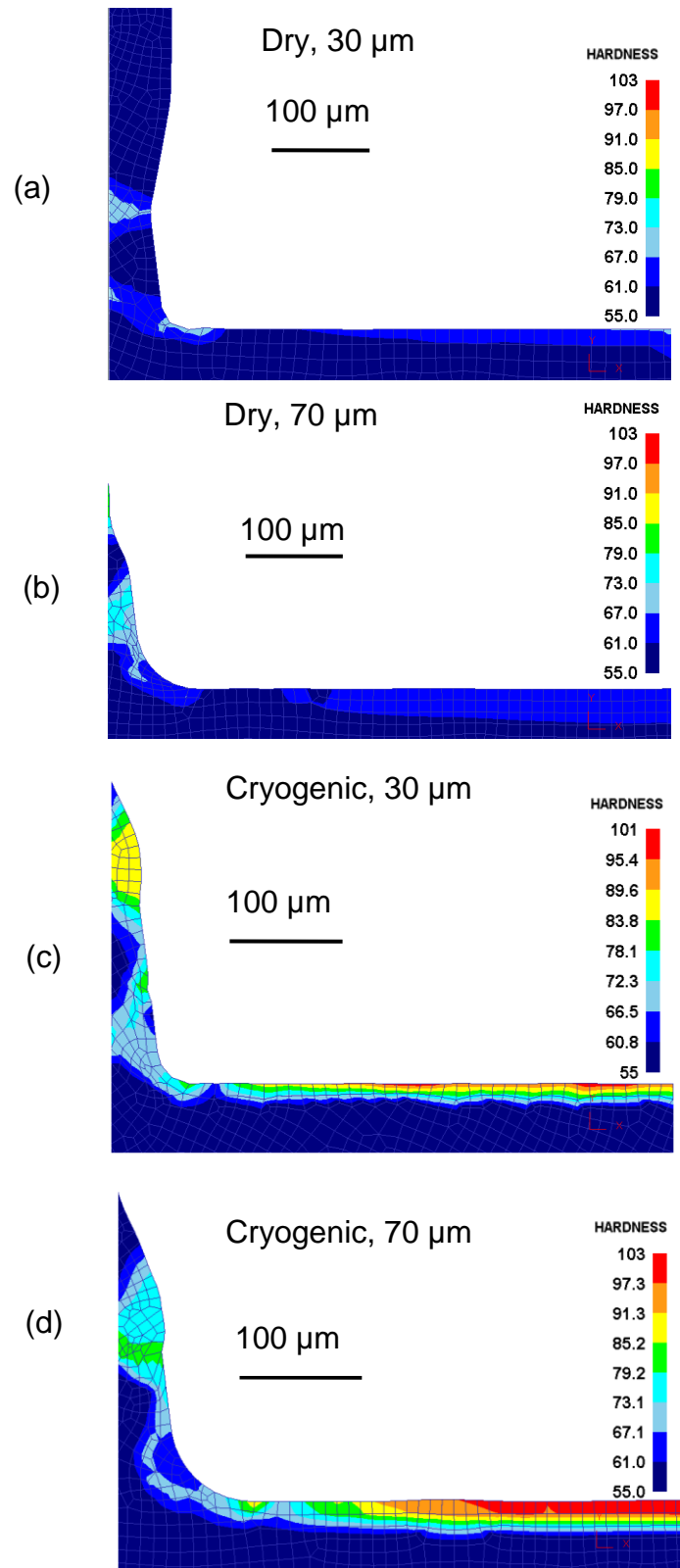
Figure 6.17: Predicted hardness after machining using different cooling methods and tools with various edge radii ($V = 100$ m/min, $f = 0.1$ mm/rev).
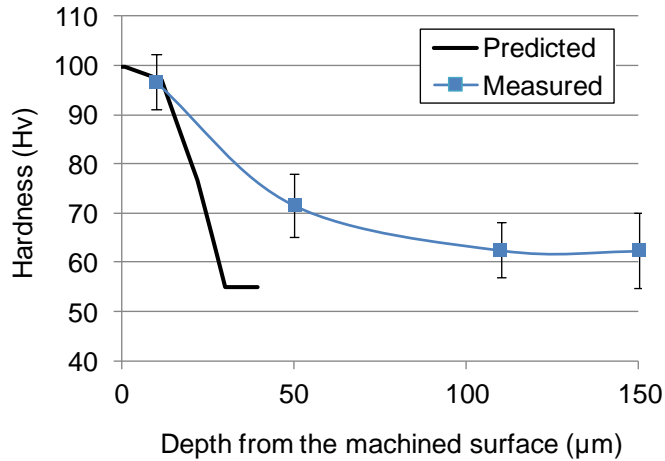
Figure 6.18: Comparison of predicted and measured hardness after cryogenic machining using 70µm edge radius tools (V = 100 m/min, f = 0.1 mm/rev).

6.4   Numerical Investigation of Surface Integrity using the User Subroutine

It can be concluded from the previous results that the calibrated user routine can predict reasonably well the grain size distribution on the surface and sub-surface of the machined workpiece. The predicted hardness is acceptable only when the grain refinement is the major cause for hardness increase. In this section, this user subroutine will be used to investigate the influence of rake angle, cutting speed and feed rate and on the formation of the featureless layers as well as key DRX factors, such as strain and temperature on the workpiece. The cooling conditions for all the simulations are cryogenic cooling and the edge radius of the cutting tools are 70 µm. The data extraction point for this section is the same as shown in Figure 6.14 (a), 0.1 mm away from the start point of newly formed workpiece surface.

186

6.4.1 Influence of rake angle

Rake angle of the cutting tools was proved experimentally to have a remarkable influence on the plastic deformation of the machined surface and sub-surface (Chandrasekar et al., 2009). The plastic strain on the brass surface machined with a -30^0 rake angle tool was 3 times larger than that machined with a $+10^0$ rake angle tool (Chandrasekar et al., 2009). Figure 6.19 (a) shows the predicted variation of grain size with depth below the surface machined under different rake angles. As summarized in Figure 6.19 (b), the thickest featureless layer (29 µm) was obtained when using the most negative rake angle and using positive rake angle results in the thinnest layer (3 µm). The predicted strains on the workpiece under different rake angles are shown in Figure 6.20 (a). Machining using a -30^0 rake angle led to 125% increase of the surface strains compared with using a $+20^0$ rake angle, which agrees with the literature(Chandrasekar et al., 2009) and is the cause for increased thickness of the featureless layer. The predicted grain size on the machined surface is shown in Figure 6.19 (b). Machining using a positive rake angle resulted in much larger grain size on the surface. This could be caused by the fact that positive rake angles induce less deformation on the workpiece and lower strain-rate. Since the difference in temperature is much smaller than the one in plastic deformation as shown in Figure 6.20, machining with a positive rake angle could lead to a smaller Z value and therefore increase the grain size after DRX. The difference in temperature is much larger than the plastic strains on the machined surface when the rake angle was changed from -7º to -30º as shown in Figure 6.20; this likely is the cause for the slightly larger grain size when a more negative rake angle was used.
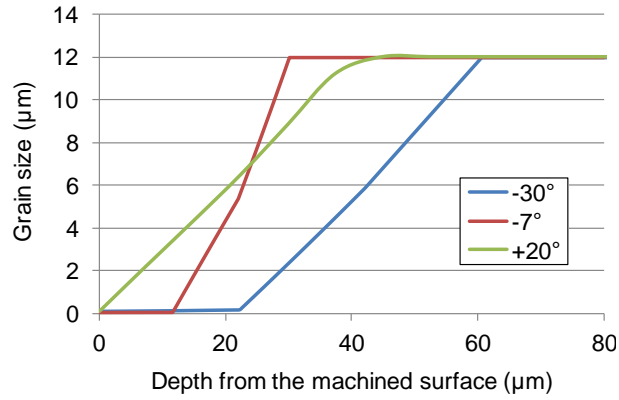
(a)
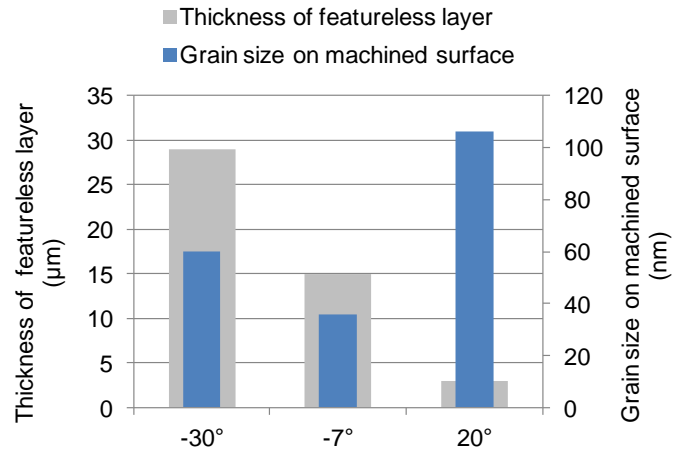
(b)

Figure 6.19: (a) Predicted variation of grain size with depth below the machined surface; and (b) comparison of featureless layer thickness and grain size on the surfaces machined under different rake angles (cryogenic, $r_n = 70$ µm, $V = 100$ m/min, $f = 0.1$ mm/rev).
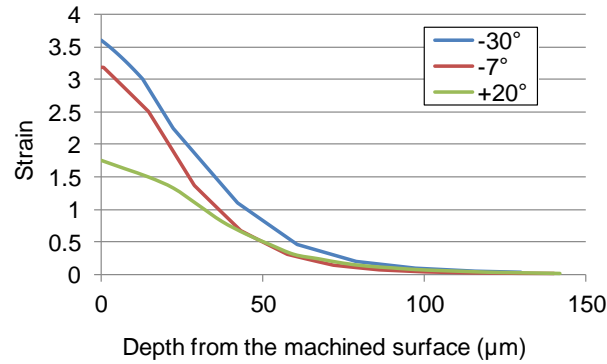
(a)
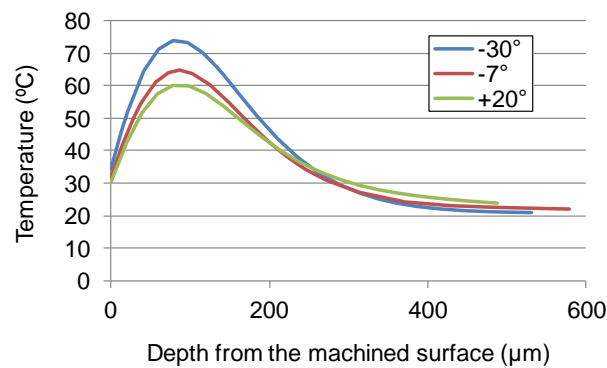
(b)

Figure 6.20: Variation of (a) predicted strain and (b) temperature with depth from the surface machined under different rake angles (cryogenic, $r_n = 70$ µm, $V = 100$ m/min, $f = 0.1$ mm/rev).

6.4.2   Influence of feed rate

Figure 6.21 (a) shows the predicted variation of grain size with depth below the machined surface under different feed rates. As summarized in Figure 6.21 (b), the thickest featureless layer (18 µm) was obtained under the smallest feed rate. It is shown in Figure 6.22 (a) that the smallest feed rate also leads to the largest strain on the machined surface. When machining at the smallest feed rate, 0.05 mm/rev, the uncut chip thickness is smaller than the edge radius of the tool (0.07 mm); therefore, ploughing

effects are dominant, which was proved by the force measurement data shown in Figure 3.23 (thrust force was larger than cutting force). The trend of the predicted thickness of the featureless layer agrees well with that observed from the experimental data where increased feed rate remarkably decreased the featureless layer thickness (Figure 3.24 (b), Figure 3.25 (b) and Figure 3.27 (b)).
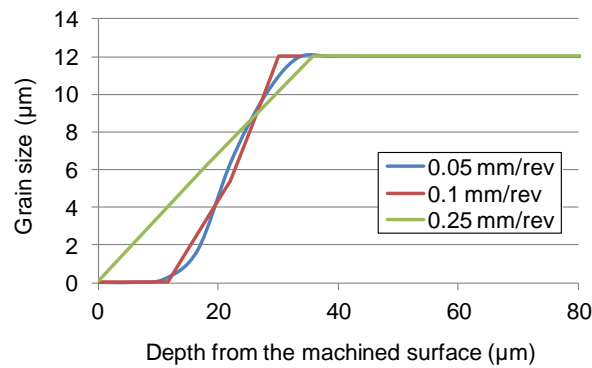
(a)
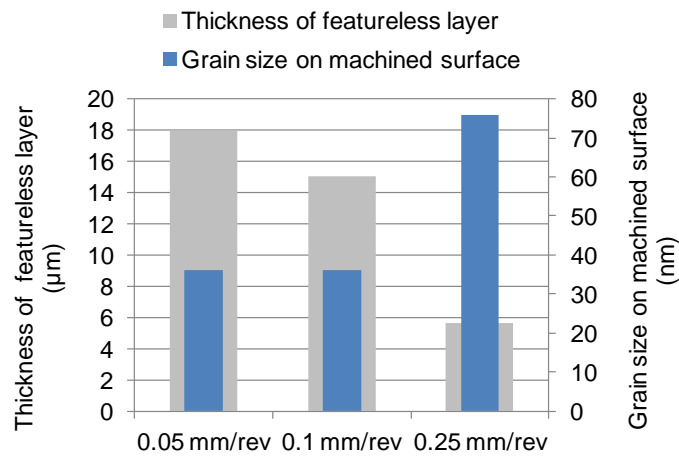
(b)

Figure 6.21: (a) Predicted variation of grain size with depth below the machined surface; and (b) comparison of featureless layer thickness and grain size on the surfaces machined under different feed rates (cryogenic, rake angle = -7°, r_n = 70 μm, V = 100 m/min).
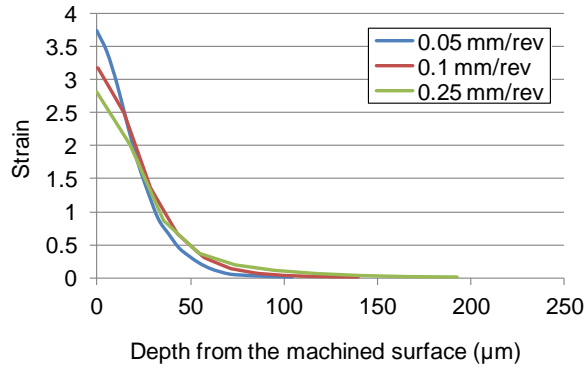
(a)
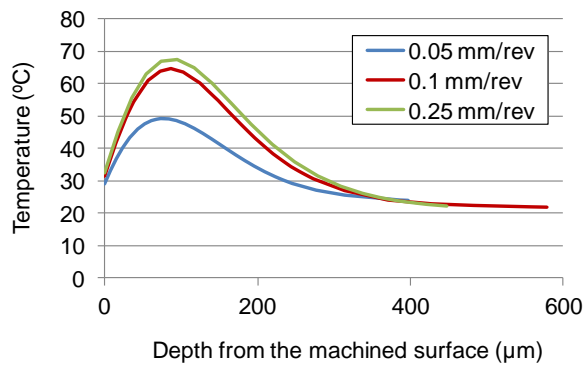
(b)

Figure 6.22: Variation of (a) predicted strain and (b) temperature with depth from the surface machined under different feed rates (cryogenic, rake angle $= -7°$, $r_n = 70$ μm, $V = 100$ m/min).

Machining when using a larger feed rate generated higher temperature as shown in Figure 6.22 (b). The decrease of the strain at higher feed rates could be caused by the softening of the material due to increased temperature, which was supported by the finding from force measure shown in Figure 3.23 (b) where the thrust force was reduced more than 30% when the feed rate was increased from 0.1 mm/rev to 0.25 mm/rev. The high temperature also leads to larger grain size on the machined surface as shown in Figure 6.21 (b). The predicted grain sizes at feed rates of 0.05 mm/rev and 0.1 mm/rev

are almost the same at 36 nm while the grain size was increased to 76 nm when the feed rate was 0.25 mm/rev.

6.4.3　Influence of cutting speed

Figure 6.23 (a) shows the predicted variation of grain size with depth below the machined surface under different cutting speeds. As summarized in Figure 6.23 (b), the thickness of the featureless layer increases with larger cutting speed, which was contradictory to the trend observed from experimental data where the thickness decreased with increased cutting speed (Figure 3.25). The difference could be caused by the fact that the user subroutine does not consider grain growth after DRX. As shown in Figure 6.24 (b), the cutting speed has a significant influence on the temperature near the machined surface. When the cutting speed was increased from 50 m/min to 250 m/min, the temperature on the surface was increased from 32 $^{\circ}$C to 52 $^{\circ}$C and the maximum temperature was more than doubled. The trend of predicted temperature agrees well with the observed chip morphology changes, where serrated chips were produced at low cutting speed and continuous chips were obtained at high cutting speed (Figure 3.25). According to Equation (6.4), higher temperature will lead to a smaller Z value and reduce the critical strain for DRX. Since the strain level on the machined surface does not change notably under different cutting speeds as shown in Figure 6.24 (a), the reduced critical strain results in a thicker featureless layer for the prediction. During the actual machining test, the recrystallized grains tend to grow after DRX finishes and the thickness of the featureless layer will be reduced. This grain growth effect was not considered in the user subroutine. Therefore, relatively large differences between predicted and measured data exist, especially when the highest cutting speed was used.
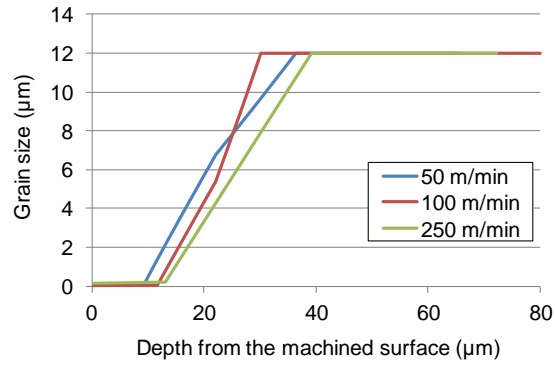
(a)
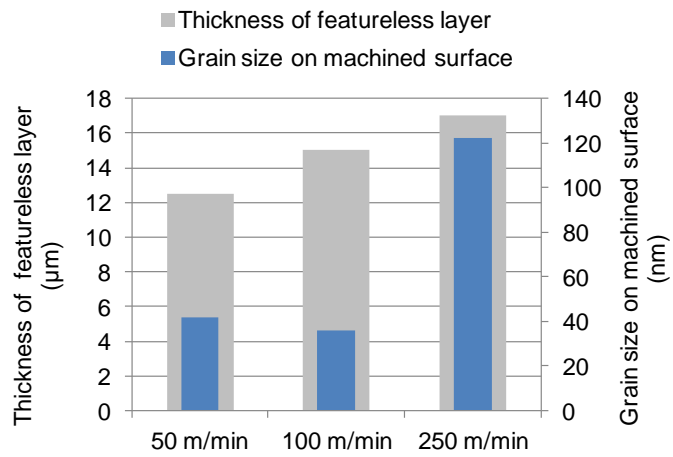
(b)

Figure 6.23: (a) Predicted variation of grain size with depth below the machined surface; and (b) comparison of featureless layer thickness and grain size on the surfaces machined under different cutting speeds (cryogenic, $-7°$ rake angle, $r_n = 70$ µm, $f = 0.1$ mm/rev).
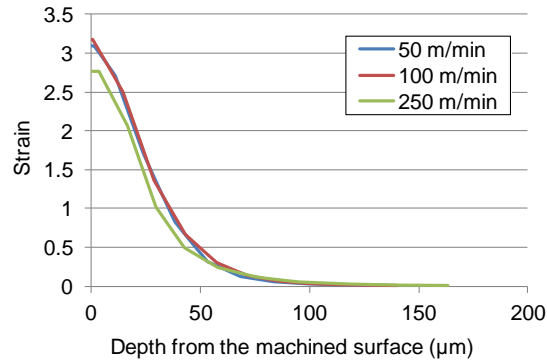
(a)
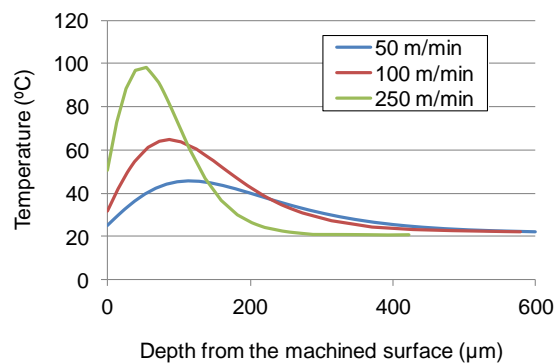
(b)

Figure 6.24: Variation of (a) predicted strain and (b) temperature with depth from the surface machined under different cutting speeds (cryogenic, -7° rake angle, r_n = 70 µm, f = 0.1 mm/rev).

6.5   Summary

An FE model was programmed to simulate the machining of *AZ31B Mg* alloy using the commercial software DEFORM 2D. The comparison between initial predictions and experimental data on forces and temperature as well as chip morphology was used to calibrate the FE model by updating the model parameters. A user subroutine was developed to predict the formation of featureless layers induced by machining based on the dynamic recystallization (DRX) mechanism of *AZ31B Mg* alloys. After evaluation using the experimental data, the user subroutine successfully predicted the formation of

featureless layers under various cutting conditions, including different cooling methods, tool edge radius, rake angle, etc. Also, critical DRX parameters, such as strain and temperature, on the machined surface and sub-surface were predicted by the FE model. Major observations from this numerical study can be summarized as follows:

- Significant reduction of temperature on the machined surface and sub-surface can be achieved with cryogenic cooling. The predicted temperatures on the machined surface under cryogenic conditions were about 30% of those under dry conditions when machining using both 30 µm and 70 µm edge radius tools.

- Increasing the tool edge radius from 30 µm to 70 µm led to 30% increase in the strain on the machined surface under dry conditions; while very small difference was found under cryogenic conditions.

- Rake angle of the cutting tool is one of the most influential factors on featureless layer thickness. The largest thickness was 29 µm when machining using a -30º rake angle, which was increased by a factor of 2 compared with machining using a -7º rake angle.

- Large strain was generated on the machined surface when the feed rate was smaller than the edge radius of the tool and resulted in thick featureless layer formation. The trend of featureless layer thickness with increased feed rate agreed well with the experimental observations.

- The predicted trend of featureless layer thickness with cutting speed is in contradiction to the experimental data. The difference could be caused by the fact that more grain growth occurs after cutting when using a high cutting speed due to the severe heat generation while the user subroutine does not take grain growth into consideration.

- In addition to grain size, the potential of using Hall-Petch relationship in the user subroutine to predict the hardness after machining was investigated. Large differences were found in the predicted and measured hardness, especially at larger depth from the machined surface. The difference could be caused by the overlooking of strain hardening effects in the user routine, which was proved to be dominant in Chapter 3.

CHAPTER 7: CONCLUSIONS AND FUTURE WORK

7.1 Concluding Remarks

In the current research, experimental studies on the influence of various machining and burnishing conditions (dry/cryogenic cooling, cutting edge radius, etc.) on surface integrity changes of *AZ31B Mg* alloy, including microstructures, residual stresses, crystallographic orientations, etc., have been conducted. The beneficial effects of cryogenic cooling during machining were reported frequently in the literature, while its influence on surface integrity was much less known, and this is one of the focuses in the current study. Another focus area of this work is how the surface integrity changes influence the corrosion performance of *AZ31B Mg* alloy which is a key criterion for its wide application. Preliminary corrosion studies were carried out to evaluate the corrosion resistance of machined and burnished *AZ31B Mg* samples in both 5% *NaCl* solution and simulated body fluid (*SBF*).

In addition to the experimental work, a numerical study was developed to investigate the influence of various machining conditions on the grain size changes on the workpiece surface and sub-surface. Major findings from this research are:

- A significant reduction of surface temperature was achieved during cryogenic machining where liquid nitrogen was sprayed onto the machined surface from the clearance side of the tool (less than half of the temperature obtained during dry machining).

- Cryogenic machining using the large honed cutting tool led to enhanced surface integrity in terms of (1) significant grain refinement from 12 μm to 31 nm in the

197

featureless surface layer; (2) large intensity of (0002) basal plane on the machined surface; (3) 10 times larger compressive areas in residual stress profiles; and (4) improved surface finish. Cryogenic machining also resulted in the best corrosion resistance in the machined samples tested in both 5% *NaCl* solution and *SBF*.

- Under cryogenic cooling conditions, cutting speed and feed rate have a notable influence on the microstructure of the machined surface and sub-surface which may be due to the fact that *Mg* alloys are sensitive to temperature changes.

- A strong correlation between grain size and corrosion resistance was found for both the machined and burnished samples. The grain refinement layer acts as protective coating and improves the corrosion resistance in the both 5% *NaCl* solution and *SBF*.

- Using the same edge radius of 70 µm and cryogenic cooling, cutting speed has more influence on corrosion resistance than does the feed rate. A larger cutting speed decreased the corrosion resistance which may be due to the larger tensile residual stresses induced by higher cutting temperatures. The differences in corrosion resistance induced by cutting speed were more obvious when the specimens were tested in the 5 wt. % *NaCl* solution than in the *SBF*.

- Under dry conditions, the surface machined with 70 µm edge radius tool is more corrosion resistant than the one machined with 30 µm edge radius tool in both the 5 wt. % *NaCl* solution and the *SBF*.

- Burnishing using a fixed roller setup remarkably increased the grain refinement layer thickness compared with machining, and also created a much stronger basal texture. The total process-influence layer where significant microstructure occurred is up to 3.4 mm. The application of liquid nitrogen during burnishing resulted in a greater

reduction in grain size on the burnished surface than dry burnishing (0.5 µm vs. 1.4 µm, initial grain size is 12 µm). However, there is little difference in corrosion resistance between the burnished samples prepared under dry and cryogenic conditions, which suggest that further grain refinement to smaller than 1µm did not result in better corrosion resistance.

- Crystallographic orientation, which has not been well studied as an important surface integrity factor in the literature, has a dramatic influence on the corrosion resistance of burnished *AZ31B Mg* alloy. Materials with a smaller grain size but little basal texture are less corrosion resistant than the ones with similar grain size and strong basal texture when tested in 5% *NaCl* solution.

- A finite element (FE) study for machining of *AZ31B Mg* alloy was developed and calibrated using the experimental dat. A user subroutine was developed to predict the grain size changes on the surface and subsurface induced by machining based on the dynamic recrystallization (DRX) mechanism in *AZ31B Mg* alloys. The user subroutine was used successfully to investigate the influence of various cutting conditions on the formation of featureless layers. The numerical study suggests that a negative rake angle resulted in a thicker featureless layer compared with the positive rake angle.

- One of the most significant implications of this study is that by proper selection of processing parameters, machining and burnishing as simple and cost effective industrially available manufacturing processes could offer a unique opportunity to significantly enhance the functional performance of metallic materials, such as corrosion/fatigue resistance, by tailoring their microstructures, crystallographic orientations, etc., on the surface and sub-surface. The interactions studied via a

combined experimental-finite element modeling approach contribute toward an optimum selection of processing conditions to achieve enhanced performance of manufactured products.

7.2   Future Work

- A better temperature measurement needs to be conducted using an infrared camera with higher resolution and magnification than the one used in the current study, as well as for various cutting conditions. The measured temperature distribution near the cutting edge will help understanding the mechanism of dynamic recyrstallization (DRX), and will also provide valuable data for modeling

- A high speed camera can be used to measure the strain and strain-rate induced by various machining/burnishing conditions. Together with the temperature measurement, this will provide comprehensive information on the thermo-mechanical field on the workpiece surface/sub-surface, as well as on the primary/secondary deformation zones, which will facilitate a greater understanding of the DRX mechanism during deformation at high strain-rate (up to 10^6 s^{-1}) and large strains (up to 10).

- Microstructure characterization using transmission electron microscopy (TEM) is needed to better understand the influence of various machining/burnishing conditions on microstructural changes near the surface. It will also reveal useful information on the transition of microstructures within the relatively thin featureless layers produced by machining (less than 20 µm).

- Electron backscatter diffraction (EBSD) can be used to gather information on how the crystallographic orientation changes during machining and burnishing. It will be of great value to understand how crystallographic orientation changes with temperature and deformation variables such as strain and strain-rate produced by various machining/burnishing conditions.

- The rake angle of the cutting tools was found to be a critical factor that influences the formation of featureless layers during machining based on the results of the numerical investigation. Machining experiments with varying rake angles need to be conducted to confirm this finding and it is possible that a thicker featureless layer (> 20 µm) can be produced at a more negative rake angle, which may further improve the corrosion resistance of the *AZ31B Mg* alloy.

- Only cooling conditions were investigated for the burnishing process. It is strongly recommended that the influence of burnishing speed, burnishing force, feed rate, etc., on surface integrity of burnished *Mg* alloys to be investigated.

- A better design of corrosion tests is needed to be able to quantitatively evaluate the corrosion performance of machined and burnished *Mg* samples. It is suggested that facing of a round bar to be conducted to produce a large flat surface area. Immersion method can be easily used when the exposed area is large enough.

- The finite element (FE) model used in the current study uses the standard Johnson-Cook flow stress equation and the Cockroft and Latham's fracture criterion to simulate serrated chip formation. The influence of DRX on flow stress was however not considered. It is important to develop a new flow stress model incorporating the DRX effects. The chip serration should come naturally without the use of any fracture

201

criterion and the model should achieve much better accuracy in predicting the grain size in machining.

- Optimization techniques can be used to find optimized processing parameters for both machining and burnishing that lead to the best corrosion performance of *AZ31B Mg* alloy in both 5% *NaCl* solution and *SBF*.

- Although only corrosion performance was primarily evaluated in the current study, the literature shows that grain refinement and compressive residual stress will also improve the fatigue life of *Mg* alloys (Zhang and Lindemann, 2005b; Wang et al., 2007). Fatigue tests can be conducted to evaluate the fatigue life of the machined and burnished *Mg* samples and it is expected that their performance will be better than the initial material.

APPENDIX A: SERRATED CHIP FORMATION

This appendix provides additional information to Section 6.2.4 on how the standard Johnson-Cook flow stress equation and Cockroft and Latham's fracture criterion were used in the present study to simulate the formation of serrated chips during machining of *AZ31B Mg* alloy. The three columns of pictures below show the changes of damage value, effective stress and effective strain respectively during a single chip segmentation cycle simulated by the DEFORM software. It was found from Section 6.2.6 that the critical damage value $D_{critical}$ for the *AZ31B Mg* alloy is 35. The elements with D values larger than 35 are displayed in red color in the left column. At Step 1616, a small red area starts to appear in the shear plane from the damage value figure and a small light blue area can be seen in the corresponding elements from the effective stress figure shown in the middle column. At Step 1625, the red area becomes bigger and a sample line is draw across the effective stress figure at corresponding positions which clearly shows that the stresses in those elements whose value are larger than 35 dropped to about 10% of the original value. In the last two pictures, more and more elements near the shear plane have damage values larger than 35 and it can be seen from the corresponding effective stress figure that the stress at these elements are significantly lower than their surrounding elements. This forced drop of flow stress by using the facture criterion crudely simulates the "flow softening" induced by dynamic recystallization. The present study shows that this approach led to reasonable results as long as the material constants involved are calibrated by experimental data.

Damage value, _D_   **Effective stress**   **Effective strain**

Step 1563

The _D_ value of these "red" elements exceed the critical value (35 and their flow stresses were dropped to 10% of the original stress.

Stress drops.

State Variable Distribution

204
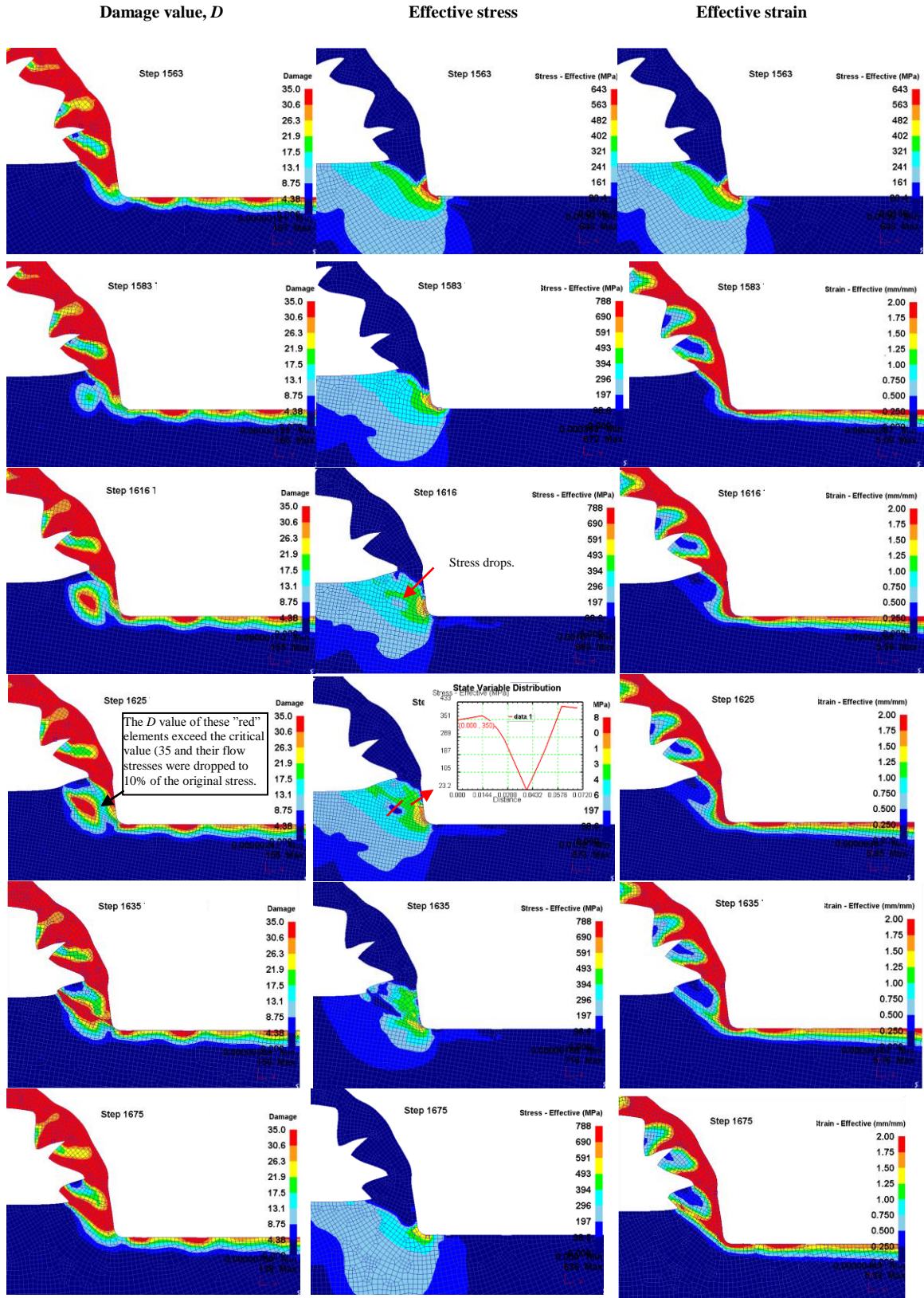
APPENDIX B: PREDICTED GRAIN SIZE DISTRIBUTION IN THE MACHINED CHIPS

The major objective of the user subroutine is to predict the grain size distribution on the machined surface and subsurface. All the material constants were calibrated using the experimental data from the workpiece surface. However, some useful information on the grain size distribution in the machined chips can also be provided by using the user subroutine. Different from the machined surface, the grain size distribution in the machined chips does not change significantly with different cooling methods, or tool edge radius. An example of the predicted grain size distribution in the chips is shown in the figure below. Although much more work is needed to make a solid conclusion, this preliminary simulation result is encouraging when compared with the experimental data. The interior of the chip segment is almost unchanged in the actual chip and agree with the simulated data. The grains near the tool-chip interface and between chip segments are very small in both the actual chip and the simulated chips.

Step 1743

Cryogenic,
rake angle = -7°,
$r_n = 70$ μm,
$V = 100$ m/min
$f = 0.1$ mm/rev

GSIZE

12.0
10.5
9.00
7.50
6.00
4.50
3.00
1.50
0.000
0.0305 Min
12.0 Max
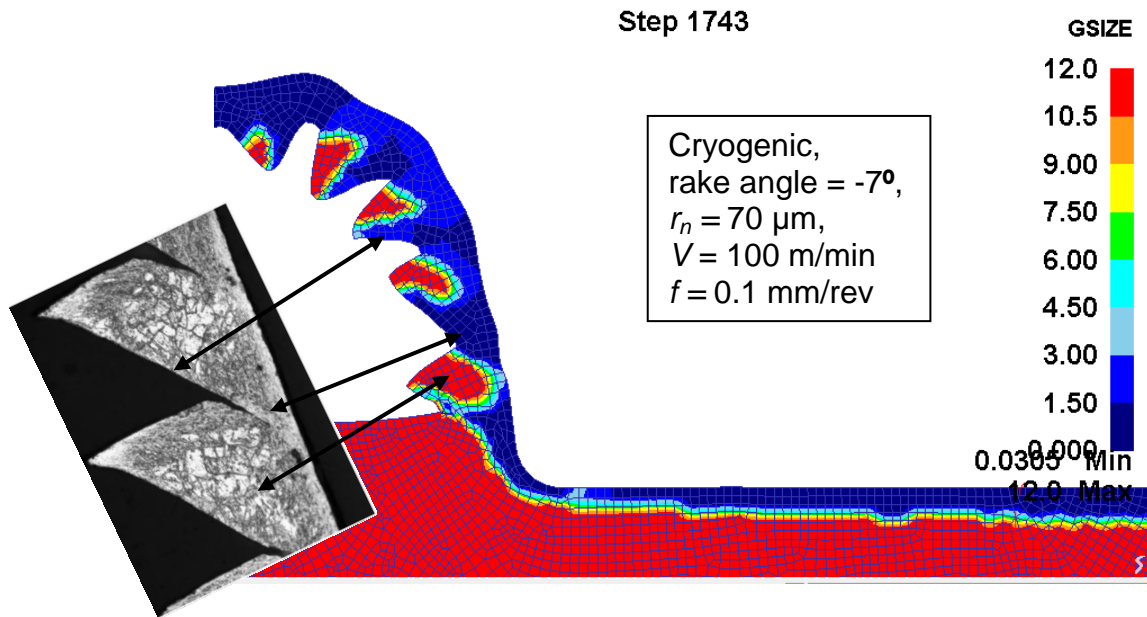
However, one major problem in the simulated chips is that DRX keeps occurring; the percentage of small grains becomes larger and larger (more and more blue areas in the above figure) with time (or steps). This phenomenon is reflected in the above picture where the red area in the chip segment becomes smaller from the bottom to the top. It was found that DEFORM could not break the chips and the plastic strain in the chips will be increased due to the bending of the chips. The accumulated strain will become larger than the critical strain and then DRX occurs. This problem needs to be solved before a good prediction of grain size can be achieved in the machined chips.

REFERENCES

Albrecht, P. (1960). "New Developments in the Theory of the Metal Cutting Process — Part 1 The Ploughing Process in Metal Cutting." *Transactions of the ASME* **82**: 348-358.

Alexander, L. (2007). Atomic Force Microscopy Grain Structure Characterization of Perpendicular Magnetic Recording Media. REU Research Accomplishments, National Nanotechnology Infrastructure Network**:** 134-135.

Alvarez-Lopez, M., M. D. Pereda, J. A. del Valle, M. Fernandez-Lorenzo, M. C. Garcia-Alonso, O. A. Ruano and M. L. Escudero (2010). "Corrosion behaviour of AZ31 magnesium alloy with different grain sizes in simulated biological fluids." *Acta Biomaterialia* **6**(5): 1763-1771.

Aung, N. N. and W. Zhou (2010). "Effect of grain size and twins on corrosion behaviour of AZ31B magnesium alloy." *Corrosion Science* **52**(2): 589-594.

Bai, Y. and B. Dodd (1992). Adiabatic Shear Localisation: Occurrence, Theories and Applications. Oxford, Pergamon Press.

Balakrishnan, A., B. Lee, T. Kim and B. Panigrahi (2008a). "Corrosion Behaviour of Ultra Fine Grained Titanium in Simulated Body Fluid for Implant Application." *Trends in Biomaterials and Artificial Organs* **22**(1): 58-64.

Beer, A. G. (2010). "The Role of Strain on the Recrystallization Behaviour of Hot Worked and Annealed Magnesium Alloy *Mg-3Al-1Zn*". *Proceeding of Magnesium Technology 2010*, Seattle, WA.

Ben Rhouma, A., C. Braham, M. E. Fitzpatrick, J. Ledion and H. Sidhom (2001). "Effects of surface preparation on pitting resistance, residual stress, and stress corrosion cracking in austenitic stainless steels." *Journal of Materials Engineering and Performance* **10**(5): 507-514.

Bermingham, M. J., J. Kirsch, S. Sun, S. Palanisamy and M. S. Dargusch (2011). "New observations on tool life, cutting forces and chip morphology in cryogenic machining *Ti-6Al-4V*." *International Journal of Machine Tools & Manufacture* **51**(6): 500-511.

Bharat, B. and Q. Jun (2003). "Phase contrast imaging of nanocomposites and molecularly thick lubricant films in magnetic media." *Nanotechnology* **14**(8): 886.

Birbilis, N., K. D. Ralston and C. H. J. Davies (2010a). "Revealing the relationship between grain size and corrosion rate of metals." *Scripta Materialia* **63**(12): 1201-1204.

Birbilis, N., K. D. Ralston, S. Virtanen, H. L. Fraser and C. H. J. Davies (2010b). "Grain character influences on corrosion of ECAPed pure magnesium." *Corrosion Engineering Science and Technology* **45**(3): 224-230.

Brown, T. L., S. Swaminathan, S. Chandrasekar, W. D. Compton, A. H. King and K. P. Trumble (2002). "Low-cost manufacturing process for nanostructured metals and alloys." *Journal of Materials Research* **17**(10): 2484-2488.

Calamaz, M., D. Coupard and F. Girot (2008). "A new material model for 2D numerical simulation of serrated chip formation when machining titanium alloy *Ti-6Al-4V*." *International Journal of Machine Tools & Manufacture* **48**(3-4): 275-288.

Calistes, R., S. Swaminathan, T. Murthy, C. Huang, C. Saldana, M. Shankar and S. Chandrasekar (2009). "Controlling gradation of surface strains and nanostructuring by large-strain machining." *Scripta Materialia* **60**(1): 17-20.

Caruso, S., S. Renzo, D. Umbrello, A. D. Jayal, O. W. Dillon and I. S. Jawahir (2011). "Finite Element Modeling of Microstructural Changes in Hard Turning." *Advanced Materials Research* **223**: 960-968.

Chandrasekar, S., R. Calistes, S. Swaminathan, T. G. Murthy, C. Huang, C. Saldana and M. R. Shankar (2009). "Controlling gradation of surface strains and nanostructuring by large-strain machining." *Scripta Materialia* **60**(1): 17-20.

Chandrasekar, S., Y. Guo, C. Saldana and W. D. Compton (2011). "Controlling deformation and microstructure on machined surfaces." *Acta Materialia* **59**(11): 4538-4547.

Chang, C., X. Du and J. Huang (2008). "Producing nanograined microstructure in *Mg–Al–Zn* alloy by two-step friction stir processing." *Scripta Materialia* **59**(3): 356-359.

Chang, C. I. (2007). "Achieving Ultrafine Nano Grains in *AZ31 Mg* Based Alloys and Composites by Friction Stir Processing", Ph.D. Dissertation, Department of Materials Science and Engineering, Sun Yat-Sen University, Kaohsiung, Taiwan, Repulic of China.

Chang, C. I., X. H. Du and J. C. Huang (2007). "Achieving ultrafine grain size in *Mg-Al-Zn* alloy by friction stir processing." *Scripta Materialia* **57**(3): 209-212.

Chang, C. I., C. J. Lee and J. C. Huang (2004). "Relationship between grain size and Zener-Holloman parameter during friction stir processing in *AZ31 Mg* alloys." *Scripta Materialia* **51**(6): 509-514.

Chang, T.-C., J.-Y. Wang, C.-M. O and S. Lee (2003). "Grain refining of magnesium alloy *AZ31* by rolling." *Journal of Materials Processing Technology* **140**(1-3): 588-591.

Cherry, D. K., E. Hing, D. A. Woodwell and E. A. Rechtsteiner (2008). National Ambulatory Medical Care Survey: 2006 Summary. National Health Statistics Reports.

Chou, Y. K. and C. J. Evans (1999). "White layers and thermal modeling of hard turned surfaces." *International Journal of Machine Tools & Manufacture* **39**(12): 1863-1881.

Cockcroft, M. G. and D. J. Latham (1968). "Ductility and workability of metals." *Journal Institute of Metals* **96** 33-39.

Denkena, B. and A. Lucas (2007). "Biocompatible magnesium alloys as absorbable implant materials - Adjusted surface and subsurface properties by machining processes." *CIRP Annals-Manufacturing Technology* **56**(1): 113-116.

Dhananchezian, M. and M. P. Kumar (2011). "Cryogenic turning of the *Ti-6Al-4V* alloy with modified cutting tool inserts." *Cryogenics* **51**(1): 34-40.

Dhar, N. R. and M. Kamruzzaman (2007). "Cutting temperature, tool wear, surface roughness and dimensional deviation in turning *AISI-4037* steel under cryogenic condition." *International Journal of Machine Tools & Manufacture* **47**(5): 754-759.

Ding, R. and Z. X. Guo (2004). "Microstructural evolution of a *Ti–6Al–4V* alloy during β-phase processing: experimental and simulative investigations." *Materials Science and Engineering: A* **365**(1–2): 172-179.

Duan, C. Z. and M. J. Wang (2005). "Some metallurgical aspects of chips formed in high speed machining of high strength low alloy steel." *Scripta Materialia* **52**(10): 1001-1004.

Ee, K. C., O. W. Dillon and I. S. Jawahir (2005). "Finite element modeling of residual stresses in machining induced by cutting using a tool with finite edge radius." *International Journal of Mechanical Sciences* **47**(10): 1611-1628.

Fatemi-Varzaneh, S. M., A. Zarei-Hanzaki and H. Beladi (2007). "Dynamic recrystallization in AZ31 magnesium alloy." *Materials Science and Engineering a-Structural Materials Properties Microstructure and Processing* **456**(1-2): 52-57.

Field, M. and J. F. Kahles (1964). "The Surface Integrity of Machined and Ground High Strength Steels." *DMIC Report* **210**: 54–77.

Field, M. and J. F. Kahles (1971). "Review of surface integrity of machined components." *Annals of the CIRP* **20**(2): 153–162.

Field, M., J. F. Kahles and J. T. Cammett (1972). "Review of measuring methods for surface integrity." *Annals of the CIRP* **21**: 219-238.

Filice, L., F. Micari, S. Rizzuti and D. Umbrello (2007). "A critical analysis on the friction modelling in orthogonal machining." *International Journal of Machine Tools & Manufacture* **47**(3-4): 709-714.

Garrett, W. E., Jr., M. F. Swiontkowski, J. N. Weinstein, J. Callaghan, R. N. Rosier, D. J. Berry, J. Harrast and G. P. Derosa (2006). "American Board of Orthopaedic Surgery Practice of the Orthopaedic Surgeon: Part-II, certification examination case mix." *Journal of Bone and Joint Surgery* **88**(3): 660-667.

Ghosh, R., Z. Zurecki and J. H. Frey (2003). "*Cryogenic Machining with Brittle Tools and Effects on Tool Life*." Proceedings of 2003 ASME International Mechanical Engineering Congress & Exposition, Washington, D.C.

Guo, Y., C. Saldana, W. D. Compton and S. Chandrasekar (2011). "Controlling deformation and microstructure on machined surfaces." *Acta Materialia* **59**(11): 4538-4547.

Guo, Y. B. and M. Salahshoor (2010). "Process mechanics and surface integrity by high-speed dry milling of biodegradable magnesium-calcium implant alloys." *CIRP Annals-Manufacturing Technology* **59**(1): 151-154.

Hasenpouth, D. (2010). "Tensile High Strain Rate Behavior of *AZ31B* Magnesium Alloy Sheet". Master thesis. Department of Mechanical Engineering, University of Waterloo, Waterloo, Ontario, Canada.

Hashimoto, F., Y. B. Guo and A. W. Warren (2006). "Surface integrity difference between hard turned and ground surfaces and its impact on fatigue life." *CIRP Annals-Manufacturing Technology* **55**(1): 81-84.

Hashimoto, F., S. N. Melkote, R. Singh and R. Kalil (2009). "Effect of finishing methods on surface characteristics and performance of precision components in rolling/sliding contact." *International Journal of Machining and Machinability of Materials* **6**(1/2): 3-15.

Hassan, A. M. and A. S. Al-Bsharat (1996). "Influence of burnishing process on surface roughness, hardness, and microstructure of some non-ferrous metals." *Wear* **199**(1): 1-8.

Henriksen, E. K. (1951). "Residual stresses in machined surfaces." *Transactions of American Society of Mechanical Engineer* **73**: 69-74.

Hibbins, S. G. (1998). "*Investigation of Heat Transfer in DC Casting of Magnesium Alloys.*" Proceedings of the International Symposium on Light Metals, Calgary, AB, Canada.

Hong, S. Y., Y. Ding and J. Jeong (2002). "Experimental evaluation of friction coefficient and liquid nitrogen lubrication effect in cryogenic machining." *Machining Science and Technology* **6**(2): 235-250.

Hong, S. Y. and Y. C. Ding (2001). "Cooling approaches and cutting temperatures in cryogenic machining of *Ti-6Al-4V*." *International Journal of Machine Tools & Manufacture* **41**(10): 1417-1437.

Hong, S. Y., I. Markus and W. Jeong (2001). "New cooling approach and tool life improvement in cryogenic machining of titanium alloy *Ti-6Al-4V*." *International Journal of Machine Tools & Manufacture* **41**(15): 2245-2260.

Hornbach, D., P. Prevey and E. Loftus (2006). "Application of Low Plasticity Burnishing (LPB) to Improve the Fatigue Performance of *Ti-6Al-4V* Femoral Hip Stems." *Journal of ASTM International* **3**.

Hoseini, M., A. Shahryari, S. Omanovic and J. A. Szpunar (2009). "Comparative effect of grain size and texture on the corrosion behaviour of commercially pure titanium processed by equal channel angular pressing." *Corrosion Science* **51**(12): 3064-3067.

Huang, G., B. Qian, L. Wang and J. J. Jonas (2007a). "Study on the critical conditions for initial dyanmic recrystallization of AZ31 Magnesium alloy." *Rare Metal Materials and Engineering* **36**: 2080-2083.

Huang, J. C., C. I. Chang and X. H. Du (2007b). "Achieving ultrafine grain size in *Mg-Al-Zn* alloy by friction stir processing." *Scripta Materialia* **57**(3): 209-212.

Jawahir, I. S., E. Brinksmeier, R. M'Saoubi, D. K. Aspinwall, J. C. Outeiro, D. Meyer, D. Umbrello and A. D. Jayal (2011). "Surface integrity in material removal processes: Recent advances." *CIRP Annals - Manufacturing Technology* **60**(2): 603-626.

Kenda, J., F. Pusavec and J. Kopac (2011). "Analysis of Residual Stresses in Sustainable Cryogenic Machining of Nickel Based Alloy---*Inconel 718*." *Journal of Manufacturing Science and Engineering* **133**(4): 041009-041007.

Klocke, F. and J. Liermann (1998). "Roller burnishing of hard turned surfaces." *International Journal of Machine Tools & Manufacture* **38**(5-6): 419-423.

Kurihara, K., T. Tozawa and H. Kato (1981). "Cutting Temperature of Magnesium Alloys at Extremely High Cutting Speeds " *Journal of Japan Institute of Light Metals* **31**(4): 255-260.

Langdon, T. G., K. Matsubara, Y. Miyahara and Z. Horita (2003). "Developing superplasticity in a magnesium alloy through a combination of extrusion and ECAP." *Acta Materialia* **51**(11): 3073-3084.

Leverant, G., B. Langer, A. Yuen and S. Hopkins (1979). "Surface residual stresses, surface topography and the fatigue behavior of *Ti-6AI-4V*." *Metallurgical and Materials Transactions A* **10**(2): 251-257.

Li, W., N. Tao and K. Lu (2008). "Fabrication of a gradient nano-micro-structured surface layer on bulk copper by means of a surface mechanical grinding treatment." *Scripta Materialia* **59**(5): 546-549.

Liang, G. L. and S. Q. Yuan (2008). "Study on the temperature measurement of *AZ31B* Magnesium Alloy in Gas Tungsten Arc Welding." *Materials Letters* **62**(16): 2282-2284.

Liu, L. M., M. S. Chi, R. S. Huang, G. Song and Y. Zhou (2005). "Infrared measurement and simulation of magnesium alloy welding temperature field." *Science in China Series E-Engineering & Materials Science* **48**(6): 706-715.

Liu, M., D. Qiu, M. C. Zhao, G. Song and A. Atrens (2008). "The effect of crystallographic orientation on the active corrosion of pure magnesium." *Scripta Materialia* **58**(5): 421-424.

Liu, X., R. E. DeVor, S. G. Kapoor and K. F. Ehmann (2004). "The mechanics of machining at the microscale: Assessment of the current state of the science." *Journal of Manufacturing Science and Engineering-Transactions of the Asme* **126**(4): 666-678.

Lu, K. and J. Lu (1999). "Surface nanocrystallization (SNC) of metallic materials-presentation of the concept behind a new approach." *J. Mater. Sci. Technol.* **15**: 193-197.

Luo, A. A. (2002). "Magnesium: Current and potential automotive applications." *Jom-Journal of the Minerals Metals & Materials Society* **54**(2): 42-48.

M'Saoubi, R., J. C. Outeiro, B. Changeux, J. L. Lebrun and A. Morão Dias (1999). "Residual stress analysis in orthogonal machining of standard and resulfurized *AISI 316L* steels." *Journal of Materials Processing Technology* **96**(1-3): 225-233.

Makar, G. L. and J. Kruger (1990). "Corrosion Studies of Rapidly Solidified Magnesium Alloys." *Journal of the Electrochemical Society* **137**(2): 414-421.

Matsumoto, Y., F. Hashimoto and G. Lahoti (1999). "Surface Integrity Generated by Precision Hard Turning." *CIRP Annals - Manufacturing Technology* **48**(1): 59-62.

McBride, E. D. (1938). "Absorbable metal in bone surgery." *Journal of the American Medical Association* **111**(27): 2464-2467.

Meyers, M. A., J. C. LaSalvia, V. F. Nestorenko, Y. J. Chen and B. K. Kad (1997). *Dynamic recrystallization in high strain rate deformation*. 3rd International Conference on Recrystallization and Related Phenomena: 279-286.

Meyers, M. A., V. F. Nesterenko, J. C. LaSalvia and Q. Xue (2001). "Shear localization in dynamic deformation of materials: microstructural evolution and self-organization." *Materials Science and Engineering a-Structural Materials Properties Microstructure and Processing* **317**(1-2): 204-225.

Miller, R. M., T. R. Bieler and S. L. Semiatin (1999). "Flow softening during hot working of *Ti-6Al-4V* with a lamellar colony microstructure." *Scripta Materialia* **40**(12): 1387-1393.

Mohanty, M., S. Baby and K. V. Menon (2003). "Spinal fixation device: a 6-year postimplantation study." *Journal of Biomaterials Applications* **18**(2): 109-121.

Mughrabi, H. and H. W. Hoppel (2010). "Cyclic deformation and fatigue properties of very fine-grained metals and alloys." *International Journal of Fatigue* **32**(9): 1413-1427.

Nasr, M. N. A., E. G. Ng and M. A. Elbestawi (2007). "Modelling the effects of tool-edge radius on residual stresses when orthogonal cutting *AISI 316L*." *International Journal of Machine Tools & Manufacture* **47**(2): 401-411.

Noyan, I. C. and J. B. Cohen (1987). Residual stress: measurement by diffraction and interpretation. New York, N.Y., Springer.

Obikawa, T. and E. Usui (1996). "Computational machining of titanium alloy - Finite element modeling and a few results." *Journal of Manufacturing Science and Engineering-Transactions of the Asme* **118**(2): 208-215.

Orlov, D., K. D. Ralston, N. Birbilis and Y. Estrin (2011). "Enhanced corrosion resistance of *Mg* alloy *ZK60* after processing by integrated extrusion and equal channel angular pressing." *Acta Materialia* **59**(15): 6176-6186.

Outeiro, J. C., A. M. Dias and I. S. Jawahir (2006a). "On the effects of residual stresses induced by coated and uncoated cutting tools with finite edge radii in turning operations." *CIRP Annals-Manufacturing Technology* **55**(1): 111-116.

Outeiro, J. C., R. Kandibanda, J. C. Pina, suffix, Jr, O. W. Dillon and I. S. Jawahir (2010). "Size-effects and surface integrity in machining and their influence on product sustainability." *International Journal of Sustainable Manufacturing* **2**(1): 112-126.

Outeiro, J. C., D. Umbrello and R. M'Saoubi (2006b). "Experimental and FEM analysis of cutting sequence on residual stresses in machined layers of *AISI 316L* steel." *Materials Science Forum* **524-525**: 179-184.

Outeiro, J. C., D. Umbrello and R. M'Saoubi (2006c). "Experimental and numerical modelling of the residual stresses induced in orthogonal cutting of *AISI 316L* steel." *International Journal of Machine Tools & Manufacture* **46**(14): 1786-1794.

Pang, C. H., P. Hing and A. See (2002). "Application of phase-imaging tapping-mode atomic-force microscopy to investigate the grain growth and surface morphology of *TiSi₂*." *Journal of Vacuum Science & Technology B: Microelectronics and Nanometer Structures* **20**(5): 1866.

Pietak, A. M., M. P. Staiger, J. Huadmai and G. Dias (2006). "Magnesium and its alloys as orthopedic biomaterials: A review." *Biomaterials* **27**(9): 1728-1734.

Poulachon, G., A. Moisan and I. S. Jawahir (2001). "Tool-wear mechanisms in hard turning with polycrystalline cubic boron nitride tools." *Wear* **250**(1–12): 576-586.

Prevéy, P. (1998). Burnishing method and apparatus for providing a layer of compressive residual stress in the surface of a workpiece. *US Patent 5,826,453*.

Prevéy, P. S. (1987). The Measurement of Subsurface Residual Stress & Cold Work Distributions in Nickel Base Alloys. *Residual Stress in Design, Process and Materials Selection*. W. B. Young**:** 11-19.

Prevéy, P. S. (2000). *The effect of cold work on the thermal stability of residual compression in surface enhanced IN718*. 20th ASM Materials Solutions Conference & Exposition, St. Louis, Missouri.

Prevéy, P. S., N. Jayaraman and R. Ravindranath (2010). "Fatigue Life Extension of Steam Turbine Alloys Using Low Plasticity Burnishing (LPB)." *ASME Conference Proceedings* **2010**(44021): 2277-2287.

Pu, Z., S. Yang, G. L. Song, O. W. Dillon Jr, D. A. Puleo and I. S. Jawahir (2011). "Ultrafine-grained surface layer on *Mg-Al-Zn* alloy produced by cryogenic burnishing for enhanced corrosion resistance." *Scripta Materialia* **65**(6): 520-523.

Pusavec, F., H. Hamdi, J. Kopac and I. S. Jawahir (2011). "Surface integrity in cryogenic machining of nickel based alloy-*Inconel 718*." *Journal of Materials Processing Technology* **211**(4): 773-783.

Rajesham, S. and J. C. Tak (1989). "A Study on the Surface Characteristics of Burnished Components." *Journal of Mechanical Working Technology* **20**: 129-138.

Ralston, K. D. and N. Birbilis (2010). "Effect of Grain Size on Corrosion: A Review." *Corrosion* **66**(7).

Ramesh, A., S. N. Melkote, L. F. Allard, L. Riester and T. R. Watkins (2005). "Analysis of white layers formed in hard turning of *AISI 52100* steel." *Materials Science and Engineering a-Structural Materials Properties Microstructure and Processing* **390**(1-2): 88-97.

Reedhill, R. E. and W. D. Robertson (1957). "The Crystallographic Characteristics of Fracture in Magnesium Single Crystals." *Acta Metallurgica* **5**(12): 728-737.

Sadat, A. B. and J. A. Bailey (1987). "Residual-Stresses in Turned *AISI-4340* Steel." *Experimental Mechanics* **27**(1): 80-85.

Sakai, T., A. Hashimoto, G. Hamada and H. Utsunomiya (2011). "Deformation and Evolution of Microstructure and Texture during High Speed Heavy Rolling of *AZ31* Magnesium Alloy Sheet". *Proceeding of Magnesium Technology 2011*. San Diego, CA.

Salahshoor, M. and Y. B. Guo (2011). "Surface integrity of biodegradable Magnesium-Calcium orthopedic implant by burnishing." *J Mech Behav Biomed Mater* **4**(8): 1888-1904.

Sasahara, H. (2005). "The effect on fatigue life of residual stress and surface hardness resulting from different cutting conditions of *0.45%C* steel." *International Journal of Machine Tools & Manufacture* **45**(2): 131-136.

Scheel, J. E., P. S. P. II and D. J. Hornbach (2010). *The Effect of Surface Enhancement On the Corrosion Properties, Fatigue Strength, And Degradation of Aircraft Aluminum*. CORROSION 2010, San Antonio, TX.

Shi, Y. N., H. Q. Sun, M. A. Zhang and K. Lu (2007). "Plastic strain-induced grain refinement in the nanometer scale in a *Mg* alloy." *Acta Materialia* **55**(3): 975-982.

Shivpuri, R., J. Hua, P. Mittal and A. K. Srivastava (2002). "Microstructure-mechanics interactions in modeling chip segmentation during titanium machining." *CIRP Annals-Manufacturing Technology* **51**(1): 71-74.

Song, D., A. B. Ma, J. H. Jiang, P. H. Lin, D. H. Yang and J. F. Fan (2010a). "Corrosion behavior of equal-channel-angular-pressed pure magnesium in NaCl aqueous solution." *Corrosion Science* **52**(2): 481-490.

Song, G., A. Atrens and D. St. John (2001). "An Hydrogen Evolution Method for the Estimation of the Corrosion Rate of Magnesium Alloys". *Proceeding of Magnesium Technology 2001*. New Orleans, LA.

Song, G. and Z. Xu (2011). "Effect of Microstructure Evolution on Corrosion of Different Crystal Surfaces of *AZ31 Mg* alloy in a Chloride Containing Solution." *Corrosion Science*: in press.

Song, G. L. (2009). "Effect of tin modification on corrosion of *AM70* magnesium alloy." *Corrosion Science* **51**(9): 2063-2070.

Song, G. L., R. Mishra and Z. Q. Xu (2010b). "Crystallographic orientation and electrochemical activity of *AZ31 Mg* alloy." *Electrochemistry Communications* **12**(8): 1009-1012.

Song, G. L. and S. Z. Song (2007). "A possible biodegradable magnesium implant material." *Advanced Engineering Materials* **9**(4): 298-302.

Song, G. L. and Z. Q. Xu (2010). "The surface, microstructure and corrosion of magnesium alloy *AZ31* sheet." *Electrochimica Acta* **55**(13): 4148-4161.

Sun, H., Y. Shi, M. Zhang and K. Lu (2007). "Plastic strain-induced grain refinement in the nanometer scale in a *Mg* alloy." *Acta Materialia* **55**(3): 975-982.

Swarninathan, S., M. R. Shankar, S. Lee, J. Hwang, A. H. King, R. F. Kezar, B. C. Rao, T. L. Brown, S. Chandrasekar, W. D. Compton and K. P. Trumble (2005). "Large strain deformation and ultra-fine grained materials by machining." *Materials Science and Engineering a-Structural Materials Properties Microstructure and Processing* **410**: 358-363.

Tao, N. R., Z. B. Wang, W. P. Tong, M. L. Sui, J. Lu and K. Lu (2002). "An investigation of surface nanocrystallization mechanism in Fe induced by surface mechanical attrition treatment." *Acta Materialia* **50**(18): 4603-4616.

Tao, S. and D. Y. Li (2006). "Tribological, mechanical and electrochemical properties of nanocrystalline copper deposits produced by pulse electrodeposition." *Nanotechnology* **17**(1): 65-78.

Thiele, J. D., S. N. Melkote, R. A. Peascoe and T. R. Watkins (2000). "Effect of cutting-edge geometry and workpiece hardness on surface residual stresses in finish hard turning of *AISI 52100* steel." *Journal of Manufacturing Science and Engineering-Transactions of the Asme* **122**(4): 642-649.

To, S., W. B. Lee and C. F. Cheung (2003). "Orientation changes of aluminium single crystals in ultra-precision diamond turning." *Journal of Materials Processing Technology* **140**: 346-351.

Tönshoff, H. K. and J. Winkler (1997). "The influence of tool coatings in machining of magnesium." *Surface and Coatings Technology* **94-95**: 610-616.

Troitskii, V. V. and D. N. Tsitrin (1944). "The resorbing metallic alloy 'Osteosinthezit' as material for fastening broken bone." *Khirurgiia* **8**: 41-44.

Turnbull, A., K. Mingard, J. D. Lord, B. Roebuck, D. R. Tice, K. J. Mottershead, N. D. Fairweather and A. K. Bradbury (2011). "Sensitivity of stress corrosion cracking of stainless steel to surface machining and grinding procedure." *Corrosion Science* **53**(10): 3398-3415.

Umbrello, D. (2008). "Finite element simulation of conventional and high speed machining of *Ti6Al4V* alloy." *Journal of Materials Processing Technology* **196**(1-3): 79-87.

Umbrello, D., J. Hua and R. Shivpuri (2004). "Hardness-based flow stress and fracture models for numerical simulation of hard machining *AISI 52100* bearing steel." *Materials Science and Engineering a-Structural Materials Properties Microstructure and Processing* **374**(1-2): 90-100.

Umbrello, D., A. D. Jayal, S. Caruso, O. W. Dillon and I. S. Jawahir (2010a). "Modeling of White and Dark Layer Formation in Hard Machining of *AISI 52100* Bearing Steel." *Machining Science and Technology* **14**(1): 128-147.

Umbrello, D., R. M'Saoubi and J. C. Outeiro (2007). "The influence of Johnson-Cook material constants on finite element simulation of machining of *AISI 316L* steel." *International Journal of Machine Tools & Manufacture* **47**(3-4): 462-470.

Umbrello, D., J. C. Outeiro, R. M'Saoubi, A. D. Jayal and I. S. Jawahir (2010b). "A numerical model incorporating the microstructure alteration for predicting residual stresses in hard machining of *AISI 52100* steel." *CIRP Annals-Manufacturing Technology* **59**(1): 113-116.

Umbrello, D., Z. Pu, S. Caruso, J. C. Outeiro, A. D. Jayal, J. O.W. Dillon and I. S. Jawahir (2012). "The effects of Cryogenic Cooling on Surface Integrity in Hard Machining." *Procedia Engineering* **19***: 371-376.

Velásquez, J. D. P., A. Tidu, B. Bolle, P. Chevrier and J. J. Fundenberger (2010). "Sub-surface and surface analysis of high speed machined *Ti-6Al-4V* alloy." *Materials Science and Engineering: A* **527**(10-11): 2572-2578.

Villegas, J. C., L. L. Shaw, K. Dai, W. Yuan, J. Tian, P. K. Liaw and D. L. Klarstrom (2005). "Enhanced fatigue resistance of a nickel-based hastelloy induced by a surface nanocrystallization and hardening process." *Philosophical Magazine Letters* **85**(8): 427-437.

Wang, H., Y. Estrin, H. Fu, G. Song and Z. Zuberova (2007). "The effect of pre-processing and grain structure on the bio-corrosion and fatigue resistance of magnesium alloy *AZ31*." *Advanced Engineering Materials* **9**(11): 967-972.

Wang, L., G. Huang and Y. Fan (2002). "Investigation on hot deform ation behavior of *AZ31* magnesium." *Journal ofChongqing University-English Edition* **1**: 57-59.

Wang, T. S., J. K. Yu and B. F. Dong (2006). "Surface nanocrystallization induced by shot peening and its effect on corrosion resistance of *1Cr18Ni9Ti* stainless steel." *Surface & Coatings Technology* **200**(16-17): 4777-4781.

Wang, X. Y. and D. Y. Li (2002). "Mechanical and electrochemical behavior of nanocrystalline surface of *304* stainless steel." *Electrochimica Acta* **47**(24): 3939-3947.

Watanabe, H., H. Tsutsui, T. Mukai, H. Ishikawa, Y.Okanda, M. Kohzu, K. Higashi (2001). "Grain Size Control of Commercial Wrought Mg-Al-Zn Alloys Utilizing Dynamic Recrystallization." Materials Transactions **42** (7): 1200-1205.

Witte, F. (2010). "The history of biodegradable magnesium implants: A review." *Acta Biomaterialia* **6**(5): 1680-1692.

Wusatowska-Sarnek, A., B. Dubiel, A. Czyrska-Filemonowicz, P. Bhowal, N. Ben Salah and J. Klemberg-Sapieha (2011). "Microstructural Characterization of the White Etching Layer in Nickel-Based Superalloy." *Metallurgical and Materials Transactions A*: 1-13.

Xin, R., B. Li, L. Li and Q. Liu (2011). "Influence of texture on corrosion rate of *AZ31* Mg alloy in 3.5 wt.% *NaCl*." *Materials & Design* **32**(8-9): 4548-4552.

Yen, Y.-C., A. Jain and T. Altan (2004). "A finite element analysis of orthogonal machining using different tool edge geometries." *Journal of Materials Processing Technology* **146**(1): 72-81.

Zhang, P., J. Lindemann, A. Kiefer and C. Leyens (2005). "Mechanical surface treatments on the high-strength wrought magnesium alloy *AZ80*." *Proceeding of the 9th International Conference on Shot Peening*: 308-313.

Zhang, P. and J. Lindemann (2005a). "Effect of roller burnishing on the high cycle fatigue performance of the high-strength wrought magnesium alloy *AZ80*." *Scripta Materialia* **52**(10): 1011-1015.

Zhang, P. and J. Lindemann (2005b). "Influence of shot peening on high cycle fatigue properties of the high-strength wrought magnesium alloy *AZ80*." *Scripta Materialia* **52**(6): 485-490.

Zhang, Y. S., Z. Han, K. Wang and K. Lu (2006). "Friction and wear behaviors of nanocrystalline surface layer of pure copper." *Wear* **260**(9-10): 942-948.

Zinn, W. and B. Scholtes (1999). "Mechanical surface treatments of lightweight materials - Effects on fatigue strength and near-surface microstructures." *Journal of Materials Engineering and Performance* **8**(2): 145-151.

Znamenskii, M. S. (1945). "Metallic osteosynthesis by means of an apparatus made of resorbing metal." *Khirurgiia* **12**: 60-63.

Zurecki, Z., R. Ghosh and J. H. Frey (2003). "Investigation of White Layers Formed in Conventional and Cryogenic Hard Turning of Steels." *ASME Conference Proceedings* **2003**(37203): 211-220.

<center>**VITA**</center>

<u>Name</u>

Zhengwen Pu

<u>Date and Place of Birth</u>

April, 18th, 1986

Laian County, Anhui Province, China

<u>Education</u>

B.S. in Mechanical Engineering, China University of Geosciences, Beijing, China
July, 2007

<u>Experience</u>

- Machining Application Engineer (11/2011 ~ present), Diamond Innovations/Sandvik, Columbus, OH
- Research Assistant (05/2008 ~ 11/2011), Machining Research Group, Institute for Sustainable Manufacturing, University of Kentucky, Lexington, KY
- Research Intern (05/2010 ~ 09/2010), Chemical Sciences & Materials Systems Lab, Research and Development, General Motors, Warren, MI
- Teaching Assistant (08/2007 ~ 05/2010), Department of Mechanical Engineering, University of Kentucky, Lexington, KY

<u>Journal Papers</u>

- **Pu, Z.**, J. C. Outeiro, A. C. Batista, O. W. Dillon Jr, D. A. Puleo and I. S. Jawahir (2012). "Enhanced surface integrity of *AZ31B Mg* alloy by cryogenic machining towards improved functional performance of machined components." *International Journal of Machine Tools and Manufacture* **56**: 17-27.
- **Pu, Z.,** G. L. Song, S. Yang, J. C. Outeiro, O. W. Dillon Jr, D. A. Puleo and I. S. Jawahir (2012). "Grain refined and basal textured surface produced by burnishing for improved corrosion performance of *AZ31B Mg* alloy." *Corrosion Science* **57**: 192-201.
- **Pu, Z.,** S. Yang, G. L. Song, O. W. Dillon Jr, D. A. Puleo and I. S. Jawahir (2011). "Ultrafine-grained surface layer on *Mg-Al-Zn* alloy produced by cryogenic burnishing for enhanced corrosion resistance." *Scripta Materialia* **65**(6): 520-523.

Conference Papers

- **Pu, Z.**, J. C. Outeiro, A. C. Batista, O. W. Dillon, D. A. Puleo and I. S. Jawahir. "Surface Integrity in Dry and Cryogenic Machining of *AZ31B Mg* Alloy with Varying Cutting Edge Radius Tools." *Procedia Engineering* **19**: 282-287 (1st CIRP Conference on Surface Integrity, Bremen, Germany, 2012).
- Umbrello, D., **Z. Pu**, S. Caruso, J. C. Outeiro, A. D. Jayal, O. W. Dillon and I. S. Jawahir. "The effects of Cryogenic Cooling on Surface Integrity in Hard Machining." *Procedia Engineering* **19**: 371-376 (1st CIRP Conference on Surface Integrity, Bremen, Germany, 2012).
- **Pu**, **Z.**, O.W. Dillon, Jr., I.S. Jawahir. "Analysis of Surface Integrity in Dry and Cryogenic Machining of *AZ31B Mg* Alloys", *Advanced Materials Research* **223:** 439-448 (13th CIRP Conference on Modeling of Machining Operations, Sintra, Portugal, 2011).
- **Pu, Z.**, G.-L. Song, Shu Yang, O.W. Dillon, Jr., D. A. Puleo, I.S. Jawahir, "Cryogenic Burnishing of *AZ31B Mg* Alloy for Enhanced Corrosion Resistance", *Proceeding of Magnesium Technology 2011*, TMS Annual Meeting & Exhibition, San Diego, California, 2011.
- Yang, S., **Z. Pu**, D.A. Puleo, O.W. Dillon, Jr., I.S. Jawahir, "Cryogenic Processing of Biomaterials for Improved Surface Integrity and Product Sustainability", *Proceedings of the 8th Global Conference on Sustainable Manufacturing*, Abu Dhabi, UAE, 2010.
- **Pu, Z.,** I. S. Jawahir, O. W. Dillon, Jr., D. A. Puleo, "Microstructural changes of *AZ31* magnesium alloys induced by cryogenic machining and its influence on corrosion resistance in simulated body fluid for biomedical applications", *Proceedings of 2010 ASME International Manufacturing Science and Engineering Conference,* Erie, PA, 2010.
- **Pu, Z.**, D. A. Puleo, O.W. Dillon, Jr., I.S. Jawahir, "Controlling the biodegradation rate of magnesium-based implants through surface nanocrystallization induced by cryogenic machining", *Proceeding of Magnesium Technology 2010*, TMS Annual Meeting & Exhibition, Seattle, WA, 2010.